STUDIES OF COOL AND EVOLVED STARS

Thesis submitted for the degree of

Doctor of Philosophy (Science)

in

Physics (Experimental)

by

SUPRIYO GHOSH

Department of Physics

University of Calcutta

March, 2019

To my parents & niece ...

Acknowledgement

This thesis is an outcome of years of research that has been done since I joined S. N. Bose National Centre for Basic Sciences (SNBNCBS), Kolkata. By that time, I have interacted with a great number of people, who have contributed in assorted ways to complete this research work. At the very outset of winding up Doctoral thesis, I would like to take this opportunity to convey my heartiest gratitude to them all in my humble acknowledgement.

First and foremost I owe my sincerest gratitude to my supervisor, Dr. Soumen Mondal, for his excellent guidance, enthusiasm, caring, support and patience that have made the years of working under him pleasant and memorable. I feel extremely lucky for having such a nice human being and charismatic personality as my supervisor. Sir, it has been a tremendous honour to work with you. He has always been there for me whenever I needed him and yet has given me the space to become a confident and independent researcher. I am indeed indebted to him for all the extra effort he wholeheartedly put in. This research work would not have been able to see the daylight without his sincere help. I am sure that his valuable advice and guidance will show me the right way in my future endeavours.

I take this opportunity to offer my profound gratitude to Dr. Ramkrishna Das for his insightful discussion and crucial contribution. I gratefully thank him for his guidance about spectroscopic data reduction, which is a backbone of this research and so to this thesis.

I gratefully acknowledge Prof. Sandip K. Chakrabarti for his valuable suggestions and comments on my research works during annual reviews. His deep commitment and attitude towards science have always been a source of inspiration to me. I am very much thankful to Prof. M. A. T. Groenewegen for helpful discussions and valuable suggestions on More of Dusty code, which I used for this thesis work. I would like to express my deep gratitude to Joe Philip Ninan for helpful discussions and valuable suggestions about the data reduction on the TIRSPEC pipeline.

I intend to pay my tribute to SNBNCBS for given me the opportunity to express myself in the global platform, for funding my research, and for providing me with excellent research facilities and a calm, cosy, peaceful environment for carrying out my research work. I would also like to offer thanks to the academic section, all the academic and non-academic staff members of SNBNCBS for their co-operation and support during the entire period of my Ph.D programme.

A significant time of my Ph.D tenure, I spent at CREST, Bangalore and Mt. Abu for scientific observations with 2.01 m Himalayan Chandra Telescope, operated by the Indian Institute of Astrophysics, Bangalore and 1.2 m Mt Abu telescope, operated by the Physical Research Laboratory, Ahmedabad, respectively. I take this opportunity to express my heartfelt thanks to all the staff of IAO, Hanle and CREST, Hosakote, who made the observations possible by losing out on sleep. In particular, I am grateful to Pramod, Venki, Kiran, Rahul, Prabhu, and Laxmi for their help and co-operation to maximize the allocated telescope time. I also convey my thank to the staff of Mt. Abu observatory.

I am deeply indebted to all the members of observational astronomy group in SNBNCBS. I feel proud that I have had the pleasure and privilege to work with them. I would never

forget their suggestions and helps. I would also like to convey my gratitude to all other Post Doctorate Fellows, Research Scholars, Project students and Integrated PhD students for giving me friendship and a memorable life during my stay at SNBNCBS hostel.

Collective and individual acknowledgement is also owed to my beloved seniors: Shinde da, Bipul da, Biplab da, Daya da, Animesh da, Suman da, Basudeb da; my batch mates : Aslam, Subrata, Kartik, Krishnendu, Chiranjit, Abhishek; my juniors : Samrat, Alik, Dhrimadri, Subhadip, Sourav, Amrit, Ananda, Shantonu, Indranil, Rafiqul, Sasti, Riju, Samir, Partha, Shubhadip, Avik for their help, well wishes and warm company. I value my association and the golden moments share with them. It is a pleasure to express my gratitude wholeheartedly to Sagar da (Mr. Sagar Sarkar) for his affections and helps during SNBNCBS days. I also cherish the sweet times we spent together. I convey my heartiest thanks to Anuvab, Rajkumar, Dhiraj, Biswajit for their spontaneous help at several stages and in several ways. My special thank goes to Rahul for his great company, constant help and never-ending support since he joined in SNBNCBS. His fond memories will echo in my mind forever.

I cherish the warm memories of many of the happy moments I spent with Souvanik, Rakesh, Sumanta, Subrata, Ejaj, Samiran, Rahul, Kallol, Debasish, Dipanajn, Mahebub, Kesab, Shubhrasish, Shubham, Vishwajeet, Sarowar da, Arup da, Subhasish da in playing cricket at SNBNCBS ground. I would never forget the batting partnership with Souvanik in the record-breaking run chase in the final of the SNBNCBS cricket tournament 2019. I do not know how to thank Rakesh for rushing me to the hospital when I suffered a laceration to the left side of my jaw in a freak fielding accident. However, I would always recall all the sweet moments on the cricket field, and the cricket will always be in my heart.

At this auspicious moment, I want to express my sincere gratitude to those people, who played an important role in my life, and, whose inspiration helped me to reach here. First, all of my teachers, Mr. Sandip Singha Ray, Mr. Subhasish Chakraborty (Gopal babu), Mr. Manoj Som, Dr. Debashis Chatterjee, Mr. Deben Ghosh during my school days; Dr. Atanu Dan during my graduation period; Prof. Sourangshu Mukhopadhyay, Dr. Abhijit Chakraborty, Dr. Abhigyan Dutta, Dr. Tanmoy Banerjee during my post-graduation studies − they all are my path-makers and helped me to dream. I am deeply grateful to Mr. Debiprasad Ghosh for his teaching, unflinching encouragement and moral support. I am indebted to him more than he knows.

Next, come all of my seniors, Somnath Sen, Kaushik Mondal, friends, Abhijit, Pronoy, Anshu, Anupam, Arnab, Sagar, Satyajit, Tufan, Debarati, and juniors, Shuvra, Atanu, Saurav, who stay very close to my heart. I always feel fortunate for having such a companion. I cannot thank Nirmal enough for his friendship, caring, support, who has been an inseparable part of my life. Being able to share my days with you have been an immense gift.

Last but not least, I would like to convey my uttermost respect and gratitude to all the members of my family, especially, my parents, elder sister, brother in law, uncle, aunt, two younger sisters, whose unconditional love and support have sustained me and kept me strong at all times. My heartfelt gratitude to my father. Without his guidance, I do not think I would have reached the point that I now find myself at. I offer my hearty and

sincere love to my mother for taking care of me. For my mother, the most important thing how the child remains safe, healthy and fit that what she most bother about. No word would be sufficient to describe the many sacrifices you both have done for me throughout the years. This section of acknowledgements would remain incomplete if I do not mention the sweet little angel, Koushiki, a daughter of my elder sister. I cherish all the moment I spent in the last few months with her.

Finally, it is my great pleasure to express my deepest gratitude to everybody who was important to the completion and successful realisation of my Doctoral thesis, as well as expressing my apology that I could not mention personally one by one.

Supriyo Ghosh
SNBNCBS
Kolkata, India
March, 2019

List Of Publication

The following papers are included in this thesis.

1. Phase-dependent Photometric and Spectroscopic Characterisation of the MASTER-Net Optical Transient J212444.87+321738.3: An Oxygen-rich Mira, **Supriyo Ghosh**, S. Mondal, R. K. Das, D. P. K. Banerjee, F. J. Hambsch and S. Dutta, 2018, The Astronomical Journal, **155**, 216, **Chapter 5**.

2. Spectral Calibration of K–M Giants from medium resolution near-infrared HK-band spectra, **Supriyo Ghosh**, S. Mondal, R. K. Das, and D. Khata, 2019, Monthly Notices of the Royal Astronomical Society, **484**, 4619–4634, **Chapter 3**.

3. Spectroscopic and photometric monitoring of a poorly known high-luminous OH/IR star, **Supriyo Ghosh**, S. Mondal, R. K. Das, and S. Dutta (*Manuscript submitted to Astronomy & Astrophysics*), **Chapter 6**.

4. New empirical correlations on fundamental parameters of K–M giants, **Supriyo Ghosh** and S. Mondal (*Manuscript to be submitted*), **Chapter 4**.

5. Near Infrared photometric and spectroscopic observations of the bright optical transient J212444.87+321738.3, S. Mondal, Das, R. K. Das, N. M. Ashok, D. P. K. Banerjee, S. Dutta, **Supriyo Ghosh**, A. Mondal, 2013, ATel, **4931**, 1, **Chapter 5**

The following papers are not included in this this.

1. The young cluster NGC 2282: a multiwavelength perspective, S. Dutta, S. Mondal, J. Jose, R. K. Das, M. R. Samal, **Supriyo Ghosh**, 2015, MNRAS, 454, 3597

2. Optical photometric variable stars towards the Galactic H II region NGC 2282, S. Dutta, S. Mondal, S. Joshi, J. Jose, R. K. Das, **Supriyo Ghosh**, 2018, MNRAS, 476, 2813

Contents

List of Figures

List of Tables

Chapter 1

Introduction

The stellar evolution describes the life cycle of a star from its birth to death, which represents various phases of evolution, for instance in a chronological sequence, Pre-Main-Sequence (PMS), Main-Sequence (MS), Red Giant Branch (RGB), Horizontal Branch (HB), Asymptotic Giant Branch (AGB), Planetary Nebulae (PN), for low- to intermediate-mass ($\sim 0.8{-}8\ M_{\odot}$) stars. More details on stellar evolution are described in the next section 1.1. The MS of a star is the most stable and quiescent phase of evolution, where nuclear burning inside the core converts hydrogen into helium. The Sun is the best example of a star on the MS phase, and the radiation over all wavelengths is coming towards the Earth due to thermonuclear burning of hydrogen. The RGB and AGB are two significant post-MS evolutionary phases of low- to intermediate-mass stars, and the main source of radiation is the burning of hydrogen (H) or/and helium (He) in a thin shell(s) on the top of the degenerate core, while the inert core begins to shrink. In the RGB phase, the stellar radius expands to carry out the energy produced mostly by the H-shell and partly by the gravitationally contracting He-core. As a consequence of envelope expansion, the stellar luminosity increases, and the star becomes cool and red. As the star ascends the RGB the fully convective envelope penetrates into the regions that had been already experienced partial H-burning. This allows the nucleosynthesis elements to mix with the surface, altering the chemical composition of the surface. The AGB almost follows the RGB for low-mass stars, however, the outcomes are more drastic with further expansion of the stellar envelop and increase in luminosity. The convective envelop deepens as in RGB, mixing the nucleosynthesis elements with the surface and altering the chemical composition. As the star ascends the AGB it starts experiencing thermal pulses, and therefore, pulsates radially and becomes unstable. The stellar pulsation levitates the gas to cool outer parts of the atmosphere facilitating the formation of

molecules and dust, and then the radiation pressure pushes it away, creating a slow but strong stellar wind. In this way, the AGB star loses its masses, which increase dramatically with its evolution through AGB. Due to the dust formation and high mass-loss rates, circumstellar envelopes (CSE) develop surrounding the photosphere, which might become opaque to visible light and emit in infrared (IR) wavelengths. Ultimately, nucleosynthesis and mass-loss of the star stop, the CSE is blown away and the post-AGB phase begins.

Since AGB are intrinsically very luminous and numerous while covering a wide range of age, their astrophysical importance is widely known. They can be used as a probe of distance indicator, galactic structure and dynamics. In addition, a large mass-loss enriches the interstellar medium (ISM), molecular clouds and chemical evolution of galaxies. Therefore, the study on the understanding and characterizing of the cool red giant is very fascinating using optical/near-infrared (NIR) photometric or/and spectroscopic observations and theoretical model atmospheres. Precise estimation of fundamental parameters, e.g., effective temperature (T_{eff}), surface gravity ($\log g$), metallicity ([M/H]), are very important, as it helps to characterize the stellar populations in the galactic and extragalactic environments. Furthermore, the AGB stars show time-dependent spectral variation because of their radial pulsation. Therefore, phase-dependent spectroscopic study of AGB stars provides a way to understand the atmosphere and formation of molecules in their atmosphere during the variability phase.

1.1 Stellar evolution – Main-Sequence to Asymptotic Giant Branch

The stellar evolution of a star mainly depends on its initial mass (progenitor mass). During its evolution, a star undergoes changes in internal structure, temperature and luminosity, and follow a specific evolutionary track that is represented by Hertzsprung-Russell diagram (HR diagram) developed independently by E. Hertzsprung and H. N. Russell in early 1900s. HR diagram basically represents the temperature of stars against their luminosity or/and colour of stars (or spectral type) against their absolute magnitude as shown in Figure 1.1.

In this thesis work, low- to intermediate-mass stars, i.e., the stars of masses (M) ranging from 0.8 to 8 $M_{\odot}$ are studied. The stars less massive than 2 $M_{\odot}$ will be referred to as low mass stars, and those of mass in between 2 to 8 $M_{\odot}$ will be defined as intermediate mass stars. The range of mass is somewhat arbitrary as the exact range depends on metallicity distribution.

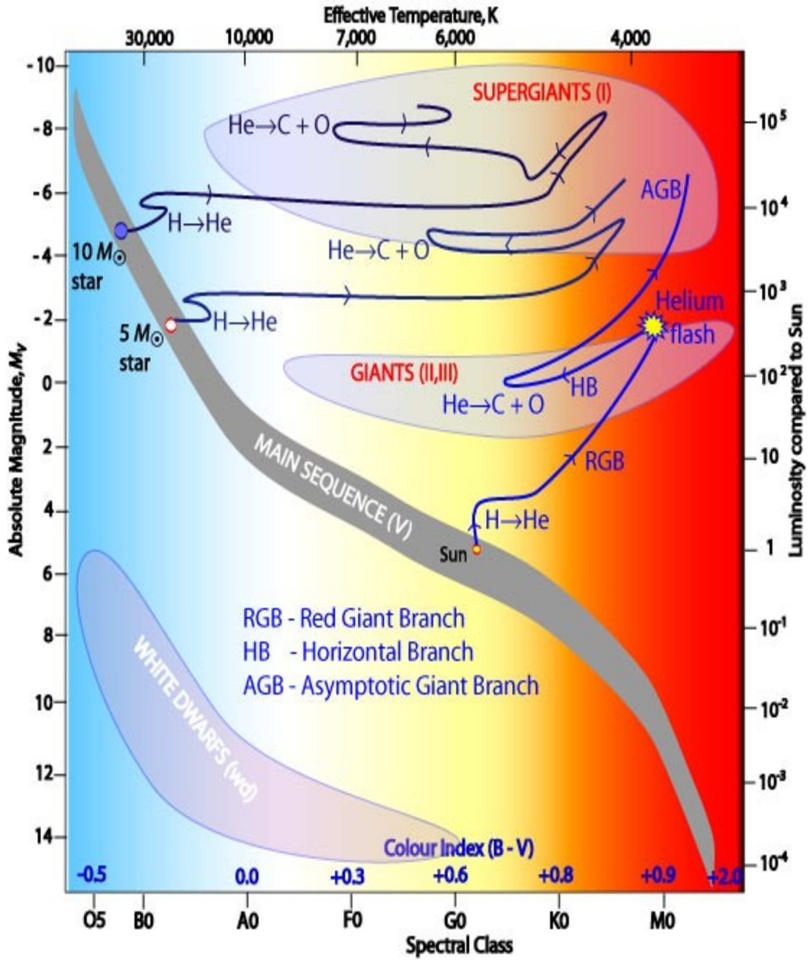

Figure 1.1: The Hertzsprung–Russell diagram shows the location of MS, Giants and AGB stars with respect to their absolute magnitude (M_V)/luminosity and effective temperature/colour index. Source of image : Australia Telescope National Facility (http://www.atnf.csiro.au/outreach//education/senior/astrophysics/).

1.1.1 Main-Sequence

The birthplace of stars is collapsing molecular clouds or nebulae that consist mainly of hydrogen. The condition of clouds for collapse due to self-gravity is to satisfy Jeans' criterion, which depends on the temperature and density of the cloud. The collapsing clouds initially form a protostar, where hydrogen fusion is yet to begin. When the temperature of the core reaches about 10^7 K the nuclear fusion of hydrogen turns on, initiating the main-sequence of the star, like the undergoing phase of our star, Sun. In this phase, hydrogen (H) burns inside the core through thermonuclear p-p chain (Figure 1.2a) reaction for low mass stars (Bethe, 1939), and CNO-cycle (Figure 1.2b) for intermediate mass stars (von Weizsäcker, 1938).

The radiation pressure owing to thermonuclear fusion reactions counteracts against further gravitational collapse, and thus hydrostatic equilibrium is established. The main-

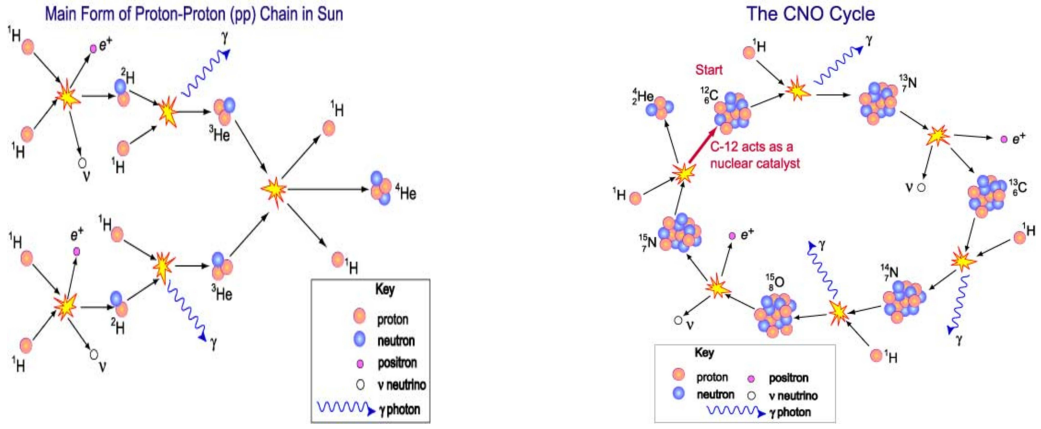

(a) p-p chain reaction (b) CNO cycle

Figure 1.2: Figure shows the p-p chain reaction and CNO cycle. Source of image : Australia Telescope National Facility (http://www.atnf.csiro.au/outreach/education/senior/astrophysics/).

sequence of a star is the most stable, quiescent phase of evolution, and lifetime depends fundamentally on the initial mass of the progenitor because the rate of hydrogen burning and energy production increases with the mass of the star. Hence, the low mass star lives longer than their heavy brethren (e.g., the main-sequence lifetime of a star of mass 1 $M_{\odot}$ (Sun) $\sim$ 10 billion years, whereas only a million years for a 40 $M_{\odot}$ star).

1.1.2 Red Giant Branch

When all the hydrogen inside the core is converted to helium (He) through thermonuclear reaction, the stars terminate from the main-sequence phase of stellar evolution, and post-main-sequence life begins, which is known as RGB (see Figure 1.1 and Figure 1.4a,b). In this phase, the thermonuclear reaction of hydrogen begins in a shell surrounding the inert helium core where fresh hydrogens are still available. As no further reaction occurs inside the core, only pressure owing to thermal motions is unable to restrain gravitational collapse, and core contraction follows, which, in turn, warms up the burning hydrogen shell. Consequently, hydrogen burns at a faster rate and energy generation rate increases, which makes the star more luminous. At the same time, the envelope of the star expands that causes the size of the star to increase, and surface temperature to decreases and the star appears as red in colour. Thus, the star becomes **'Red Giant'**. The opacity of the star now increases due to lowering of surface temperature, and stellar envelop becomes convective. As the evolution continues, the hydrogen burning shell moves outwards, and the convective envelop deeps down into such regions that allow nucleosynthesis elements (^{4}He, ^{14}N) to mix with the convective layer, hence chemical composition and abundance ratio of the stellar surface alter. This process is referred to as the first dredge-up. Concur-

rently, the mass of the core is gradually increasing due to the dumping of helium by the burning hydrogen shell, and core contraction continues, making the density of the core gas to enhance. The core contraction continues until the density becomes high enough to make the core electron-degenerate, and the electron degeneracy pressure inhibits further gravitational collapse. At the end of the RGB phase, the temperature ($\sim 10^8$ K) becomes high enough to lift the electron degeneracy and trigger the helium burning by the triple-alpha process. Once the triple-alpha process begins, the generated heat quickly spreads and ignites the rest of the core in a thermonuclear runaway process, and the enormous amount of energy releases in a very short time. This phenomenon is referred to as the *helium flash*. However, flash never observe from outside of the star because most of the energy is absorbed by the surrounding layers (Iben & Renzini, 1983; Ostlie & Carroll, 1996; Zeilik, 2001; Habing & Olofsson, 2003; Jiménez-Esteban, 2004; Stancliffe, 2005; Wong, 2017).

However, the degenerate helium core only occurs for low mass stars. The cores of intermediate mass stars are massive and hot enough to ignite helium before stars can actually acquire sufficient density to be degenerate. Hence, helium flash never takes place inside the core of those stars, gentle triple-alpha reaction produces the energy and move to the next phase of evolution.

1.1.3 Horizontal Branch

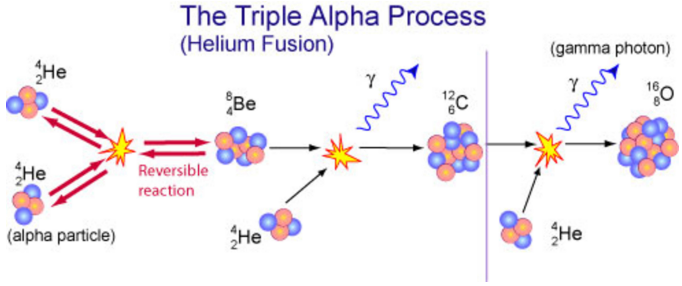

Figure 1.3: Figure represents the triple alpha reaction. Source of image : Australia Telescope National Facility(http://www.atnf.csiro.au/outreach//education/senior/astrophysics/).

The triple alpha process and helium flash result in an increase in temperature inside the core, which is followed by an expansion of the core. Subsequently, density, temperature, and energy production rate decreases, which, in turn, reduces stellar radius and luminosity. The convective stellar core continues to burn helium at a steady rate and produces carbon and oxygen through triple alpha reactions as in Figure 1.3. Also, hydrogen is burning outside the core, converting to helium. This phase of stellar evolution of low mass stars is referred to as **Horizontal Giant Branch** (HB). Cool HB stars with solar metallicity tend

to clump at a similar location (same absolute luminosity) in the H-R diagram, known as the *'red clump'* stars (Iben & Renzini, 1983; Ostlie & Carroll, 1996; Zeilik, 2001; Habing & Olofsson, 2003; Jiménez-Esteban, 2004; Stancliffe, 2005; Wong, 2017).

1.1.4 Asymptotic Giant Branch (AGB)

Early AGB (E-AGB)

For low mass stars, the life span in the HB ends with the completion of helium burning inside the core. The core of the star again begins to contract until it becomes electron degenerate. Nuclear fusion now continues in two shells: the helium burning shell around the core and hydrogen burning shell above the helium burning shell as shown in Figure 1.4. The region in between two shells is called inter-shell region. At the same time, the envelope of the star becomes almost convective, which expands further, consequently, surface temperature decreases. Once again the star becomes **'Red Giant'**, and begins to ascend an evolutionary track, what is referred as the AGB, a stage in the H-R diagram that asymptotically follows the RGB with greater luminosity (see Figure 1.1 and Figure 1.4a,b).

For the intermediate-mass star, following helium exhaustion, the core of the star again begins to contract, developing a helium burning shell, which is followed by the expansion and cooling of overlying layer above the helium burning shell. Consequently, hydrogen burning shell momentarily turns off its activity, and the convective envelop deeps down as far as the product of thermonuclear reaction inside the dormant hydrogen burning shell can mix with the surface, and subsequently, the chemical composition of the stellar surface alters. This process is referred to as *second dredge-up* that increases the abundance of helium and nitrogen in the surface. The second dredge-up only occurs if the mass of the star, $M > 4M_{\odot}$, otherwise convective envelop is unable to penetrate the hydrogen shell. Following the second dredge-up, the star evolves to the AGB phase and dormant hydrogen burning shell eventually reignites (Iben & Renzini, 1983; Ostlie & Carroll, 1996; Zeilik, 2001; Habing & Olofsson, 2003; Jiménez-Esteban, 2004; Stancliffe, 2005; Wong, 2017).

Thermaly Pulsing AGB (TP-AGB)

At the beginning of the AGB phase, the structure of all the stars is qualitatively similar irrespective of the stellar mass, i.e. all the stars have C-O degenerate core (O-Ne for most massive), two thermonuclear active zones and a convective envelope as in Figure 1.4c. As the star ascends the AGB phase, it again cools further, expands and increases in luminosity, and eventually enters thermally pulsing (TP-AGB) phase (Schwarzschild &

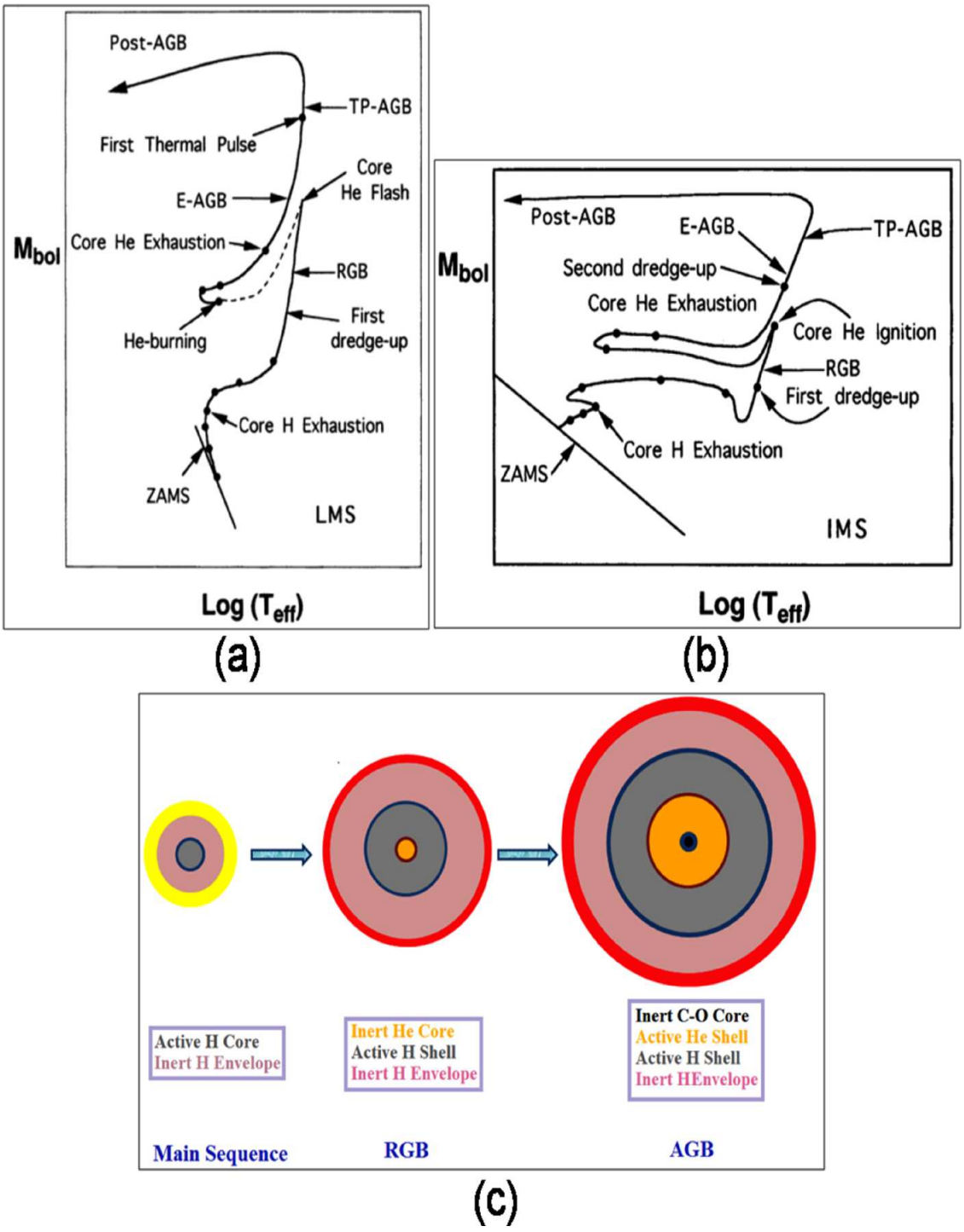

Figure 1.4: The top panel presents the evolutionary track corresponding to two different progenitor mass stars, 1 $M_{\odot}$ (left) and 5 $M_{\odot}$ (right). The bottom panel shows the increasing size of the stars from MS to AGB (not in scale) and their internal structures. Source of image (top) : Busso et al. (1999)

Härm, 1965). In this phase, hydrogen and helium shells ignite intermittently. So, the helium shell becomes thermally unstable because of an increase in mass of the He-layer by the H-burning shell, and hence the helium shell flashes occur periodically. Following

the thermal pulses, He-burning shell precipitates an enormous amount of energy that deposits in surrounding materials. It has two major impacts on the star − a flash driven convection zone develops throughout the inter-shell region in between the He and H-burning shell, which mixes the He-burning products (mainly ^{12}CO) throughout the inter-shell region, and the H-burning shell expands and becomes cool. Consequently, the H-burning shell temporarily turns off, and overall luminosity of the star decreases. Also, convective envelop deeps down to the inter-shell region and brings the carbon to the stellar surface. This process is referred to as *third dredge-up* that increases the C/O ratio at the surface. Eventually, the He-shell cools down, the star contracts again, H-shell reignites, pre-flash condition of the star reinstates, and sets for another thermal pulse. The interval between two successive thermal pulses is of the order of 10^5 years (depending on mass and composition of the progenitor).

The thermal instability increases as the stars evolve through AGB and experience many thermal pulses with progressively increasing amplitude. Consequently, the convective envelope deepens through the intershell region, and eventually reaches into the layers where 3α nucleosynthesis produces fresh carbon (Ostlie & Carroll, 1996), makes C/O in the stellar surface >1, and M-type stars (C/O $\sim$ <1) become carbon stars (C-stars). Thermal pulses make those stars to be carbon-rich which have a certain mass ranging from 1.5 to $4M_{\odot}$ with solar composition. For more massive stars (M $\sim 4{-}8M_{\odot}$, exact range depends on metallicity distribution), proton capture nucleosynthesis occurs at the base of the outer envelop − known as *Hot Bottom Burning* (HBB, Sackmann & Boothroyd 1992) that prevails the formation of C-star, and the stars remain as M-type (García-Hernández et al., 2013).

The instability generated during thermal pulses makes the star to pulsate radially. The atmospheres of AGB stars are strongly affected by this time-dependent highly dynamical phenomena, and the surface temperature and luminosity of the stars change significantly over a pulsation cycle. The stars become **Large Amplitude Long Period Variables** (LALPV, Jiménez-Esteban 2004). In the final phases on the AGB, the stars undergo a heavy mass-loss process ($10^{-8}{-}10^{-4}$ M $yr^{-}1$) that determines the AGB lifetime and its ultimate luminosity. The reason for mass-loss is most likely due to wind acceleration mechanism and stellar pulsation (see, review of Höfner & Olofsson 2018). The wind acceleration mechanism drives the loosely bound dust grains outward, which is levitated due to stellar pulsation. Thus, the CSE of gas and dust develops around the central star. As the evolution continues, CSE gradually thickens and finally, obscures the photospheric radiation completely and re-radiated at infrared (IR, Bedijn 1987). The star now becomes an infrared source, like an OH/IR star. The OH counterpart of the name comes from the

fact that they often show OH maser emission (at 1612, 1665, and 1667 MHz) originating in a circumstellar thin shell (Blommaert et al., 2018). A simplified schematic depiction of an AGB star structure, its circumstellar environment and mass-loss process are shown in Figure 1.5.

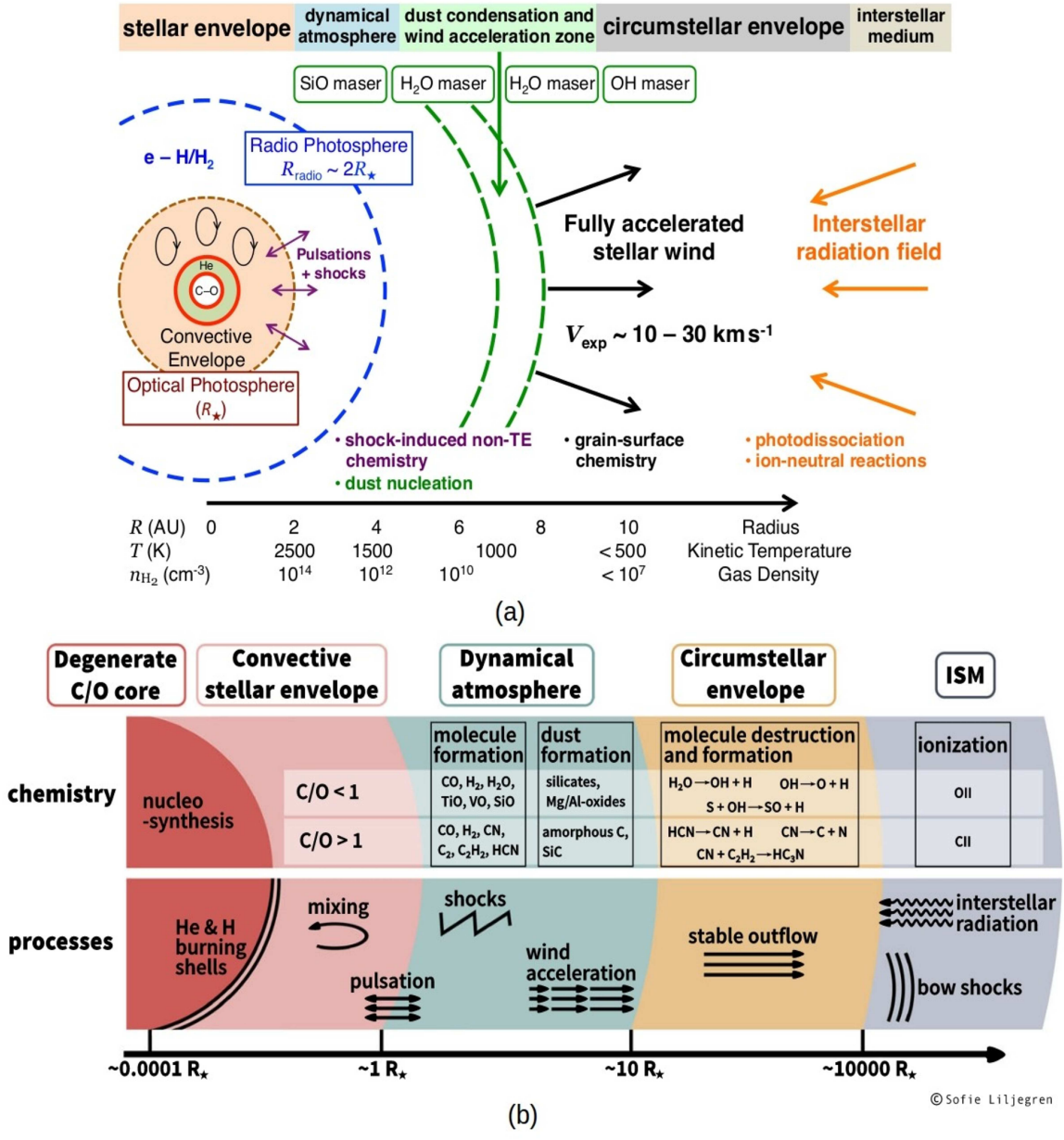

Figure 1.5: A simplified schematic depiction of an AGB star structure, its circumstellar environment and mass-loss process are shown. Source of Images : (a) Wong (2017); (b) Höfner & Olofsson (2018)

Post-AGB

Ultimately, thermonuclear reaction and mass-loss of the stars stop, a new phase of stellar evolution begins, called Post-AGB as in Figure 1.4. In this phase, the C-O core of the start contracts and hence, the temperature of the star increases. At the same time, the CSE expands and becomes optically thin. Eventually, the temperature of the star becomes high enough ($\sim$ 25000 K) so-that it ionises the surrounding CSE, and stars become **Planetary Nebula**. Finally, the CSE disappears, exposes the hot core of the star that cools to become **White Dwarf** star and ultimately dies. For a binary system, white dwarfs accumulate matter from the companion and become type Ia supernova.

The evolution of high mass (M $> 8M_{\odot}$) stars are somewhat different from the low to intermediate mass stars. Their core never becomes electron-degenerate and thermonuclear reaction produces heavier and heavier elements until iron. Heavier elements than iron form by slow neutron capturing process (s-process). The details discussion on the evolution of a high mass star is out of the scope of this thesis.

1.2 Stellar Pulsation

During the stellar pulsation, the star expands and contracts, accordingly, luminosity and surface temperature vary with time. For any mode of oscillation, the core of the star is considered as a node, where the gases do not move. Eddington compared the pulsating stars with thermodynamic heat engines. The work done of a star is the difference between the heat flowing into the gas and heat leaving from the gas by each layer during each cycle. The oscillation is possible only when the total work done ($\oint P\,dV$) by all the layers of the star is positive for a cycle, i.e., the heat flowing into the gas must be greater than the heat leaving from the gas that demands absorption of heat by the driving layer of the oscillation during the compression of the star (Ostlie & Carroll, 1996). The **ϵ-mechanism** that operates in the core can full fill the requirement of oscillation, but near the node (i.e., at centre) the small pulsation amplitude is unable to drive the star's pulsation. Alternatively, Eddington suggested the valve mechanism that apprises the enhancement of opacity during compression. It can be simply explained following Kramers law ($\kappa \propto \rho/T^{3.5}$, where κ, ρ, and T $-$ the opacity, density and temperature, respectively) that opacity decreases with compression in most of the stellar region. However, the opacity does increase with the compression in a stellar region, where the gases are partially ionised. This special regions, identified by S. A. Zhevakin in the 1950, are named as *partial ionization zones* or *Zhevakins zones*. In these regions, during compression, part of the

energy absorbs for further ionisation of the gasses and the density of ions increases, and during expansion, energy releases because of recombination of ions with electrons and subsequently, the density decreases. But, temperature does not alter as much as expected for both the cases. Consequently, the density term dominates in Kramers law and satisfies the requirement of Eddington's valve mechanism. This opacity mechanism is referred to as **κ-mechanism**. Two main partial ionisation zones − the hydrogen partial ionisation zone, and the helium II ionisation zone are believed to exist in most of the stars. The characteristic temperature of first ionisation zone is $1-1.5 \times 10^4$ K, where the ionisation of neutral hydrogen ($H \longleftrightarrow H^+ + e^-$) and first ionisation of helium ($He \longleftrightarrow He^+ + e^-$) occurs. The helium II partial ionisation zone with a characteristic temperature of 4×10^4 K involves the second ionisation of helium ($He^+ \longleftrightarrow He^{++} + e^-$). The effective temperature of the stars defines the location of the ionisation zones that control the pulsation properties. Details numerical simulation shows that the first ionisation zone is responsible for observed phase lag between the stars maximum luminosity and minimum radius, and the second is for driving the pulsation on the instability strip (Ostlie & Carroll, 1996).

Due to the pulsation, the star attains maximum radius at about minimum light and then starts to fall back for the next light cycle. The outer layers are falling back at an acceleration while the inner layers move comparatively slowly and become almost stationary after a certain time interval (phase 0.8). Now, the motion of infalling photospheric gas retarded by the underlying inner gas and Mach number is high enough to produce a shock in that region. The static pressure, density and temperature in that region increases instantaneously. For the next cycle, underlying gas layers are moving upwardly and lag behind the shock wave. As the light cycle moves further, photospheric gas from the previous light cycle decreases above the shock. So, shock becomes optically thin (Hinkle, 1978).

1.3 Classification of Red Giants

In 1905 Hertzsprung introduced the term **'Giant'** and **'Dwarf'** for stars of different luminosity despite having the same spectral classification (Harvard classification). A few years later Russell independently drew the same conclusion as Hertzsprung and used the term 'Giant' for the more luminous star and 'Dwarf' for the relatively less luminous star. According to MK classification on the basis of the luminosity, the 'Giant' corresponds to luminosity class III and lie above the MS or 'Dwarf' (luminosity class V). The red giants are the cool giants with spectral type K, M, S and C representing stars of RGB, red clump and AGB evolutionary phases (see Figure 1.6). In the TP-AGB phase, due to

stellar oscillation stars become **Long Period Variable** (LPV). They are classified into three subclasses; **Irregular variables** – variable star with irregular periodicity, **Semi-regular** (SR) – amplitude variation (ΔV) less than 2.5 magnitudes with a well defined period ('SRa') or a poorly defined period ('SRb') and **Mira Variable** – a well defined period with large variation in amplitude ($\Delta V > 2.5$) (General Catalog of Variable Stars, Kholopov 1987). However, the existence of an irregular variable in this classification is arguable (Kerschbaum et al., 2001; Lebzelter & Obbrugger, 2009).

On the basis of carbon to oxygen (C/O) ratio in the atmosphere and so as to spectral features, Mira variables can be classified as M-type or oxygen-rich (O-rich, C/O <1), S-type (C/O = 1) and C-type or carbon-rich (C/O >1). Scalo & Ross (1976) have demonstrated that oxygen-rich atmosphere become carbon-rich because of third dredge-up following the sequence :
M (strong TiO and VO)$\longrightarrow$ **MS** $\longrightarrow$ **S** (strong ZrO) $\longrightarrow$ **SC** $\longrightarrow$ **C** (C_2 and CN bands). As soon as C/O ratio becomes >1, the difference in chemical composition leads to a significant decrease in the effective temperature.

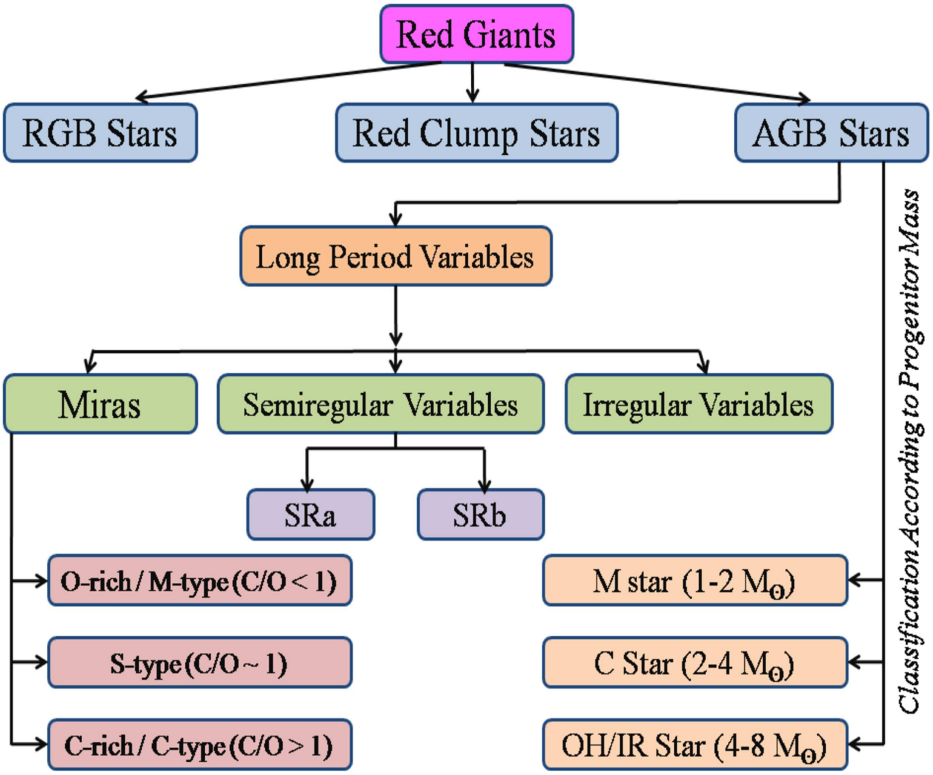

Figure 1.6: The AGB classification on the basis of progenitor mass and variability are shown. For details, see the text.

Depending on mass the progenitors AGB stars can also be classified as **M-stars** ($M < 2M_\odot$), **C-stars** ($2\ M_\odot < M < 4\ M_\odot$) and **OH/IR stars** ($M > 4M_\odot$). The mass range is

arbitrary and actual range depends on the metallicity distribution. However, Mira variables and OH/IR stars share many common characteristics implying a close relationship between them. It is not well-defined whether OH/IR stars differ from Mira variables on the basis of different evolutionary phase or different progenitor mass or combination of both (Blommaert et al., 1998). The above classification signifies different progenitor mass is the main difference between Mira variables and OH/IR stars (e.g., Ortiz & Maciel 1994; Lepine et al. 1995). Furthermore, the M-stars never undergo the third dredge-up process, so C/O always remains >1. C-star begins AGB phase as C/O < 1 and then third dredge up makes C/O > 1 (Marigo & Girardi, 2007). However, HBB makes C/O > 1 for OH/IR stars (Jiménez-Esteban & Engels, 2015). Thus, OH/IR stars and their low-mass cousins, both are O-rich.

On the other hand, IRAS colour-colour diagram as shown in Figure 1.12 shows OH/IR stars following a well-defined sequence with its blue end connected with Mira variables (Olnon et al., 1984), that suggests OH/IR stars being the evolved phase of Mira variables with increasing mass-loss rate (e.g., van der Veen 1988). Many believe that the sequence of a star along AGB phase is **SR** $\longrightarrow$ **Mira variable** $\longrightarrow$ **OH/IR** with increasing period, luminosity and mass-loss rate (Bedijn, 1987).

However, few studies (e.g., Likkel 1989; García-Lario 1992) consider both progenitor mass and evolutionary phase to differentiate the Mira variables from OH/IR stars. They suggest that AGB stars would start their evolution as Mira variables, and solely the massive one becomes OH/IR star and reaches to the high mass-loss rate regime. Furthermore, OH/IR stars can also be classified into two types − type I that shows strong 1665 and 1667 MHz OH masers, and type II that show double-peak 1612 OH maser.

1.4 Observational Characteristics of Red Giants

In this thesis work, we focus only on O-rich stars, and thus our description biases towards the observational characteristics of those stars. However, we do scarcely mention observational properties of S-stars or C-stars merely to compare with O-rich stars.

1.4.1 Light Curve and Period

The period of the Mira variable can be determined from the long-term photometric monitoring program (light curve). Period plays a crucial role to understand the luminosity, age, initial metallicity, and evolution. However, Mira variable light curve does not consis-

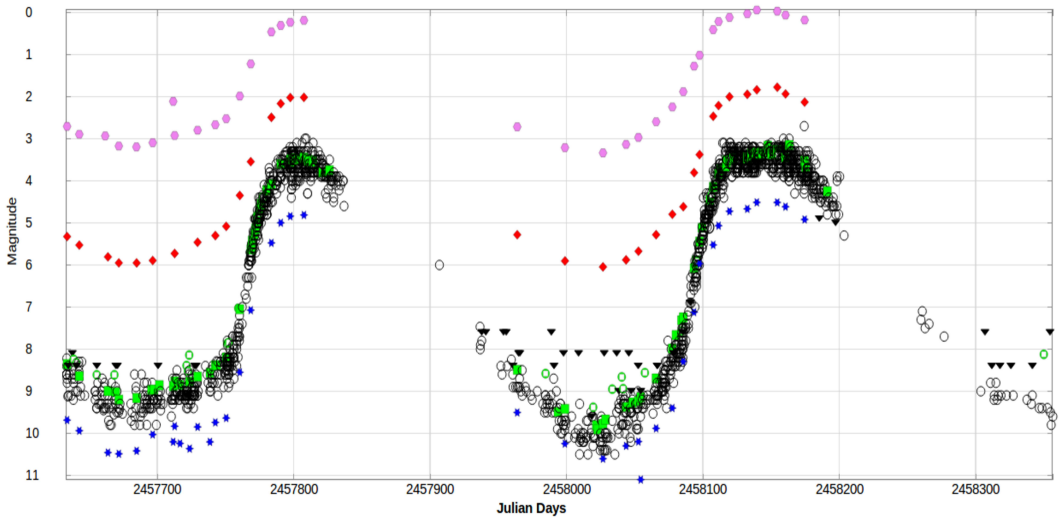

Figure 1.7: The light curve of the first discovered Mira variable – Omicron Ceti (O Ceti). Source of image : AAVSO(`https://www.aavso.org/vsots_mira/`)

tently show strict periodic behaviour, and period, ranging from 100 to 2000 days, might vary from cycle-to-cycle from average period (Mattei, 1997). Furthermore, maximum and minimum brightness vary from one cycle to another in a very complex manner. Barthes et al. (1996) suggested that the circumstellar dust shells are responsible for this complex behaviour. Moreover, it is found that the shape of the light curve somewhat correlated with the period (Campbell, 1955). Mira variables with a period less than 200 days show the symmetrical light curve, and those with a period greater than 200 days have characteristic greater fall time (maximum to minimum) than the rise time (minimum to maximum, Mattei 1997). Mira variables with a period greater than 300 days show large amplitude having small and irregular bumps on their rising or falling part of the light curve (e.g. Lockwood & Wing 1971). Some Mira variables also show systematic modulation of their period, either towards shorter or longer periods. Wood & Zarro (1981) suggested that this is because of recent He-shell flash. A typical light curve of a Mira variable is presented in Figure 1.7.

The mode of pulsation in the Mira variable is arguable. It is thought that Mira variable is a radial fundamental mode pulsator (Wood & Sebo, 1996; Wood et al., 1999; Wood, 2000). Recent studies have presented evidence for Mira variables to be the fundamental mode pulsators (e.g., Perrin et al. 2004; Woodruff et al. 2004; Fedele et al. 2005; Mondal & Chandrasekhar 2005). However, some studies preclude the fundamental mode pulsation and support the first-overtone or higher overtone mode of pulsation (e.g., Robertson & Feast 1981; Tuthill et al. 1994; Haniff et al. 1995; Tej et al. 1999). van Belle et al. (1996) found that Mira variables are both the fundamental as well as the first-overtone mode pulsators, depending on the period, mass and radius of the individual star.

1.4.2 Variability

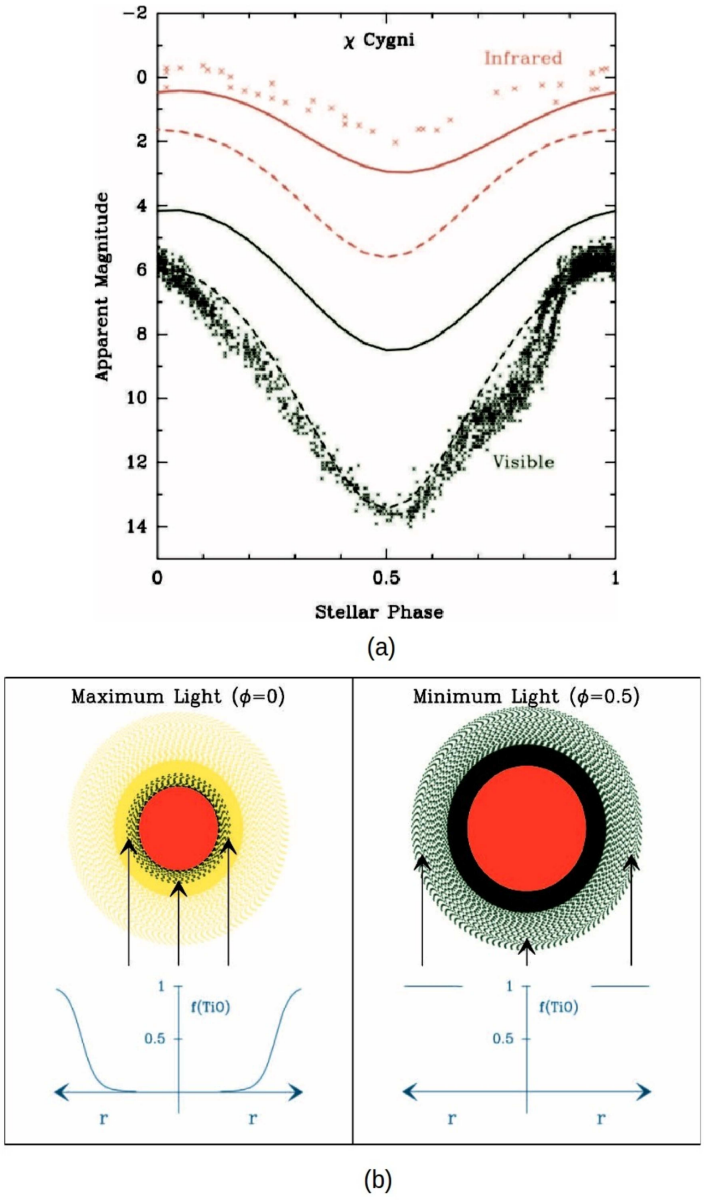

Figure 1.8: Figure at the top shows the observed light curves in the visible (green crosses) and NIR (red crosses) for the Mira variable χ Cygni. Note the phase lag and amplitude difference between two light curves. The solid lines and dashed lines are for blackbody models. Figure at the bottom shows a simplified schematic view in the visual appearance of a Mira variable, and how the opacity of metal oxides, such as TiO (green), change at maximum (left) and minimum (right) light. At maximum light, the temperature increases, the opacity of metal oxides decrease, the extended atmosphere becomes partially transparent (yellow), and the stellar surface (arrows) are seen in visible light, whereas near minimum light, the temperature decreases, hence opacity increases and the star becomes opaque to visible light. Source of image : Reid & Goldston (2002)

An important property of Red giants in the TP-AGB evolutionary phase is the significant variation of their flux owing to long-period radial pulsation. Mira variables show magnitude variation ranging from 2.5 to 8 mag in the visible wavelength, whereas NIR

variation is about 1−2 mag (Whitelock et al., 1994b) as shown in Figure 1.8a for a Mira variable, χ Cygni.

Broadband studies suggest that the amplitude of variation tend to decrease with increasing wavelength (e.g., Lockwood & Wing 1971; Bessell et al. 1996), also high resolution study shows the significant variation of observed radii with wavelengths (e.g., Thompson et al. 2002; Ireland et al. 2004; Perrin et al. 2004; Mondal & Chandrasekhar 2005). Furthermore, wavelength dependent phase lags observed in Mira variables (Pettit & Nicholson, 1933b; Smith et al., 2002a). The fact that the large visual amplitude, the wavelength dependent variation of pulsation amplitude and the phase lag are attributed to the formation and destruction of TiO molecules during the passage of periodic shock waves that results in the variation of TiO opacity (Reid & Goldston, 2002; Smith et al., 2006) as shown in Figure 1.8b. Moreover, the amplitude of variability increases with the period (Jones et al., 1990) and colours (Wood, 1998; Whitelock et al., 2003). A small fraction of OH/IR stars shows very small and irregular variation or no variation of amplitude. Bedijn (1987) classified those object as Post-AGB stars.

1.4.3 Period−Luminosity relation

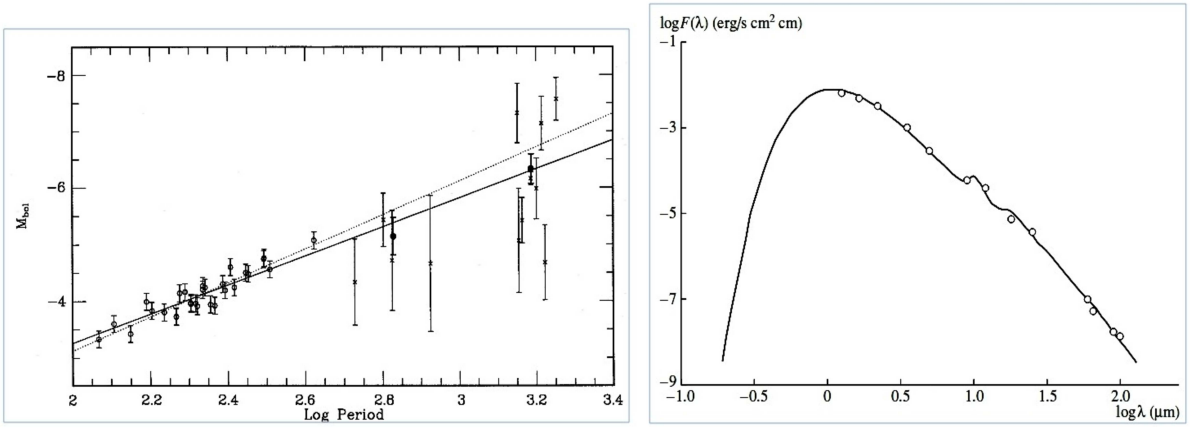

Figure 1.9: Figure shows the period-luminosity relation (left) and SED of a LPV. Source of image : (a) Whitelock et al. (1991) (b) Bogdanov et al. (2015)

The period–luminosity (PL) relations (see Figure 1.9a) are especially important because they indicate the distance of the objects, suggests the mode of pulsation and provide the information on the effect of pulsation on mass-loss. Since the discovery of the PL relation of Mira variables (Glass & Evans, 1981), significant progress, predominantly from the late 1990s to the early 2000s, was made by several authors in the study of PL relations of LPVs using the Hipparcos Catalogue (van Leeuwen et al., 1997; Whitelock & Feast, 2000) and

samples of objects at the same distance − in the Large Magellanic Cloud (Glass & Evans, 1981; Feast et al., 1989; Groenewegen & Whitelock, 1996; Whitelock et al., 2008; Ita & Matsunaga, 2011) or in the bulge of the galaxy (Alard et al., 2001). Furthermore, the data of the large optical survey projects with robotic telescopes, e.g., MACHO, OGLE, EROS, MOA (searching for gravitational lensing events), boosted immense investigation of the PL relationship for LPVs. The luminosities of AGB stars are in the range 2200–55000$L_{\odot}$, corresponding to $M_{bol} \sim -3.6$ to -7.1 (Engels, 2005), and the PL relations (e.g., Feast et al. 1989; Groenewegen & Whitelock 1996) tentatively provides L $\approx 3000L_{\odot}$ for P $\approx$ 200 days and L $\approx$ 20 000$L_{\odot}$ for P $\approx$ 1 000 days. However, stars with periods in excess of about 400 days, luminosity is overestimated, may be due to the HBB (e.g. Whitelock et al. 2003), or underestimated, because of the significant circumstellar reddening (Whitelock et al., 2008). Blommaert et al. (1998) and Wood et al. (1998) towards the galactic centre, Blommaert et al. (2018) in galactic bulge, found that OH/IR stars systematically have lower luminosity than predicted (from classical Mira variable PL relations) value. It should be noted that the individual luminosities depend on pulsational phase, and the slope of the PL relationship shows wavelength dependent variation (Riebel et al., 2010). Therefore, it is unlikely to exist a unique PL relation for all AGB stars.

1.4.4 Spectral Energy Distribution (SED)

The spectral energy distribution (see Figure 1.9b) of Mira variables peak around NIR wavelength and at long wavelength, it deviates from normal black-body due to circumstellar materials that absorb visible light and re-emits in the IR region. So, emission from the CSE is important for longer wavelength (> 3 μm) (Woolf & Ney, 1969). The spectral energy distribution (SEDs) of O-rich AGB stars are characterised by alumina (Al_2O_3), silicates or both spectral signatures in the mid-IR region. Alumina appears in the range $9-15$ νm and amorphous silicates are around 9.7 μm and 18 μm. In general, alumina is present in less evolved low mass-loss rate stars, whereas silicate is ubiquitous in more evolved high mass loss rate stars (Guha Niyogi et al., 2011; Gobrecht et al., 2016). Recent interferometric studies indicate alumina formed close to the star (r $< 2R_{star}$) and silicates are at r $\sim 5R_{star}$ (Wittkowski et al., 2007; Sacuto et al., 2013; Karovicova et al., 2013).

1.4.5 Mass-Loss

Mass-loss means outflow of gas and dust from the stellar atmosphere in a continuous form, more or less steady. The mass-loss rate is defined as total mass-loss per unit time in all directions. As the stars evolves through the AGB mass-loss rate increases from typically

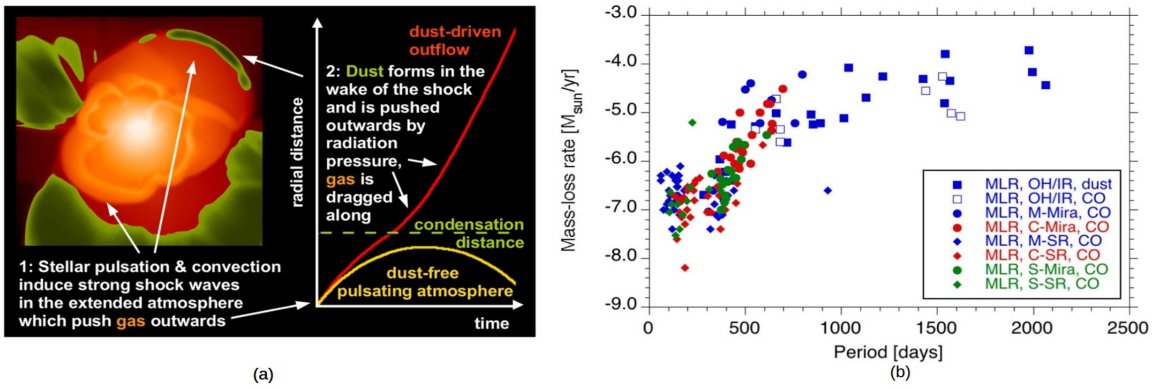

Figure 1.10: A schematic depiction of Mass-loss process (left) and relation of Period vs Mass-loss rate (right) are shown. Source of image : Höfner & Olofsson (2018)

$10^{-7} M_{\odot}\ yr^{-1}$ for Mira variables, to $10^{-4} M_{\odot}\ yr^{-1}$ for OH/IR stars. The first substantial evidence of mass-loss for evolve stars was observed in the binary system α Her by Deutsch (1956). Renzini (1981) proposed 'Superwind' theory, confirmed by Baud & Habing (1983) and Herman & Habing (1985), regarding the intense mass-loss at the end of AGB phase. In the present scenario, the underlying mass-loss mechanism has been well demonstrated by Pulsation-Enhanced Dust-DRiven Outflow (PEDDRO) models (Höfner & Olofsson, 2018). This model explains that stellar pulsation and convection induced strong shock waves levitates the gas to cool out part of the atmosphere where the density is high enough to start dust formation. This dust is pushed outwards by the radiation pressure that drags the gas with them creating a slow but strong stellar wind as shown in Figure 1.10a. This scenario is supported by various observations (e.g., Whitelock et al. 1991, 2003; Glass et al. 2009; McDonald & Zijlstra 2016; Ohnaka et al. 2017). Reimers (1975) derived an empirical relation between the mass-loss rate and stellar characteristics (luminosity, mass, and radius). Lots of effort have been made since then to establish relations between mass-loss rate and K–[12] (Whitelock et al., 2006), K−[8] and K−[24] (Matsuura et al., 2013), [6.4]−[9.3] (Groenewegen et al., 2007), and [3.6]−[8.0] (Matsuura et al., 2013; Reiter et al., 2015), where [12] is the IRAS 12 μm flux while the others are Spitzer fluxes. From the Figure 1.10b, it is evident that the mass-loss rate is positively correlated with the period in the range 300-800 days, attains its maximum value at period $\sim$ 800 days. Furthermore, the mass-loss rate increases with metallicity as expansion velocity increases (Wood, 1998).

1.4.6 s-Process Elements

The s-process elements are formed in the inter-shell region of an AGB star during thermal pulsing phase by slow neutron capture (s-process) reactions (Iben & Renzini, 1983). In s-process, a seed nucleus captures a neutron and produces a stable or unstable isotope

with one higher mass number. The stable isotope again captures a neutron and produces isotopes with increase mass number, while unstable isotopes undergo beta decay and produce isobars with increasing atomic number. The term 'slow' refers to the slow rate of neutron capture that signifies that the isotope gets sufficient time for beta decay before capturing another neutron. The efficiency of the s-process depends on the abundance of free neutrons in the inter-shell region. $^{13}C(\alpha,n)^{16}O$ (low mass stars) and $^{22}Ne(\alpha,n)^{25}Mg$ (massive stars) are believed two dominant neutron sources. The process produces elements (^{88}Sr to ^{208}Pb) heavier than iron (^{56}Fe) (Arlandini et al., 1999) that are distributed in three peaks, corresponding to nuclei with neutron magic numbers N=50, 82 and 126. The first peak (N=50) corresponds to the formation of light s-process (ls) elements (Sr-Y-Zr), the second peak leads to the production of heavy s-process (hs) elements (Ba-La-Ce-Pr-Nd), and the third peak is characterised by lead (Pb) (Magrini et al., 2018). Furthermore, it can be divided into three process: the 'main' process is believed to occur during TP-AGB that produces the s-isotopes from Sr to Pb (e.g., Gallino et al. 1998), the 'weak' process is believed to come from massive stars that are responsible for the s-isotopes from Fe to Sr (e.g., Pignatari et al. 2010), and the 'strong' process is associated with 50% of solar ^{208}Pb production under some circumstances (e.g., very low metallicity) in the AGB stars (e.g., Gallino et al. 1998). The first observational signature of the s-process elements in the AGB star atmosphere is the radioactive element ^{99}Tc (Merrill, 1952) that has the longest half-life (2.1×10^5 yr) of the order of the inter-pulse period.

1.4.7 Spectral Features

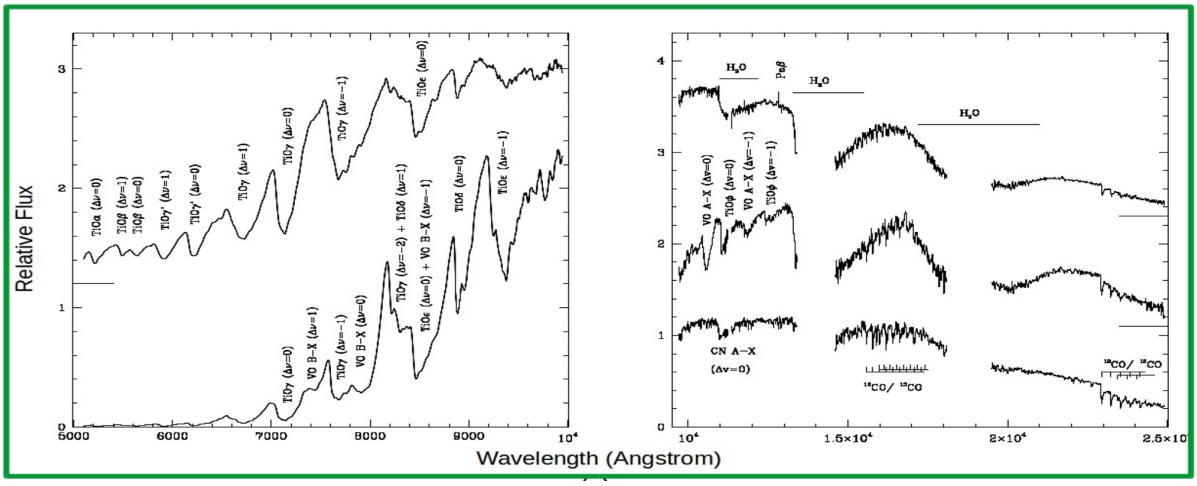

Figure 1.11: Characteristic spectral features of M-type Red giants in optical and NIR region are presented. Source of image : Lançon & Wood (2000)

The 'Red giants' have a large cool extended atmosphere. Spectro-interferometric observations of Mira variables confirm presence of molecular atmospheres extending to a few stellar radii above the continuum-forming photosphere (Mennesson et al., 2002; Perrin et al., 2004; Ohnaka et al., 2005; Wittkowski et al., 2008). The K giants spectra dominated by the Ca triplet (8498, 8542, 8662 $\AA$) that is stronger at K0 subtype and becomes weaker for the later spectral type. The spectra of M giants (Figure 1.11) are dominated by molecular TiO and VO bands in the wavelength range 6000−10300 $\AA$ (Merrill et al., 1962; Castelaz et al., 2000; Kurtev et al., 2001; Rayner et al., 2009). The characteristic TiO bands appear from M0 subtype and get stronger with spectral type, whereas VO bands appear for somewhat later spectral type than TiO. However, the ZrO twin features at 1.03 and 1.06 μm (Hinkle et al., 1989; Wright et al., 2009) are the prominent features for S stars. The 15000−18000 $\AA$ wavelength region are dominated by ^{12}CO second overtone bands and OH molecules (Rayner et al., 2009) for O-rich star, whereas the characteristic C2 bandhead at 17700 $\AA$ line present for carbon stars. The characteristic ^{12}CO first overtone bands and some metallic lines (Na I, Ca I) are found in the wavelength range 20000−24000 $\AA$.

Presence of Balmer emission lines at a certain phase is one of the most interesting features of the Mira variable that was the first identified by Pickering (1887). The strength of these lines varies over the pulsation cycle and becomes strongest at or shortly after maximum visual brightness (Phase zero, e.g., Merrill 1921; Joy 1926; Gray & Corbally 2009. Merrill (1940) suggested that some kind of "hot front" moving outward is the origin of this variation and assumed that the hot front is possibly a shock wave. Nowadays, shock-wave generation of the atmosphere is widely accepted (Deutsch & Merrill, 1959; Gorbatskii, 1961; Willson, 1976; Fadeyev & Gillet, 2004). For Balmer emission lines, one would expect the 'Balmer increment' (i.e., $F_{H\alpha} < F_{H\beta} < F_{H\gamma} < F_{H\delta} < F_{H\epsilon}$) because of their oscillator strength. However, it is miraculously found that the inversion of 'Balmer increment' up to $F_{H\delta}$ for O-rich star, whereas no inversion observed in S-type and carbon star (Merrill, 1940). The TiO absorption (Merrill, 1940; Joy, 1947; Gillet, 1988) and/or on local thermal equilibrium (NLTE) radiative transfer (Bowen, 1988; Luttermoser & Bowen, 1992) whatever attributes the inversion of the 'Balmer increment', the Balmer emission lines only form in the the innermost shock region (Fox et al., 1984a; Richter et al., 2003). Not only Balmer emission lines, Paβ and Brγ also appear for Mira variables at a certain phase as well (Lançon & Wood, 2000). The appearance of many metallic emission lines (e.g., Mg I, Mn I, Si I, Fe I) also reported late in the pulsation cycle, however, they vary independently of the hydrogen lines (Joy, 1954; Richter & Wood, 2001). Furthermore, the doubling of absorption lines around maximum light appears (Merrill & Greenstein,

1958; Maehara, 1968) that is more clearly visible in the NIR region (e.g., Gillet et al. 1985; Hinkle et al. 1997).

1.5 Bits of history and brief overview in the study of AGB

1.5.1 Discovery of LPV − Mira variable

It was August 3, 1596, an amateur astronomer, David Fabricius, had started to monitor the sky aiming to locate the position of a planet assumed as Mercury. He also followed a star as a comparison star that actually is a long period variable. He observed gradually increasing the brightness of the comparison star from magnitude 3 to magnitude 2 until August 21, afterwards, the brightness decreased and disappeared entirely by October from the position (Clerke, 1902). He thought that it was a nova, later got the name o (omicron) Ceti by Johann Bayer in 1603. In 1638, Johann Fokkens Holwarda estimated period (eleven months) of the star (Hoffleit, 1997). Johannes Hevelius named the object Mira, "The Wonderful" in 1642. Afterwards, many other LPVs were detected with the advent of advanced technologies and improvement of detector qualities.

Following the foundation of the American Association of Variable Star Observers (AAVSO)[1] in 1911, great progress in the study of a variable star was achieved. Several authors mainly concerned with photometric variability of Mira variables at different wavelength region and studied the behaviour of the light curve and the characteristic of the energy distribution (Pettit & Nicholson, 1933a; Campbell, 1955; Wing et al., 1966; Lockwood & Wing, 1971).

On the other hand, after the detection of titanium oxide as the characteristic bands of M-type stars by Alfred Fowler in 1904, many earlier works had been confined to the detection of characteristic atomic lines (Sanford, 1947; McKellar, 1954), molecular oxide (McKellar, 1956; Lockwood, 1968, 1969) and stellar water vapour features (Spinrad & Newburn, 1965; Spinrad et al., 1966).

1.5.2 Detection of OH MASER

Wilson & Barrett (1968) first detected type II OH maser through radio observation in two extreme infrared stars. Following the discovery, several sky survey program were

[1] `https://www.aavso.org/`

made to search infrared sources (IRC catalogue − Neugebauer & Leighton 1969; AFGL catalogue − Price & Walker 1976). The optically identified OH maser emitting objects were found to be associated with Mira variables and M-Supergiants (Wilson & Barrett, 1972). The optically unidentified OH maser emitting IRC or AFGL objects are also late M-stars (Hyland et al., 1972; Allen et al., 1977). However, AFGL object is redder than IRC object. On the other hand, hundreds of type II OH maser were discovered along the galactic plane from previously detected infrared sources (IRC, AFGL) by 1612 MHz radio survey (e.g., Caswell & Haynes 1975; Johansson et al. 1977a,b; Bowers & Sinha 1978; Baud et al. 1979a,b), and presumed to be infrared sources without having no obvious optical or infrared counterpart. Subsequently, these new sources were named OH/IR sources that were later confirmed by Schultz et al. (1976) and (Evans & Beckwith, 1977). Meanwhile, H_2O and SiO maser were discovered in the Supergiant VY CMa (Knowles et al., 1969) and late-type stars (Kaifu et al., 1975). Gehrz & Woolf (1971) evinced the presence of circumstellar dust in the long period variable (LPV) from the infrared excess measured long-ward of 3 μm. Reid et al. (1977) proposed that OH maser originates from circumstellar expanding gas and dust shell, where the blue shifted peak comes from the front and red-shifted peak from the rear side of the shell. One can measure the expansion velocity of the envelope as well as the radial velocity of the star from the peak velocity.

1.5.3 A new era with IRAS

Following the data release of IRAS Point Source Catalogue (IRAS-PSC)[2], significant progress in the study of AGB stars in the mid to far infrared was achieved. One of them is the Colour-Colour Diagram formed from the IRAS 12, 25, and 60 μm fluxes. The [12]−[25][3] vs [25]−[60][4] Colour-Colour diagram showed continuous sequence from classical Mira variables of large amplitude to reddest OH/IR stars of small or no amplitude (Olnon et al., 1984). Herman (1983) suggested that those stars of weak pulsation might be reached at the tip of the AGB. This results also confirmed the evolution of OH/IR stars from Mira variables. Bedijn (1987) with the help of models explained the importance of considering continuously increasing mass-loss rate along the sequence and no mass-loss for non-variable OH/IR stars. Also, potential new OH/IR candidates were identified by colour selection and confirmed by detecting their 1612 MHz masers (Engels et al., 1984; Lewis et al., 1985).

[2]IRAS-PSC generated from survey data of Infrared Astronomical Satellite (IRAS) that was launched in 1983 (Beichman et al., 1988)

[3][12]−[25] = $-2.5\ \log F_\nu(12)/F_\nu(25)$

[4][25]−[60] = $-2.5\ \log F_\nu(25)/F_\nu(60)$

van der Veen & Habing (1988a) studied dust and gas envelope stars on the basis of IRAS two-colour diagrams, together with data from the LRS catalog[5] and information on the IR variability. They distinguished stars with O-rich circumstellar shells from C-rich and supported the model prediction of Bedijn (1987) that the evolutionary sequence represents increasing mass loss rate as shown in Figure 1.12. Garćia-Lario (1992) observationally verified the evolutionary sequence obeys the following relation :

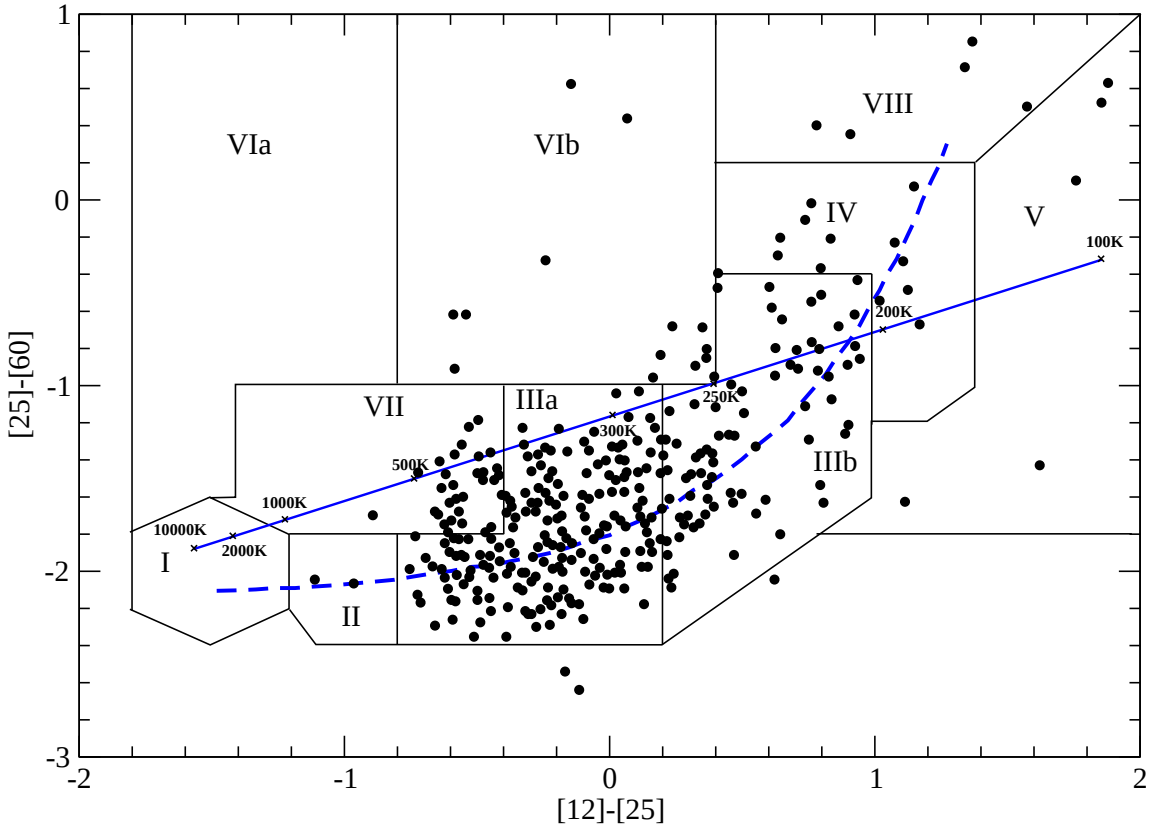

Figure 1.12: In IRAS color−color diagram, the solid line represents the loci of blackbodies at different temperatures, the solid boxes separate different sort of stars with dust-gas CSE, and dashed curve is for the evolutionary sequence of O-rich AGB stars given by the relation [25]−[60] = −2.15 + 0.35 exp(1.5([12] − [25])) (See, van der Veen & Habing 1988a). Basically Region I (O-rich non-variable stars without circumstellar shells), II (variable stars with 'young' O-rich circumstellar shells), IIIa (variable stars with more evolved O-rich circumstellar shells), IIIb (variable stars with thick O-rich circumstellar shells) and IV (variable stars with very thick O-rich circumstellar shells) are representing the O-rich AGB sequence (See, van der Veen & Habing 1988a). The downward arrows denote the upper limit of [25]−[60]. Figure Courtesy : van der Veen & Habing (1988a)

[5]This catalogue was generated from IRAS Low Resolution Spectrometer (LRS) in the range 7.5 to 23 μm

1.5.4 Various Surveys

Following IRAS-PSC various surveys were constructed to study LPVs (e.g., Eder et al. 1988; Benson et al. 1990; te Lintel Hekkert et al. 1991; Le Squeren et al. 1992; Lindqvist et al. 1992; Blommaert et al. 1994; Sevenster et al. 1997a,b). Among them, the most efficient was the search of 1612 MHz OH maser line with the Arecibo radio telescope (Eder et al., 1988; Lewis et al., 1990a; Chengalur et al., 1993a). The Arecibo sample of OH/IR stars consists of 396 IRAS sources with flux densities $\geq$ 2 Jy at 25μm with declination $0^\circ < \delta < 37^\circ$ and colours similar to the known OH/IR stars. A complimentary 1667 and 1665 MHz OH survey of these objects is presented in Lewis (1997).

Various surveys (e.g., MACHO − Wood et al. 1999, OGLE − Soszyński et al. 2009) advance the understanding of AGB stars in galaxies and at the galactic bulge. A number of studies have been specifically focussed on specific parts of the galaxy − solar neighbourhood (e.g., Olivier et al. 2001), galactic centre (e.g., Wood et al. 1998; Glass et al. 2001), galactic bulge (e.g., Whitelock et al. 1991; Jiménez-Esteban & Engels 2015), and in the galactic disk (e.g., Nakashima et al. 2000). Following lots of survey program and detection of new LPVs, extensive optical and NIR monitoring program of those samples were initiated (Whitelock et al., 1994a; Whitelock & Feast, 1994; Olivier et al., 2001; Jiménez-Esteban et al., 2005a, 2006c,b). A number of galactic AGB star catalogues are available in the literature representing all main types of AGB stars (e.g., Loup et al. 1993; Guandalini et al. 2006). A recent database of circumstellar OH masers can be found in Engels & Bunzel (2015).

In more recent time, the Herschel Space observatory (Pilbratt et al., 2010) reveals new insights in the structure and chemistry of CSEs by collecting data at far-infrared and submillimetre wavelengths with good spatial and spectral resolution. A new era begins in the LPV study with the advent of Gaia mission (Gaia Collaboration et al., 2016). The first Gaia catalog of LPVs is now available following Gaia data release 2 (Gaia Collaboration et al., 2018a), that provides 151761 candidates with G-band variability amplitude larger than 0.2 mag (Mowlavi et al., 2018).

Furthermore, interferometry and high-resolution imaging programs play a key role for revealing both the structure and the dynamics of AGB stars atmospheres, providing new insights into shock propagation and dust condensation distances (e.g., Ohnaka et al. 2012, 2016 and reference therein).

1.5.5 Theoretical model

Theoretical modelling of the complex and dynamic atmosphere of AGB star, in particular, the region between the continuum-forming photosphere and circumstellar environment is a challenging task considering the interaction between pulsation-driven shocks, non-equilibrium chemistry, the formation of dust grain and radiation pressure (Ireland et al., 2008). However, various theoretical model atmospheres (e.g., Hoefner et al. 1998; Höfner et al. 2003; Ireland et al. 2008) have been developed over the years for abundance analysis and to understand the physical processes, mass-loss, dust formation of AGB stars since the pioneering works of Wood (1979) and Bowen (1988). The dynamical 1D model atmospheres (Upsalla: Höfner et al. 2003, CODEX: Ireland et al. 2008) can successfully reproduce various observational results like, basic dust-driven mass-loss process, extended molecular layers above continuum-forming photosphere, time-dependent variations of photometric colors and molecular shells (e.g., Tej et al. 2003a,b; Gautschy-Loidl et al. 2004; Nowotny et al. 2005a,b; Ireland & Scholz 2006; Nowotny et al. 2010; Lebzelter et al. 2014; Ohnaka et al. 2012; Wittkowski et al. 2007, 2008, 2015; Woodruff et al. 2009). Still, 1D dynamical models are insufficient to provide a comprehensive picture of the physical processes involving mass-loss and stellar convection (responsible for the non-spherical and clumpy morphology of the atmosphere, Freytag et al. 2017). Moreover, comparative analysis of different 1D models provides a wide range of parameters for a given star's spectrum, and different input parameters and analysis methods are the main sources of these discrepancies (e.g., Lebzelter et al. 2012). Three dimensional (3D) radiation-hydrodynamic model of the outer convective envelope and the inner atmosphere of an AGB star has been developed (Freytag & Höfner 2008), that provides a realistic modelling of the effects of surface convection on the stellar spectra. However, this model only explored in small stellar parameter space, for instance.

1.6 Estimation of fundamental parameters for Red Giants

The estimation of fundamental parameters for the red giants is a long-standing and challenging problem in astronomy. Precise estimation of those fundamental parameters, e.g., effective temperature (T_{eff}), surface gravity ($\log g$), metallicity ($[Fe/H]$), mass (M) and radius (r) provide important information to understand and classify the stellar populations in the galactic and extragalactic environments.

Following Stefan-Boltzmann law, T_{eff} can be directly determined by the equation :

$$T_{eff} = (\frac{4}{\sigma})^{1/4} \theta^{-1/2} F_{bol}^{1/4} \tag{1.2}$$

where, σ is the Stefan-Boltzmann constant, θ angular diameter, and F_{bol} is the bolometric flux measured on the surface of the earth. The main ingredients of this method are to obtain F_{bol} and θ. θ can be measured from long-baseline interferometric method (e.g., Perrin et al. 1998; van Belle et al. 1999) and/or lunar occultation method (e.g., Richichi et al. 1996, 1999; Tej & Chandrasekhar 2000; Mondal & Chandrasekhar 2005). F_{bol} can be derived from multi-wavelength photometric data that are accessible nowadays from the various sky and/or ground-based program in optical to the far-infrared regime with precise measurements. On the basis on this fundamental equation, one of the most popular methods of T_{eff} determination is InfraRed Flux Method (IRFM), introduced by Blackwell & Shallis (1977). Afterwards, many authors have applied this method to constrain the T_{eff} in stars of different spectral types and metallicities (e.g., van Belle et al. 1999; Ramírez & Meléndez 2004; Casagrande et al. 2010, and reference therein). However, this method currently limits reliable measurements of the angular diameter brighter than V $\simeq$ 8 mag star with $\theta \gtrsim 0.3$ mas (Karovicova et al., 2018). Also, T_{eff} can be measured with an accuracy of better than 2.5% only, if angular diameter measured with a precision better than 5%, considering no error in the bolometric flux (Huang et al., 2015; Casagrande et al., 2010). Furthermore, the angular diameter of LPVs such as Mira variables is a function of wavelength (Thompson et al., 2002; Mondal & Chandrasekhar, 2005). Hence, a unique determination of angular diameter is a challenging task. Alternatively, T_{eff} of an unknown sample can be obtained from empirical relation between colour indices versus T_{eff} of standard samples with/without considering metallicity effect (e.g., Casagrande et al. 2010 and reference therein). The empirical relation between T_{eff} versus $(V - K)$ index is most preferential one to determine photometric T_{eff} for late-type giants (see, Plez et al. 1992; Ramírez & Meléndez 2004; Casagrande et al. 2010). The method is independent of the model, however, it depends on photometric data that are greatly affected by reddening and extinction. Moreover, the giants with 2MASS K_s mag < 4.5 gets saturated, and the uncertainty of their colours become larger (Skrutskie et al., 2006). Moreover, no alternative colour index is useful because of saturation for $T_{eff} < 4000$ K (see, da Silva et al. 2006).

Alternatively, the temperature can be determined by the spectroscopic study. The techniques like fitting the profiles of Balmer lines (Gray, 1992; Heiter et al., 2002), globally comparing the observed and synthesized spectra (e.g., Prugniel et al. 2011), fitting the stellar continuum flux with synthesized fluxes (Norris et al., 2013), strength of the

Balmer jump (Sokolov, 1995), line-depth ratio (Kovtyukh et al., 2006; Fukue et al., 2015; Taniguchi et al., 2018) are used in T_{eff} estimations. All these mentioned methods need reliable model atmosphere. The available theoretical model atmospheres like MOOG (Sneden, 1973), or BaSeL (Kurucz, 1992; Lejeune et al., 1997; Westera et al., 2002), or PHOENIX (Allard et al., 2012; Husser et al., 2013), or SME (Valenti & Piskunov, 1996) or MARCS (Gustafsson et al., 2008a) are generally used for stellar population models. The theoretical model atmospheres offer a large wavelength coverage, sufficiently large coverage in parameter space, and arbitrarily high spectral resolution. Moreover, these model atmospheres are free from atmospheric absorption and flux calibration. However, the goodness of model atmospheres relies on available atomic and molecular lines list and approximations in computations. Furthermore, the estimated fundamental parameters for LPVs becomes more inconsistent as model estimation depends on whether pulsation mode or phase in the pulsation cycle is taken into account or not (van Belle et al., 1996; Bessell et al., 1996). Moreover, the model atmosphere becomes uncertain as they diverge from the solar abundances. Consequently, the synthetic model may reproduce the observed spectrum with different parameters than the actual one. Also, such codes lack integrity for stars having spectral type K4 and later ($T_{eff} \leq 4700$ K) because of the incomplete line lists and associated quantum mechanical properties (Yee et al., 2017). In this context, the empirical relationships based on observed spectral libraries would be beneficial in the cool star regime.

The empirical relations based on several optical spectral libraries [e.g., ELODIE (Prugniel & Soubiran, 2001), STELIB (Le Borgne et al., 2003), Indo-US (Valdes et al., 2004), MILES(Sánchez-Blázquez et al., 2006), CaT (Cenarro et al., 2001, 2007)] are generally used to construct reasonable stellar population models. However, stars located in a region with strong interstellar extinction are very difficult to observe in the optical regime. Alternatively, we can probe the stellar atmosphere in the NIR or mid-infrared (MIR) regime because interstellar extinction is comparatively less than the optical regime. Moreover, cool stars ($T_{eff} \sim 3000-6000$ K) emit maximum energy (peak near 1 μm) in the NIR regime and show lots of atomic and molecular spectral signatures (e.g., Na I, Ca I, ^{12}CO overtone bands) that correlates remarkably with fundamental parameters (e.g., T_{eff}, log g, $[Fe/H]$) as in Figure 1.13 considering ^{12}CO first overtone feature.

Since the pioneering work of Johnson & Méndez (1970), a tremendous amount of works were done by many authors in the NIR regime for estimating the physical properties of stars, stellar classification, and to mimic stellar populations of fixed age and metallicity (see, Origlia et al. (1993); Wallace & Hinkle (1997) for reviews). Subsequently, many empirical spectral libraries have been developed to construct stellar population models

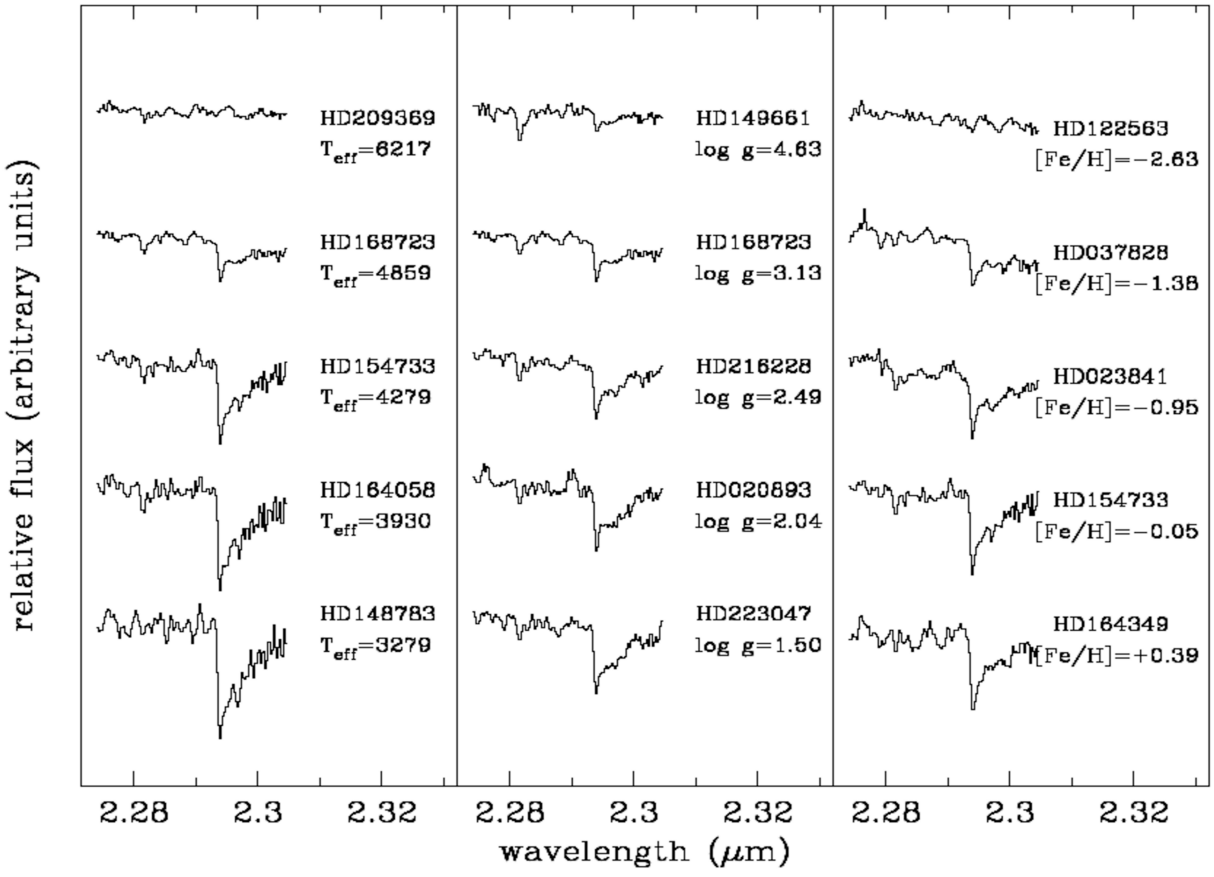

Figure 1.13: Behaviour of the strength of spectral feature with fundamental parameters are shown considering ^{12}CO(2-0) at 2.29 μm. Source of image : Mármol-Queraltó et al. (2008).

in the NIR regime (e.g., Kleinmann & Hall (1986); Terndrup et al. (1991); Origlia et al. (1993); Wallace & Hinkle (1996, 1997, 2002); Blum et al. (1996); Joyce (1998); Förster Schreiber (2000); Lançon & Wood (2000); Ivanov et al. (2004); Mármol-Queraltó et al. (2008); Rayner et al. (2009); Chen et al. (2014); Feldmeier-Krause et al. (2017); Villaume et al. (2017)). A compilation of available important NIR spectral libraries are presented in Table 1.1. However, it has been known for a long time that pulsating stars have molecular bands strength that static giants cannot reach (e.g., Bessell et al. 1989; Alvarez & Plez 1998). Moreover, Mira variables with very similar optical spectra can have very different NIR spectra (Lançon & Wood, 2000), and also colours, spectral types (e.g.,Lockwood & Wing 1971; Wing & Lockwood 1973) as well as Doppler shift and shapes of emission and absorption lines (e.g., Joy 1954; Hinkle et al. 1982) often do not repeat in successive cycles. Thus, estimating fundamental parameters from molecular bands using static reference models provides large uncertain and inconsistent results when dealing with large amplitude variables.

Furthermore, the NASA Infrared Telescope Facility (IRTF) spectral library (Cushing et al., 2005; Rayner et al., 2009) offers the unique advantage of continuous coverage in the NIR and mid-IR regime (0.8−5 μm). The key limitation of this library is of limited coverage in the stellar parameter range. Another empirical library, the X-Shooter stellar library (Chen et al., 2014), which covers optical to NIR (0.35−2.5 μm), would be beneficial once it is complete. Moreover, ongoing large-scale spectroscopic surveys like, e.g., Sloan Extension for galactic Understanding and Exploration (SEGUE; Yanny et al. 2009), the Radial Velocity Experiment (Steinmetz et al., 2006), the Apache Point Observatory Galactic Evolution Experiment (Eisenstein et al., 2011), the LAMOST Spectroscopic Survey of the galactic Anti-center (LSS-GAC; Liu et al. (2014); Yuan et al. (2015)) and Gaia (Perryman et al., 2001) will be valuable for our understanding of the formation and evolution of the Milky Way.

1.7 Motivation

Spectroscopic studies of cool evolved Giants in optical/NIR are very important to understand the atmosphere and formation of molecules in their atmosphere and also help to characterize their fundamental parameters (e.g., effective temperature, spectral class, gravity, metallicity etc.). Stellar spectral libraries have a particularly important role to understand and classify the stellar population as well as an evolutionary synthesis for individual sources in the field, star clusters of our galaxy and integrated stellar lights in the extra-galactic sources. Despite of all the efforts in the understanding of stellar population in a different system, precise estimation of fundamental parameters of cool stars still remains a challenge and have highly sparse databases. The additional database in this spectral range would be highly valuable for the classification and characterisation. Furthermore, the understanding of quantitative diagnostic tools and quality of spectral indices have an important role to quantify the stellar absorption features.

The atmospheres of AGB stars are strongly affected by time-dependent highly dynamical phenomena due to radial pulsation. Over a pulsation cycle, surface temperature and luminosity change significantly. These cause several molecules to form and destroy, and hence they show large spectral variation over the period of pulsation. Lots of observational and/or modelling efforts have been made to understand the dynamical atmosphere, the mass-loss process, the properties of the CSE or characterise those objects, however, a number of questions are yet to answer. Moreover, it is not very well understood how these dynamical behaviours relate to the variability. Thus, the phase-dependent spectroscopic study of AGB stars like Mira variables provides a way to probe their dynamic stellar

Table 1.1: Previous Spectral Libraries and its Characteristics

Literature	Wavelength Coverage	Spectral Type	Luminosity Class	Number of Stars	Resolution (R $\sim \lambda/\Delta\lambda$)
Johnson & Méndez (1970)	1.2−2.5	A−M	I−V	32	550
Kleinmann & Hall (1986)	2.0−2.5	F−M	I−V	26	2500−3100
Lambert et al. (1986)	1.5−2.5	C	–	30	75,000
McGregor et al. (1988)	1.0−2.5	Be, Ae	I	13	500
Tanaka et al. (1990)	1.5−2.5	C	–	33	2000
Terndrup et al. (1991)	0.45−2.45	M	III	32	1000
Lancon & Rocca-Volmerange (1992)	1.4−2.5	O−M	I−V	56	550
Origlia et al. (1993)	1.5−1.7	G−M	I−V	40	1500
Lazaro et al. (1994)	1.1−4.2	C	–	15	500
Ali et al. (1995)	2.0−2.4	F−M	V	33	1380
Oudmaijer et al. (1995)	2.1−2.4	post-AGB	–	18	400−700, ∼1500
Dallier et al. (1996)	1.57−1.64	O−M	I−V	37	1500−2000
Hanson et al. (1996)	2.0−2.4	O−B	I−V	180	800−3000
Jones et al. (1996)	1.16−1.22	M	V	13	1085
Morris et al. (1996)	1.45−2.4	WR, O, B, LBV	I	26	570−1600
Wallace & Hinkle (1996)	2.02−2.41	G−M	I−V	12	45000
Blum et al. (1996)	1.5−1.8	O−B	I−V	11	575
Figer et al. (1997)	2.0−2.4	WR	–	38	525
Ramirez et al. (1997)	2.19−2.34	K−M	III	43	1380, 4830
Wallace & Hinkle (1997)	2.0−2.4	O−M	I−V	115	3000
Joyce (1998)	1.0−4.1	C	–	29	$\sim$ 500
Joyce et al. (1998)	1.0−1.3	M,S, C, AGB	III	103	1100
Meyer et al. (1998)	1.5−1.7	O−M	I−V	85	3000
Pickles (1998) (compilation)	0.15−2.5	O−M	I−V	131	50−6000
Förster Schreiber (2000)	1.95−2.45	G−M	I−III	31	830, 3000
Lançon & Wood (2000)	0.5−2.5	K−M, AGB	I−III	77	1100
Wallace et al. (2000)	1.05−1.34	O−M	I−V	88	3000
Frogel et al. (2001)	2.17−2.34	RGB	–	129	1500
Lenorzer et al. (2002)	2.36−4.05	O−B	I−V	75	1500−2000
Malkan et al. (2002)	1.08−1.35	O−M	I−V	105	650
Vandenbussche et al. (2002)	2.36−4.05	O−M	I−V	293	1500−2000
Wallace & Hinkle (2002)	3.3−4.2	G−M, AGB	I−V	42	3000
Ivanov et al. (2004)	1.48−2.45	G−M	I−V	218	2000−3000
Ranade et al. (2004)	1.5−1.8	O5−M3	I−V	135	1000
Cushing et al. (2005)	0.8−4.2	M, L, T	V	30	940−2000
Lodieu et al. (2005)	0.6−1.0, 1.0−2.5	M6−L2	V	71	600
Hanson et al. (2005)	1.6−2.2	O−B	I−V	37	8000−12000
Ranada et al. (2007)	2.0−2.2	O7−M7	I−V	114	1000
van Loon et al. (2008)	2.9−4.1	C, AGB, RSG	–	50	200−400
Ranade et al. (2007)	1.1−1.3	O5−M8	I−V	125	1000
Venkata Raman & Anandarao (2008)	1.5−1.8,2.0−2.4	AGB	–	78	1000
Mármol-Queraltó et al. (2008)	2.1−2.4	O−M	I−V	220	2500
Rayner et al. (2009)	0.8−5	F−M, S, C, AGB	I−V	212	2000, 2500
Winge et al. (2009)	2.02−2.43	G8−M3	I−III	13	6000
Villaume et al. (2017)	0.7−2.5	F−M	III−V	284	2000
Ghosh et al. (2019)*	1.5−2.4	K−M	III	72	1200

*This work

atmospheres and underlying pulsation mechanisms occurring during the variability phase. Extensive spectroscopic studies of the pulsation cycle on that Mira variable provide a wealth of information on phase dependent variation of several fundamental parameters, e.g., surface temperature, spectral type, etc. Furthermore, no models still can interpret dynamical variation with pulsation or Mira variables spectral indices at late spectral types, and that is not really surprising considering the amplitude of variability. But, the data that can show correlations between lines in the optical and in the NIR for one Mira variable (or a group of Mira variables in a cluster), as it varies in time, are interesting to collect. Lots of time-dependent or phase dependent data are needed to set constraints on models at least in a statistical sense or to model the complex convective atmosphere of a Mira variable as it happens to be at the instant of observation.

The OH/IR stars are also very poorly understood and lots of questions remain elusive. OH/IR stars are characterised with 1612 MHz maser emission and optically thick CSE. However, extreme Mira variables also show 1612 MHz masers, and on the other hand, many AGB stars showing 1612 MHz masers have optically thin envelops. Thus, the fundamental question comes into mind how one can make a distinction between Mira variables and OH/IR stars, is it on the basis of progenitor mass or evolutionary phase (see section 1.3). However, it is evident that all the OH/IR stars in the AGB phase show Mira variable like pulsation (few OH/IR stars that show no pulsation are considered as Post-AGB stars). It is also very interesting to study phase dependent variation of atomic and molecular lines of OH/IR stars that help to understand whether Mira variable and OH/IR stars behave similarly or not. Although it is very difficult to draw any conclusive evidence because the same physical characteristic might not occur persistently in pulsating AGB. However, it is worth to spectroscopically study those objects at different variability phase as the phase dependent study are very rare in literature, although provides important information about the stellar interior and dynamical atmosphere.

1.8 Outline of the Thesis

The focus of this thesis is twofold. Firstly, it endeavours a theoretical and empirical analysis of the behaviour of the spectral signature with fundamental parameters for K−M giants. Secondly, it brings out the importance of little known time-dependent behaviour of O-rich AGB stars. The outline of this thesis is as follows (see also Figure 1.14).

Chapter 2: In this chapter, we describe the telescopes and instruments, obtaining the data for this work. The analysis techniques – observations, data reduction, data

acquisition method are also presented. The chapter offers a description of the theoretical models used in this thesis.

Chapter 3: In this chapter, we present a medium-resolution ($\lambda/\Delta\lambda \sim 1200$) spectral library of 72 K−M giants covering a wavelength range 1.50–2.45 μm obtained with medium resolution TIFR Near-Infrared Spectrometer and Imager on the 2.0 m Himalayan Chandra Telescope located at Hanle, India. In addition, we have taken all available 35 giants spanning a spectral range K0−M8 from archival spectral library observed with the medium-resolution ($\lambda/\Delta\lambda \sim 2000$) infrared spectrograph, SpeX, at the 3.0 m NASA Infrared Telescope Facility on Mauna Kea, Hawaii. Assembling 107 giants, we investigate the variation with stellar parameters of equivalent widths of some important spectral features like Si I, Na I, Ca I, and ^{12}CO and compare the behaviour of those spectral features predicted by the theoretical model atmosphere. In addition, we derive the empirical relations between stellar parameters and equivalent widths of four strong ^{12}CO bandheads from the observed sample and study their relative effectiveness for stellar parameters estimation.

Chapter 4: In this chapter, we extend the investigation of empirical relations with stellar parameters for various CO index definition to provide improved parameters. The CO indices in K-band are adopted from the literature for ^{12}CO bandhead at 2.29 μm, whereas two H-band CO indices for ^{12}CO bandhead at 1.62 μm are newly defined in this thesis for line-strength measurement. For the better characterisation of late M subtype (> M4), we explore the H_2O−K2 index, which was originally defined to characterise the dwarf stars. Finally, we study the comparative behaviour of spectral indices between the observed sample and theoretical model atmosphere.

Chapter 5: In this chapter, we study the red optical transient MASTER OT J212444.87+321738.3. We characterise the object as a classical O-rich Mira variable from long-term optical/NIR photometric and spectroscopic observations. The object was selected from the list of optical transients discovered by Mobile Astronomical System of TElescope Robots (MASTER) based on large $(J - K)$ colour index. We estimate the variability period and study the wavelength-dependent variability of the object from the best-fits of optical/NIR light curves. From the PL relation, the luminosity and the distance to the source are estimated. We have fitted the SED from NIR to far-IR data and evaluated dust temperature, mass-loss rate, optical depth etc. Finally, we present a rare study on spectral variability with the pulsation phase of the Mira variable.

Chapter 6: In this chapter, we present the photometric and spectroscopic characterisation of a high-luminous OH/IR star, MASTER OT J183012.04+093342.6, which is an extreme AGB star. From optical *RI*-band variability data, we fit the light curve and estimate the variability period. We present the SED fitting from multi-wavelength photometric and IRAS spectral data. The obtained luminosity and mass-loss rate from best-fit SED are compared with various PL relations for AGB stars and period–mass-loss rate relation available in the literature, respectively. We evaluate the mass of the object and study the evolutionary scenario of the object. We study the spectral variability from time-dependent optical/NIR spectroscopic data at the end of this chapter.

Chapter 7: In the last chapter of this thesis, the summary of this thesis and the future aspect of this work are presented.

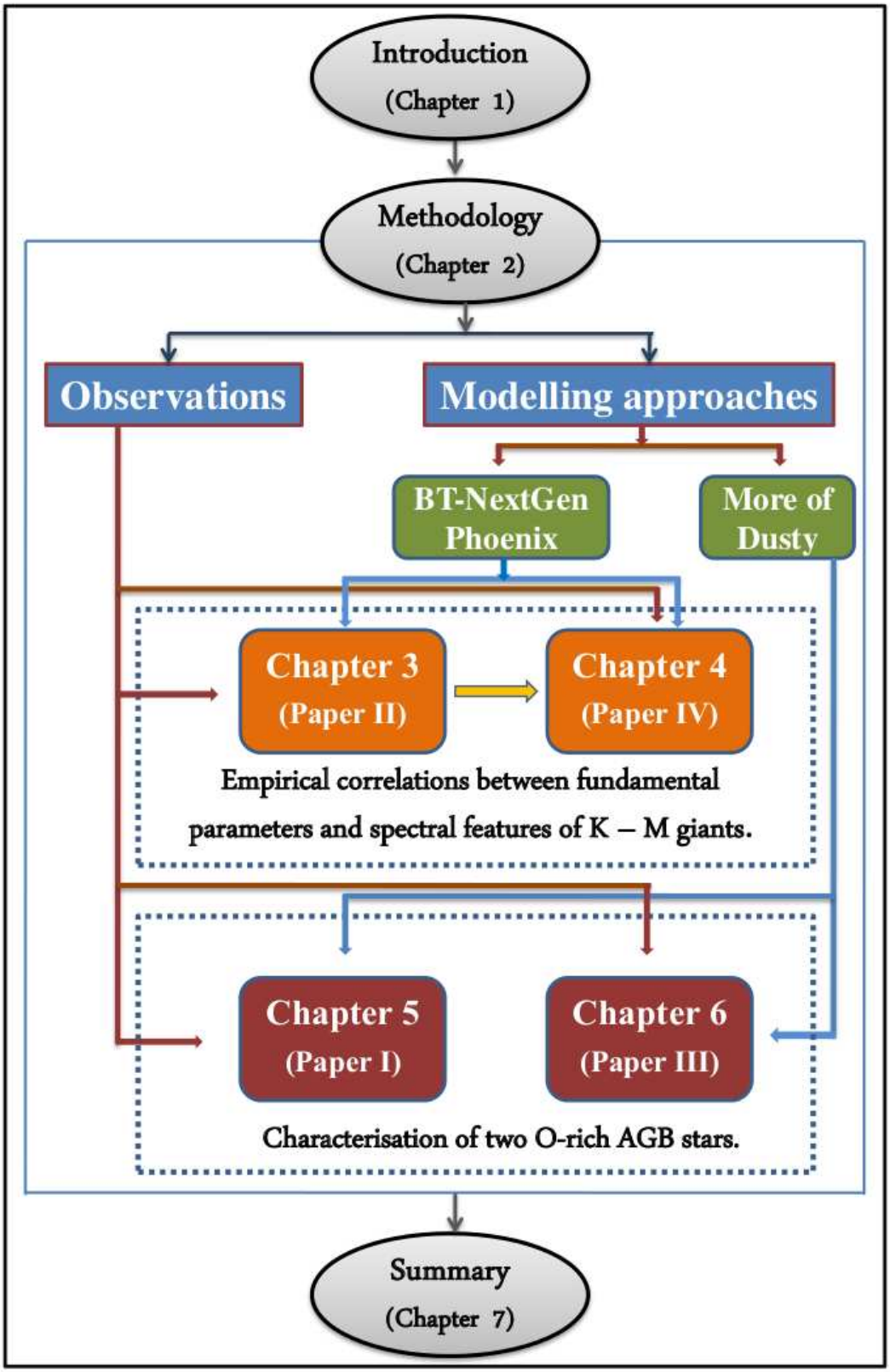

Figure 1.14: Schematic view of the outline of this thesis.

Chapter 2

Methodology

This chapter begins with an overview of the aspect of observations as well as data analysis techniques, which have been performed for this thesis work. This will be followed by describing archival dataset and spectral library relevant for this work. Afterwards, the theoretical models implemented in this work for the SED fit from multi-wavelength observational data and for the qualitative study between fundamental parameters and spectral indices from synthetic spectra will be described.

2.1 Observations & Data Analysis

This section provides a brief introduction of the telescope facilities used for optical/NIR photometric and spectroscopic observations and a brief description of the back-end instruments attached to those telescopes. This will be followed by a brief description of general photometric and spectroscopic observational procedures, and data reduction techniques used in this thesis.

2.1.1 Telescopes

The optical/NIR observations are carried out using two ground-based Indian telescopes: the 1.2 m telescope at the Mount Abu Infrared Observatory (Latitude: 24° 39′ 10″ N, Longitude: 72° 46′ 47″ E, altitude 1680 m above MSL), Mount Abu, Rajasthan, operated by the Physical Research Laboratory (PRL), Ahmedabad, and the 2.01 m Himalayan *Chandra* Telescope (HCT) at Indian Astrophysical Observatory (IAO, Latitude: 32° 46′ 46″ N, Longitude: 78° 57′ 51″ E, altitude 4500 m above MSL), Mt. Saraswati, Hanle,

Table 2.1: Details of telescope used for observations

Telescope Parameters	Mt. Abu telescope	HCT
Aperture of Primary mirror (m)	1.2	2.01
Mirror Shape	primary − paraboloid secondary − hyperboloid	primary − hyperboloid secondary − hyperboloid
Mount	Equatorial	Alt − Azimuth
Focus	Cassegrain and Coude	Cassegrain and Nasmyth
F-ratio	Primary − $f/3$ Cassegrain − $f/13$	Primary − $f/1.75$ Cassegrain − $f/9$
Image Scale ($''$/mm)	13.2	11.5

operated by Indian Institute of Astrophysics (IIA), Bangalore. The pictorial view of both observatories is shown in Figure 2.1. The Mt. Abu telescope consists of a 1.2 m paraboloid primary mirror, and a hyperboloid secondary mirror that directs the light to the back-end instruments at the Cassegrain focus, whereas HCT has a 2.01 m hyperboloid primary, and a hyperboloid secondary mirror. The HCT is operated remotely from CREST, Hosakote, Bangalore, via a dedicated satellite link. Some important parameters of those telescopes are listed in Table 2.1.

2.1.2 Back-end instruments

The back-end instruments of the Mt. Abu telescope for the different mode of observations are Near Infrared Camera and Multi Object Spectrometer (NICMOS-3), Near Infrared Camera/Spectrograph (NICS), Liquid Nitrogen cooled CCD Camera, PRL Optical Polarimeter (PRLPOL) and PRL Advanced Radial velocity Abu Sky Search (PARAS) Echelle spectrograph, whereas HCT is equipped with the Himalaya Faint Object Spectrograph (HFOSC), the NIR Imaging Spectrograph (TIRSPEC) and the Hanle Echelle Spectrograph (HESP). The remarkable advantage of HCT is that the TIRSPEC and the HESP are permanently mounted at the Cassegrain focus through side ports of the instrument mount cube, while the HFOSC is on the main port. Therefore, one could easily switch over one instrument to another almost immediately in a single night. In this thesis work, all the spectroscopic and photometric observations were obtained using **NICMOS-**

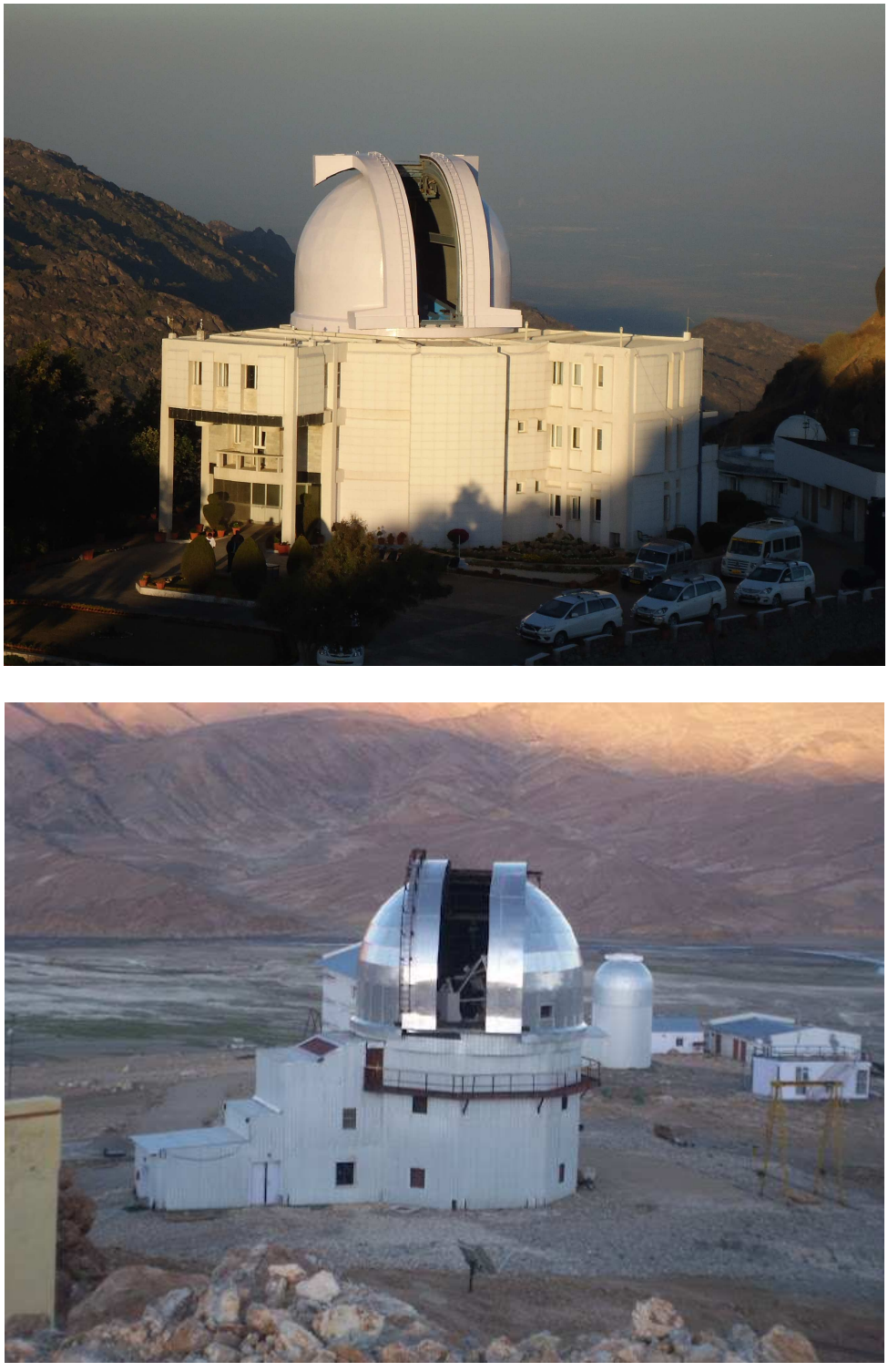

Figure 2.1: Figure shows the front view of the Mt. Abu observatory, Mt. Abu (top) and the Indian Astrophysical Observatory (IAO), Hanle (bottom). IAO Image credit : Raghu Kalra
Source of IAO Image : `www.aaadelhi.org/vt2012/circumstances.html`

3 instrument on Mt. Abu telescope, **HFOSC** and **TIRSPEC** instruments on HCT. An overview of these instruments are provided in Table 2.2.

NICMOS-3

The NICMOS-3 instrument that is located at the Cassegrain focus of the telescope, which has the capabilities of operating in imaging as well as spectroscopy mode. The F/13 telescope beam enters the optics of the instrument after being reflected by the 45° gold-coated mirror passes through a focal reducer lens. The focal reducer optics can compress the F-ratio to $f/6.5$ and enhance the field of view (FOV) from $2' \times 2'$ to $4' \times 4'$. After passing through two filter wheels, Lyot stop (aperture) and a parabolic mirror (collimator), the light beam then directs either towards the plane mirror (imaging mode) or grating assembly (spectroscopic mode). First filter wheel consists of broadband filters ($JHKK'$) and the other one consists of narrowband filters. Different types of Lyot stops are available for imaging (circular and square) and spectroscopy (slit of width 75 μm $\sim$ 2 pixels). Finally, the light beam collected by a 256 $\times$ 256 HgCdTe detector array after being reflected by a camera optics (parabolic mirror). The entire instrument is cooled at liquid nitrogen (LN2) temperature (77 K). A schematic diagram of the NICMOS-3 instrument and layout of the optics are shown in Figure 2.2.

HFOSC

The HFOSC instrument that is located at the Cassegrain focus of the telescope is an optical imager cum spectrograph. The $f/9$ converging light beam from the secondary mirror of the telescope enters the instrument after passing through the Filter and Spectral Lamp Unit (FASU) interface unit and falls on the aperture wheel located at the focal plane of the telescope. FASU has two filter wheels (FASU-A and FASU-B for narrowband filters and calibration-mirror), three wavelength calibration lamps (Fe-Ar, Fe-Ne hollow cathode and Hg-Cd lamps) and a flat-fielding lamp (Halogen lamp). Aperture wheel has eight slots in which seven various slits are available for the spectroscopy and one slot is free for the imaging mode. The optical light beam emerging out of the aperture wheel passes through the collimator to form a parallel beam. The parallel beam then passes through filter wheel and the grism wheel and ultimately falls on the camera which converges the light beam to a thinned and back-illuminated 2048 $\times$ 4096 SITe ST-002 CCD chip with pixel size of 15 $\times$ 15 μm. Filter wheel and grism wheel have eight slots, in which, one slot are made free. In spectroscopic mode, the FASU-A and FASU-B, and filter wheel are in the 'free' position. In imaging mode, the filter/grism wheels and the FASU wheels that are not

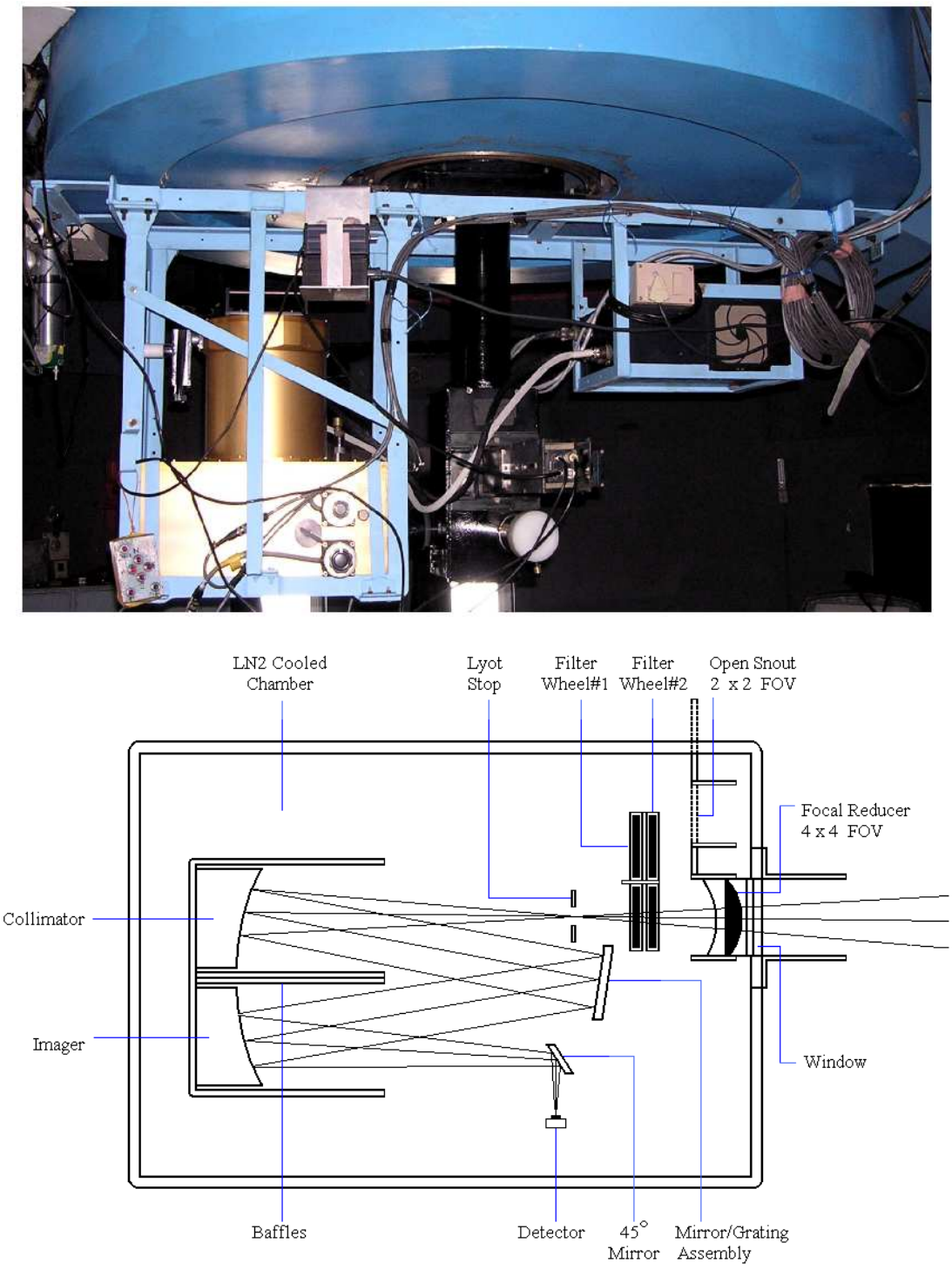

Figure 2.2: The figure represents the view of NICMOS-3 instrument (golden) at top and schematic diagram of ray optics at the bottom panel. Image credit : Das (2009)

required set in 'free' position. The instrument is a focal reducer type instrument, which can reduce the effective focal length of the telescope, and also provides relatively wide-field coverage for a given detector. The focal reducer optics provides the unvignetted imaging FOV on 2K × 2K chip area of 2K × 4K CCD. A detailed description of the instrument is available at the HFOSC user's manual[1]. A schematic diagram of HFOSC instrument is shown in Figure 2.3.

TIRSPEC

The TIRSPEC instrument is located at the Cassegrain focus of the HCT, and it is a NIR Spectrometer-cum-Imager. The $f/9$ converging light beam from a secondary mirror of the telescope enters the instrument after passing through the CaF_2 window and falls on an eleven-position slit wheel located at the telescope focal plane. The slit wheel houses five short slits ($10''$ long) and five long slits ($300''$ long) for spectroscopy and one position remains open for the imaging mode of observation. The emerging beam of the slit wheel is collimated by a BaF_2-LiF-BaF_2 triplet lens system that sends the collimated achromatic beam on to the cold stop which is sandwiched between two filter wheels. Both filter wheels have twelve positions. The first wheel houses broadband filters (J, H, K_s), order shorter filters (Y, J, H, K), and cross-dispersing grisms (YJ and HK), whereas, the other wheel houses seven narrow band photometric filters as well as one grism, and one open position. The beam is then directed towards a camera system that images the beam on to the focal plane Teledyne 1024 × 1024 pixel Hawaii-1 PACE array detector. The camera system consists of BaF_2-LiF-ZnSe triplet lens and a BaF_2 singlet lens. The entire instrument is kept inside an LN2 cooled enclosure. Three gold coated fused silica plane mirrors (Fold 1, Fold 2, and Fold 3) are used to fold the optical path and fit the entire optics inside a cooled enclosure. In spectroscopy mode of observation, a calibration lamp assembly (argon lamp with a movable plane mirror) can be moved into the optical path for calibration purpose. Additional details of the instrument can be found in Ninan et al. (2014) and at the TIRSPEC users manual[2]. A schematic diagram of this instrument and layout of the optics are shown in Figure 2.4.

2.1.3 General observing strategy

The data for this thesis work are acquired in the photometric and the spectroscopic mode of observations. The photometric data are obtained with the HFOSC instrument in the

[1] https://www.iiap.res.in/iao_hfosc/
[2] http://web.tifr.res.in/~daa/tirspec/

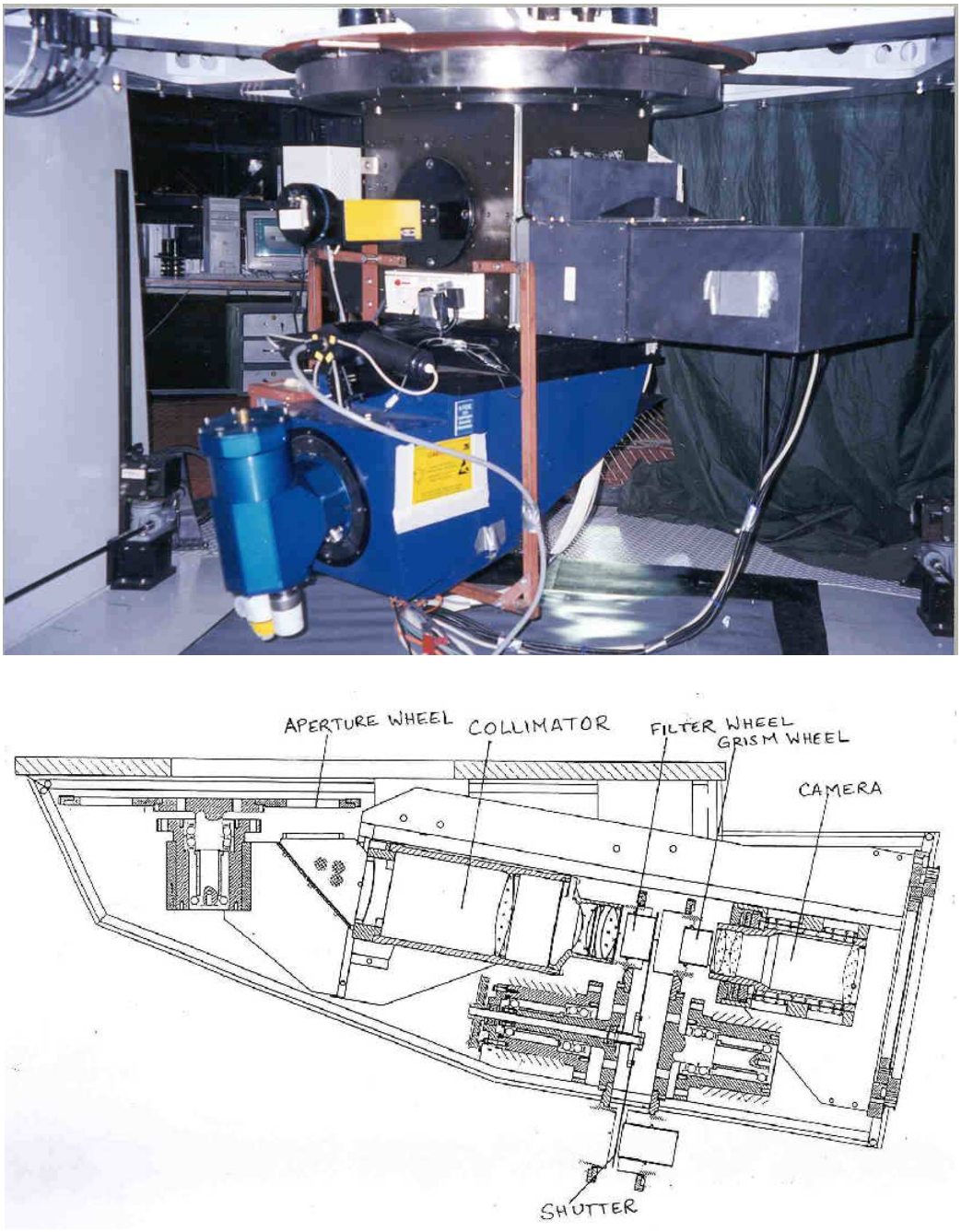

Figure 2.3: The schematic view of HFOSC instrument are shown in this figure. Image credit: IIA
Source of Image : HFOSC Users Manual (`https://www.iiap.res.in/iao/hfosc.html`)

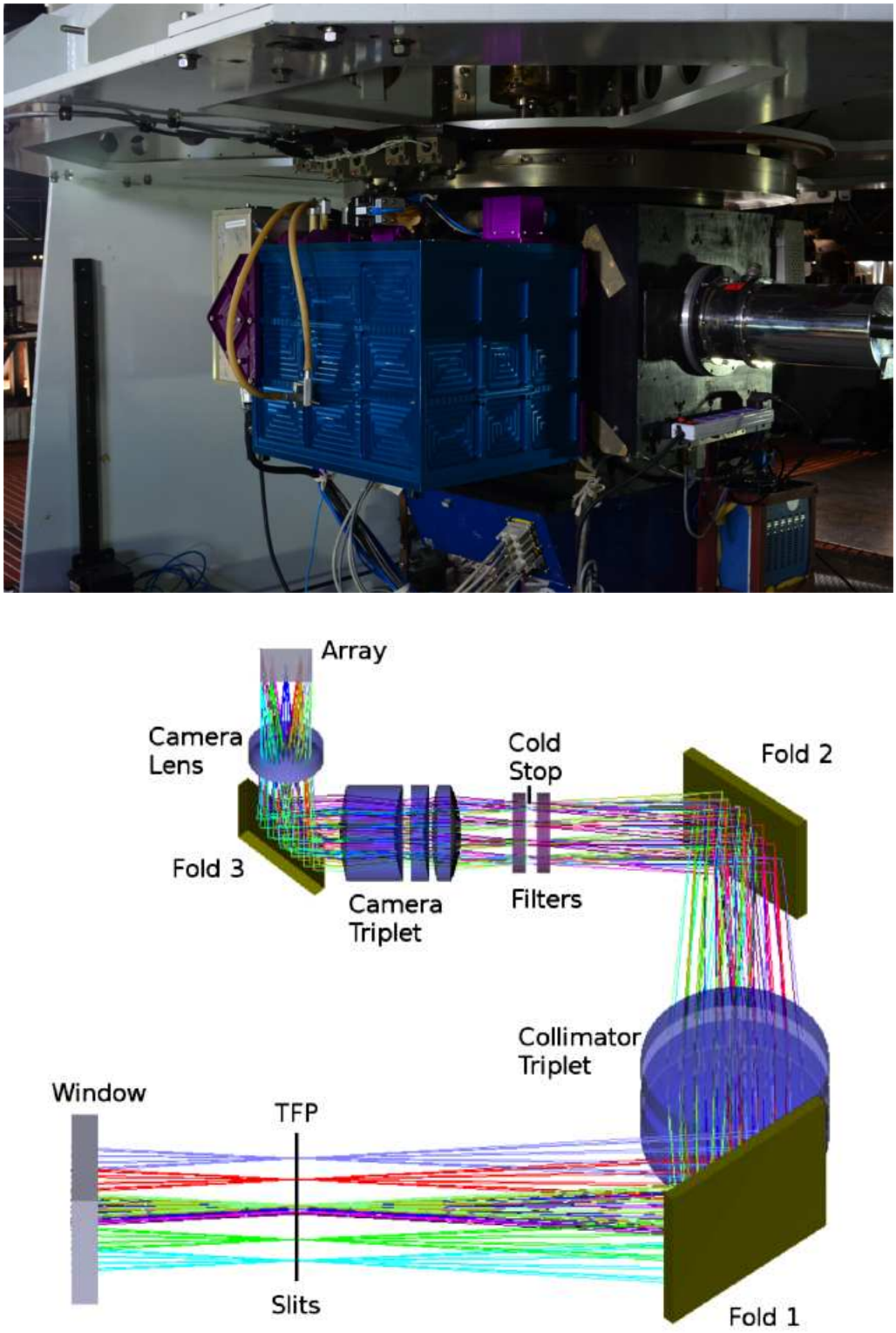

Figure 2.4: Figure represents cryostat and folded ray optics of TIRSPEC. Source of Image : Ninan et al. (2014).

Table 2.2: Description of the detectors and filters used for observations

Telescope	Mt. Abu	HCT	
Instrument	NICMOS-3	HFOSC	TIRSPEC
Detector	256 × 256 HgCdTe	2K × 4K SITe	1K × 1K Hawaii-1 array
Pixel Size (μm)	40	15	18
Pixel Scale ($''$/pixel)	0.528	0.296	0.3
Field of View ($'$)	2 × 2	10 × 10	5 × 5
Gain (e^-/ADU)	10.0	1.22	5
Read Noise (e^-)	53	4.8	4.3
Photometric filters	J, H, K	Bessell R, I	–
Spectroscopic filter/grism	J (1.105−1.401 μm) H (1.514−1.803 μm) K (1.981−2.389 μm) KA (1.940−2.30 μm)	Grism#8 (0.580−0.920 μm)	$GYJX$ (1.02−1.49 μm) $GHKX$ (1.50−1.84 & 1.95−2.45 μm)
Slit Width ($''$)	2	1.92	1.97
Spectral Resolution	1000	2200	1200

optical wavelength using R and I broad-band filter and with the NICMOS-3 instrument in the NIR region using JHK filter. The optical/NIR spectroscopic observations are carried out using three different back-end instrument on two telescopes: HFOSC for optical region 600−920 nm using Grism #8 on the HCT; TIRSPEC for NIR wavelength wavelength (YJ/HK) on the HCT; and NICMOS-3 for NIR regime covering the wavelength from 1 to 2.4 μm. NIR and optical observations are in principle similar, however, differences arise due to higher dark current in the detector and large temporal variation of the NIR sky. The reason behind the sky variation is non-thermal emission from excited molecules in the upper atmosphere because of hydroxyl radical (OH^-), O_2 at 1.27 μm and H_2O at the red part of K-band (Ramsay et al., 1992) at the atmospheric window of $0.8 < \lambda < 2.4$ μm region and the thermal emission from the telescope and surrounding dome beyond 2 μm.

It has to be noted that the following steps should be followed before starting the observations.

- 3 'Dark' frames with 100 second exposure should be taken for TIRSPEC instrument.
- Twilight sky 'Flat' frames should be taken for imaging mode of operation for TIRSPEC as well as HFOSC.
- 'Bias' frames (image bias/spec bias) are taken for imaging/spectroscopic mode of operation of HFOSC instrument.

To begin the scientific observation, the Equatorial coordinates (right ascension, declination) of the source are provided to the telescope control system (TCS) so that the telescope can point at the object and consecutively the dome of the telescope aligns properly with the telescope. It is customary to expose the object or object field with short exposure, and compare the image at the detector with the finder chart of the object to ensure that the telescope is pointing at the desired field despite high pointing accuracy of the telescope ($< 1.5''$ for $> 10°$ move for HCT). The object then becomes ready for imaging or spectroscopic mode of observations.

Brief description of photometric observations

Photometry is a basic technique in astronomy that primarily yields the apparent magnitude of an astronomical object. Measurement of magnitude corresponds to the measurement of flux, which provides information on the luminosity, size, and effective temperature of the object, combined with the distance of the object. The time series photometric data

offer a unique opportunity to measure brightness variations, the period of the variable objects. The basic procedure of photometric observations is as follows.

- After matching the field of the star, the desired filter is selected, and the object is exposed with a suitable integration time depending on the magnitude of the star. As the NIR sky is ≈ 800 times brighter than optical, and sky varies on time scales of a few minutes, the star is observed at least at five dithered positions, offset typically by $20''$ (Mt. Abu) or $15''$ (HCT). The multiple dithering is needed for NIR observations to generate the good sky-background, and also eliminate bad pixel of the detector. The NIR detectors usually become saturated beyond 20-30 seconds of exposure in H or K filter due to sky background. Hence, multiple frames with short exposure are taken to improve the signal-to-noise ratio (SNR).
- For photometric calibration, suitable standard star field is observed following the same method. Landolt standard field is generally used for optical imaging.

Brief description of spectroscopic observations

Spectroscopy is one of the most powerful tools in astronomy by which one can learn enormous information about stars and their physical properties. Spectra of stellar objects unveil information on the elemental abundances, temperature, pressure, radial velocity, spectral energy distribution and line profiles. The basic constituents of a spectrograph are a slit that defines the spectral resolution, a collimator that makes light beam parallel, a dispersing element (commonly a reflection/transmission grating) that disperses the light beam into its constituent colours, and a camera that focuses the beam onto the detector. The procedure of spectroscopic observations is as follows.

- First, the required slit is selected and the object is centred on the slit. After selecting the desired filter, the object is exposed with a suitable integration time depending on the magnitude of the star. If the exposure of more than 300 seconds is required the auto-guider should be started that guides the telescope automatically to point the same object. For NIR observation, the object is observed simultaneously at least two dither positions along the slit to counter the NIR sky contributions. Furthermore, multiple frames are taken at each dither to improve the SNR.
- After the observation of the science frame in each filter, lamps and flats are taken before moving that filter and slit. For TIRSPEC, Argon lamp (Ar lamp) spectrum for wavelength calibration and a tungsten lamp spectra for the continuum flat (3

frames with 10 second exposure each) for flat correction are taken. For HFOSC, FeNe or FeAr lamp spectra is taken for wavelength calibration purpose depending on which grism is used to observe the science frame. For NICMOS-3, no calibration lamp is taken for wavelength calibration. OH sky lines and telluric lines are used for this purpose.

- Following the science frame observation, a suitable spectroscopic standard star is observed in nearby airmass for telluric corrections. The NIR standard stars are mainly B9V or A0V or A1V spectral type because these stars show no other feature except Hydrogen lines, which can be easily identified and removed at the time of spectral reduction.

- The spectrograph in the NICMOS-3 instrument does not cover the whole K-band in a single shot. Hence, the spectra were observed in two parts: the first part covers 1.9−2.3 μm wavelength region (termed as K), and the second part covers 2.1−2.4 μm (termed as KA). Some portion at the middle part of the spectra overlap. This overlapping portion is used to splice together to form the whole spectra.

- The TIRSPEC instrument provides the single order mode to obtain the spectrum of each order separately or the cross-dispersed mode to obtain spectra in two orders simultaneously. Two cross-dispersed modes, YJ and HK, are used for our observations to get larger wavelength coverage in one exposure than single order modes. The YJ mode covers the Y and J windows (1.02−1.49 μm) and the HK mode covers the H and K windows (1.50−1.84 & 1.95−2.45 μm).

2.1.4 Data reduction

Data reduction is a process in which raw data are transfigured into a corrected and simplified form such that data can be more easily implemented for science case. The observed raw images sustain not only star signature but also unwanted instrumental signatures (background emissions from the telescope and the atmosphere, pixel to pixel quantum efficiency variation of the detector, electronic amplifier noise, bad pixels), and some unwanted signals (e.g., cosmic rays) affect the raw images. Cleaning of the raw images is essential to get rid of these unwanted signatures. The data reduction was performed with the help of standard tasks of the Image Reduction and Analysis Facility (IRAF[3]) which is supported by the National Optical Astronomy Observatories (NOAO)

[3] `https://iraf.noao.edu/`

in USA. The TIRSPEC data was reduced with the TIRSPEC pipe-line[4] and was cross-checked with the IRAF reduction.

Photometric data reduction

Bias correction:
Bias correction means subtraction of 'Bias frames' from raw image frames. The 'bias frame' estimates 'bias level' (underlying dc offset voltage) and 'readout noise' within each raw images. The 'bias frame' is taken at zero exposure time with the shutter closed. Multiple 'bias frames' are observed throughout the whole night of observing run to check the health of the detector. The master bias frame is produced using the 'ZEROCOMBINE' task in 'IRAF' by average combining of all these bias frames.

Flat-field correction:
A Flat field is the combined response of the optical system and CCD throughput at each pixel to a source of uniform illumination. Flat-field correction signifies counteracting the pixel-to-pixel sensitivity variations in the CCD, correction for anomalies in the optical path, such as dust or scratches on the CCD window, and removal of illumination variations by the telescope or camera lens optics (vignetting). Flat-field frames are obtained by imaging the sky during evening or morning twilight for each filter in the observations run. To obtain good results, several bright flat-field frames are observed, where the detector is well exposed. The counts of flat-field are preferably 50−70 per cent of maximum CCD counts (CCD saturation level). The master flat is generated in each filter using the 'FLATCOMBINE' task in 'IRAF' by average combining of all these flat-field frames that are bias subtracted. Flat-field correction is done by dividing the science image in each filter by the master flat which is normalised by the mean counts.

Both Bias and Flat-field correction are done using the 'CCDPROC' task in 'IRAF' using master bias and master flat frame.

Dark correction:
Dark correction corresponds to the removal of thermally accumulated charge in the image ('dark counts'). The dark counts depend on detector temperature. When the detector is exposed for a long time (longer than 5 minutes), a considerable amount of charge can acquire in the detector pixels due to thermal fluctuations. These are termed as 'hot-pixels'. The dark counts can be measured by exposing the detector at various exposure times with the shutter closed. These dark frames are subtracted from the science images to get rid of dark counts. The dark image frame at an exposure of zero second is called a bias frame

[4] https://github.com/indiajoe/TIRSPEC/wiki

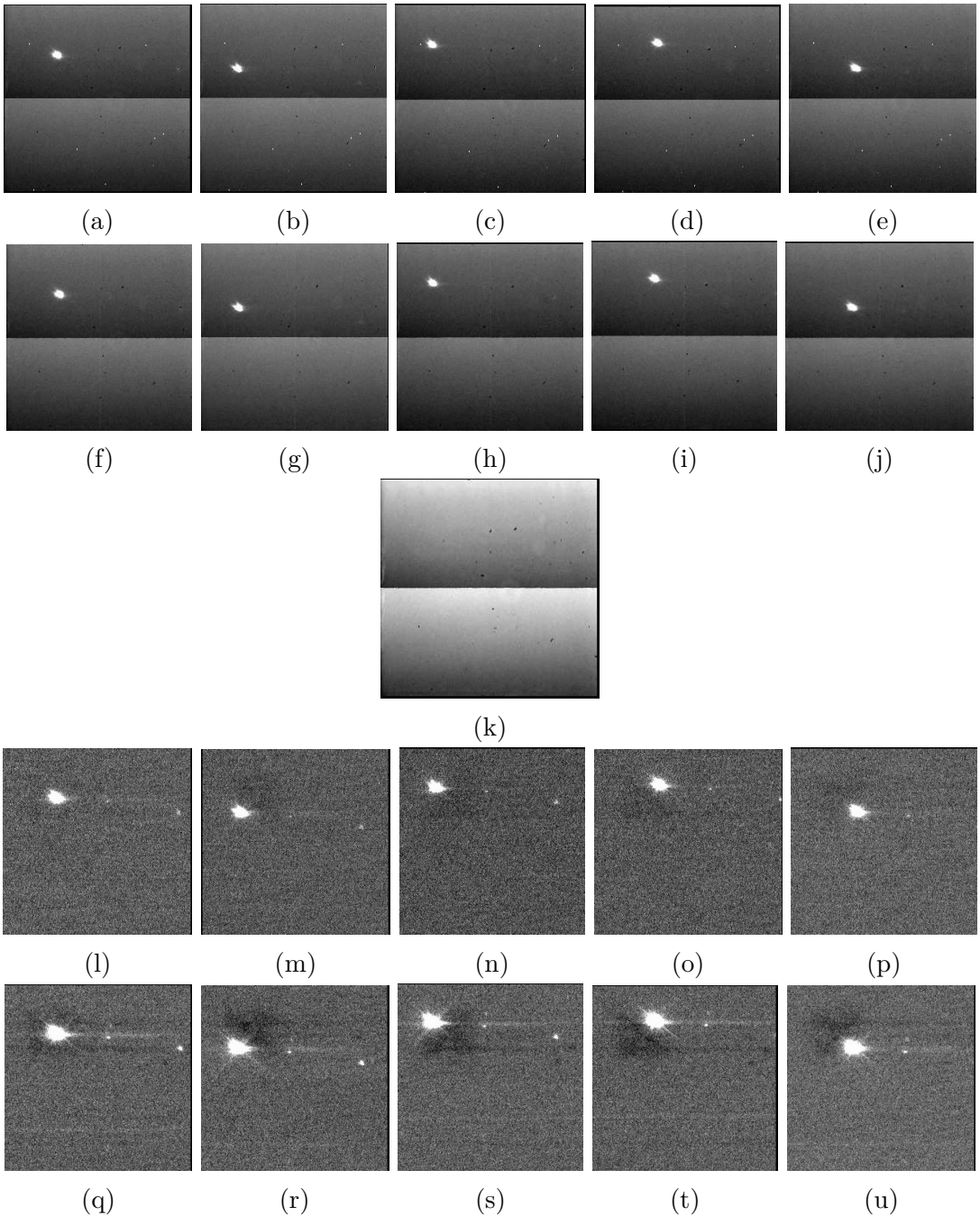

Figure 2.5: Figure explains a few basic steps of photometric data analysis of Mt. Abu data. Sub-figures (a)−(e) on the top panel represent the Raw Images. Objects are observed five dither positions and multiple frames are taken in each dither position. Sub-figures (f)−(j) are the raw images after removal of cosmic ray (cosmic ray corrected). Sub-figure (k) is the sky image generated by median combining of all the cosmic ray removed raw images excepting the 1st frame of each dither position. Sub-figures (l)−(p) represents the sky-subtracted image. Sub-figures in the bottom panel represents the average-combined image of multiple frames taken in each dither position. The images are ready to run 'Phot' task for magnitude determination. The same procedure is also followed for photometric standard stars.

which is discussed above. The dark counts can be reduced significantly by adequate cooling of the detector by ThermoElectric Cooler (TEC) that operates according to the Peltier effect. When electric current flows the CCD removes the heat to a radiator which is cooled by coolant LN2 (≈77K). Consequently, the dark counts become insignificant even at long exposure like 20−30 minute.

No dark frame is taken during the observation run with NICMOS-3 and HFOSC instrument. But, dark frames are taken during the observation run with TIRSPEC instrument. The measured dark counts rise exponentially at the beginning of the exposure and stabilize to a constant value after 27 seconds from the start of the exposure. The high dark counts at the beginning of the exposure are due to the non−linear behaviour of the detector immediately after reset (termed as 'Reset anomaly'), but not due to high dark current. Additional details can be found in Ninan et al. (2014). One set of 3 dark frames each of 100 seconds exposure are taken at the beginning and end of each night. However, no dark correction is required at the time of TIRSPEC data analysis as the final raw data provided to the observers are dark subtracted.

Cosmic ray correction:
The cosmic ray, the high energy positively charged protons or nuclei, or negatively charged electrons radiation, hit the detector indiscriminately and give spurious signals, that can be obliterated by the median combine of several frames. However, this technique is not suitable for a single frame. Thus, the IRAF task L.A.Cosmic[5], developed by van Dokkum (2001), is used to get rid of cosmic rays from astronomical frames via a Laplacian algorithm.

Aperture photometry:
After the aforementioned cleaning process (see Figure 2.5), the raw images are now ready for photometry. In this thesis work, the photometric analysis was done for two objects (see, in Chapter 5 and Chapter 6). The aperture photometry suffices to determine the magnitude of the stars. In photometry, apparent magnitude (mag) of an object is measured from observed flux (flux), i.e., photons per second of the star after removing instrumental signatures using the relation: mag = constant − $2.5\log_{10}$(flux), where constant the zero-point (Z_{mag}) of the magnitude scale. This 'mag' is called an instrumental magnitude. The Z_{mag} is measured by observing standard stars of known apparent magnitude (true value of standard star magnitude) with extinction and airmass corrections.

We need first to measure instrumental magnitude from a standard star. To perform aperture photometry, the desired sources are selected from the physical coordinate of the displayed image. The selection can be done by automatic star finder algorithm 'DAOFIND'

[5] http://www.astro.yale.edu/dokkum/lacosmic/

task or by manually marking the objects on the image display using the 'TVMARK' task. The 'tvmark' task would suffice our purpose. The instrumental magnitudes of the marked standard stars are measured using the 'PHOT' task in the apphot package. The 'PHOT' task provides the option to include the data dependent parameters at 'datapars', centring parameters at 'centerpars', sky fitting parameters at 'fitskypars', and photometry parameters at 'photpars'. All of these parameters are either acquired from a FITS image header or estimated from the FITS image. The task uses a default parameter value set in the uparm directory for an undefined parameter. One of the critical parameters of 'photpars' task is the selection of aperture size. Aperture is a fixed size circular region inside of which fallen starlight is measured through aperture photometry. Thus, aperture size should be such that it contains ideally all light. But, the probability of bad pixels or uncertainties due to the sky background increases with large aperture. Also, seeing and guiding limit of choosing the too small aperture. So, optimal aperture selection is crucial for aperture photometry. Usually, an optimal aperture is selected from the curve-of-growth analysis. An example of 'PHOT' parameters are listed in Table 2.3.

Spectroscopic reduction

The goal of the spectroscopic data reduction is to acquire the flux information of a star at different wavelengths. The raw image of spectra are bias-corrected (HFOSC) and flat-field corrected (TIRSPEC) following the method described earlier of this section. In the case of NIR spectra, the observed frames on one dither position are subtracted from the second dither position to remove the sky contribution as shown in Figure 2.6 (e and f). The subsequent steps in the one-dimensional (1D) spectrum extraction process are as follows.

Extraction of spectrum:
The dispersion axis is specified, along which the stellar spectrum lies down. The dispersion axis is 1 that is along with the x-axis of the object frame for Mt. Abu and 2 i.e., along with the y-axis for HCT. The 'APEXTRACT' task is used to select the dispersion axis. The axis perpendicular to the dispersion axis is called the spatial axis that defines other axes of the two-dimensional (2D) image. The next step followed by dispersion axis selection is aperture size and background region selection along the spatial axis. In the next step, the spectrum has traced the centre of the spatial profile along the dispersion axis. Tracing is essential because the spectrum does not exactly lie down perpendicular to the spatial axis, rather the centre of the spatial profile shifts slightly towards dispersion axis. This is caused due to camera optics distortion, atmospheric refraction etc. Finally, the 1D spectrum is extracted from the 2D object frame. The single 'APALL' task suffices for

Table 2.3: Parameters of Phot and Apall task at photometric and spectroscopic data reduction observed with HFOSC and TIRSPEC instrument respectively

Photometry			Spectroscopy		
TASK=PHOT			TASK=APALL		
Parameters		Value	Parameters		Value
datapars	fwhmpsf	5	interac*		yes
	datamax	55000	find		yes
	readnoi	4.8	recente*		yes
	epadu	1.22	resize		yes
	exposur	EXPTIME	edit		yes
	airmass	AIRMASS	trace*		yes
	filter	FILTER	fittrac		yes
	obstime	JD	extract		no
	itime	45	review		yes
	xairmass	1.28	line		INDEF
	ifilter	3BesI			
	otime	2458226.1	b_sampl		$-25:-15, 15:25$
centerpars	calgori	centroid	Aperture	lower	-15
	cbox	2*fwhm		upper	15
fitskypars	salgori	mode	Tracing	t_funct	spline3
	annulus	3-4*fwhm		t_order	1
	dannulu	2*fwhm			
photpars	aperture	3-4*fwhm	Extraction	backgro	fit
	zmag†	25		weights	none

Notes. † The calculated z_{mag} (see the text) from the photometric measurement of standard is used at the time object frame photometry.
The parameters marked with '*' are made 'no', 'backgro' becomes 'none' for extraction of 'Argon' lamp spectrum.

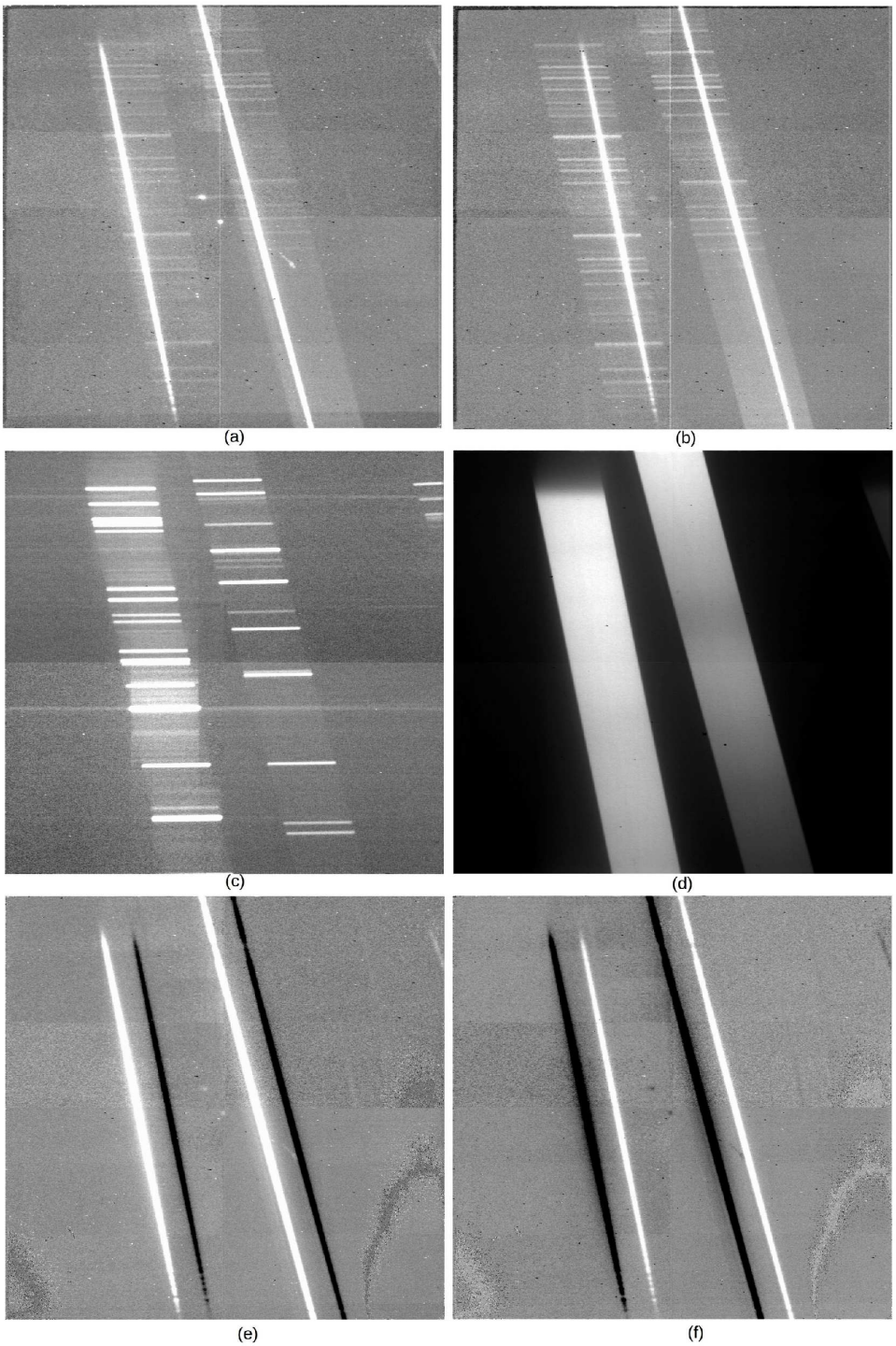

Figure 2.6: Figure corresponds to the various step of the analysis process. Sub-figures (a) and (b) represent the observed raw frames at two dither positions of the same wavelength range, (c) is for Argon lamp, and (d) is continuum flat. Sub-figures (e) and (f) represent the frames after subtraction of two dither frames, one with other, to remove sky variation.

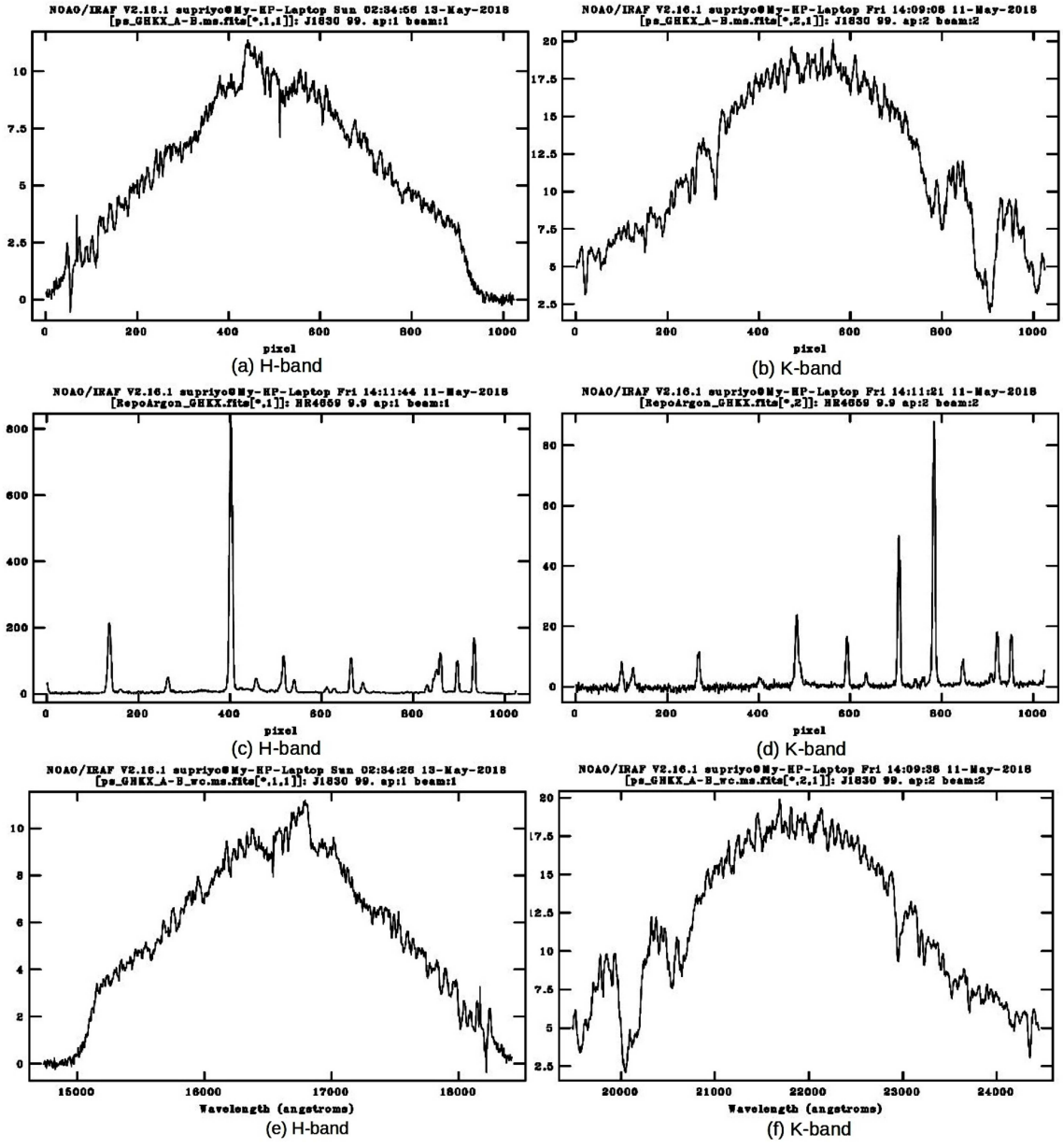

Figure 2.7: Figure explains various analysis steps of spectroscopic data observed with TIRSPEC instrument on 2 m HCT. The object was observed in cross-dispersed mode (1.50−1.84 μm (H-band) and 1.95−2.45 μm (K-band)). The left panel figures correspond to H-band, and right panel figures are for K-band. The extracted object spectra (top) and Ar-lamp spectra (bottom) using 'Apall' task are presented. The x-axis represents pixel, whereas y-axis represents counts. Figures in the bottom panel represent the wavelength calibrated spectra (wavelength versus counts).

all these steps. The extracted spectrum represents the number of counts as a function of pixel number as shown in Figure 2.7 (a and b).

Wavelength calibration:
Wavelength calibration means mapping of pixel scale to wavelength scale in the extracted spectrum, which, in general, is done using an arc lamp observed with the same filter or slit as the object frame. The wavelength calibration process is as follows.

1. 1D lamp spectrum is extracted from the 2D arc lamp image by 'APALL' task as discussed in the above section by providing the corresponding object frame as a reference image. This is done to provide identical apertures as previously defined for the object frame. The other alteration of the 'APALL' parameters used to extract the spectrum of the object frame are listed in Table 2.3. The 1D lamp spectrum of Ar lamp is shown in Figure 2.7 (c and d).

2. The features of the lamp spectrum are interactively marked and assigned by the wavelength scale, which, in turn, fits a function mapping pixel scale to the wavelength scale to find dispersion solution for arc spectra. The task 'IDENTIFY' is used for this purpose.

3. The dispersion solution of the object spectrum is then found by the task 'REFSPEC' with the reference spectrum that has been used to find the wavelength solution with the task 'IDENTIFY'.

4. Finally, the task 'DISPCOR' is applied to set or change the dispersion coordinate of the object spectrum that provides a linear wavelength scale defined by a starting and ending wavelength, a wavelength interval per pixel, and the number of pixels, from the dispersion solution. The final wavelength-calibrated object spectrum is shown in Figure 2.7 (e and f).

The wavelength calibration of NICMOS-3 spectrum is done using a combination of OH sky lines and telluric lines registered with the spectrum. So, the first step of wavelength calibration is not required.

Flux calibration: The flux calibration of the wavelength calibrated spectra are done as,

1. Flux calibration of optical data − Once wavelength calibration is achieved for the object as well as spectrophotometric standard, we implement three following 'IRAF' tasks to obtain a flux calibrated spectrum.

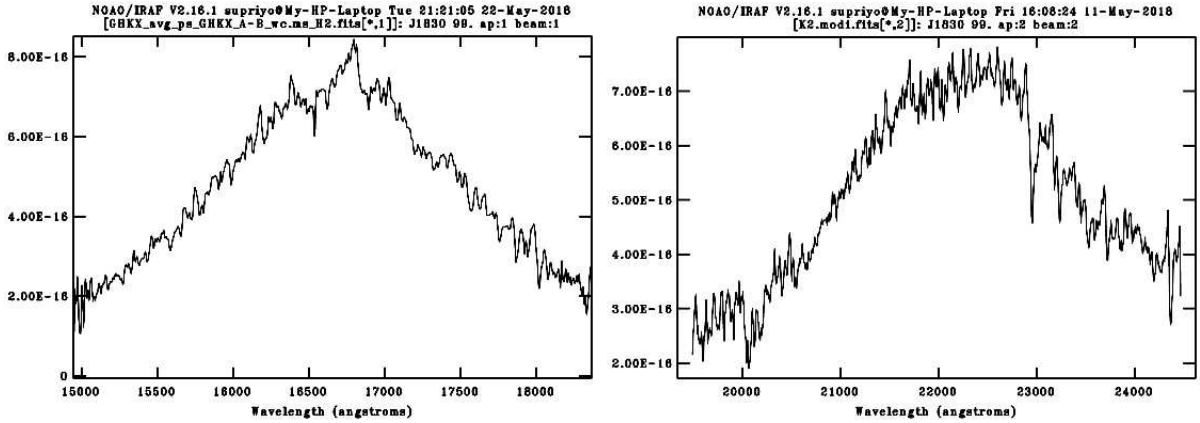

(a) H-band spectra (b) K-band spectra

Figure 2.8: The flux calibrated spectra corresponding to H-band (left) and K-band are represented.

- STANDARD − This task associates the observed standard star to the previously tabulated flux distribution of standard star available in the 'IRAF' directory (the directory containing standard star data). The wavelength calibrated spectrum of the standard, extinction file of the particular observatory, and path of the directory containing standard star data are provided as an input of the task. The extinction file of the observatory is utilized to remove the extinction across the bandpasses.
- SENSFUNC − This task determines sensitivity and extinction functions having the output file of the previous task and same extinction file used in the STANDARD task as an input.
- CALIBRATE − This task removes atmospheric extinction of the input spectrum and yields a flux calibrated spectrum. The wavelength calibrated object spectrum, the output of the task 'SENSFUNC' and the extinction file are specified as an input.

2. Flux calibration of NIR data − For NIR spectra, one additional important step needs to address for many strong telluric absorption features before flux calibration. The following steps are followed after the wavelength calibration of the object as well as a telluric standard star to achieve final flux calibrated spectra.

   - Telluric corrections − First, the spectral signature (hydrogen lines for A-type stars) of the telluric standard (e.g., Brγ at 2.16 μm) are removed by Gaussian fit. The object spectrum is now divided by the telluric standard to eliminate the absorption features as well as instrument response, and the fringes in the K-band spectrum formed by TIRSPEC detector.

- Black-body correction − As the object is divided by the standard star, the output results in a spectrum of the relative strength of fluxes. To recover the real strength of the object fluxes, the ratioed spectrum is multiplied with the model black-body curve generated using 'MK1DSPEC' task in 'IRAF' corresponding to the temperature of the standard. This steps also provides the continuum-corrected spectrum. This telluric and continuum-corrected spectrum is scaled to the 2MASS magnitude of the object, and finally, the flux calibrated spectrum of the object is achieved as shown in Figure 2.8.

2.2 Archival Photometric Data and Spectral Library

In addition to the data from our own observations, some of the available archival data and spectral libraries are also used in a context for the better interpretation of our results. The archival data and spectral libraries are briefly introduced in this section.

2.2.1 Photometric Data

2MASS NIR data

The Two Micron All Sky Survey (2MASS) project, designed for ground-based NIR survey, is a joint project of the University of Massachusetts (UMass) and the Infrared Processing and Analysis Center (IPAC) funded by the National Aeronautics and Space Administration (NASA) and the National Science Foundation (NSF). In this project, two dedicated highly-automated 1.3 m telescopes are mounted in both the northern and southern hemispheres to map the entire sky simultaneously at three NIR bands J (1.25 mum), H (1.65 mum), and Ks (2.17 mum) with 1 millijansky (mJy) sensitivity in each band. The northern telescope is placed at the Whipple Observatory on the Mt. Hopkins, Arizona, while the other is at the Cerro Tololo Inter-American Observatory on Cerro Tololo, Chile. Each telescope was equipped with a 3-channel camera, and each channel contains a NICMOS-3 256×256 HgCdTe arrays. The 2MASS All-Sky Data Release[6] offers a Point Source Catalog of 471 million objects, and Extended Source Catalog of 1.6 million sources observed between 1997 June and 2001 February covering 99.998 per cent of the sky. 2MASS observed each sky location using a pixel scale of $2.0'' \times 2.0''$ with a total integration time of 7.8 s that includes six dithering of 1.3 s exposures. The limiting magnitudes of 2MASS point-source detection level are 15.8, 15.1, and 14.3 mag at the J, H, and Ks bands

[6] `http://www.ipac.caltech.edu/2mass/releases/allsky/`

respectively, with a SNR ratio better than 10. Additional details can be found in Cutri et al. (2003), and Skrutskie et al. (2006).

WISE Mid-IR data

The Wide-field Infrared Survey Explorer (WISE) project is a space mission for mid-IR survey operated and funded by JET Propulsion Laboratory (JPL), NASA. The WISE spacecraft, launched on December 14, 2009, carried the 40 cm telescope and camera and began to map the sky on January 14, 2010. It surveyed the whole sky in four infrared bands W1 (3.3526 μm), W2 (4.6028 μm), W3 (11.5608 μm), and W4 (22.0883 μm) with an angular resolution of 6.1″, 6.4″, 6.5″, and 12.0″ respectively. WISE observed each sky location with a total integration time of 11.002 s that includes 1.1 s of readout of the arrays followed by 8.8 s of integration, and collected data with HgCdTe arrays with 1024×1024 pixels each 18 μm square for the WISE short-wavelength channels, and Si:As BIB arrays with the same 1024×1024 pixel format and pitch. This science data is transmitted through a fixed high gain antenna to the Tracking and Data Relay Satellite System (TDRSS) for downloading. Additional details can be found in Cutri & et al. (2012), and Wright et al. (2010).

AKARI IR data

The AKARI[7] (formerly ASTRO-F or IRIS - Infrared Imaging Surveyor), is the first dedicated Japanese satellite developed by the members of Japanese Aerospace Exploration Agency/ Institute of Space and Astronautical Science (JAXA/ISAS) and collaborators. The mission was successfully launched on February 21, 2006, by an M-V rocket. AKARI surveyed the entire sky in the near to far-infrared spectral regions using a 68.5 cm telescope and two focal-plane instruments; the FIS (Far-Infrared Surveyor) for far-infrared observations and the IRC (InfraRed Camera) for near and mid-infrared observations. The FIS operated in four wavelength; N60 (65 μm), and WIDE-S (90 μm), WIDE-L (140 μm), and N160 (160 μm) with spatial resolutions ranging from 1′ to 1.5′. The short wavelength bands (N60 and WIDE-S) employ Monolithic Ge:Ga array with a 26.8″ × 26.8″ Pixel scale, whereas, Stressed Ge:Ga array with a Pixel scale 44.2″ × 44.2″ is the detector for the long wavelength bands (WIDE-L and N160). The IRC contains three independent camera system: NIR camera (1.7–5.5 μm) consisting of a 512×412 array of InSb detector, MIR-S camera (5.8–14.1 μm, S9W) consisting of a 256×256 array of Si:As detector, and MIR-L camera (12.4–26.5 μm, L18W) with a similar detector as MIR-S.

[7] https://www.ir.isas.jaxa.jp/AKARI/

Table 2.4: Specifications of IRAS instrument

Centre Wavelength (μm)	Field of View (arcmin)	Bandpass (μm)	Detector Material	Dwell Time (ms)	Average 10 σ Sensitivity (Jy)
12	0.75 × 4.5	8.5 - 15	Si:As	190	0.7
25	0.75 × 4.6	19 - 30	Si:Sb	190	0.65
60	1.5 × 4.7	40 - 80	Ge:Ga	390	0.85
100	3.0 × 5.0	83 - 120	Ge:Ga	780	3.0

Note. Ref : Neugebauer et al. (1984)

IRAS IR data

The Infrared Astronomical Satellite (IRAS)[8] was developed by the U.S. National Aeronautics and Space Administration (NASA), the Netherlands Agency for Aerospace Programs (NIVR), and the United Kingdom Science and Engineering Research Council (SERC). IRAS, launched on 1983, was the first-ever space telescope to survey the whole sky with a 57 cm IR telescope in four broad wavelength bands centred at 12, 25, 60 and 100 μm (Neugebauer et al., 1984). The details of the IR instrument are listed in Table 2.4. In addition to photometric observations (the IRAS Point Source Catalog, Version 2 (1988)), IRAS contained a Low Resolution slitless Spectrometer (LRS) that observed any source brighter than ∼2 Jy at 12 or 25 μm in two sections, a blue section from 8 to 15 μm, and a red section from 13 to 23 km μm with resolution $\lambda/\Delta\lambda$ ∼40, and ∼20 respectively (Volk & Cohen, 1989) .

2.2.2 Spectral Library

IRTF spectral Library

The IRTF spectral library[9] offers flux calibrated medium-resolution spectra observed with SpeX spectrograph (Cushing et al., 2005; Rayner et al., 2009). The SpeX is mounted on 3.0 m NASA Infrared Telescope Facility (IRTF) on Mauna Kea, Hawaii. The spectrograph saw first light in May 2000 and was upgraded in 2014. The spectra from the IRTF spectral library used in this study were observed with the old SpeX[10] (2000−Jan 2014) instrument equipped with a 1024×1024 Aladdin 3 InSb array. It observed in two cross-dispersed

[8] https://lambda.gsfc.nasa.gov/product/iras/
[9] http://irtfweb.ifa.hawaii.edu/~spex/IRTF_Spectral_Library/
[10] http://irtfweb.ifa.hawaii.edu/~spex/

modes: the short-wavelength cross-dispersed mode (SXD) covering wavelength from 0.8 to 2.42 μm with resolution (R $\equiv \lambda/\Delta\lambda$) $\sim$2000, and the long-wavelength cross-dispersed mode (LXD) covering 2.5 to 5.2 μm with R $\sim$2500. Additional details of SpeX can be found in Rayner et al. (2003). The spectra provide the SNR of $\sim$100 across the whole wavelength (λ) interval except $\lambda < 4$ μm. Presently, the spectral library contains mainly 210 spectra of F, G, K, and M stars of solar metallicity with luminosity classes between I and V, but also includes some AGB stars, carbon and S stars, L and T dwarfs, and the gas giant planets. We exploited only K and M giants spectra in this thesis.

TNG spectral Library

The TNG spectral Library is a collection of medium-resolution spectra observed with NICS instrument (Mármol-Queraltó et al., 2008). The NICS is mounted at one (Nasmyth A) of the two Nasmyth foci of 3.58 m Telescopic Nazionale Galileo (TNG)[11] at Roque de los Muchachos Observatory, La Palma, Spain operated by the Centro Galileo Galilei (CGG). NICS is the TNG infrared (0.9-2.5 μm) instrument equipped with HgCdTe Hawaii 1024×1024 array that offers multimode observing facilities (e.g., imaging, high-throughput low-resolution spectroscopy, medium resolution spectroscopy, imaging polarimetry). Mármol-Queraltó et al. (2008) observed a sample of fifty-two stars of spectral types A to M and luminosity classes I to V with KB (i.e. K broad) grism disperser (R $\sim$1250) in the wavelength regime 1.95$-$2.34 μm. In this study we have taken the spectra of K and M giants from this stellar library[12].

2.3 Theoretical models implementation

This section provides an overview of the different types of implemented models in this work. The radiative transfer code More of Dusty (Groenewegen, 2012) are adopted for the SED fit, and one-dimensional static model atmosphere code Phoenix (Allard et al., 1995) are used for the qualitative study between fundamental parameters and spectral indices.

[11] http://www.tng.iac.es/
[12] http://webs.ucm.es/info/Astrof/ellipt/CO.html

2.3.1 More of Dusty

The radiative transfer code More of Dusty[13] (MoD), developed by Groenewegen (2012). The model uses the slightly updated and modified version of a publicly available one-dimensional dust radiative transfer code, "DUSTY" (version 2.01), developed by Ivezic et al. (1999), as a subroutine within a minimisation code. The detail mathematical formulation of "DUSTY" can be found in Ivezic & Elitzur (1997). Dusty models for different optical-depth and dust temperatures are presented in Figure 2.9. The "Dusty" encounters the consequences on the original radiation from some source (star, galactic nucleus, etc.) due to scattering, absorption and re-emission by the dusty environment. It can solve both planar and centrally-heated spherical density distributions. However, within the present framework of "Dusty", it is very difficult to constrain all the input parameters (e.g., grain size, dust composition, effective temperature, optical depth, the slope of the density) at a time to obtain the best fit for a set of observations. In this context, MoD was developed that performs direct minimisation of these parameters and allows the user to determine the best fitting parameters to a set of observations by a Levenberg-Marquardt minimization procedure. These observations can be magnitudes, spectra, visibility curves and intensity profiles.

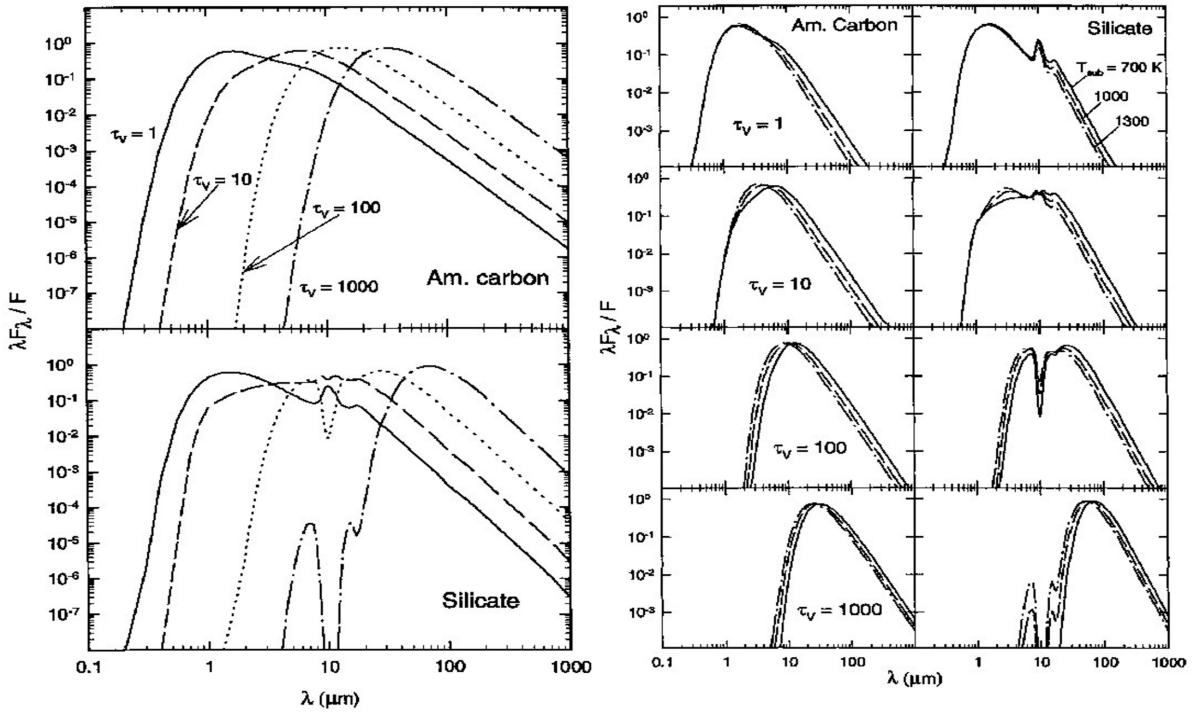

Figure 2.9: Dusty models for different optical-depth (left), and dust temperatures (right). Source of image : Ivezic & Elitzur (1997).

[13] http://homepage.oma.be/marting/codes.html

In the presently released version of the model, the MoD works to find best-fitting luminosity (L), dust optical depth ($\tau_{0.55}$), dust temperature at the inner radius (T_c) and slope, p, of the density distribution ($\rho \sim r^{-p}$). The quality of the fit is obtained through a χ^2 analysis

$$\chi^2 = \sum_{i=1}^{n} (m_{obs}(i) - m_{pred}(i))^2 / \sigma^2_{m_{obs}(i)}, \tag{2.1}$$

where, m the observed or predicted magnitude (for photometry) or flux (for spectroscopy) or visibility at a given spatial frequency (for interferometry) or normalised intensity at a radial offset (for intensity curves), with error bars σ_{obs} and n is the total number of observations. Given p number of free parameters, the reduced χ^2 is defined as,

$$\chi^2_{red} = \chi^2/(n-p) \tag{2.2}$$

The interstellar reddening (A_V), the path to the file containing the absorption and scattering coefficients of the dust, hydrostatic model atmosphere, the effective temperature of the model atmosphere, distance (D), number of shells (N), outer radius in a unit of inner radius, the exponents of the density law, p(N) (p(1) only considered), and scaling factor, s(N) (s(1) is set to 1), are provided as an input in the master-input file. Finally, the initial guess of the fit parameters (L, $\tau_{0.55}$, T_c, and p) are also supplied, and a code (0 or 1) to decide whether these parameters would be fixed (0) or varied (1). MoD offers two versions of the code to choose between one shell and two shell structure for the fitting. However, we apply one shell structure to the purpose of the thesis. In the present model, the outer radius is set to 1600 times the inner radius, to where the dust temperature becomes approximately 20 K, typical of the ISM.

Several dust compositions (depending on O-rich or C-rich behaviour of the object) can be used that comes with the subdirectory ModelsDust of MoD. To obtain the best fit, we use a different combination of dust spices like olivine (amorphous $MgFeSiO_4$), compact amorphous aluminium oxide and metallic iron as we concern only O-rich star in this work. The absorption and scattering coefficients are calculated using the 'distribution of hollow spheres' (DHS, Min et al. 2003) and a maximum volume fraction of a vacuum core f_{max} = 0.7 μm with various grain sizes (0.1, 0.2 and 0.5 μm).

The subdirectory ModelsDust also contains the model atmospheres both for C-rich and O-rich stars. For O-rich stars, MARCS[14] hydrostatic model atmospheres are adopted (Gustafsson et al., 2008b) that are convolved and rebinned to a lower resolution.

[14] `http://marcs.astro.uu.se/`

Additionally, observational data are supplied in separate files as an input to MoD. Four data files correspond to four types of observations. For photometric data, the file contains filter information, magnitudes and error in the magnitudes, and for others (spectroscopic data, visibility data and intensity profiles), these would be a master files that provide the information about the number of spectra or dataset to be used, the path to the file containing the observational data for each dataset and instructions on how to constrain the data. However, MoD need not all types of observed data (except photometric) to be available simultaneously for determining the best-fitting parameters. In that case, one can put one line with '0' in the file or files of unavailable data.

The error on the parameters returned by MoD are typically very small as the resulting χ^2 are large. Because of the large variability amplitude of the stars and the typical non-simultaneous taking of the available photometric data in combination with the small photometric error in any measurement the χ^2 of the fit is typically large. Therefore, the errors in the parameters are therefore smallish. Thus, one estimate for the error can be given by scaling the internal errors (i.e. the errors reported output file of MoD) to a reduced χ^2 of 1. The second way of estimating the error comes from the dispersion in the parameters above the best-fitting value.

2.3.2 Phoenix Model Grid

We explore the behaviour of atomic or molecular features of the red giants in NIR H- and K-band with fundamental parameters (effective temperature, surface gravity and metallicity) qualitatively using BT-NextGen synthetic model spectra[15](Allard et al., 2012).

BT-NextGen is modified version of NextGen that are calculated using multipurpose stellar atmosphere code Phoenix[16] (Allard et al., 1997; Hauschildt et al., 1999a,b), with updated opacities. The new BT-NextGen synthetic spectra incorporates the water vapour line list of Barber et al. (2006) and the solar abundances of Asplund et al. (2009). The model grid with 2 Å resolution extends from T_{eff} = 2600 K to 70000 K in steps of 100 K, log g = 0.0 to 6.0 in steps of 0.5, and $[Fe/H] = -4.0$ to $+0.5$, accounting for alpha element enhancement.

The name of the file itself provides the model parameters. For example, in the case of lte040-0.5-0.5a+0.2.BT-NextGen.7.bz2 (lte{T}-{G}{M}a{A}.{GridName}.7.bz2), the file represents that it contains a synthetic spectrum in an ASCII format of effective temperature 4000 K (T×10), surface gravity 0.5 (G), metallicity −0.5 (M) with respect to

[15] `https://phoenix.ens-lyon.fr/Grids/BT-NextGen/AGSS2009/`
[16] `https://phoenix.ens-lyon.fr/`

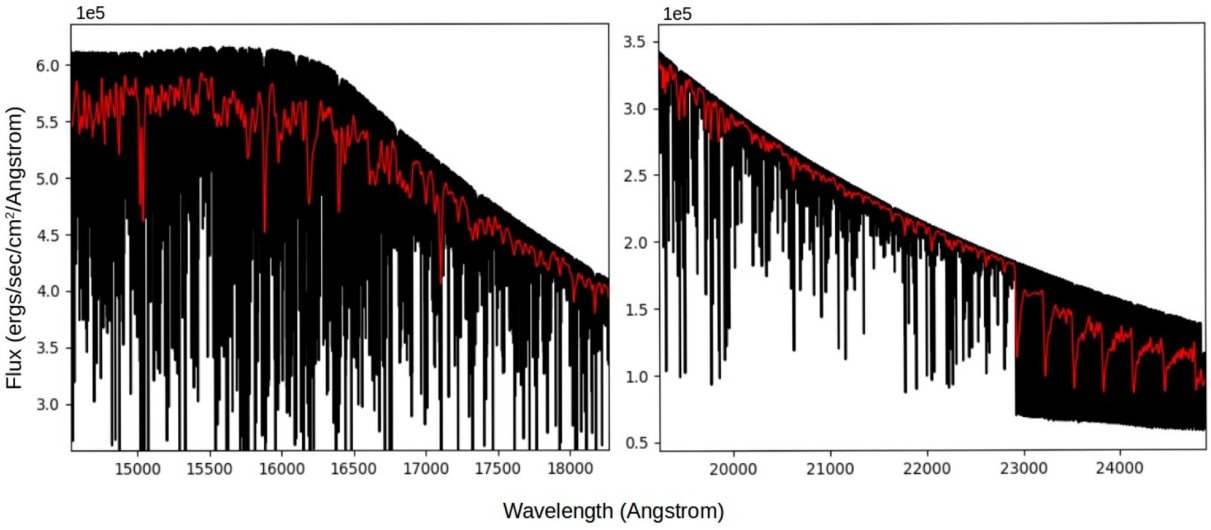

Figure 2.10: Figure shows the BT-NextGen model spectra before (black) and after (red) Gaussian convolution.

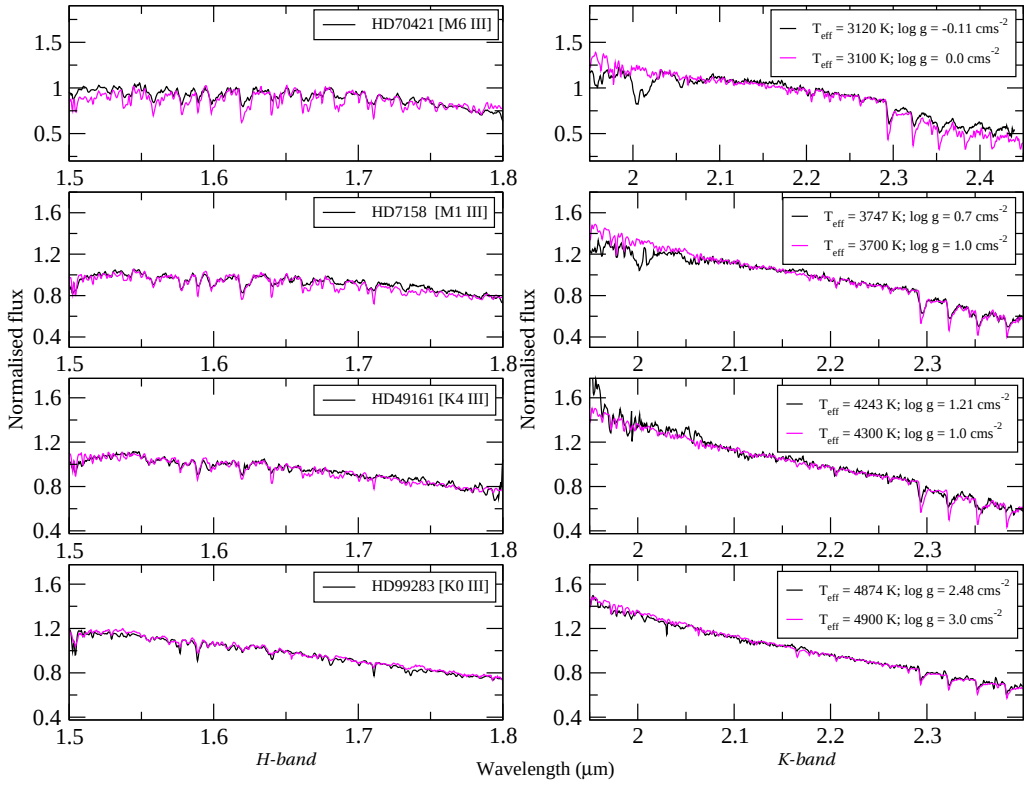

Figure 2.11: Figure represents the comparison of few spectra from the TIRSPEC instrument with synthetic spectra. The black colour is for observed spectra, and the magenta is for synthetic spectra.

solar value, alpha element enhancement +0.2 (A) relative to solar value and name of the model grid BT-NextGen (GridName). The first column of the ASCII file provides the wavelength (Å) in the vacuum. Vacuum wavelength (VAC) is converted to air wavelength (AIR) following Morton (1991). Flux (= $10^{Flam+DF}$ in erg/sec/cm^2/Å) of the

synthetic spectrum in each wavelength is generated using the second column (Flam) of the ASCII file and DF (= −8.0) is the dilution factor. Additional details can be found in `https://phoenix.ens-lyon.fr/`). The synthetic spectrum is convolved with a Gaussian to degrade the spectral resolution as TIRSPEC spectral resolution (R $\sim$ 1200) as shown in Figure 2.10. Comparison of a few spectra from the TIRSPEC instrument with synthetic spectra is shown in Figure 2.11.

Chapter 3

The TIRSPEC spectral library for K−M giants and spectral calibration with fundamental parameters

The part of this chapter is based on the paper Ghosh et al. (2019).

Title: Spectral Calibration of K−M Giants from medium resolution near-infrared HK-band spectra.
Authors: Supriyo Ghosh, S. Mondal, R. K. Das, and D. Khata
Year : 2019
Journal: Monthly Notices of the Royal Astronomical Society, 484, 4619–4634

In this chapter, we present the new medium resolution ($\lambda/\Delta\lambda \sim 1200$) spectral library of K−M giants covering the wavelength range 1.50–2.45 μm. The main motivation of the present work is widening the existing cool stellar libraries and more importantly precise estimation of fundamental parameters of cool giant stars from the NIR spectral indices. The sample includes 72 K0−M8 giants from our TIRSPEC observations and all available 35 giants in that spectral range from archival IRTF spectral library. We have calibrated here the empirical relationship between fundamental parameters [e.g., effective temperature (T_{eff}), spectral type (ST), metallicity ($[Fe/H]$), surface gravity ($\log g$)] and

equivalent widths of some important spectral features like Si I, Na I, Ca I, ^{12}CO. We also explored the behaviour of those spectral features predicted by BT-NextGen Phoenix model grids.

3.1 Introduction

Stellar spectral libraries have a particularly important role to understand and classify the stellar population as well as an evolutionary synthesis for the individual sources in the field, star clusters of our Galaxy and integrated stellar lights in the extra-Galactic sources. For example, the original stellar classification process, developed by Hoffleit (1943), uses a set of reference stellar spectra to compare the spectrum of an individual star (see Garrison 1994). Several optical (e.g., Prugniel & Soubiran 2001; Sánchez-Blázquez et al. 2006) and NIR (e.g., Kleinmann & Hall 1986; Lançon & Wood 2000; Rayner et al. 2009) empirical libraries have been developed to construct stellar population synthesis models. The major advantage of the stellar library is that within covered stellar atmospheric parameters space, it provides full information of stellar spectral types, luminosity classes and metallicities about the unknown samples. Thus, the usefulness of the stellar library relies on the complete sampling of stellar atmospheric parameters space at the appropriate spectral resolution. Unfortunately, in the present scenario, most of the available empirical libraries have limited coverage in stellar parameters space. Alternatively, empirical correlations between the strength of previously defined spectral features and the main atmospheric parameters (e.g., Ramirez et al. 1997; Cenarro et al. 2002; Frogel et al. 2001) can be employed to demonstrate the evolutionary synthesis models (e.g., Worthey 1994; Vazdekis et al. 2003). The fundamental parameters for different populations can be estimated directly by implementing these calibrations and derived features strength. However, accurate, prior knowledge of the behaviour of the spectral features of interest with stellar parameters are required for precise characterisation.

Since the pioneering work of Johnson & Méndez (1970), significant effort has been made in the NIR regions (see, e.g., Origlia et al. 1993; Wallace & Hinkle 1997 for reviews) to understand the behaviour of the atomic (e.g., Si I at 1.59 μm, Na I at 2.20 μm, Ca I at 2.26 μm) and molecular (e.g., ^{12}CO bandhead at 1.62, 2.29 μm) features of cool giants in various galactic environments, and subsequently many empirical correlations have established between the stellar parameters (T_{eff}, log g, $[Fe/H]$) with these features (e.g., Kleinmann & Hall 1986; Origlia et al. 1993; Ramirez et al. 1997; Frogel et al. 2001; Ivanov et al. 2004; Mármol-Queraltó et al. 2008; Pfuhl et al. 2011; Schultheis et al. 2016). Moreover, the NIR spectral regions are more advantageous than optical as it

suffers relatively less interstellar extinction, and the NIR regime allows us to probe long distance in the galaxy. NIR spectra are particularly useful for understanding the physics of cool stars like K−M giants (e.g., Joyce 1998; Gautschy-Loidl et al. 2004) as these cool stars ($T_{eff} \sim 3000-6000$ K) emit maximum energy (peak near 1 μm) in the NIR, which can probe the deepest regions of the stellar photosphere (Förster Schreiber, 2000). Particularly, classifying and characterizing of individual stars in nearby embedded young clusters (e.g., Greene & Meyer 1995; Peterson et al. 2008) and optically obscured regions of the galaxy (e.g., Figer et al. 1995; Frogel et al. 2001; Kurtev et al. 2007; Lançon et al. 2007; Riffel et al. 2008) are much benefited by the use of NIR spectra.

Despite all these efforts in the understanding of stellar population in different systems, precise estimation of fundamental parameters of cool giants still remains a challenge because of their molecular near-photospheric environment (Lançon & Wood, 2000). The spectral database of these cool giants is highly sparse, and more additional database would be highly valuable for their classification and characterization. Furthermore, the understanding of quantitative diagnostic tools and quality of spectral indices have an important role to quantify the stellar absorption features. In this chapter, a new NIR stellar spectral library of K−M giants have been undertaken using the medium resolution spectra ($\lambda/\Delta\lambda \sim 1200$) covering the wavelength range 1.50−2.45 μm. The main motivation of this work is to widen the existing cool stellar libraries, and more importantly, investigate how accurately the fundamental parameters (e.g., T_{eff}, ST, $[Fe/H]$ and log g) can be estimated from the medium-resolution NIR HK-band spectra. In addition, the present work evaluates the systematic differences between our established relations in this chapter and the existing relations in the literature derived from relatively high-resolution spectra. Particularly, the present calibration could be used to derive the fundamental parameters for relatively faint sources in the high-extinction regions from such medium-resolution spectra compared to higher-resolution spectra using big aperture telescopes. Moreover, the estimation of fundamental parameters of K- and M-giants, precisely later than M3, is still a challenging task, and none of the existing libraries contains a large sample of later M3 giants for such calibrations.

3.2 Observations and Data reductions

3.2.1 Observations

NIR spectra of 72 K−M giants are obtained using medium resolution TIRSPEC spectrograph on the 2.01 m HCT located at Hanle, India. Additional details of TIRSPEC instru-

Table 3.1: Identification of Stars observed with TIRSPEC and SpeX instruments

Stars Names	V mag	ST	T_{eff} (K)	log g (cm/s^2)	$[Fe/H]$ (dex)	Parallax (mas)	Date Of Observation	Exp. Time (s)†	SNR ‡	Remarks	Ref
TIRSPEC :											
HD54810	4.92	K0III	4715	2.395	-0.25	16.08	2014-12-12	2*(5*60)	138	clear sky	T1,M1
HD99283	5.70	K0III	4874	2.476	-0.18	10.63	2017-04-09	2*(3*100)	181	clear sky	T1,M2
HD102224	3.72	K0III	4482	1.844	-0.33	17.76	2015-01-17	2*(5*17)	171	clear sky	T1,M5
HD69994	5.79	K1III	4571	2.157	-0.07	5.79	2017-04-07	2*(5*80)	144	clear sky	T1,M2
HD40657	4.52	K1.5III	4400	1.389	-0.58	7.75	2014-12-12	2*(5*25)	130	clear sky	T1,M2
HD85503	3.88	K2III	4504	2.306	0.25	26.28	2015-01-14	2*(5*40)	116	clear sky	T1,M1
HD26846	4.86	K2III	4547	2.125	0.09	13.46	2014-12-12	2*(5*50)	106	clear sky	T1,M6
HD30834	4.77	K3III	4096	0.925	-0.24	5.42	2015-01-13	2*(5*40)	164	clear sky	T1,M5
HD92523	4.99	K3III	4115	1.349	-0.38	7.81	2015-01-17	2*(5*32)	240	clear sky	T1,M2
HD97605	5.79	K3III	4606	2.701	–	16.51	2017-04-09	2*(3*80)	130	clear sky	T1
HD49161	4.77	K4III	4243	1.212	-0.03	6.62	2014-12-12	2*(5*30)	121	clear sky	T1,M2
HD70272	4.25	K4+III	3900	0.914	-0.24	8.53	2015-01-17	2*(5*8)	174	clear sky	T1,M9
HD99167	4.80	K5III	3865	1.133	-0.06	8.67	2015-01-14	2*(5*30)	153	clear sky	T1, M10
HD83787	5.84	K6III	3816	0.892	-0.21	4.22	2015-01-14	2*(5*70)	117	clear sky	T1,M7
HD6953	5.79	K7III	4021	1.662	–	8.28	2014-12-12	2*(6*50)	103	clear sky	T1
HD6966	6.04	M0III	3998	1.483	–	6.06	2015-12-18	2*(3*40)	144	clear sky	T1
HD18760	6.13	M0III	3605	0.569	–	3.92	2016-12-20	2*(5*30)	133	clear sky	T1
HD38944	4.74	M0III	3799	0.727	–	6.24	2015-01-14	2*(5*25)	95	clear sky	T1
HD60522	4.06	M0III	3881	1.110	-0.36	12.04	2014-12-12	2*(5*7)	79	thin cloud	T1,M9
HD216397	4.93	M0III	3889	1.352	–	10.03	2015-08-11	2*(3*30)	117	thin cloud	T1
HD7158	6.11	M1III	3747	0.700	–	5.16	2015-12-18	2*(3*30)	123	clear sky	T1
HD82198	5.37	M1III	3875	1.153	–	6.80	2015-01-14	2*(3*40)	101	clear sky	T1
HD218329	4.52	M1III	3874	1.123	0.17	9.92	2015-08-11	2*(3*15)	86	thin cloud	T1,M5
HD219215	4.22	M1III	4307	1.749	–	16.14	2015-08-11	2*(6*7)	71	thin cloud	T1
HD119149	5.01	M1.5III	3675	0.714	–	6.40	2015-01-14	2*(5*30)	94	clear sky	T1
HD1013	4.80	M2III	3792	1.028	–	8.86	2015-12-18	2*(3*7)	131	clear sky	T1
HD33463	6.42	M2III	3491	0.299	-0.05	3.11	2015-01-14	2*(5*30)	115	clear sky	T1, M3
HD39732	7.43	M2III	3448	0.380	–	2.42	2016-12-19	2*(5*25)	111	clear sky	T1
HD43151	8.49	M2III	3335	0.231	–	1.99	2016-12-19	2*(5*30)	170	clear sky	T1
HD92620	6.02	M2III	3500	–	–	4.02	2016-12-19	2*(5*20)	182	clear sky	T1
HD115521	4.80	M2III	3690	0.418	–	4.83	2015-01-17	2*(4*7)	142	clear sky	T1
HD16058	5.37	M3III	3572	0.489	0.08	5.16	2015-01-13	2*(5*20)	94	clear sky	T1, M11
HD28168	8.42	M3III	3344	0.497	–	2.77	2015-01-13	2*(5*60)	83	clear sky	T1
HD66875	5.99	M3III	3509	0.441	–	4.38	2016-12-19	2*(5*12)	143	clear sky	T1
HD99056	8.79	M3III	3137	0.439	–	4.52	2016-12-19	2*(5*6)	119	clear sky	T1
HD215953	6.84	M3III	3460	0.823	–	4.17	2015-08-11	2*(3*100)	80	thin cloud	T1
HD223637	5.78	M3III	3622	0.567	–	3.86	2015-12-19	2*(3*15)	125	clear sky	T1
HD25921	7.10	M3/M4III	3522	0.721	–	3.62	2016-12-20	2*(5*40)	110	clear sky	T1
HD33861	8.64	M3.5III	3365	0.565	–	2.49	2015-01-13	2*(5*70)	115	clear sky	T1
HD224062	5.61	M3/M4III	3429	0.299	–	5.12	2015-12-19	2*(3*5)	93	clear sky	T1
HD5316	6.24	M4III	3481	0.693	–	5.75	2015-12-18	2*(3*10)	129	clear sky	T1
HD34269	5.65	M4III	3427	0.353	–	5.79	2015-01-13	2*(5*10)	141	clear sky	T1
HD64052	6.39	M4III	3460	0.783	–	6.45	2016-12-19	2*(5*10)	84	clear sky	T1
HD81028	6.89	M4III	3482	0.147	–	2.08	2016-12-19	2*(5*20)	135	clear sky	T1
HD206632	6.23	M4III	3367	0.195	–	4.77	2015-08-11	2*(3*5)	73	thin cloud	T1
HD16896	8.25	M5III	3358	0.360	–	2.68	2016-12-20	2*(5*30)	123	clear sky	T1
HD17491	6.90	M5III	3313	0.071	–	3.90	2016-12-20	2*(5*6)	107	clear sky	T1
HD17895	7.16	M5III	3294	-0.021	–	2.72	2016-12-20	2*(5*7)	120	clear sky	T1
HD22689	7.16	M5III	3144	-0.135	–	3.85	2015-12-18	2*(3*4)	77	clear sky	T1
HD26234	8.90	M5III	3191	0.390	–	2.95	2015-01-13	2*(5*50)	94	clear sky	T1
HD39983	8.26	M5III	3145	0.430	-0.23	4.73	2016-12-19	2*(5*10)	154	clear sky	T1,M3
HD46421	8.21	M5III	3225	0.215	–	3.57	2016-12-19	2*(5*10)	114	clear sky	T1
HD66175	7.04	M5III	3156	0.158	–	3.41	2015-01-17	2*(5*12)	128	clear sky	T1
HD103681	6.20	M5III	3215	-0.056	–	2.81	2016-12-19	2*(5*50)	124	clear sky	T1
HD105266	7.18	M5III	3246	0.001	–	3.69	2015-01-14	2*(5*10)	83	clear sky	T1
HD64657	6.85	M5/M6III	3269	0.031	–	3.78	2016-12-19	2*(5*6)	114	clear sky	T1
HD65183	6.40	M5/M6III	3359	0.020	–	2.93	2016-12-19	2*(5*6)	94	thin cloud	T1
HD223608	8.86	M5/M6III	3228	–	–	0.57	2015-12-19	2*(3*15)	136	clear sky	T2
HD7861	8.54	M6III	3259	–	–	4.20	2015-01-13	2*(5*40)	100	clear sky	T2
HD18191	5.93	M6III	3336	0.332	-0.24	9.28	2015-12-18	2*(3*4)	98	clear sky	T1,M5
HD27957	8.03	M6III	3383	0.298	–	2.38	2016-12-20	2*(5*40)	127	clear sky	T1
HD70421	8.55	M6III	3120	-0.112	–	2.22	2016-12-19	2*(5*12)	104	clear sky	T1

Stars Names	V mag	ST	T_{eff} (K)	log g (cm/s^2)	$[Fe/H]$ (dex)	Parallax (mas)	Date Of Observation	Exp. Time (s)	SNR	Remarks	Ref
HD73844	6.67	M6III	3206	0.109	...	6.40	2015-12-18	2*(3*5)	87	clear sky	T1
HIP44601	9.20	M6III	3200	...	...	1.25	2015-03-02	2*(5*50)	151	clear sky	T2
HIC55173	7.42	M6III	3288	0.280	...	4.48	2016-12-19	2*(5*10)	134	clear sky	T1
HIP57504	8.74	M6III	2920	0.011	...	3.86	2016-12-19	2*(5*10)	150	clear sky	T1
HD115322	7.21	M6III	3458	...	...	1.3	2015-01-16	2*(5*35)	97	clear sky	T2
HD203378	7.32	M6III	3284	0.035	...	3.23	2015-08-11	2*(3*20)	57	clear sky	T1
HD43635	7.93	M7III	3240	...	...	...	2015-12-19	2*(3*10)	115	clear sky	T3
HIC51353	9.84	M7III	3224	...	...	-0.39	2015-01-14	2*(6*70)	65	clear sky	T2
HIC68357	9.03	M7III	3138	0.362	...	3.58	2015-01-14	2*(6*60)	91	clear sky	T1
HD141265	10.45	M8III	2701	...	...	2.35	2015-12-18	2*(3*20)	82	clear sky	T2
SpeX :											
HD100006	5.54	K0III	4714	2.288	-0.12	10.36	...	...	260	...	T1,M12
HD9852	7.92	K0.5III	4750	...	...	1.58	...	...	210	...	T4
HD25975	6.09	K1III	5022	3.320	-0.20	22.68	...	...	244	...	T1,M4
HD36134	5.78	K1-III	4519	1.893	...	6.62	...	...	244	...	T1
HD91810	6.53	K1-III	4561	2.059	...	5.22	...	...	192	...	T1
HD124897	-0.05	K1.5III	4280	1.70	-0.52	88.53	...	...	261	...	T5,M1
HD137759	3.29	K2III	4570	2.248	0.03	32.23	...	...	215	...	T1,M1
HD132935	6.69	K2III	4220	1.483	...	3.59	...	...	248	...	T1
HD2901	6.92	K2III	4319	1.850	-0.02	4.32	...	...	278	...	T1,M3
HD221246	6.15	K3III	4145	1.255	...	3.61	...	...	184	...	T1
HD178208	6.43	K3III	4315	1.803	...	5.18	...	...	167	...	T1
HD35620	5.05	K3III	4239	1.449	0.11	7.20	...	...	174	...	T1,M8
HD99998	4.77	K3+III	3976	0.864	-0.39	5.40	...	...	189	...	T1,M8
HD114960	6.53	K3.5III	4130	1.795	...	6.19	...	...	168	...	T1
HD207991	6.85	K4-III	3837	1.002	...	2.97	...	...	197	...	T1
HD181596	7.51	K5III	3893	0.588	...	1.24	...	...	168	...	T1
HD120477	4.07	K5.5III	3962	1.263	-0.23	12.38	...	...	167	...	T1,M8
HD3346	5.12	K6III	3820	0.782	...	5.29	...	...	166	...	T1
HD194193	5.93	K7III	3819	0.850	...	3.86	...	...	169	...	T1
HD213893	6.73	M0III	3855	1.278	-0.09	4.22	...	...	182	...	T1,M11
HD204724	4.50	M1+III	3847	0.967	...	8.28	...	...	176	...	T1
HD120052	5.43	M2III	3598	0.488	...	4.82	...	...	160	...	T1
HD219734	4.86	M2.5III	3677	0.525	0.04	5.79	...	...	145	...	T1,M5
HD39045	6.26	M3III	3582	0.871	...	5.44	...	...	143	...	T1
HD28487	6.99	M3.5III	3441	0.533	...	3.59	...	...	132	...	T1
HD4408	5.38	M4III	3492	0.155	...	4.20	...	...	128	...	T1
HD204585	5.95	M4.5III	3379	0.161	...	4.90	...	...	117	...	T1
HD27598	7.04	M4III	3490	0.489	...	2.94	...	...	135	...	T1
HD19058	3.39	M4+III	3479	0.302	-0.15	10.60	...	...	124	...	T1,M4
HD214665	5.16	M4+III	3476	0.482	...	7.23	...	...	122	...	T1
HD175865	4.00	M5III	3363	0.092	0.14	10.94	...	...	112	...	T1,M4
HD94705	5.78	M5.5III	3371	0.379	...	8.39	...	...	113	...	T1
HD196610	5.89	M6III	3227	0.180	...	8.56	...	...	114	...	T1
HD108849	7.28	M7-III	2936	...	-0.34	5.53	...	...	88	...	T1,M13
BRI2339-0447	...	M7-8III	3200	...		...	...	...	76	...	T4

Notes: V mag − visual magnitude, ST − spectral type, T_{eff} − effective temperature, log g − surface gravity, $[Fe/H]$ − metallicity.

†Exp Time = no. of dither position*(no. of frame in each dither position* integration time).

‡ SNR are estimated by the method as in (Stoehr et al., 2008) considering the whole H-band.

Ref − references of T_{eff}, log g and $[Fe/H]$. T corresponds to ref. of T_{eff} and log g; M corresponds to ref of $[Fe/H]$.

Ref : (T1) McDonald et al. (2017); (T2) McDonald et al. (2012) ; (T3) Wright et al. (2003); (T4, M4) Cesetti et al. (2013) ; (T5, M5) Prugniel et al. (2011);

(M1) Jofré et al. (2015); (M2) Soubiran et al. (2016); (M3) Ho et al. (2017); (M6) Massarotti et al. (2008); (M7) Wu et al. (2011); (M8) McWilliam (1990); (M9) Reffert et al. (2015); (M10) Gáspár et al. (2016); (M11) Boeche et al. (2018); (M12) Luck & Heiter (2007); (M13) Luo et al. (2016).

V mag, ST, Parallax are taken from SIMBAD.

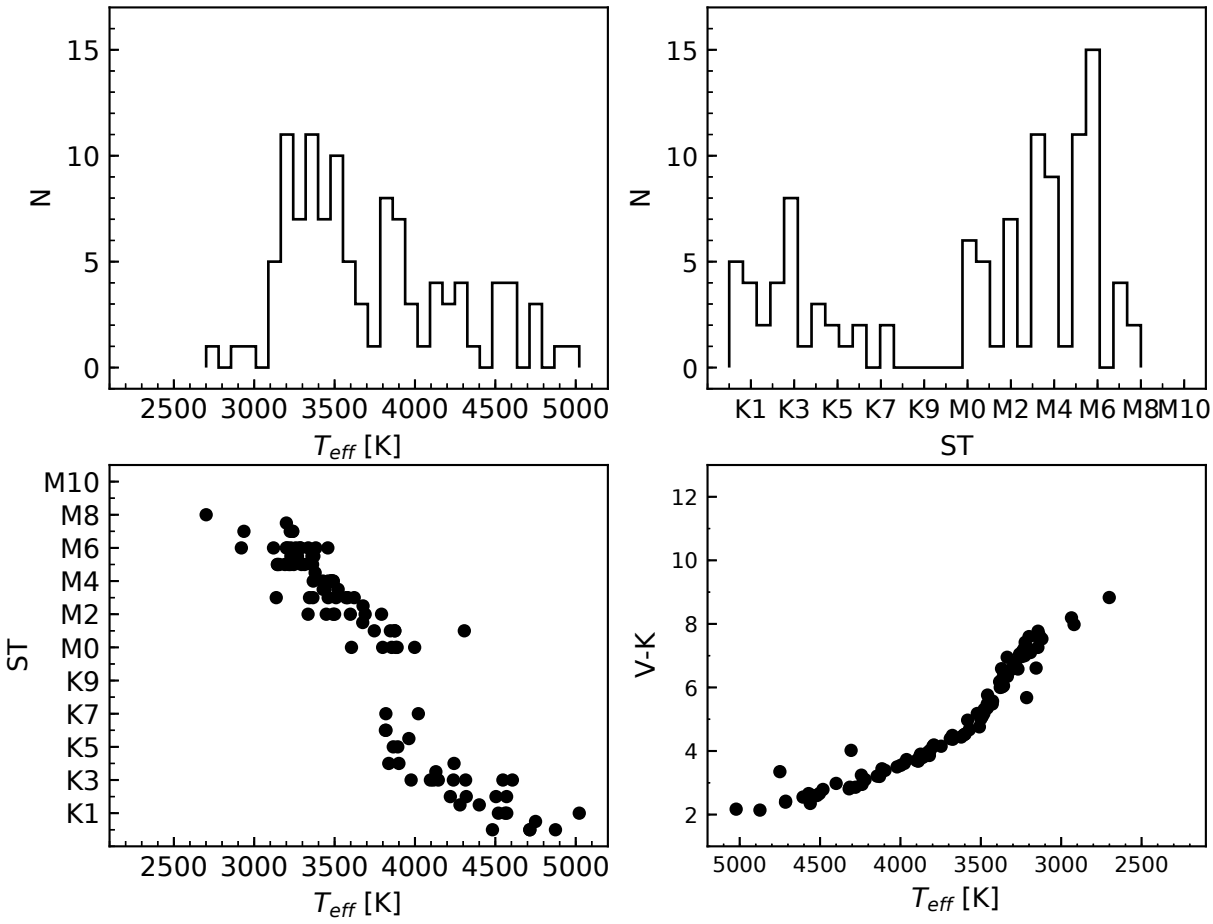

Figure 3.1: Effective temperature (T_{eff}) and Spectral type (ST) distribution of the sample are shown in the top-left and top-right panel respectively. T_{eff} versus ST and T_{eff} versus $V - K$ for the sample are shown in the bottom-left and bottom-right panel respectively.

ment can be found in Ninan et al. (2014). The spectra are taken with cross-disperser mode (1.50−1.84 μm and 1.95−2.45 μm) with a slit width 1.97 arcsec during several observing runs spanning over 2014−2017, and the log of observations is mentioned in Table 3.1. The spectra are taken at two different positions along the slit, one after another, immediately to subtract the sky, and several frames are observed to improve the SNR. The integration time varied from 4 to 100s depending on the magnitude of stars. The ST of sample stars spans from K0 to M8 with declination higher than −32 deg. The main criterion is to populate the space with the sample stars of T_{eff} from 2500 to 5000 K. Special attention is given to observe the stars of M3 III or later. About 60 per cent giants in our sample have ST M3 or beyond for better characterization in late M-region. We select very bright sample stars in order to get high SNR. Suitable standard stars of ST A0V to A1V are observed after each observation. We select very bright sample stars in order to get high SNR. Suitable standard stars of ST A0V to A1V are observed after each observation. Additional details of the IRTF spectral library can be found in Chapter 2.

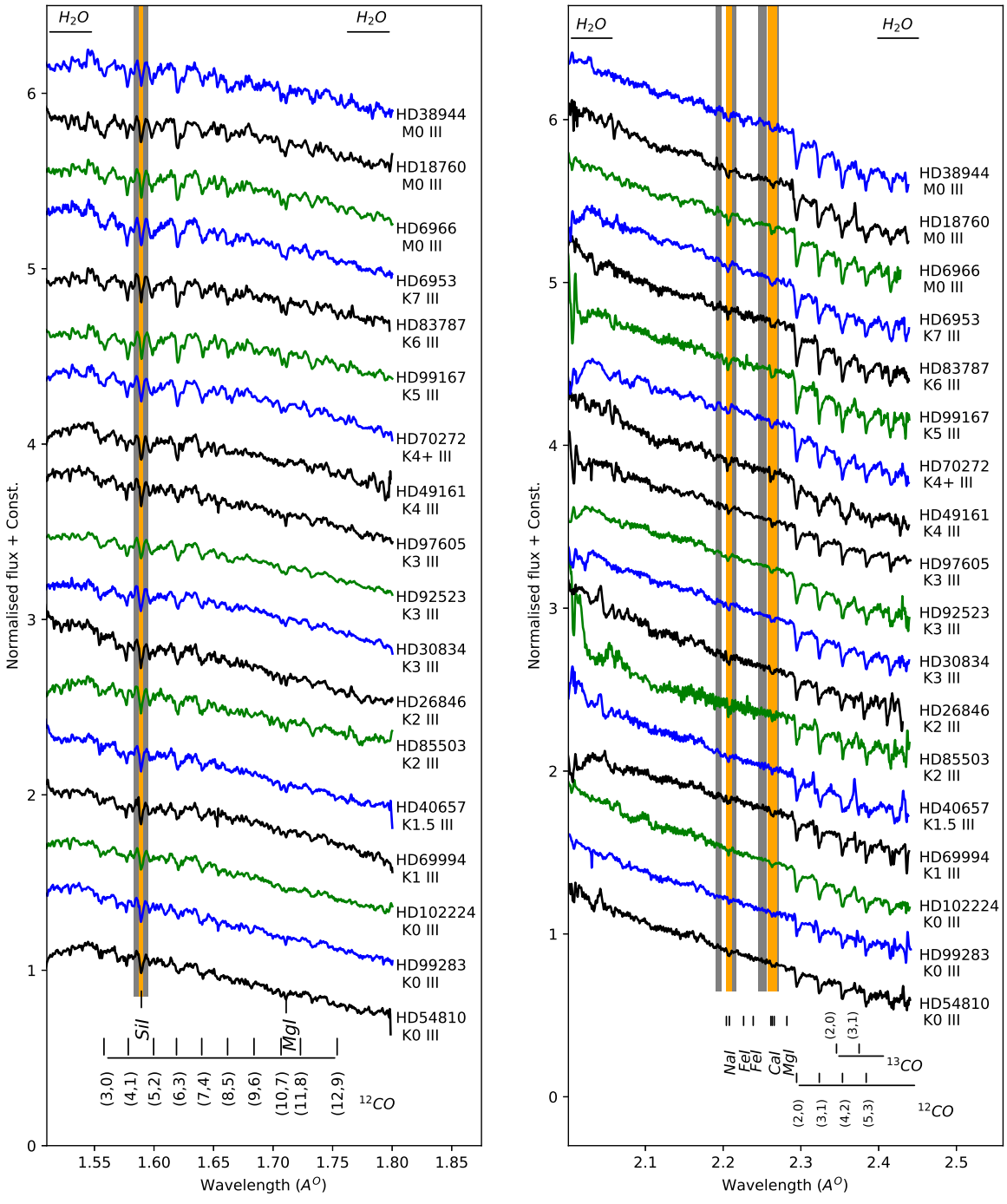

Figure 3.2: The HK-band spectra of giants (K0−M0) observed with TIRSPEC instrument are shown in Figure. All the spectra have normalised to unity at 1.65 μm (H-band) and 2.17 μm (K-band), and offset by constant value with respect to the bottom-most spectrum for displaying purposes. The names of the stars and spectral types have been mentioned right end of the corresponding spectra. All the prominent features in HK-band are marked. The orange regions represent the continuum bandpasses, and the silver region represents the feature bandpasses of Si I (H-band), Na I (K-band) and Ca I(K-band) as mentioned in Table 3.2).

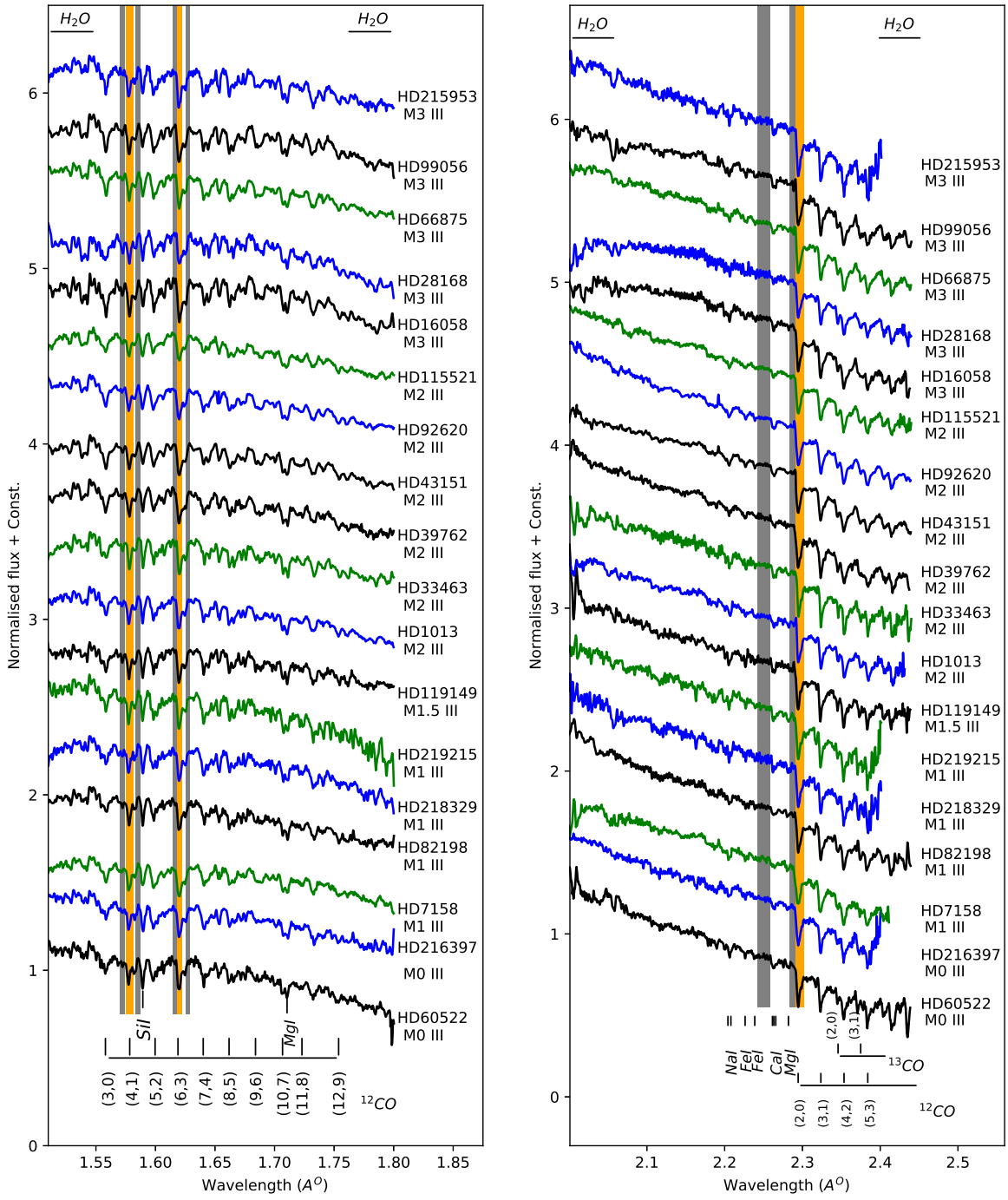

Figure 3.3: Same as Figure 3.2 but HK-band spectra of giants (M0−M3). The orange regions represent the continuum bandpasses, and the silver region represents the feature bandpasses of CO1, CO2 and CO3 as mentioned in Table 3.2).

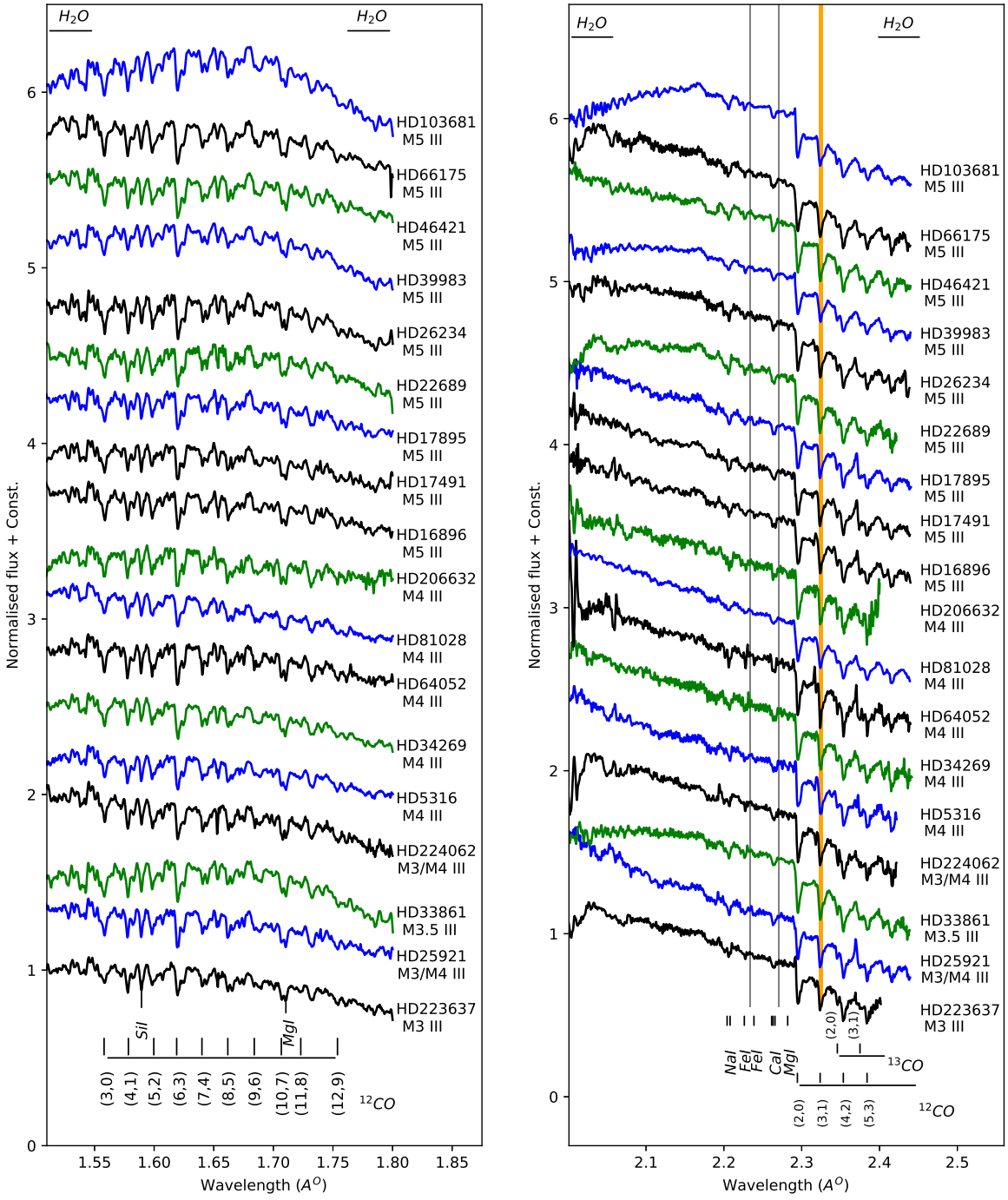

Figure 3.4: As in Figure 3.2, but *HK*-band spectra of giants (M3−M5). The orange regions represent the continuum bandpasses, and the silver region represents the feature bandpasses of CO4 as mentioned in Table 3.2).

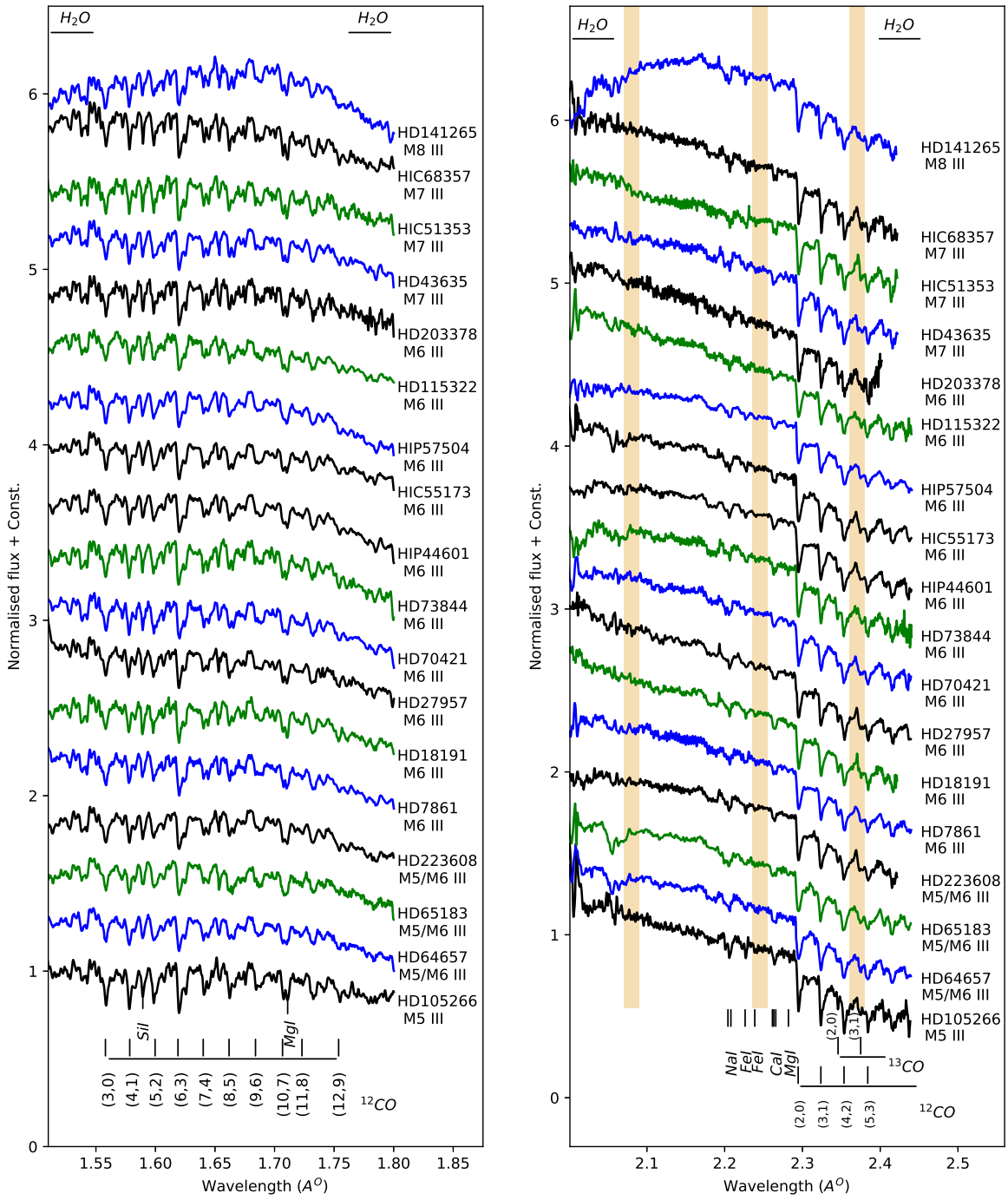

Figure 3.5: Same as Figure 3.2, but *HK*-band spectra of giants (M5−M8). The marked regions represents the three bandpasses used to estimate H_2O−K2 index, which is explored in Chapter 4.

To populate our sample, we have used all available thirty-five giants spanning spectral range K0 to M8 in the IRTF spectral library (Cushing et al., 2005; Rayner et al., 2009). Those spectra are observed with the medium-resolution ($\lambda/\Delta\lambda \sim 2000$) SpeX infrared spectrograph in the wavelength range 0.8−2.4 μm mounted on the 3.0 m IRTF at Mauna Kea, Hawaii. Thus, we have assembled one hundred seven giants for this study. We ignore the known Mira variables and OH/IR stars belonging to M-spectral types of the IRTF library from our study.

The photometric data of those stars are taken from literature as listed in Table 3.1. The T_{eff} and log g of the sample giants (97 out of 107) are uniformly taken from McDonald et al. (2017), which are derived by comparing multi-wavelength archival photometry to BT-Settle model atmospheres. The uncertainties in their measurements are ±125 K in T_{eff}. The parameters of the rest 10 giants are taken from other literature as mentioned in Table 3.1. The metallicity of only 32 giants in our sample is available in the literature (see, Table 3.1). Figure 3.1 represents T_{eff} and ST distribution of the sample, and their population in the T_{eff}−ST and T$_{eff}$−$(V - K)$ planes.

3.2.2 Data Reduction

The spectroscopic analysis is done using APALL task of IRAF. The TIRSPEC data are reduced with TIRSPEC pipe-line[1] (Ninan et al., 2014), and have been cross-checked with the IRAF reduction. The data reduction consists of flat-fielding, sky subtraction, bad pixel correction, cosmic-ray removal, subtracting the pairs of images taken at two different slit positions, the wavelength calibration with Argon arc lamp, spectrum extraction. To remove the telluric features of the Earth's atmosphere, the spectra of program stars are divided by the spectra of a standard star which is taken on the same night. Prior to division, all hydrogen lines are removed from the spectra of the standard stars by interpolating the stellar continua. This is followed by the flux calibration of the target stars by using their 2MASS H- and K-band photometric magnitudes. Additional details of data reduction can be found in Chapter 2.

[1]https://github.com/indiajoe/TIRSPEC/wiki

Table 3.2: Definitions of spectral bands to measure EW.

Index	Feature	Feature Bandpass (μm)	Continuum Bandpass (μm)	Ref.
SiI	Si I (1.59 μm)	1.5870-1.5910	1.5830-1.5870, 1.5910-1.5950	1
CO1	^{12}CO(2-0) (1.58 μm)	1.5752-1.5812	1.5705-1.5745, 1.5830-1.5870	2
CO2	^{12}CO(2-0) (1.62 μm)	1.6175-1.6220	1.6145-1.6175, 1.6255-1.6285	1
NaI	Na I (2.21 μm)	2.2040-2.2107	2.1910-2.1966, 2.2125-2.2170	3
CaI	Ca I (2.26 μm)	2.2577-2.2692	2.2450-2.2560, 2.2700-2.2720	3
CO3	^{12}CO(2-0) (2.29 μm)	2.2910-2.3020	2.2420-2.2580, 2.2840-2.2910	2
CO4	^{12}CO(3-1) (2.32 μm)	2.3218-2.3272	2.2325-2.2345, 2.2695-2.2715	2

Note. Ref : (1) Origlia et al. (1993); (2) *This work*; (3) Frogel et al. (2001)

3.3 Equivalent widths measurement

The standard definition of equivalent width (EWs) is

$$EW_\lambda = \int_{\lambda 1}^{\lambda 2} \left[1 - \frac{F(\lambda)}{F_c(\lambda)}\right] d\lambda \tag{3.1}$$

Here, $F(\lambda)$ represents the flux density inside the feature bandpass from $\lambda 1$ to $\lambda 2$, $F_c(\lambda)$ represents the value of the local continuum (Cesetti et al., 2013). To measure EWs, feature band and continua bands are adopted as shown in Table 3.2 and in Figure 3.2 to Figure 3.5. Bands of ^{12}CO at 1.58 μm are newly defined in this study. We compute the ^{12}CO at 1.62 μm band-strength according to the recipe of Origlia et al. (1993). Instead of four continua adopted by Frogel et al. (2001) to measure ^{12}CO at 2.29 μm absorption depth, we use here two continua as mentioned in Table 3.2. We adopt the feature bandpass of ^{12}CO at 2.32 μm from Kleinmann & Hall (1986); however we use two different continuum bands instead of one continuum used in Kleinmann & Hall (1986). Different continuum bands are also verified as mentioned in Ivanov et al. (2004); Cesetti et al. (2013), but better results are obtained from our selected bandpasses.

Before computing EWs, the spectral features are corrected for the zero velocity by shifting. The EWs are estimated with the IDL script[2] (Newton et al., 2014). In the script, pseudo-continuum, i.e. continuum in featured bandpass, is defined by fitting a straight line through the continuum bandpass and EWs are measured by numerically integrating (trapezoidal method) the flux within the feature bandpass.

The average spectral resolution of TIRSPEC data is, R $\sim$ 1200. The spectral resolution varies with wavelengths and such resolution variation in TIRSPEC can be found in Ninan et al. (2014). The resolution of SpeX data is R $\sim$ 2000. Uncertainties on the EWs are

[2] `https://github.com/ernewton/nirew`

computed with the Monte Carlo approach in the IDL script. The script adds normally-distributed (Gaussian) random noise to the stars' spectrum by using RANDOMN function (Newton et al., 2014). Provided errors (photon, residual sky, and read noise) in SpeX pipeline are used for Gaussian random noise simulation to estimate uncertainties in EWs. But, our TIRSPEC pipeline does not provide such errors, and the errors are estimated using the technique provided by Stoehr et al. (2008). The computed EWs of our sample are listed in Table 3.4 along with their uncertainties. To explore the behaviour of atomic and molecular features of K−M giants with fundamental parameters, we adopt BT-NextGen synthetic model spectra (see, section 2.3.2 for details, Hauschildt et al. 1999b). A grid of synthetic spectra with effective temperature from 2600 to 5000 K, surface gravity from 0.0 to 3.0, and overall metallicity ([M/H]) equal to −1.0, −0.5, 0.0, +0.3, and +0.5 dex was constructed to study the behaviour, that covers the whole parameter space spanned by our sample giants. The SpeX spectra and model grid are convolved with a Gaussian to degrade the spectral resolution as of TIRSPEC before all the indices are estimated. Additional details can be found in Chapter 2.

3.4 RESULT AND DISCUSSION

3.4.1 Behaviour of spectral features

We have studied here the behaviour of spectral signatures of the giants with stellar atmospheric parameters like T_{eff}, ST, log g, and $[Fe/H]$. The most prominent atomic lines of HK-band spectra are Si I at 1.59 μm, Na I at 2.20 μm, and Ca I at 2.26 μm as shown in Figure 3.2 to Figure 3.5. EWs of those lines are estimated using the methods as described in section 3.3. The behaviour of those lines with T_{eff}, ST, log g, and $[Fe/H]$ are shown in Figure 3.6. The Si I lines is one of the strongest absorption features in K-giants, and its strength steadily increases as the temperature decreases from 5000 to 4000 K, after that remains unchanged up to 3500 K and decreases further below 3500 K. The corresponding behaviour of Si I with spectral type is also observed, e.g., increasing in the range K0−K7, unchanged to M4 and decreasing further, and it appears insensitive to the log g.

The strengths of Na I and Ca I strongly depend on the effective temperature and show increasing trend with decreasing T_{eff} as found by others (Kleinmann & Hall, 1986; Ramirez et al., 1997; Förster Schreiber, 2000; Frogel et al., 2001; Ivanov et al., 2004; Rayner et al., 2009; Cesetti et al., 2013). Correlation of Na I line with ST shows increasing strength for K giants, but no trend is conclusive for M giants. In the case of Ca I, the strength indi-

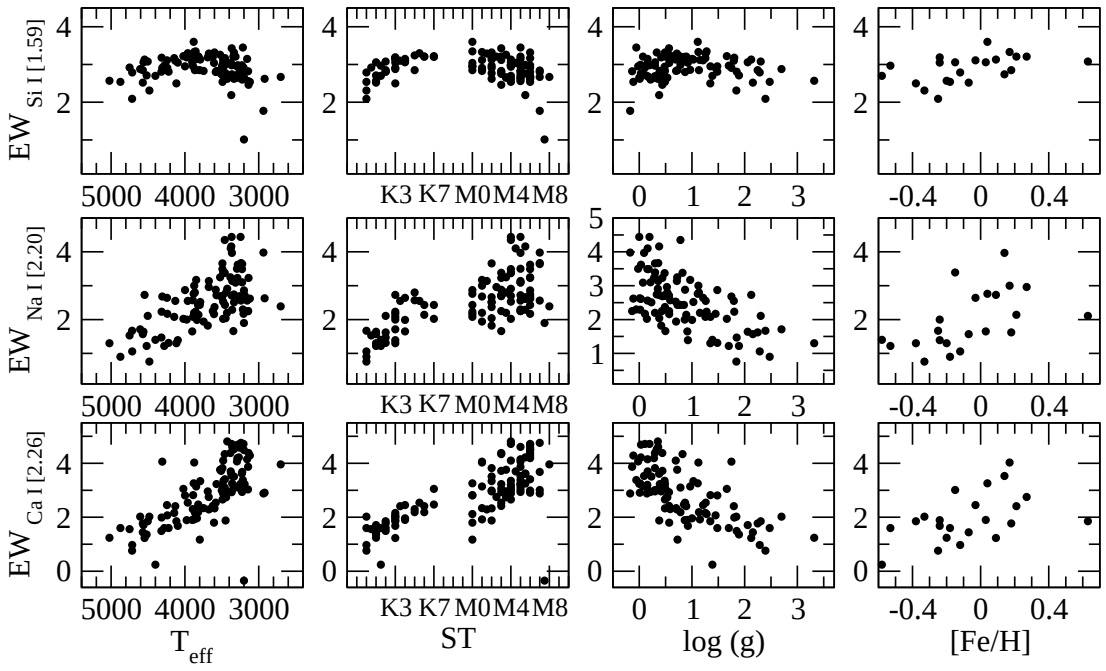

Figure 3.6: Behaviour of measured equivalent widths of atomic features with T_{eff}, ST, log g, and $[Fe/H]$ are shown in this figure.

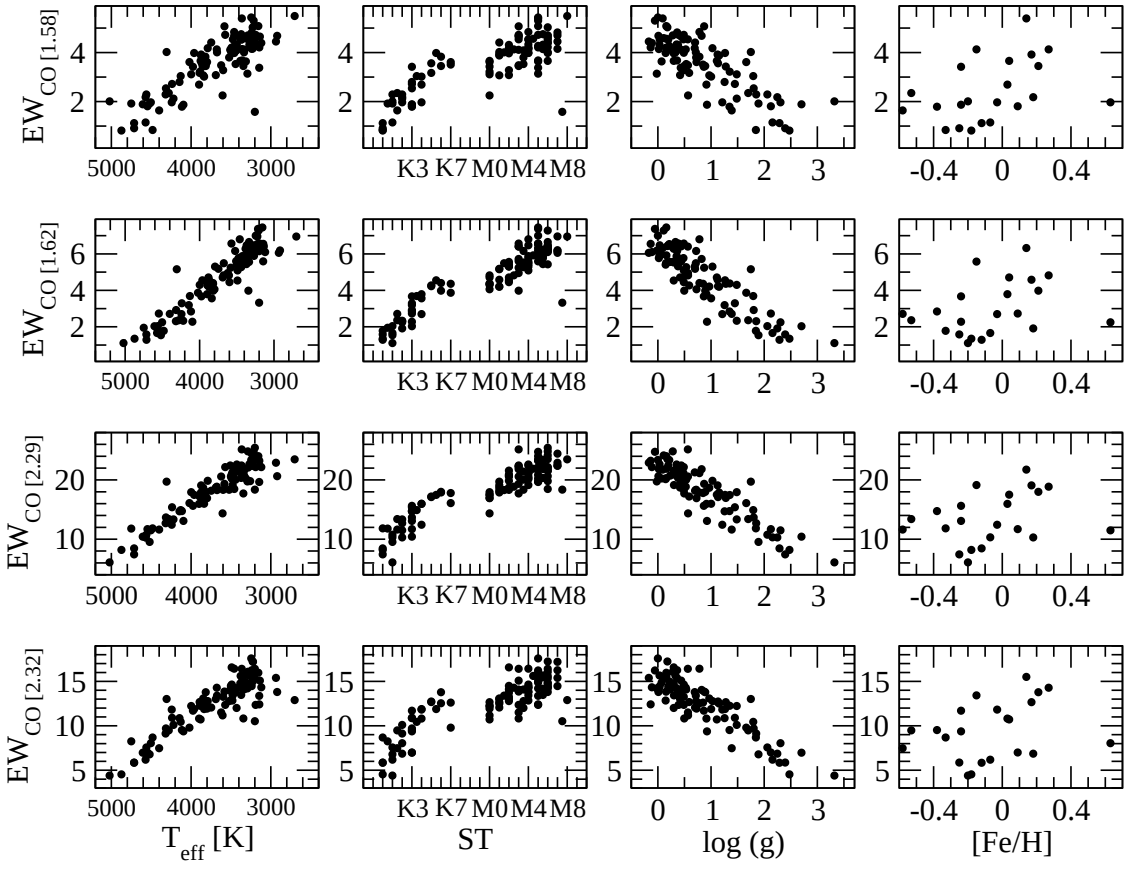

Figure 3.7: Behaviour of measured equivalent widths of molecular features with T_{eff}, ST, log g, and $[Fe/H]$ are shown.

cates an increasing trend with ST, similar to T_{eff}. The Na I and Ca I lines get stronger with decreasing log g.

There is significant dispersion in both correlations (T_{eff} and ST) for all the atomic lines. The poor band strengths in our medium-resolution spectra have some important role in such dispersion. Furthermore, contamination from other atomic lines is also affecting on such studies, and relatively better spectral resolution are required for better characterization. Origlia et al. (1993) mentioned that Si I feature is somewhat contaminated by OH line at lower temperature and the strength of the OH line dominated beyond M2, i.e. T_{eff} $\leq$ 3800 K. The Na doublet at 2.2 μm is blended with metallic lines like Si I (2.2069 μm), Sc I (2.2058 and 2.2071 μm) and V I (2.2097 μm) in our medium-resolution spectra, and such dispersion in M giants might be related to other lines behaviour (Wallace & Hinkle, 1996). For late M giants, few low excitation lines like Ti I (2.2627 and 2.2639 μm) and Sc I (2.2642 and 2.2663 μm) contaminate the Ca triplet at 2.26 μm.

In the 1.5−2.4 μm regions, the first-overtone ($\Delta\nu$=2) and the second-overtone ($\Delta\nu$=3) bandheads of ^{12}CO are the dominant features in K−M giants, and show increasing strength from K to M. In Figure 3.7, comparative behaviour of different CO bandheads [1.58 (CO1), 1.62 (CO2), 2.29(CO3), and 2.32 (CO4) μm] with T_{eff}, ST, log g, and $[Fe/H]$ show an increasing trend of band strengths with decreasing T_{eff}, early-to-late ST, and decreasing value of log g (see, e.g. Origlia et al. 1993; Ramirez et al. 1997; Cesetti et al. 2013). The behaviour of EWs with metallicity $[Fe/H]$ in Figure 3.6 and Figure 3.7 does not show any conclusive trend as expected because most of our sample belongs to solar-neighbourhood giants.

To investigate the origin of the dispersion especially in Figure 3.6, we plot index–index relations as shown in Figure 3.8. Figure 3.8 shows a tight index–index correlation at least for CO[1.62]–CO[2.29] and CO[2.32]–CO[2.29] as CO bands are strong features in the medium-resolution spectra. Small dispersion of CO index–index correlations might be due to various reasons, such as the variation of abundance ratios, residuals of telluric lines. Note that we discard the known Mira variables and OH/IR stars belonging to M spectral type of the IRTF library due to their large variability, and they might have different behaviour compared to the static giants (Lançon & Wood, 2000).

3.4.2 Predictions on the behaviour of spectral features from theoretical model atmospheres

Based on the synthetic spectra of the theoretical model Phoenix BT-NextGen (Allard et al., 1997; Hauschildt et al., 1999a,b), the sensitivity analysis on the strength of several

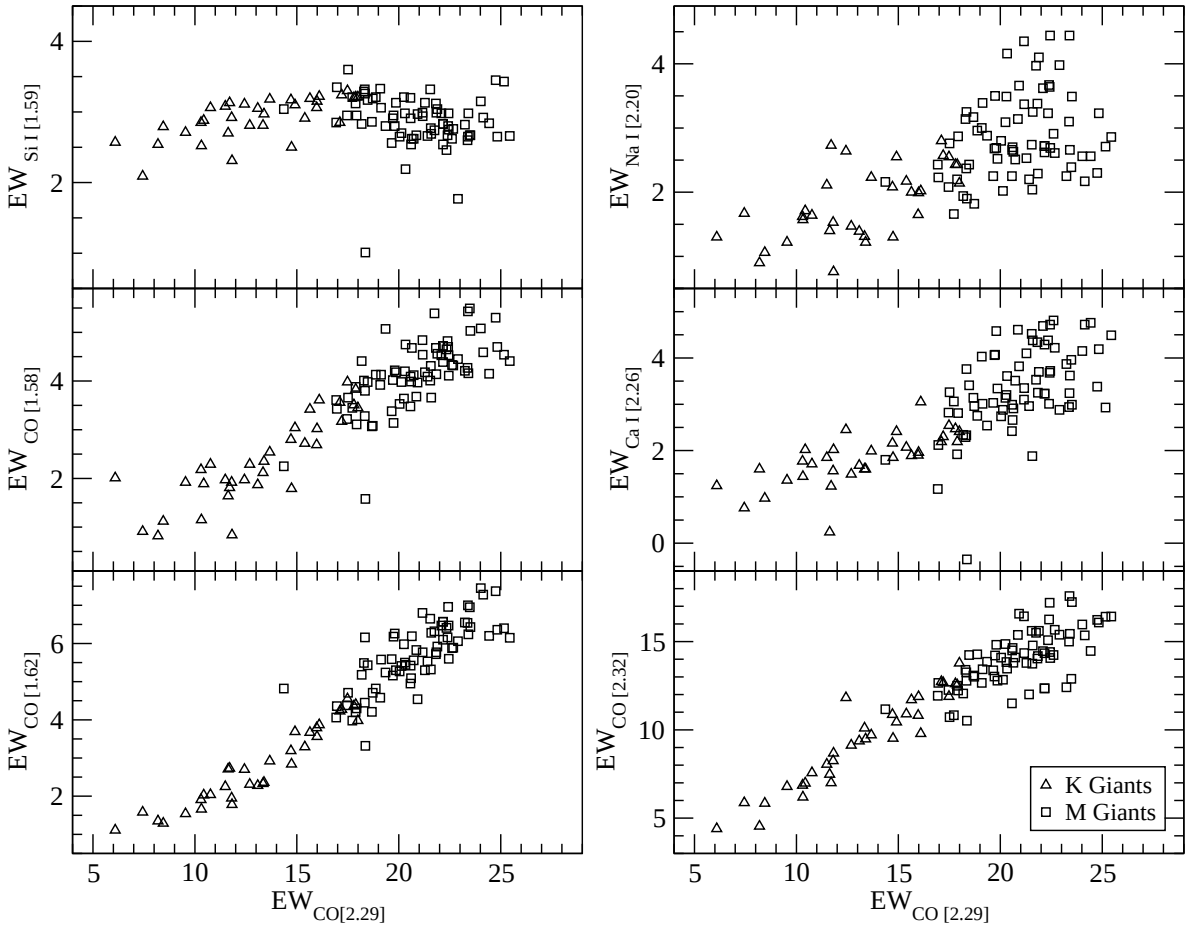

Figure 3.8: Measured equivalent widths of ^{12}CO at 2.29 μm feature versus measured equivalent widths of Si I, Na I, Ca I and ^{12}CO at 1.58, 1.62 and 2.32 μm.

atomic lines (Si I at 1.59, Na I at 2.20 and Ca I at 2.26 μm) and molecular lines (^{12}CO at 1.58, 1.62, 2.29 and 2.32 μm) over fundamental parameters like T_{eff}, log g, $[M/H]$ are shown in Figure 3.9 and Figure 3.10. The observed variation of those lines could be seen in Figure 3.6 and Figure 3.7. Comparative studies between observational and theoretical prediction might be interesting and can constrain the models.

In Figure 3.9 and Figure 3.10, the strength of Si I predicted from the synthetic spectra appears to behave similarly with the observational finding in the top panel of Figure 3.6 over T_{eff} of K−M giants in the range 5000 to 3000 K; a steady increase from K0-giants at 5000 K and drop beyond 3500 K (after M4) are seen in those figures. Comparing with the predicted value in Figure 3.9 and Figure 3.10, the effect of log g and $[M/H]$ appears to be seen as a dispersion in the observational data in Figure 3.6. Please note that the metallicity effect in the observational data is in the limited range as our sample of bright giants is all in solar-neighbourhood. Origlia et al. (1993) pointed out that Si I feature is

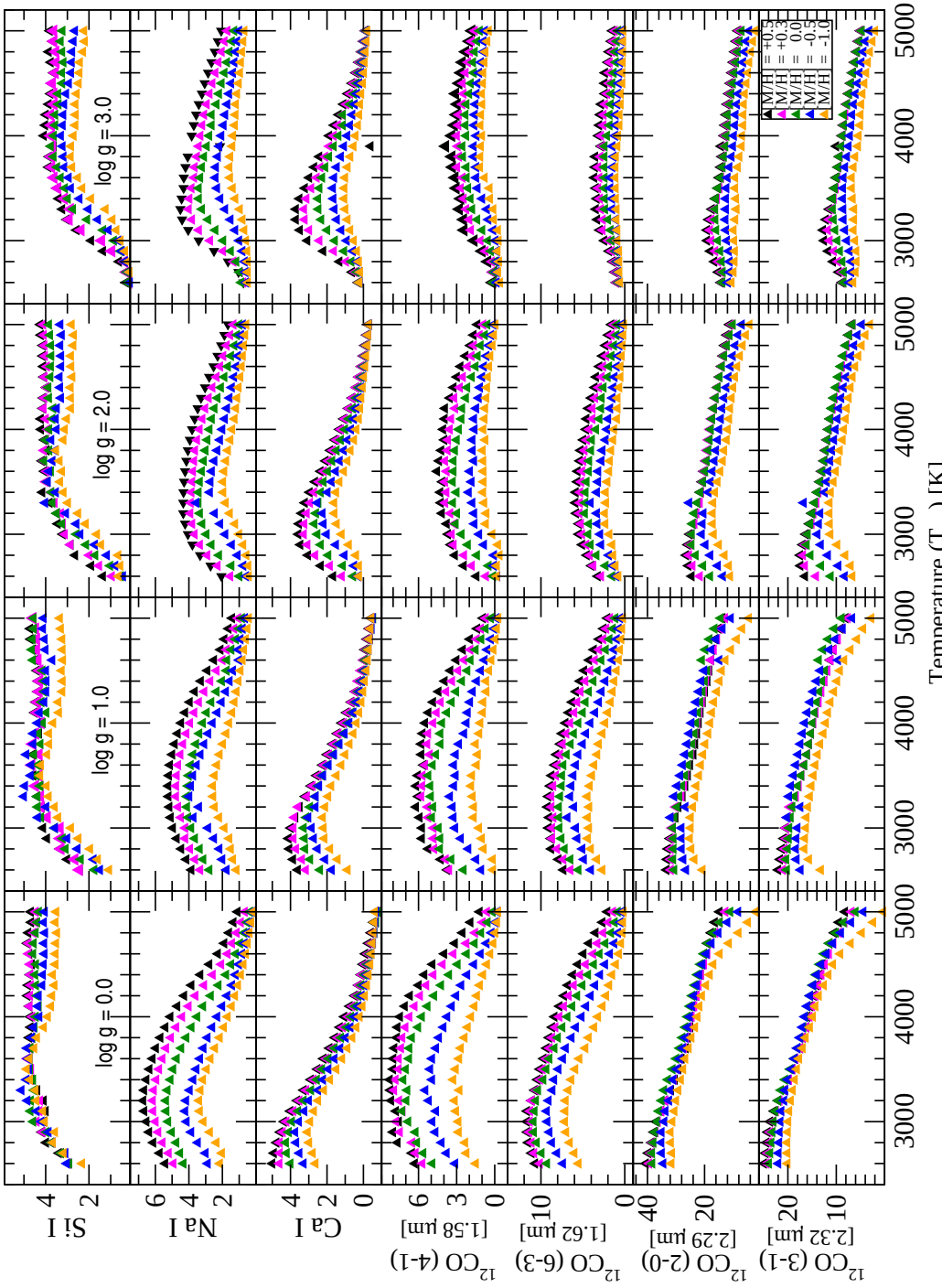

Figure 3.9: Behaviour of measured equivalent widths of spectral features from model grid with T_{eff}, log g, and [M/H] are shown in this figure.

contaminated by OH lines and becomes micro-turbulent velocities (ξ) than on log g or $[M/H]$.

The predicted strength of Na I doublet and Ca I triplet in Figure 3.9 and Figure 3.10 show a strong steady increase with decreasing temperature up to certain temperature ($\sim$ 3000−3200 K) and a decreasing trend below that certain temperature. The similar increasing trend up to a certain temperature is evident for the observed sample in the middle and bottom panels of Figure 3.6. However, the observed data do not have much coverage beyond 3000 K, where we have seen the decreasing strength of those lines in the prediction. The strength of both lines show variation over log g and $[M/H]$ in Figure 3.9 and Figure 3.10, which could be accounted for the dispersion in the observed data in Figure 3.6.

The predicted behaviour of CO bands strength with the T_{eff} are shown in Figure 3.9 and Figure 3.10 for different $[M/H]$ and log g, respectively. For all log g and $[M/H]$ model grids, the band strength of CO1 (1.58 μm) and CO2 (1.62 μm) show an increasing trend as temperature decreases as seen in observed data in the first column of Figure 3.7, and peak at a certain temperature and then begin to decrease below that peak temperature. The decreasing trend below about 3000 K in the observed data in Figure 3.7 is less obvious because of the dearth of the sample. The weakening of CO1 and CO2 bands strength below 3000 K could be due to the strong appearance of water bands and OH lines. However, the peak of bands strength shift towards warm temperature with increasing log g, and the strong dependence of log g is also evident in the observational data in the third column of Figure 3.7. The predicted strength of those bands shows variation over $[M/H]$ in Figure 3.7, which is not seen in the observed data because of the small metallicity range of our sample. The predicted strength of CO3 (2.29 μm) and CO4 (2.32 μm) continues to increase up to 3200 K and then saturates below that temperature as seen in the observational data in the first column of Figure 3.7. The appreciable weakening of these bands strength is seen over increasing log g and super-solar to sub-solar [M/H], which is visible in the third column of Figure 3.7 for log g. Origlia et al. (1993) pointed out that this could be explained by the effect of CO column density, ξ and pressure dependence of the H^- abundance on CO band strength.

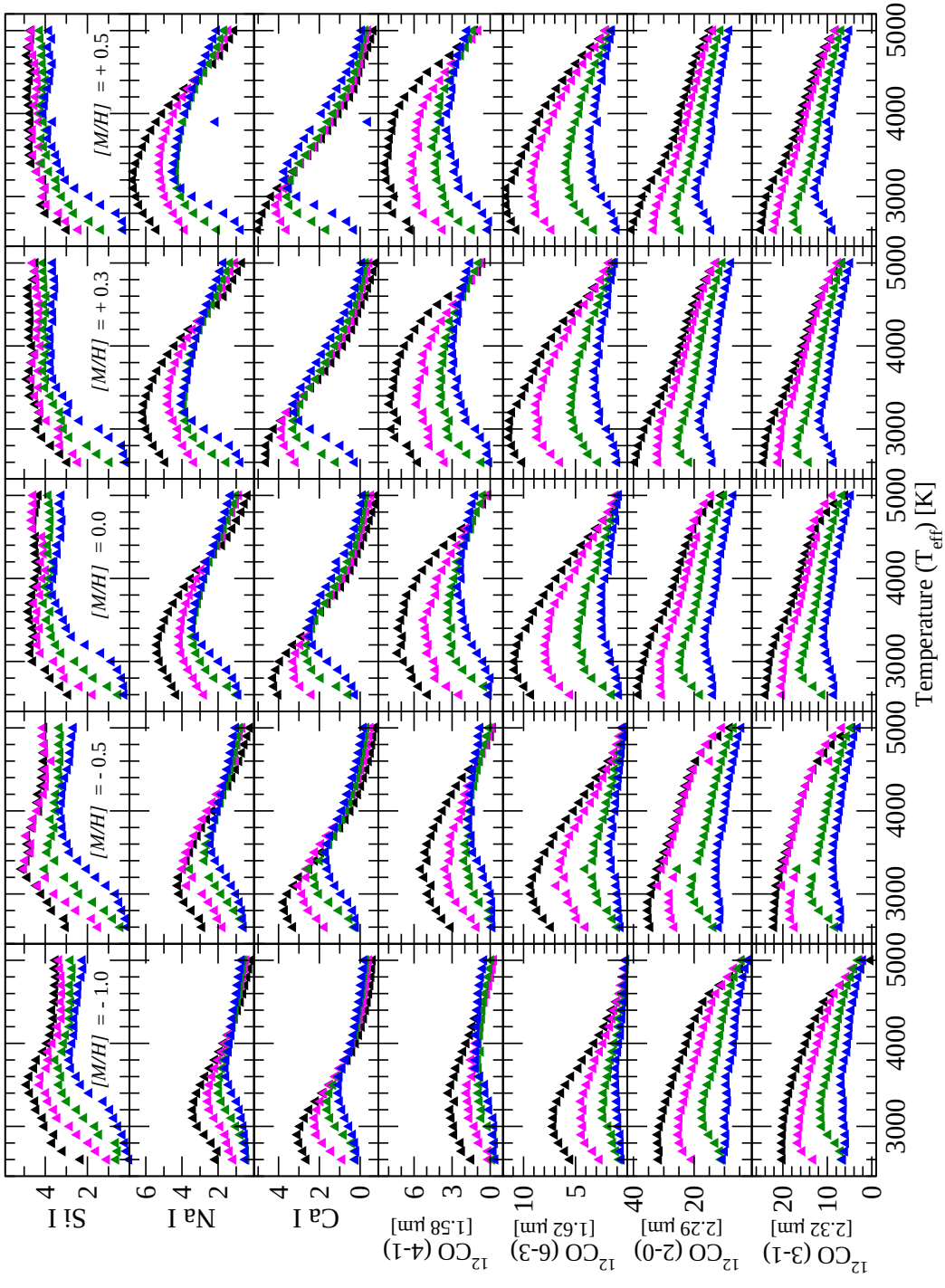

Figure 3.10: Behaviour of measured EWs of spectral features from model grid with T_{eff}, log g, and [M/H] are shown in this figure.

3.4.3 Empirical calibrations

Correlation between effective temperature and EW

The most strong CO(2−0) bandhead at 2.29 μm has been widely used as a stellar T_{eff} indicator. Several index definitions have been adopted to measure its strength (see Kleinmann & Hall 1986; Ramirez et al. 1997; Frogel et al. 2001; Blum et al. 2003; Maness et al. 2007; Mármol-Queraltó et al. 2008). Different index definitions lead to overestimation of the stellar temperatures (see Pfuhl et al. 2011). Pfuhl et al. (2011) computed the CO strength according to the recipe of Frogel et al. (2001) to determine T_{eff} using thirty-three giants with ST G0−M7, and have found smaller systematic error than other definitions. Other ^{12}CO bandheads at 2.32 and 1.62 μm are also used as a reasonable good temperature indicator (see Kleinmann & Hall 1986; Origlia et al. 1993; Ivanov et al. 2004; Schultheis et al. 2016). Schultheis et al. (2016) showed ^{12}CO(3−1) bandhead at 2.32 μm is an excellent temperature indicator in alternative of the strong ^{12}CO bandhead at μm.

We used all of the four bandheads CO1, CO2, CO3, and CO4 for new empirical relations of the giants, and for relative comparison of their effectiveness. Following Origlia et al. (1993) and Frogel et al. (2001), we have used the bandpasses as mentioned in Table 3.2. In the case of CO1, we have defined here new bandpasses as in Table 3.2, which has not been explored earlier. For CO3 and CO4, we have used two bands of the continuum from Frogel et al. (2001), where the authors had used four bands of the continuum. The estimated EWs for all the sample stars are listed in Table 3.4. The EWs of COs is plotted against T_{eff} as shown in Figure 3.11. To establish the empirical relation between EWs of COs and T_{eff}, a linear fit is explored for each bandhead separately using the linear equation T_{eff} = a0 − a1 × EWs (where a0 and a1 are the coefficients of the fit). The 2σ outliers are excluded for such fittings. Three different cases are excised for the best-fit, where case 1 is considered for all the 107 giants in our sample, case 2 for $T_{eff} \geq 3200$ with 98 giants, and case 3 for $T_{eff} \geq 3400$ with 70 giants. The results of fitting in three different cases are listed in Table 3.3. The best fit is judged by the three parameters – correlation coefficient (R), the coefficient of determination (Rsqr) and the standard error of estimate (SEE). In case 1 (all the sample), the SEE are 207 K, 140 K, 130 K, and 166 K for CO1, CO2, CO3, and CO4, respectively. In a comparison of all the four bandheads, the SEE is minimum in case of strong bandhead CO3. It is noticed that a better fit is obtained by narrowing down the temperature range and the SEE improves from case 1 to case 3 for all bandheads. The least-square linear fits for case 1 only are shown in Figure 3.11. For comparison, the existing relations in the literature are overplotted in Figure 3.11, where

the green dot line is the linear-fit from Feldmeier-Krause et al. (2017), the blue dash line is the three-degree polynomial fit of Pfuhl et al. (2011) and the black dot-dashed line is the linear fit from Ramirez et al. (1997).

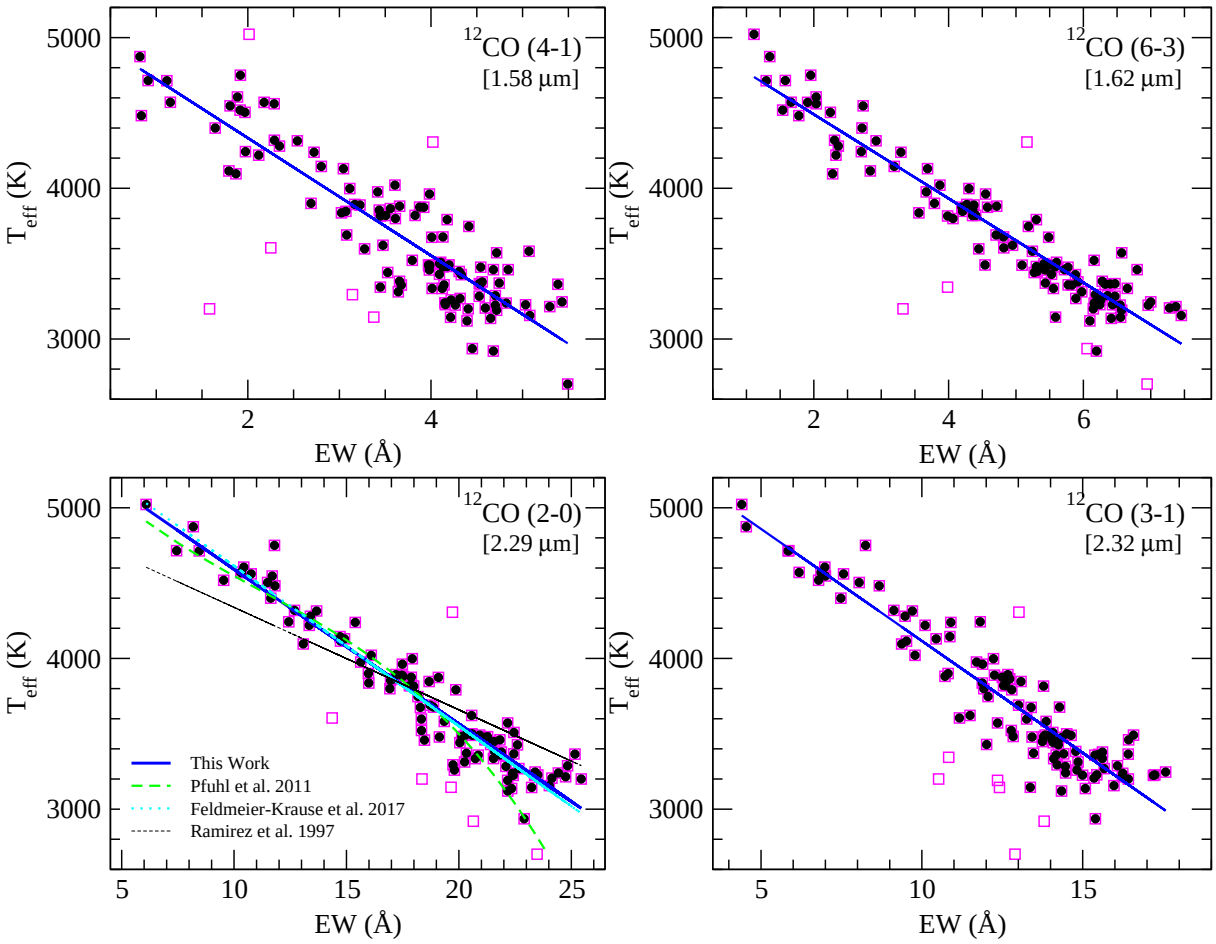

Figure 3.11: Figure shows the relation between T_{eff} and EWs of the ^{12}CO (4−1) at 1.58 μm, (6−3) at 1.62 μm, (2−0) at 2.29 μm and (3−1) at 2.32 μm. For ^{12}CO at 2.29μm, we compare our results with literature. The square symbol represents all the stars of our sample. Black dot represents the stars from our sample used for empirical relation. The blue solid line shows our best fit relation.

To establish the empirical relations, Feldmeier-Krause et al. (2017) used 69 stars with luminosity classes II-IV at a R $\sim$ 3310−4660, Pfuhl et al. (2011) used 33 giants at R $\sim$ 2000 and R $\sim$ 3000, and Ramirez et al. (1997) used 43 giants at R $\sim$ 1380 and R $\sim$ 4830. Our correlation with T_{eff}–CO3 differs significantly from the correlation of Ramirez et al. (1997), and the difference could be due to different bandpass and continuum to measure EWs. However, the correlation of T_{eff}–CO3 agrees well with that of Pfuhl et al. (2011) for $T_{eff} > 3000$ K and Feldmeier-Krause et al. (2017). However, we reproduced almost the same or better correlation with lower residual scatter (SEE) in spite of using the lower resolution spectra. It is important to note here that spectral resolution (i.e. R $\sim$ 3310−4660 versus R $\sim$ 1200) is insensitive to the T_{eff}–CO3 correlation as seen

in Feldmeier-Krause et al. (2017). Also, EWs of CO3 (2.29) are estimated using the two continuum bands, out of four continua as in Frogel et al. (2001). However, our established correlation shows no significant variation compared with the relations of Pfuhl et al. (2011) and Feldmeier-Krause et al. (2017) as shown in Figure 3.11, where the authors had used four continua of Frogel et al. (2001). Thus, two continua could be used instead of four to calculate EWs of CO3 without any systematic offset.

We also investigate simple parametrizations of the multi-line functions (e.g., CO1−SiI, CO1/SiI, CO2/CO1, CO2−CO1, CO3−(NaI+CaI), CO3/(NaI + CaI), etc.), and perform least-square regression to test the correlation with T_{eff} for each combination qualitatively. No combining feature results significant improvement of the relationship discussed above. It is noted that the correlation between combined features follows the trends of the stronger feature of that combination. Further discussion on the combined features is therefore excluded.

Correlation between spectral type and EW

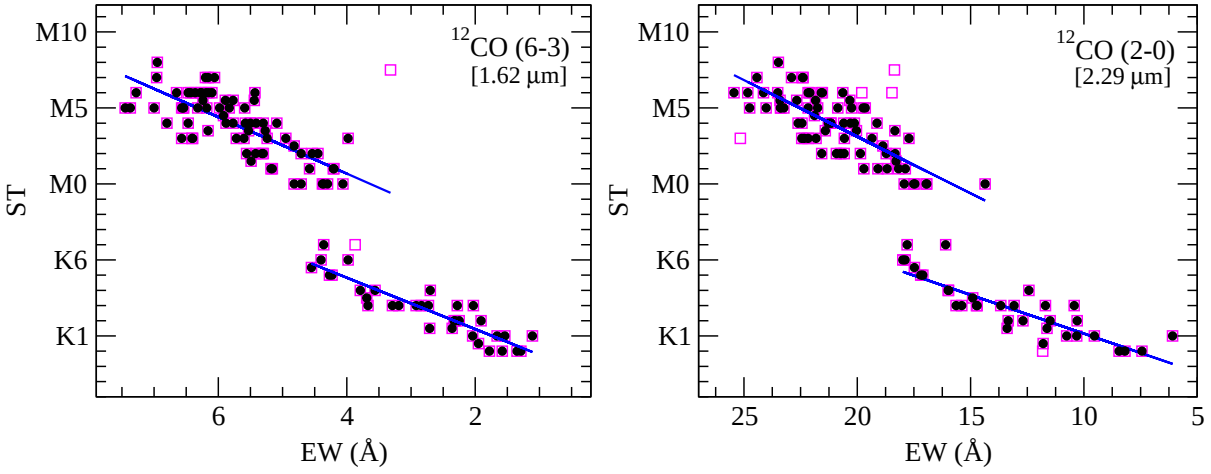

Figure 3.12: Figure presents the relation between ST and EWs of the ^{12}CO (6−3) at 1.62 μm and (2−0) at 2.29 μm. The square symbol represents all the stars of our sample. Black dot represents the stars from our sample used for empirical relation. The blue solid line shows our best fit relation for K and M giants separately.

In this section, we have established the empirical relation between the ST (hence, the luminosity) and EWs of CO2 at 1.62 μm and CO3 at 2.29 μm spectral bands. As described earlier (see Figure 3.11), these bands show reliability to estimate the T_{eff}. Hence, these band could be used for the estimation of ST. We establish an empirical relation between EWs of these two bands and ST using a linear fit adopting the equation ST = a0 + a1 × EWs (where, a0 and a1 are the coefficients of the fit) for K- and M-giants separately. We assign an integer number G to each ST (K0=−11, ..., K5=−6, ..., M0=0, ..., M5=5, ...,

M8=8) to establish the correlation. We excluded the limiting 2σ outliers for fitting. The linear fits are shown in Figure 3.12, and the corresponding fitting parameters are listed in Table 3.3 along with SEE of the fits. We have found that the ST can be predicted from the correlations with a typical accuracy of 1 subtype. However, the dispersion in the correlation between ST–CO is greater for M-giants than K. This might be due to the enhancing effect of metallic line blending and molecular (e.g., water, OH) absorption in the K to M giants. The SEE of the fits increases to a typical uncertainty of 2 subtype if all the K and M giants are considered together for the correlation.

di Benedetto & Rabbia (1987) established the improved empirical relations for effective temperature (using visual surface brightness) versus colour indices for K and M-giants separately. The authors pointed out that a clear difference in colour indices of K and M-giants might be due to the molecular absorption in the transition from K to M-giants. Ramirez et al. (1997) derived the T_{eff} and ST (K0–M7) relation by a second-order polynomial fit, while the estimation of T_{eff} is based on the linear fit of CO3 band. González-Fernández et al. (2008) obtained the correlation between ST (K0–M7) and the EWs of CO bandhead at 2.29 μm with a typical uncertainty of 1.2 subtype. However, the authors found a large deviation of ST beyond M5, and their relationship is valid up to M5. Hence, our empirical relations are more accurate than the previous estimations, and it could also be applied beyond M5.

Correlation between metallicity and EW

We adopt Na I, Ca I, and CO3 to establish a $[Fe/H]$ scale for solar-neighbourhood giants based on our medium-resolution K-band spectra. The technique to establish a $[Fe/H]$ scale is followed from Ramírez et al. (2000) and Frogel et al. (2001). 32 stars of our sample have known $[Fe/H]$. To establish the correlation, we performed a linear least square fit between the three EWs and $[Fe/H]$ using the equation 3.2 that provides an empirical relation with SEE 0.17 dex.

$$\begin{aligned} [Fe/H] &= a_0 + a_1 EW_{NaI} + a_2 EW_{CaI} + a_3 EW_{CO} \\ a_0 &= -0.222 \pm 0.105 \\ a_1 &= 0.135 \pm 0.057 \\ a_2 &= 0.090 \pm 0.058 \\ a_3 &= -0.029 \pm 0.014 \\ SEE &= 0.17 dex \end{aligned} \tag{3.2}$$

Frogel et al. (2001) showed that the quadratic fit to three EWs provides a better fit than the linear one and demonstrated the nonlinear behaviours between EWs and $[Fe/H]$. However, in this work, quadratic fit to three EWs ensues no improved SEE. We feel that this may due to the narrow metallicity range $[(-0.58) - (0.25)$ dex] of our sample. Thus, we limit our discussion on the linear fit of the three EWs. With the equation 3.2, we measure a value of $[Fe/H]$ for each star from EWs, and compare our measurements with the calibration sample as shown in Figure 3.13. We find that our measurements agree with the literature value of $[Fe/H]$ with an average dispersion of $\pm$ 0.13 dex. The mean distribution of $[Fe/H]$ are also derived for all 107 giants of our sample, which peaks at -0.16 dex i.e. just above solar metallicity with an average propagation uncertainty of $\pm$ 0.15 dex. These results match well with the expected values of the sample giants in the solar-neighbourhood (e.g., Hinkel et al. 2014; Adibekyan et al. 2012; Hayden et al. 2015). Estimation of $[Fe/H]$ from high-resolution spectra are available for 18 sample giants. We compare the high-resolution measurements with the estimated $[Fe/H]$ from our low-resolution spectra using the equation 3.2, and find that the average dispersion between those measurements is of the order of $\sim$ 0.18 that agrees well with the study of Schultheis et al. (2016) who found a general correlation between the metallicities derived from high-resolution IR spectra and those from low-resolution spectra for galactic bulge M giants with a dispersion of the order of $\sim$ 0.2 dex. Four of our sample giants are available in Luck & Heiter (2007) and 12 of our sample giants are available in Prugniel et al. (2011). We note that our measurements reproduce their results with an average dispersion of the order of $\sim$ 0.2 dex. Finally, it should be noted that we calibrate our relation to giants in the solar-neighbourhood. Hence, caution should be taken while applying this relation to metal-poor or metal-rich stars.

Correlation between surface gravity and EW

To establish the empirical relation between EWs and log g, a linear fit is explored for CO2 and CO3 bandhead separately using the linear equation $\log g = a_0 + a_1 \times$ EWs. We have used here CO2 and CO3 bands as their SNR are relatively better than other CO bands. Among 107 giants, 97 have known log g in the literature and we have used those giants for the correlation. We excluded the limiting 2σ outliers for fitting. The least-square linear fits are shown in Figure 3.14. The number of the stars used for the fit after 2σ clipping and the coefficients of fit are listed in Table 3.3 along with SEE. The best fit is judged on the basis of SEE, which is 0.29 for both bands. Our study suggests that both CO2 and CO3 are good log g indicator and the result differs from Origlia et al. (1993), who

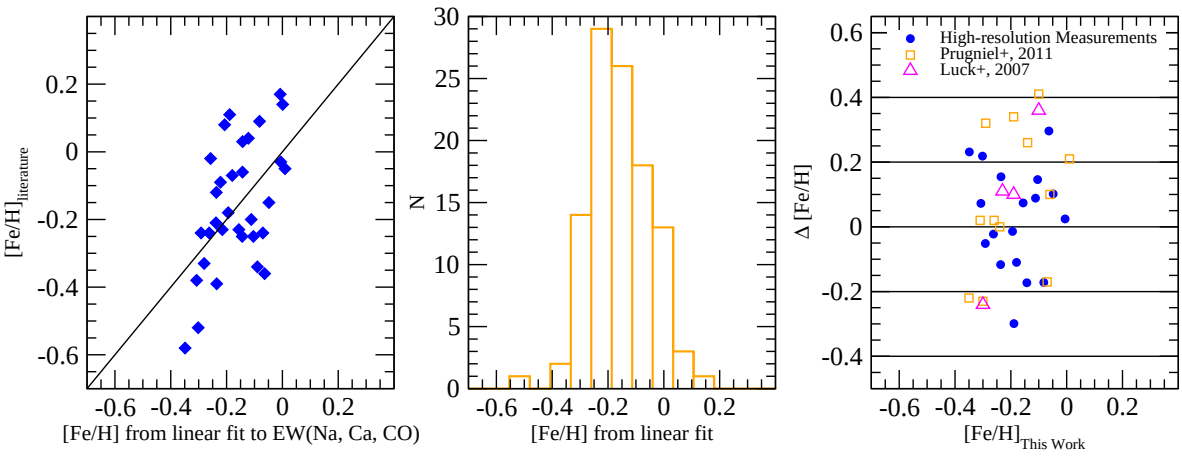

Figure 3.13: Comparison for 32 giants of $[Fe/H]$ is given in the Table 3.1 and those derived from best fit relation are presented (left). The distribution of $[Fe/H]$ are shown considering all the 107 giant, that are derived from our empirical relation (middle). Comparison of $[Fe/H]$ taken from various literature and those derived from our relation are presented (right).

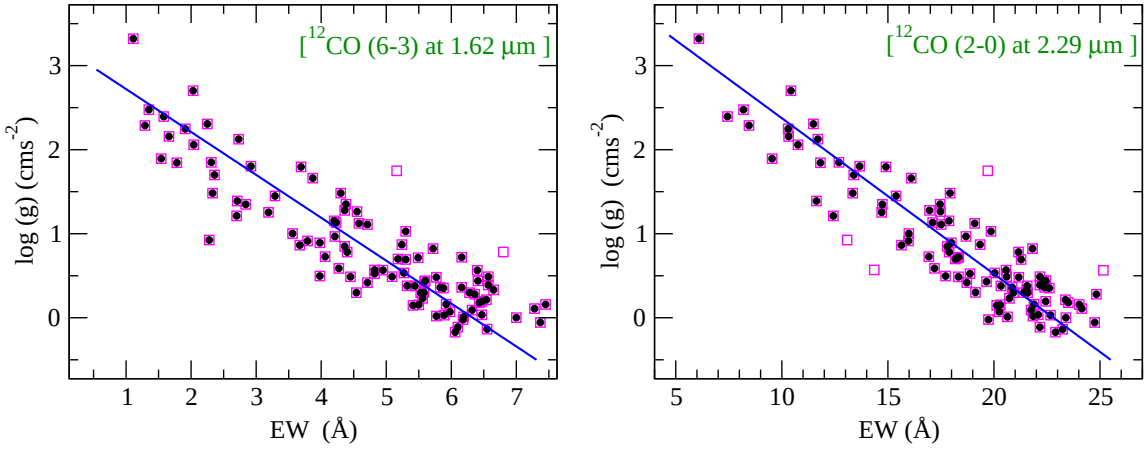

Figure 3.14: The relation between log g and EWs of the ^{12}CO (6−3) at 1.62 μm, (2−0) at 2.29 μm are shown. The square symbol represents all the stars of our sample. Black dot represents the stars from our sample used for empirical relation. The blue solid line shows our best fit relations.

demonstrated that CO2 is a better representative of log g than CO3 from the behaviour of synthetic spectra.

Effect of surface gravity on effective temperature versus EW correlation

To take into account the effects of log g on the calibration of T_{eff} and the EWs of ^{12}CO at 1.62 and 2.29 μm, we recalibrate the empirical relations as,

$$T_{eff} = a_0 + a_1 EW + a_2 \log g. \tag{3.3}$$

where a_i (i=0,...,2) are the coefficients of the fit obtained iteratively. The SEE corresponds to 78 and 90 K for CO2 and CO3, respectively. The results of fitting are listed in Table 3.3. To test the effects of log g quantitatively, we fit the equation 3.3 without considering log g, i.e. making $a_2 = 0$. The SEE is equivalent to 132 K for both cases. It is noted that the SEE is improved significantly when the effect of log g is considered in the T_{eff} vs EWs correlation as shown in Figure 3.15.

Table 3.3: Comparison between Goodness of Fit for various correlations.

Index	T	N	R	Rsqr	SEE	a0†	a1†	a2†	Remarks*
					T_{eff}	= f(EW) :			
^{12}CO (4-1)	107	101	0.90	0.82	207	5114 ± 70	-390 ± 19	...	1
1.58 μm	98	93	0.90	0.82	197	5070 ± 69	-372 ± 19	...	2
(CO1)	70	67	0.90	0.82	177	5039 ± 68	-346 ± 20	...	3
^{12}CO (6-3)	107	102	0.96	0.92	140	5049 ± 42	-279 ± 8	...	1
1.62 μm	98	95	0.96	0.92	130	5038 ± 40	-274 ± 8	...	2
(CO2)	70	67	0.96	0.92	124	5092 ± 45	-287 ±11	...	3
^{12}CO (2-0)	107	100	0.96	0.93	130	5619 ± 54	-103 ± 3	...	1
2.29 μm	98	93	0.97	0.93	119	5563 ± 51	-99 ± 3	...	2
(CO3)	70	67	0.97	0.94	104	5571 ± 53	-99 ± 3	...	3
^{12}CO (3-1)	107	100	0.94	0.88	166	5603 ± 71	-149 ± 5	...	1
2.32 μm	98	94	0.95	0.90	147	5549 ± 64	-143 ± 5	...	2
(CO4)	70	65	0.95	0.91	127	5532 ± 65	-140 ± 6	...	3
					ST	= f(EW) :			
CO2	34	33	0.91	0.83	0.78	-12.94 ± 0.40	1.69 ± 0.14	...	K giants
	73	72	0.76	0.58	1.34	-6.76 ± 1.09	1.85 ± 0.19	...	M giants
CO3	34	33	0.87	0.75	0.96	-14.94 ± 0.70	0.51 ± 0.05	...	K giants
	73	69	0.77	0.59	1.31	-11.79 ± 1.61	0.75 ± 0.08	...	M giants
					log g	= f(EW) :			
CO2	97	92	0.91	0.82	0.29	2.69 ± 0.01	-0.40 ± 0.02	...	1
CO3	97	93	0.93	0.86	0.29	3.75 ± 0.13	-0.16 ± 0.01	...	1
					T_{eff}	= f(EW, log g) :			
CO2	97	90	0.99	0.97	78	4148 ± 72	-142 ± 11	315 ± 25	1
CO3	97	92	0.98	0.96	90	4465 ± 116	-54 ± 5	308 ± 30	1

Notes. T − total nos. of data points; N − no. of points used for fitting after eliminating 2σ outlayers; R − correlation coefficient; Rsqr − coefficient of determination; SEE − standard error of estimate.
† T_{eff} = a0 + a1 × EWs + a2 × log g.
*1 − Fitting with all the sample stars.
*2 − Fitting with sample stars; $T_{eff} \geq 3200$.
*3 − Fitting with sample stars; $T_{eff} \geq 3400$.

Effect of surface gravity and metallicity on effective Temperature versus EW correlation

To take into account the effects of log g as well as $[Fe/H]$, we recalibrate the empirical relation as,

$$T_{eff} = a_0 + a_1 EW + a_2 \log g + a_3 [Fe/H]. \quad (3.4)$$

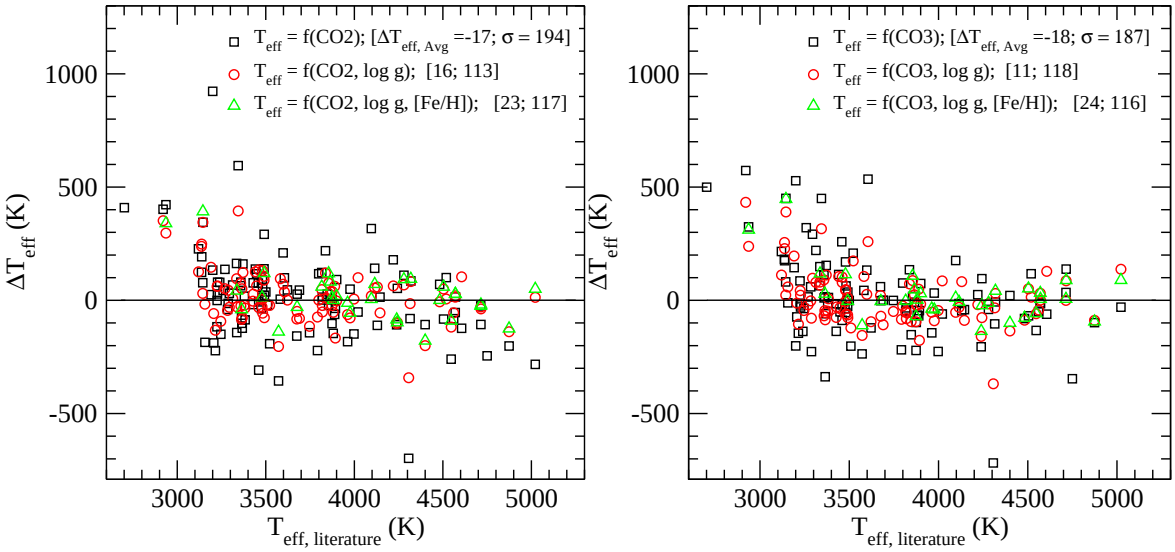

Figure 3.15: Comparison of T_{eff} given in the Table 3.1 and those derived from different established relations. We investigate the dependency of EWs, log g and $[Fe/H]$ on the derived T_{eff}. It shows that effect of $[Fe/H]$ is insignificant on T_{eff}, but log g significantly affects the results.

where a_i (i=0,...,3) are the coefficients of the fit obtained iteratively using 32 giants available in our sample having known $[Fe/H]$. The SEE corresponds to 80 and 71 K for CO2 and CO3, respectively. To test the effects of $[Fe/H]$ quantitatively, we fit the equation (3.4) making a_3=0. The SEE is equivalent to 80 and 70 K for CO2 and CO3, respectively. It is noted that the SEE is almost same with or without $[Fe/H]$ taking into account. Therefore, we conclude that the effect of $[Fe/H]$ on the correlation is insignificant owing to the abundance of our sample near solar metallicity. Schultheis et al. (2016) also found no critical metallicity dependence on the T_{eff}–CO correlation in the temperature range of 3200−4500 K within metallicity range $(-1.2)-(+0.5)$ dex.

The T_{eff} obtained from our empirical calibrations are compared with the previous published values of T_{eff} estimated using various techniques. It is to be noted that we obtain the best T_{eff} considering the effect of log g along with the EWs of CO as described earlier. Hence, we derive values of T_{eff} from the equation 3.3 using both CO2 and CO3 features, and compare distinctly with the literature values as shown in Figure 3.16. First, we focus on the Catalog of Earth-Like Exoplanet Survey Targets (CELESTA), a database of habitable zones around 37000 nearby stars (Chandler et al., 2016). We have 85 giants in common with our current sample of giants, but 5 of them (HD92620, HD115322, HD7861, HIP44601, HD141265) have not been considered owing to absence of log g values in the literatures. We find that their T_{eff} are on average $\sim$ 50 K cooler than our measurements, with a standard deviation, $\sigma \sim$ 165 K for both (CO2 and CO3) cases. A total of 27 giants are found in common with PASTEL catalogue (Soubiran et al., 2016). We find that the

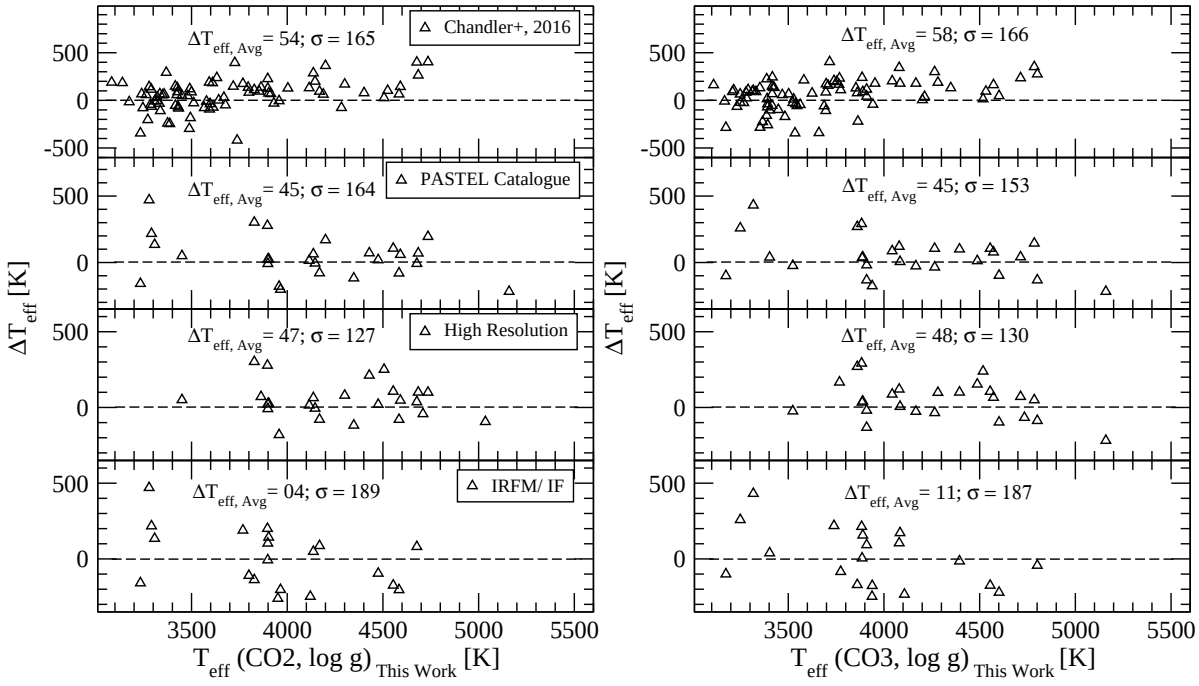

Figure 3.16: Comparison of T_{eff} estimated from previous studies and those derived from our T_{eff} − CO − logg relation. We provide the comparison for both CO2 (left panel) and CO3 (right panel). The residuals are plotted in the Figure.

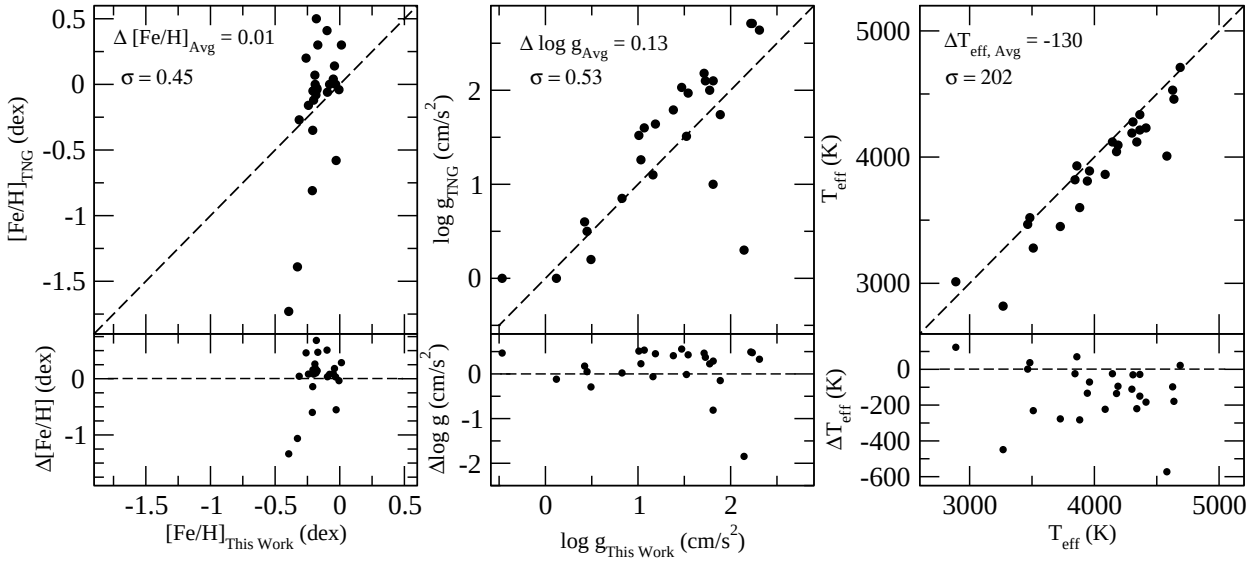

Figure 3.17: Comparison of $[Fe/H]$, log g and T_{eff} derived by Mármol-Queraltó et al. (2008) and those derive from our calibrations using TNG spectra. The residuals are plotted at the bottom panel.

T_{eff} of giants obtained in this work are on average 45 K warmer than the measurement in the PASTEL catalogue, with $\sigma \sim 155$ K. Estimation of T_{eff} from high resolution spectra are available for 25 giants with our current sample[3]. A comparison of common objects provides an average difference of 16 K (CO2) and 11 K (CO3), with $\sigma = 113$ K (CO2) and 118 K (CO3). T_{eff} of 4 giants are derived from IRFM method[4] and 16 giants are measured from interferometric data[5]. The mean difference is ~ 10 K, with $\sigma \sim 180$ K considering all the 20 giants.

3.4.4 Application of our empirical relations

To inspect reliability of our empirical relations, we estimate T_{eff}, log g, and $[Fe/H]$ from the spectra (R $\sim$ 1250) of K−M giants observed with NICS on 3.58 m TNG at Roque de los Muchachos Observatory, La Palma, Spain (Mármol-Queraltó et al., 2008). A total of 25 K−M giants yield the opportunity to compare the parameters measured from our empirical relations with that of literature values[6]. We measure the EWs of Na I, Ca I, and ^{12}CO (2−0) using similar methods as described in section 3.3. First, $[Fe/H]$ are estimated from equation 3.2. The average difference and a standard deviation are Δ[Fe/H]$_{Avg} = 0.01$ dex and $\sigma = 0.45$ dex. Note that in the above comparison, the relation yields the $[Fe/H]$ that deviates significantly for metal-poor stars. Thus, we draw the limit of this relation for good $[Fe/H]$ estimation at $-0.6 < [Fe/H] < +0.3$. Within this $[Fe/H]$ interval, the σ reduces to 0.22 for TNG stars (N=20), that is almost near to the SEE of the fit of our empirical relation. The log g is estimated from log g–CO3 relation. The results are in good agreement with average difference, $\Delta \log g_{Avg} = 0.13\ cm/s^2$ and a standard deviation, $\sigma = 0.53\ cm/s^2$. The T_{eff} are estimated using the measured log g and CO3 from equation 3.3. The T_{eff} are on average 130 K cooler than literature value with a standard deviation, σ = 202 K. Excluding the two giants, HD232708 (residual=572 K), a long-period variable, and HD126327 (residual=448 K), an asymptotic giant branch star, the $\Delta T_{eff,Avg}$ and σ reduce to −97 K and 146 K, respectively. The origin of this discrepancies might be due to the fact that pulsating long-period variables behave differently than the static giants (Bessell et al., 1989; Alvarez & Plez, 1998; Lançon & Wood, 2000; Ghosh et al., 2018).

[3]HD54810, HD137759 (Jofré et al., 2015); HD99283 (Reffert et al., 2015); HD102224, HD70272, HD60522, HD124897 (Hekker & Meléndez, 2007); HD69994, HD26846, HD97605, HD83787, HD91810, HD178208 (Feuillet et al., 2016); HD85503 (Bruntt et al., 2011); HD30834, HD92523, HD49161, HD99167, HD35620, HD99998, HD120477 (McWilliam, 1990); HD100006 (Luck & Heiter, 2007); HD25975, HD19058 Smith & Lambert (1986); HD207991 Kovtyukh (2007).

[4]HD54810 (Blackwell & Lynas-Gray, 1998); HD219215, HD35620, HD99998 (Alonso et al., 1999)

[5]HD102224, HD85503, HD92523, HD70272, HD99167, HD6953, HD38944, HD60522, HD216397, HD137759, HD120477, HD3346 (Bordé et al., 2002), HD18191, HD175865, HD196610, HD108849 (Dyck et al., 1998)

[6]https://webs.ucm.es/info/Astrof/ellipt/CO.html

The dispersion of all three fundamental parameters from our measurements is shown in the Figure 3.17.

3.5 Summary and Conclusions

We have constructed a new medium resolution (R $\sim$ 1200) NIR (1.50−2.45 μm) spectral library of 72 K−M giant stars with the aim of populating existing NIR stellar libraries with cool giants specifically after the M3 spectral type. The EWs of prominent atomic (Si I at 1.59 μm, Na I at 2.20 μm, Ca I at 2.26 μm) and molecular (^{12}CO first-overtone bandheads at 2.29 μm, 2.32 μm and, second-overtone bandheads at 1.58 μm, 1.62μm) features are estimated. We have studied the behaviour of those EWs with the fundamental parameters (e.g. effective temperature, spectral type, surface gravity, and metallicity). The main results are summarized as.

1. We obtained reliable new empirical relations between the EWs of ^{12}CO bandheads and T$_{eff}$. We found that the ^{12}CO first-overtone band at 2.29 μm and second-overtone band at 1.62 μm are reasonably good temperature indicator above 3400 K. This relation is also insensitive to the spectral resolution, and therefore, could be used more generally.

2. From the EWs of Na I, Ca I and CO, we establish a new empirical relation for obtaining $[Fe/H]$, which is able to reproduce literature values with an average dispersion of the order of $\sim$ 0.2 dex in the range $-0.6 < [Fe/H] < +0.3$.

3. We present empirical calibrations between the EWs of ^{12}CO bandheads (CO2 and CO3) and log g. Our study suggests that both ^{12}CO are a very good log g indicator.

4. We find that the significant improvement of empirical relations between ^{12}CO and T_{eff} on the inclusion of log g, and more reliable T_{eff} could be predicted. However, the inclusion of metallicity does show no change in the previous prediction of T_{eff}. This might be due to the narrow metallicity range in our sample. Further investigation regarding metallicity (particularly for metal-poor stars) from high-resolution spectra would be greatly appreciated.

Table 3.4: Measured equivalent width of all the sample

Star Names	Si I	CO1	CO2	Na I	Ca I	CO3	CO4
			TIRSPEC : :				
HD54810	2.09 ±0.24	0.91 ±0.66	1.58 ±0.23	1.67 ±0.36	0.76 ±0.44	7.44 ±2.24	5.87 ±1.13
HD99283	2.54 ±0.56	0.82 ±0.61	1.35 ±0.29	0.90 ±0.33	1.60 ±0.64	8.19 ±1.77	4.54 ±1.88
HD102224	2.31 ±0.86	0.84 ±0.38	1.78 ±0.46	0.76 ±0.38	2.02 ±0.34	11.82 ±1.20	8.68 ±0.92
HD69994	2.52 ±1.14	1.15 ±0.92	1.66 ±0.66	1.57 ±0.55	1.44 ±0.53	10.32 ±2.31	6.19 ±1.53
HD40657	2.70 ±0.28	1.64 ±0.53	2.71 ±0.34	1.40 ±0.32	0.24 ±0.76	11.63 ±2.16	7.48 ±2.27
HD85503	3.08 ±0.47	1.97 ±0.65	2.25 ±0.60	2.11 ±1.38	1.85 ±1.16	11.49 ±2.74	8.05 ±1.91
HD26846	3.13 ±0.60	1.81 ±0.86	2.73 ±0.48	2.73 ±0.98	1.23 ±0.71	11.70 ±2.62	7.00 ±2.15
HD30834	3.05 ±0.38	1.87 ±0.77	2.28 ±0.35	1.39 ±0.41	1.68 ±0.51	13.08 ±0.95	9.37 ±1.71
HD92523	2.50 ±0.46	1.79 ±0.37	2.84 ±0.31	1.30 ±0.20	1.85 ±0.34	14.74 ±1.23	9.52 ±1.27
HD97605	2.88 ±0.92	1.89 ±1.86	2.03 ±0.73	1.71 ±0.38	2.02 ±0.70	10.43 ±1.36	6.98 ±1.71
HD49161	3.11 ±0.24	1.97 ±1.19	2.70 ±0.56	2.64 ±0.54	2.45 ±0.90	12.43 ±2.34	11.82 ±1.59
HD70272	3.06 ±0.49	2.69 ±0.28	3.79 ±0.62	1.65 ±0.32	1.90 ±0.40	15.97 ±1.75	10.82 ±1.32
HD99167	2.85 ±0.27	3.56 ±0.46	4.23 ±0.65	2.80 ±0.42	2.19 ±0.78	17.11 ±2.65	12.73 ±2.78
HD83787	3.21 ±0.67	3.45 ±0.60	3.98 ±1.15	2.14 ±0.71	2.41 ±0.51	17.99 ±1.97	13.78 ±2.12
HD6953	3.22 ±0.33	3.61 ±0.53	3.87 ±0.41	2.02 ±0.28	3.05 ±0.53	16.10 ±1.50	9.79 ±1.65
HD6966	2.95 ±0.77	3.11 ±0.44	4.30 ±0.96	2.87 ±0.36	2.81 ±0.45	17.93 ±1.73	12.23 ±2.18
HD18760	3.04 ±0.84	2.25 ±0.64	4.82 ±0.61	2.16 ±0.52	1.80 ±0.84	14.36 ±1.67	11.17 ±3.13
HD38944	2.85 ±0.76	3.61 ±1.10	4.06 ±0.31	2.43 ±0.55	1.17 ±1.02	16.93 ±2.42	11.93 ±1.10
HD60522	3.60 ±0.80	3.66 ±0.60	4.71 ±1.30	2.76 ±0.20	3.26 ±0.26	17.51 ±1.58	10.72 ±1.36
HD216397	2.95 ±0.58	3.22 ±1.11	4.38 ±0.87	2.08 ±0.41	2.82 ±0.71	17.46 ±1.88	12.26 ±1.81
HD7158	2.83 ±1.09	4.41 ±0.49	5.18 ±0.41	1.94 ±0.40	2.34 ±0.46	18.18 ±0.68	12.06 ±2.28
HD82198	3.12 ±0.83	3.88 ±0.46	4.20 ±0.40	2.20 ±0.46	1.92 ±0.33	17.88 ±2.15	12.50 ±1.83
HD218329	3.33 ±0.90	3.92 ±0.65	4.58 ±0.46	3.00 ±0.99	4.03 ±0.71	19.09 ±4.36	12.66 ±3.53
HD219215	2.91 ±0.49	4.02 ±0.64	5.16 ±0.46	2.68 ±0.70	4.06 ±0.89	19.71 ±1.73	13.02 ±2.31
HD119149	3.29 ±0.62	4.01 ±0.60	5.49 ±0.77	3.14 ±0.47	2.29 ±1.20	18.29 ±3.03	13.40 ±3.19
HD1013	3.13 ±1.43	4.18 ±1.20	5.30 ±1.00	2.52 ±0.96	3.34 ±0.96	19.86 ±2.58	12.79 ±2.36
HD33463	2.97 ±1.57	3.97 ±1.46	4.54 ±1.09	3.66 ±0.77	3.82 ±1.60	20.92 ±2.07	16.58 ±2.52
HD39732	2.77 ±0.69	4.31 ±0.71	5.32 ±0.32	2.04 ±0.39	1.88 ±0.54	21.57 ±2.52	13.75 ±1.86
HD43151	2.62 ±0.18	4.12 ±0.41	5.56 ±0.78	2.51 ±0.26	3.51 ±0.38	20.73 ±1.24	14.10 ±1.80
HD92620	2.91 ±0.40	4.09 ±0.24	5.42 ±0.31	2.66 ±0.23	2.99 ±0.29	20.58 ±1.26	14.50 ±2.14
HD115521	3.19 ±0.51	3.08 ±0.66	4.71 ±0.57	1.82 ±0.25	2.96 ±0.47	18.72 ±1.77	13.01 ±1.30
HD16058	2.83 ±0.88	4.72 ±0.51	6.57 ±1.05	2.72 ±0.63	3.23 ±0.92	22.17 ±2.81	12.35 ±1.72
HD28168	3.21 ±1.00	3.45 ±1.61	3.98 ±0.74	1.66 ±1.01	3.06 ±1.36	17.72 ±10.61	10.83 ±2.02
HD66875	2.75 ±0.31	4.11 ±0.73	5.60 ±0.52	2.69 ±0.40	3.72 ±0.80	22.45 ±1.23	14.07 ±2.88
HD99056	2.46 ±0.50	4.65 ±0.67	6.41 ±0.45	3.23 ±0.44	4.38 ±1.09	22.34 ±2.38	15.08 ±3.13
HD215953	3.12 ±0.47	4.68 ±1.53	5.72 ±0.87	3.38 ±1.26	4.34 ±0.98	21.82 ±2.74	14.04 ±1.99
HD223637	3.20 ±0.52	3.48 ±0.73	4.95 ±0.34	2.25 ±0.76	2.42 ±0.82	20.57 ±2.78	11.50 ±2.15
HD25921	3.26 ±0.75	3.80 ±0.98	6.16 ±1.28	3.25 ±0.49	3.76 ±0.63	18.34 ±2.13	12.78 ±2.14
HD33861	3.43 ±0.90	4.54 ±1.14	6.40 ±0.50	2.71 ±0.41	2.93 ±0.36	25.16 ±1.58	16.41 ±2.10
HD224062	2.66 ±0.17	4.09 ±0.66	5.53 ±0.51	2.20 ±0.61	2.96 ±0.97	21.41 ±1.86	12.01 ±2.33
HD5316	3.13 ±0.40	4.18 ±0.44	5.30 ±1.27	2.53 ±0.61	4.10 ±1.00	21.28 ±1.51	13.79 ±2.55
HD34269	2.62 ±1.13	4.33 ±0.58	5.88 ±0.70	2.91 ±0.59	4.81 ±1.35	22.61 ±3.61	14.24 ±1.91
HD64052	2.99 ±1.49	4.84 ±1.17	6.80 ±0.69	4.35 ±0.66	3.10 ±1.49	21.16 ±3.74	16.43 ±3.21
HD81028	2.70 ±0.48	3.98 ±0.51	5.41 ±0.27	2.02 ±0.24	2.88 ±0.42	20.13 ±1.39	12.84 ±2.13
HD206632	2.98 ±0.91	4.53 ±0.59	6.47 ±0.60	4.44 ±0.73	4.72 ±1.64	22.44 ±3.05	14.41 ±3.79
HD16896	2.67 ±0.46	3.68 ±0.75	5.83 ±1.08	3.14 ±0.63	4.61 ±1.33	20.86 ±2.45	15.38 ±2.37
HD17491	3.21 ±1.36	3.64 ±0.72	5.98 ±0.72	3.09 ±0.55	3.14 ±0.44	20.25 ±2.52	14.86 ±2.12
HD17895	2.95 ±1.33	3.14 ±0.79	6.18 ±0.50	3.50 ±0.53	4.07 ±0.47	19.74 ±1.48	14.21 ±1.95
HD22689	2.82 ±0.41	4.21 ±0.77	6.55 ±0.86	2.25 ±0.85	3.87 ±0.57	23.24 ±3.49	12.41 ±2.22
HD26234	2.83 ±0.46	4.72 ±1.44	6.57 ±0.78	2.72 ±0.44	3.23 ±0.59	22.17 ±2.69	12.35 ±2.21
HD39983	2.56 ±0.48	3.38 ±0.36	5.59 ±0.57	2.25 ±0.40	3.03 ±0.48	19.65 ±1.76	13.37 ±1.77
HD46421	2.60 ±0.55	4.27 ±0.65	6.54 ±1.12	3.10 ±0.25	2.94 ±0.80	23.37 ±2.53	15.00 ±1.90
HD66175	3.15 ±0.29	5.08 ±0.80	7.45 ±0.56	2.56 ±0.31	4.15 ±0.32	24.02 ±1.21	15.97 ±1.42

Star Names	Na I	CO1	CO2	Na I	Ca I	CO3	CO4
HD103681	3.45 ±0.68	5.30 ±0.48	7.37 ±0.37	2.30 ±0.31	3.38 ±0.30	24.75 ±0.63	16.23 ±1.43
HD105266	2.65 ±0.32	5.43 ±0.55	7.00 ±0.93	4.44 ±0.60	3.24 ±1.16	23.39 ±2.98	17.58 ±3.42
HD64657	2.76 ±0.42	4.32 ±0.21	5.89 ±1.33	2.61 ±1.03	4.22 ±1.24	22.67 ±2.52	15.67 ±3.42
HD65183	2.99 ±0.88	4.14 ±0.94	5.77 ±0.63	2.29 ±0.42	3.25 ±1.46	21.84 ±2.95	14.18 ±1.67
HD223608	2.98 ±0.69	4.16 ±0.42	6.24 ±0.34	2.66 ±0.58	3.62 ±0.72	23.41 ±1.12	15.44 ±1.63
HD7861	2.80 ±1.48	4.22 ±0.75	6.26 ±1.48	2.69 ±0.49	4.58 ±0.95	19.80 ±1.99	14.82 ±1.51
HD18191	3.32 ±0.93	4.01 ±0.49	6.65 ±1.04	2.74 ±0.64	4.52 ±0.73	21.54 ±1.81	15.61 ±2.09
HD27957	2.69 ±1.04	3.66 ±0.54	6.28 ±0.63	3.25 ±0.36	4.38 ±0.29	21.59 ±1.51	14.78 ±2.25
HD70421	2.54 ±0.52	4.39 ±0.98	6.10 ±1.04	2.62 ±0.45	4.29 ±0.50	22.17 ±1.78	14.34 ±2.17
HD73844	2.92 ±1.08	4.59 ±0.85	7.28 ±1.15	2.17 ±0.77	4.72 ±1.10	24.14 ±2.50	15.35 ±1.60
HIP44601	2.66 ±0.45	4.41 ±0.52	6.15 ±0.71	2.86 ±0.25	4.49 ±0.87	25.44 ±2.06	16.42 ±1.64
HIC55173	2.65 ±0.62	4.70 ±0.51	6.36 ±0.85	3.23 ±0.65	4.19 ±0.58	24.83 ±2.23	16.08 ±2.93
HIP57504	2.62 ±1.09	4.68 ±0.61	6.19 ±0.66	2.63 ±0.29	2.91 ±0.27	20.64 ±1.00	13.80 ±2.25
HD115322	3.17 ±0.59	3.98 ±0.66	5.43 ±0.66	2.43 ±0.83	3.41 ±0.81	18.47 ±3.15	14.24 ±1.42
HD203378	2.98 ±1.41	4.53 ±0.85	6.47 ±1.60	3.62 ±0.71	4.69 ±1.06	22.09 ±2.63	14.46 ±2.81
HD43635	2.84 ±0.57	4.15 ±0.51	6.20 ±1.47	2.56 ±0.69	4.76 ±0.56	24.43 ±2.26	14.47 ±2.51
HIC51353	2.80 ±0.70	4.70 ±2.16	6.96 ±0.63	3.64 ±1.10	3.68 ±0.72	22.42 ±1.35	17.20 ±2.52
HIC68357	2.67 ±0.96	4.82 ±1.14	6.16 ±1.45	3.67 ±0.79	3.01 ±1.23	22.39 ±3.62	16.25 ±2.94
HD141265	2.67 ±0.64	5.49 ±0.80	6.95 ±1.39	2.39 ±0.66	3.96 ±0.78	23.48 ±1.62	12.89 ±2.72
			SpeX : :				
HD100006	2.79 ±0.60	1.12 ±0.67	1.29 ±0.33	1.06 ±0.21	0.97 ±0.15	8.45 ±1.10	5.84 ±1.48
HD9852	2.92 ±0.52	1.92 ±0.82	1.95 ±0.29	1.53 ±0.24	1.56 ±0.25	11.80 ±1.47	8.25 ±1.36
HD25975	2.57 ±0.33	2.01 ±0.68	1.11 ±0.27	1.30 ±0.24	1.24 ±0.22	6.09 ±0.89	4.40 ±1.05
HD36134	2.71 ±0.21	1.92 ±0.62	1.54 ±0.27	1.22 ±0.20	1.36 ±0.21	9.54 ±1.64	6.79 ±1.28
HD91810	3.06 ±0.30	2.29 ±0.55	2.04 ±0.25	1.64 ±0.28	1.71 ±0.50	10.76 ±1.48	7.57 ±1.67
HD124897	2.97 ±0.44	2.35 ±0.43	2.36 ±0.37	1.22 ±0.16	1.60 ±0.45	13.39 ±1.93	9.48 ±1.73
HD137759	2.85 ±0.59	2.18 ±0.42	1.91 ±0.29	1.62 ±0.25	1.77 ±0.17	10.30 ±1.47	6.86 ±1.19
HD132935	2.81 ±0.49	2.12 ±0.35	2.33 ±0.41	1.31 ±0.19	1.60 ±0.36	13.34 ±1.53	10.10 ±2.15
HD2901	2.81 ±0.45	2.29 ±0.47	2.31 ±0.24	1.47 ±0.28	1.49 ±0.29	12.69 ±1.41	9.13 ±1.91
HD221246	3.17 ±0.90	2.80 ±0.67	3.19 ±0.46	2.08 ±0.26	2.16 ±0.28	14.71 ±1.70	10.87 ±2.05
HD178208	3.18 ±0.49	2.54 ±0.92	2.92 ±0.36	2.23 ±0.33	1.99 ±0.40	13.67 ±1.44	9.71 ±1.85
HD35620	2.91 ±0.36	2.72 ±0.90	3.29 ±0.41	2.17 ±0.49	2.07 ±0.39	15.39 ±1.52	10.90 ±2.01
HD99998	3.19 ±0.75	3.42 ±0.46	3.67 ±0.58	2.00 ±0.43	1.89 ±0.34	15.64 ±1.45	11.70 ±2.30
HD114960	3.10 ±0.68	3.04 ±0.61	3.69 ±0.54	2.55 ±0.52	2.41 ±0.40	14.91 ±2.18	10.44 ±2.05
HD207991	3.15 ±0.71	3.02 ±0.56	3.56 ±0.53	1.99 ±0.27	1.96 ±0.34	15.99 ±1.61	11.88 ±1.52
HD181596	3.24 ±0.74	3.17 ±0.48	4.27 ±0.48	2.57 ±0.37	2.30 ±0.30	17.20 ±1.78	12.67 ±2.58
HD120477	3.30 ±0.73	3.98 ±0.47	4.55 ±0.55	2.55 ±0.53	2.54 ±0.40	17.48 ±1.54	11.89 ±2.29
HD3346	3.21 ±0.40	3.83 ±0.36	4.40 ±0.57	2.43 ±0.47	2.19 ±0.25	17.89 ±2.15	12.54 ±2.21
HD194193	3.20 ±0.35	3.51 ±0.45	4.36 ±0.81	2.43 ±0.36	2.47 ±0.42	17.80 ±1.90	12.61 ±2.86
HD213893	3.35 ±0.88	3.43 ±0.45	4.36 ±0.69	2.23 ±0.42	2.12 ±0.32	16.96 ±2.22	12.66 ±2.25
HD204724	2.86 ±0.70	3.07 ±0.26	4.21 ±0.73	3.17 ±0.48	3.14 ±0.53	18.68 ±2.81	13.08 ±3.02
HD120052	3.32 ±1.63	3.28 ±0.42	4.45 ±0.70	2.37 ±0.25	2.33 ±0.32	18.33 ±2.35	13.26 ±2.20
HD219734	3.21 ±1.69	4.13 ±0.45	4.82 ±0.51	2.96 ±0.42	2.75 ±0.46	18.87 ±2.32	14.28 ±2.25
HD39045	2.80 ±1.15	5.07 ±0.60	5.24 ±0.61	2.88 ±0.81	2.54 ±0.41	19.35 ±2.23	13.86 ±2.84
HD28487	2.65 ±0.60	3.53 ±0.56	5.27 ±0.90	2.80 ±0.40	2.74 ±0.55	20.04 ±2.45	14.09 ±3.42
HD4408	2.98 ±0.36	4.20 ±0.84	5.50 ±0.81	3.49 ±0.55	3.20 ±0.36	20.30 ±2.35	13.84 ±2.81
HD204585	3.04 ±0.36	4.56 ±0.91	5.92 ±0.84	4.10 ±0.60	3.70 ±0.48	21.89 ±2.54	15.61 ±3.39
HD27598	2.54 ±0.43	3.99 ±0.84	5.09 ±0.59	2.70 ±0.33	2.66 ±0.39	20.60 ±2.43	14.64 ±2.31
HD19058	3.06 ±0.76	4.13 ±0.52	5.58 ±0.70	3.39 ±0.44	3.01 ±0.33	19.13 ±2.40	13.43 ±2.33
HD214665	2.94 ±0.98	4.54 ±0.53	5.77 ±0.72	3.37 ±0.63	3.35 ±0.54	21.17 ±2.73	14.35 ±2.19
HD175865	2.74 ±1.23	5.39 ±0.70	6.32 ±0.79	3.97 ±0.62	3.53 ±0.54	21.75 ±2.24	15.50 ±2.69
HD94705	2.19 ±1.03	4.75 ±0.74	5.44 ±1.18	4.16 ±0.91	3.61 ±0.64	20.33 ±2.55	13.47 ±2.59
HD196610	2.67 ±0.74	5.03 ±0.71	6.43 ±0.79	3.49 ±0.50	2.99 ±0.69	23.51 ±2.80	17.24 ±2.77
HD108849	1.77 ±0.67	4.45 ±0.71	6.06 ±2.82	3.98 ±0.42	2.88 ±0.51	22.90 ±2.39	15.39 ±2.67
BRI2339-0447	1.01 ±0.45	1.58 ±1.21	3.32 ±0.87	1.90 ±0.16	-0.35 ±0.40	18.36 ±1.44	10.52 ±1.73

Chapter 4

New empirical relations on fundamental parameters of K–M giants

This chapter explores new empirical correlations between few strong spectral features, particularly, the ^{12}CO first-overtone bandhead at 2.29 μm and second-overtone bandhead at 1.62 μm, and fundamental parameters in K–M giants. Total NIR spectra of 107 K–M giants are taken for such studies. These spectra are taken from a new TIRSPEC NIR spectral library of 72 K–M giants, and all available 35 –KM giants from IRTF spectral library as described in Chapter 3. New and improvement of the existing different NIR empirical relations on fundamental parameters of K–M giants are described here, which are not covered in the earlier Chapter 3. Here, different indices in K-band for ^{12}CO (2−0) first-overtone bandhead at 2.29 μm are explored to determine the T_{eff} and the log g of cool giants. We define new indices for ^{12}CO (6−3) second-overtone bandhead at 1.62 μm and compare them for optimal CO index. We investigate here which index could be used to estimate fundamental parameters more precisely for cool M giants, particularly, T_{eff} below 3400 K. Finally, the behaviour of indices with fundamental parameters are compared in between the observed sample and theoretical models.

4.1 Introduction

The ^{12}CO(2−0) bandhead at 2.29 μm is a remarkably good temperature indicator for late-type giants (e.g., Ramirez et al. 1997; Förster Schreiber 2000; Frogel et al. 2001; Ivanov

et al. 2004) and has been widely used to investigate the stellar content of galaxies (e.g., Silva et al. 2008), starbursts and active galactic nuclei (e.g., Ridgway et al. 1994; Puxley et al. 1997). Numerous definitions have been adopted over the years to evaluate CO band strength, e.g., photometric CO index that measures the difference in magnitudes between two narrow filters, one for the feature and other for the continuum estimate (Baldwin et al., 1973; Frogel et al., 1978), spectroscopic index that measures the flux ratio between the feature band and the nearby continuum band (Kleinmann & Hall, 1986), percentage absorption index that measures the percentage of flux in the feature band relative to a continuum band (Blum et al., 1996), equivalent width that measures the area of the feature with respect to local continua (e.g., Ramirez et al. 1997; Förster Schreiber 2000; Frogel et al. 2001; Pfuhl et al. 2011), generic discontinuity that measures the average flux ratio between the continuum and the absorption bands (Mármol-Queraltó et al., 2008).

Furthermore, Origlia et al. (1993) showed that the ^{12}CO(6−3) bandhead at 1.62 μm is also a very good temperature indicator for late-type giants. This bandhead might be advantageous than ^{12}CO(2−0) at 2.29 μm for evaluating fundamental parameters of cool giants as it appears from the photospheric region and is directly related to the CO column density. However, this bandhead is comparatively less explored than that one at 2.29 μm. Up to date, most of the previous authors have hardly explored both H- and K-band indices simultaneously. Ghosh et al. (2019) (presented in Chapter 3) recently studied the comparative behaviour of these two bandheads from measured EWs ($EW_{CO(1.62)}$ for 6−3 bandhead at 1.62 μm and $EW_{CO(2.29)}$ for 2−0 bandhead at 2.29 μm) and found that both are very good temperature indicator above 3400 K and surface gravity. It was also seen that the dispersion of empirical correlations between ^{12}CO and T_{eff} significantly improved considering the effect of surface gravity.

Moreover, over the years, most studies focus to estimate fundamental parameters by computing EWs of the spectral features from their adopted feature and continuum bandpasses without considering the use of those definitions in general situations. A comparative studies of regularly used indices based on ^{12}CO(2−0) bandhead at 2.29 μm showed that some indices are more sensitive to spectral resolution, velocity dispersion, errors in wavelength calibration, curvature of the spectrum, and signal to noise (SNR) than other definitions (see Mármol-Queraltó et al. 2008; Pfuhl et al. 2011 for review).

Furthermore, due to broad water absorption features centred at 1.4 μm, 1.9 μm & 2.7 μm, the H and K-band spectra bend downward at the end and depress overall low-resolution continuum (Rayner et al., 2009). The water absorption is dominant in late-M type stars and is sensitive to the luminosity class. Its' strength decreases from supergiants through giants to dwarfs (Lançon et al., 2007). Several index definition are adopted to consider

the water absorption for evaluating the stellar parameters, such as T_{eff} for long period variables (Blum et al., 2003), spectral index of young brown dwarfs, field dwarfs, and giant (Allers et al., 2007), the strength of the water absorption in the H-band (Weights et al., 2009), ST of young objects (Scholz et al., 2012), T_{eff} and ST for dwarfs (Rojas-Ayala et al., 2012) and phase-dependent variation of the water index in the H-band of a Mira variable (Ghosh et al., 2018). Among all, the H_2O-K2 index, defined by Rojas-Ayala et al. (2012) for measuring the change in the curvature depending on the water absorption, is capable of precise characterisation of planet-hosting M dwarfs. However, the H_2O-K2 index have not been explored for fundamental parameters estimation of giants until now.

Over the years, lots of effort have been made to construct stellar libraries and to establish empirical correlations between the strength of previously defined spectral features and the main atmospheric parameters. Models provide the full information of stellar ST, $[M/H]$, and luminosity classes about the unknown samples within covered stellar atmospheric parameters space. Therefore, the usefulness relies on the complete sampling of stellar atmospheric parameters space at the appropriate spectral resolution and accurate, prior knowledge of the behaviour of the spectral features with stellar parameters. Unfortunately, in the present scenario, most of the available empirical libraries and empirical correlations built on the sample stars having limited coverage in stellar parameters space. In this context, theoretical model atmospheres are very useful, offering a large coverage of the parameter space and wavelength in spite of lacking integrity because of incomplete line lists and approximations in computations. The Phoenix (Allard et al., 1997; Hauschildt et al., 1999a,b) is one such theoretical model atmosphere, and the synthetic spectra from the Phoenix model grids can be employed to demonstrate the behaviour of spectral features. Additional details of the Phoenix model grids can be found in Chapter 2.

In the present study, we made an effort to find an optimal CO index for proper characterization of fundamental parameters in stellar population studies and to find how much systematic deviations among different empirical relations exist due to the different approaches for measuring atmospheric parameters. It remains unclear whether applying alternating indices (except EW) of ^{12}CO (2−0) are able to improve the correlations for both T_{eff} and log g. Could additional new index for ^{12}CO (6−3) bandhead similar to generic discontinuity and percentage absorption index as discussed previously [for ^{12}CO (2−0)] provide better correlations? How could the fundamental parameters be precisely estimated below 3400 K? The H_2O-K2 index are explored for precise estimation of fundamental parameters, especially for cool giants. Finally, we compare the behaviour of

indices with fundamental parameters in the observed sample with the synthetic spectra from the Phoenix theoretical model grids.

4.2 Observations and Data reductions

For this work, we assemble 107 K−M giants, which includes all 72 giants from the library introduced in Chapter 3 obtained with medium resolution ($\lambda/\Delta\lambda \sim 1200$) TIFR Near-Infrared Spectrometer and Imager (TIRSPEC, Ninan et al. 2014) on the 2.01 m Himalayan Chandra Telescope (HCT) located at Hanle, India and all 35 giants in that spectral range from archival spectral library observed with the medium-resolution ($\lambda/\Delta\lambda \sim 2000$) NIR spectrograph, SpeX, at the 3.0-m NASA Infrared Telescope Facility (IRTF, Rayner et al. 2009) on Mauna Kea, Hawaii. The log of observations and additional details of the observation can be found in Chapter 3. Our sample contains with giants of T_{eff} ranging from 2700 K to 5000 K, ST spanning over K0−M8, and surface gravity ($\log g$) < 3.5 cm/s^2 (see, Table 3.1 of Chapter 3). It is worthwhile to mention that our library provides about 60 per cent giants having ST M3 or beyond which allows us to characterize the late M-region precisely.

4.3 Spectroscopic diagnosis

The average spectral resolution of TIRSPEC data is, R $\sim$ 1200, whereas that of SpeX data is $\sim$ 2000. The SpeX spectra are degraded to the same spectral resolution as of TIRSPEC and the correction for zero velocity are made by shifting the spectral features before all the indices are evaluated. Additional details are mentioned in Chapter 2. The explored spectral indices for the present work are defined as follows.

4.3.1 Generic discontinuity index

The definition of generic discontinuity ($D_{generic}$) is adopted from Mármol-Queraltó et al. (2008) as

$$D_{generic} \equiv \frac{\frac{\sum_{i=1}^{n_c} \int_{\lambda_{c,i_1}}^{\lambda_{c,i_2}} F_{c,i}(\lambda)\ d\lambda}{\sum_{i=1}^{n_c} (\lambda_{c,i_2} - \lambda_{c,i_1})}}{\frac{\sum_{i=1}^{n_a} \int_{\lambda_{a,i_1}}^{\lambda_{a,i_2}} F_{a,i}(\lambda)\ d\lambda}{\sum_{i=1}^{n_a} (\lambda_{a,i_2} - \lambda_{a,i_1})}} \tag{4.1}$$

Here, n_c and n_a represent the continuum and feature bands, respectively. $F_{c,i}(\lambda)$ are the flux in the continuum bands from λ_{c,i_1} to λ_{c,i_2}, whereas $F_{a,i}(\lambda)$ are the flux in the feature bands from λ_{a,i_1} to λ_{a,i_2}. Mármol-Queraltó et al. (2008) proposed this generic discontinuity index to measure the ^{12}CO(2−0) feature at 2.29 μm, which is named here as D_{CO-K}. Similar to this generic discontinuity index, we introduce a new index (D_{CO-H}) to measure the ^{12}CO(6−3) feature at 1.62 μm. The continuum and feature bands for both of these indices are listed in Table 4.1.

4.3.2 Percent absorption index

To compute the absorption strength for the ^{12}CO(2−0) feature at 2.29 μm, Blum et al. (1996) introduced a new index which measures the percentage of flux in the feature band relative to a continuum band. The index is termed here I_{CO-K}, which is defined as

$$I_{CO-K} = (1 - \frac{F_{band}}{F_{continuum}}) \times 100 \tag{4.2}$$

where F_{band} and $F_{continuum}$ are the integrated flux in the feature and continuum band, respectively. We adopted their definition with slight modification of feature and continuum bands as the ^{12}CO(2−0) spectral feature is corrected for the zero velocity and centred at 2.2935 μm for all giants. Similar to Blum et al. (1996), we define a index (I_{CO-H}) to compute the absorption strength for the ^{12}CO(6−3) feature at 1.62 μm. However, we estimate the integrated flux in continuum band as an average of two different continua bands (both sides of the feature) for I_{CO-H} instead of one used in I_{CO-K} index. All of these bands are listed in Table 4.1.

4.3.3 H_2O-K2 index

The H_2O-K2 index is adopted from Rojas-Ayala et al. (2012), and it is written as.

Table 4.1: Definitions of Spectral Bands to measure spectroscopic indices.

Index	Feature	Feature Bandpass (μm)	Continuum Bandpass (μm)	Ref.
D_{CO-H}	^{12}CO(6−3) (1.62 μm)	1.6180−1.6205	1.6150−1.6175, 1.6260−1.6285	1
I_{CO-H}	^{12}CO(6−3) (1.62 μm)	1.6180−1.6205	1.6150−1.6175, 1.6260−1.6285	1
D_{CO-K}	^{12}CO(2−0) (2.29 μm)	2.2880−2.3010	2.2460−2.2550, 2.2710−2.2770	2
I_{CO-K}	^{12}CO(2−0) (2.29 μm)	2.2915−2.3065	2.2735−2.2885	1

Note.Ref : (1) *This work; (2) Mármol-Queraltó et al. (2008)*

$$H_2O - K2 = \frac{\langle F(2.070 - 2.090)\rangle / \langle F(2.235 - 2.255)\rangle}{\langle F(2.235 - 2.255)\rangle / \langle F(2.360 - 2.380)\rangle} \tag{4.3}$$

Where $\langle F(a-b)\rangle$ represents the median flux level in the wavelength range defined by a and b in μm. Rojas-Ayala et al. (2012) calculated this index for M and K-type dwarfs. Here the same index is explored to represent an overall change in the shape of the spectra for M-type giants due to water absorption from 2.07μm to 2.38μm.

4.4 Result And Discussion

4.4.1 CO-bands as spectral diagnostics for fundamental parameters

The strongest absorption bands for K−M giants is ^{12}CO(6−3) at 1.62 μm and ^{12}CO(2−0) at 2.29 μm in the H- and K-band, respectively. In this work, we computed the D_{CO-H}, I_{CO-H}, D_{CO-K} and I_{CO-K} as defined in the previous section for new empirical relations and relative comparison of effectiveness and efficiency between different indices to constrain fundamental parameters like T_{eff} and log g as shown in Figure 4.1, Figure 4.2, Figure 4.3 and Figure 4.4. The T_{eff} and log g of the sample giants are taken from the literature as mentioned in Table 3.1 of Chapter 3.

Correlation between effective temperature and index

In order to establish a relationship between the indices and T_{eff}, we explored a linear fit to the indices using the equation T_{eff} = a0 + a1 × Index (where, a0, a1 are the coefficients of the fit) after excluding limiting 2σ outliers. Two different cases are studied for the best-fit of all the indices. In the first case (Case I), all the one hundred seven giants in our sample are considered, and seventy giants of $T_{eff} \geq 3400$ are used for second case (Case

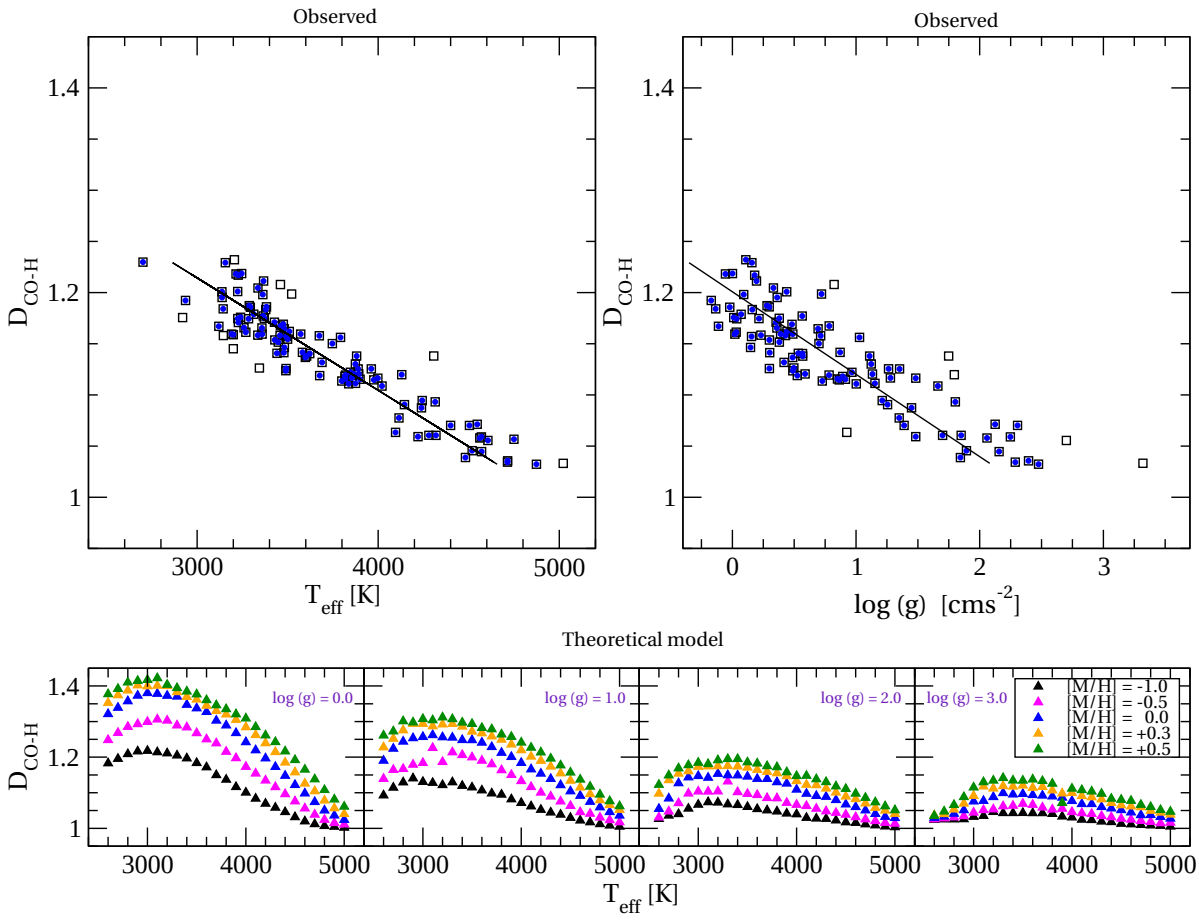

Figure 4.1: The top panels represent the correlation of the D_{CO-H} with T_{eff} (top left) and log g (top right) for observed sample. The square represents all the stars of our sample (107 giants). The blue dot represents the stars from our sample used for empirical relation. The solid line shows our best-fit relation. The bottom panels (from left to right) show the behaviour of D_{CO-H} with T_{eff} for different log g qualitatively for BT-NextGen Phoenix synthetic model spectra, while each bottom panel represents the behaviour of D_{CO-H} with T_{eff} for different $[M/H]$.

II). The indices are compared quantitatively on the basis of three fitting parameters – correlation coefficient(R), the coefficient of determination (Rsqr) and the standard error of estimate (SEE). All the fitting parameters, as well as coefficients of the fits, are listed in Table 4.2. It is to note that a better-correlation is obtained with improving SEE from Case I to Case II for all the indices when we narrow down the temperature range (i.e., sample giants with $T_{eff} \geq 3400$ K). A comparative study between all the indices shows that the correlation between I_{CO-K} and T_{eff} provides the best correlation for both cases with smallest residual scatter (SEE) among those being established in this chapter as well as in Chapter 3. One should keep in mind that I_{CO-K} have been computed according to the recipe of Blum et al. (1996) by adjusting the continuum and feature bands. Moreover, feature and continuum bands play a significant role to estimate the indices value, hence the residual scatter of fitted relations (see, e.g., Ivanov et al. 2004; Schultheis et al. 2016).

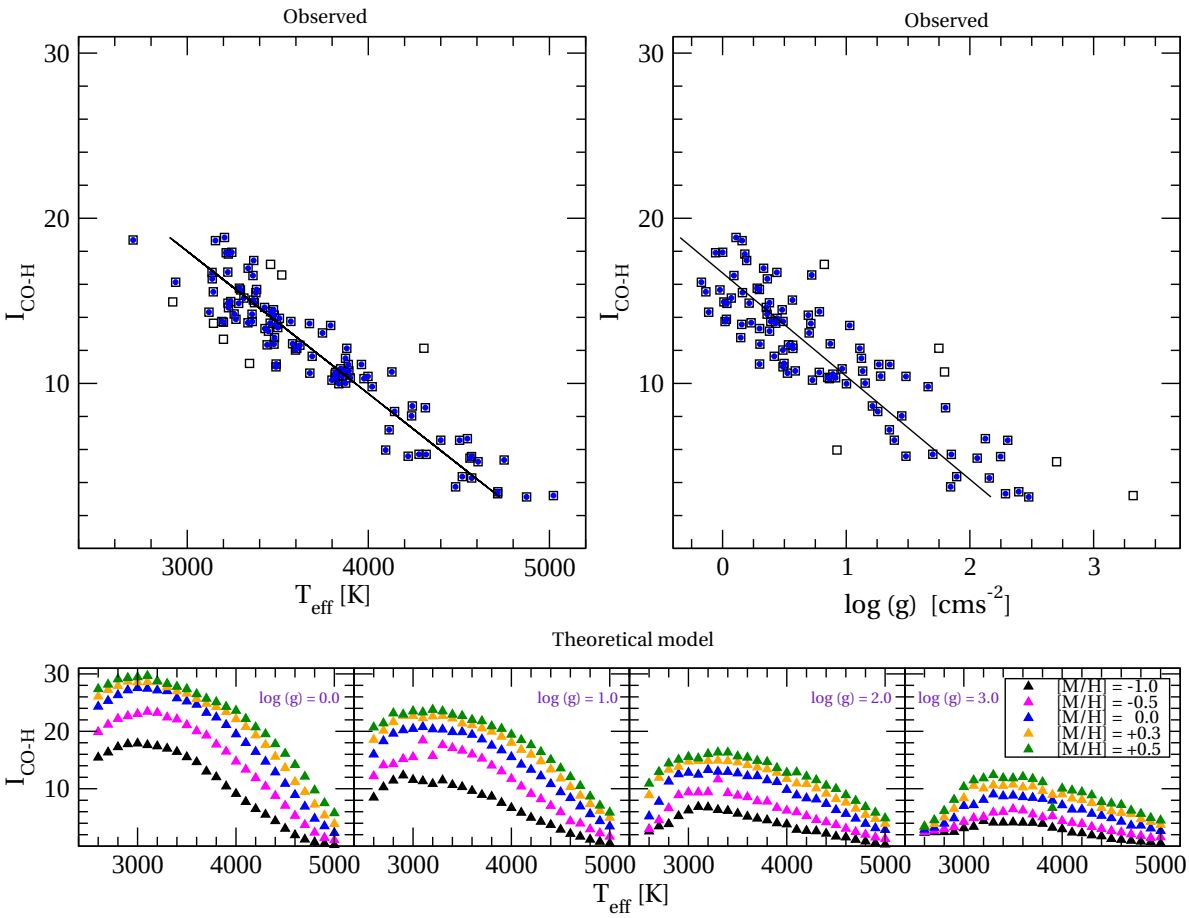

Figure 4.2: Same as Figure 4.1 but for I_{CO-H}.

However, the SEE of $I_{CO-K} - T_{eff}$ correlations is comparable with the rms scatter of Schultheis et al. (2016). It is important to note that I_{CO-K} index is insensitive to spectral resolution and metallicity within the range, $-1.2 <$ [Fe/H] $< +0.5$, as seen in Schultheis et al. (2016).

Correlation between surface gravity and index

The empirical relations between indices and log g have been achieved by fitting the equation, log $g = a_0 + a_1 \times$ Index, using 97 giants of available log g in the literature among 107 sample stars. We excluded the limiting 2σ outliers for fitting. The results of fitting are listed in Table 4.2. The best-fit is decided on the basis of SEE and the smallest SEE is obtained in the case of I_{CO-K}. Moreover, we found that the other obtained relations in this chapter as well as in Chapter 3 also provide comparable SEE values. Therefore, our conclusion is that any of the indices could be used reliably as a proxy of log g.

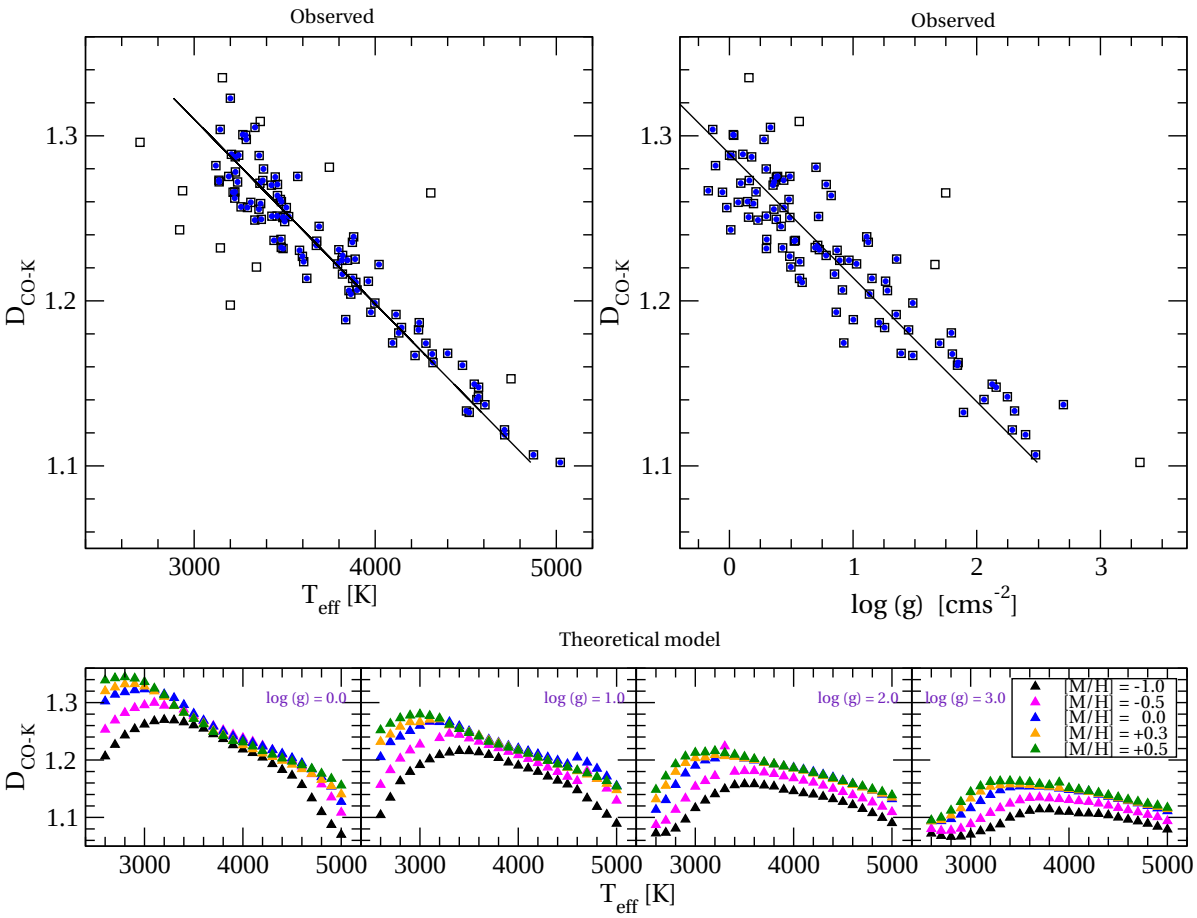

Figure 4.3: Same as Figure 4.1 but for D_{CO-K}.

Effect of surface Gravity on effective temperature vs index correlation

In Chapter 3, we found that the SEE of the correlation improved appreciably considering log g in the T_{eff}−Index correlation. Here, we investigate how much-improved relation could be obtained for other CO index. Therefore, we recalibrate the empirical relations to investigate the dependency of T_{eff}−Index correlations on log g using the linear equation T_{eff}=a0 + a1 × Index + a2 × log g (where a0, a1 and a2 are the coefficients of the fit) excluding 2σ outliers. The coefficients of fit are listed in Table 4.2 along with SEE. We found the improved correlation with respect to the SEE as observed in Chapter 3, when the log g is considered in the T_{eff}−Index correlation as shown in Figure 4.5. Therefore, we validate the improvement of empirical correlations between CO indices and T_{eff} taking account of log g. The smallest SEE is obtained in case of $EW_{CO(1.62)}$ among all established relations in this chapter as well as in Chapter 3 considering log g in T_{eff}−Index correlation, however, we see that other CO index definitions in H- and K-band also are efficient to provide a correlation with a SEE less than 100 K except D_{CO-K} as shown in Table 4.3. Therefore, any of them could be used to estimate T_{eff}

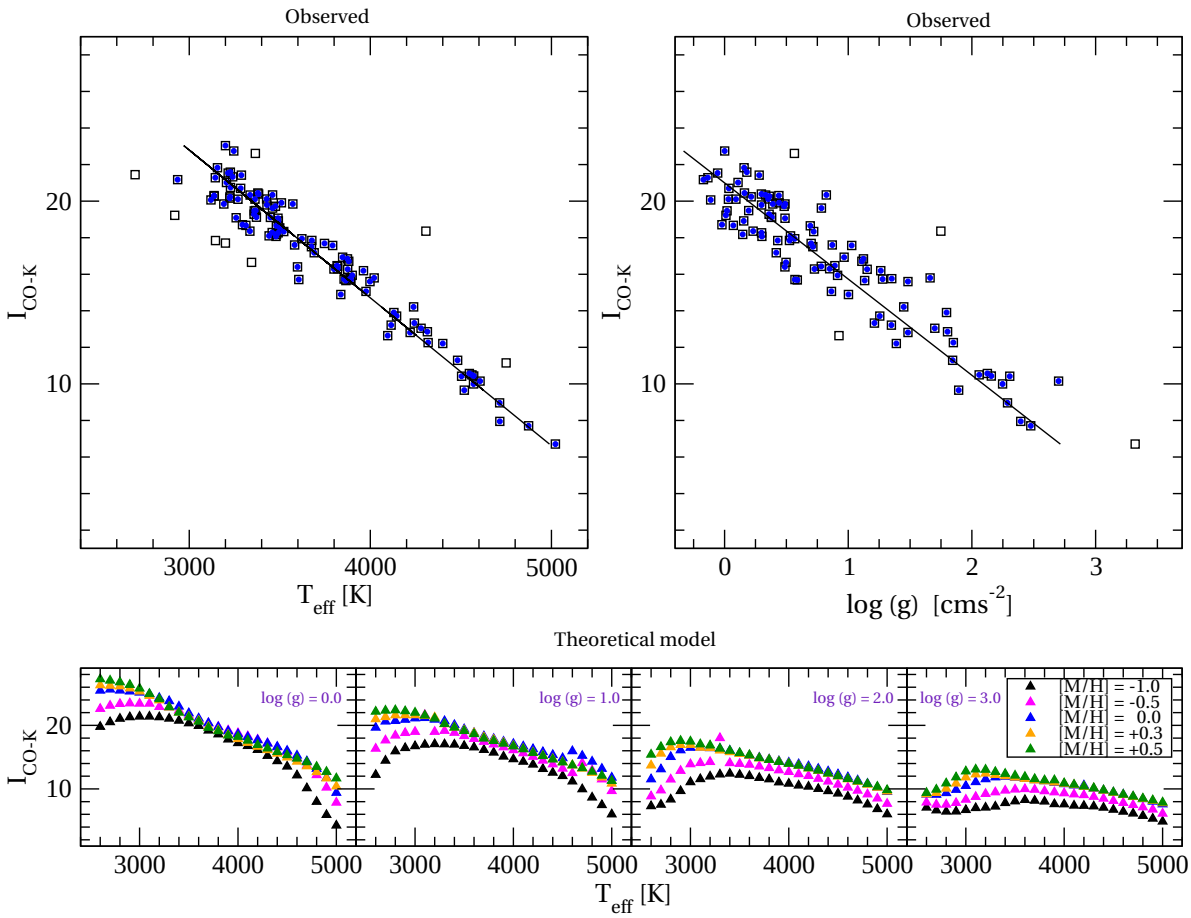

Figure 4.4: Same as Figure 4.1 but for I_{CO-K}.

with a typical accuracy below 100 K, however one can prefer percent absorption index (I_{CO-H} and I_{CO-K}) because of its simplest measurement technique.

We compare the obtained T_{eff} from four new empirical calibrations with the previously published values of T_{eff} following the similar method as described in Chapter 3. However, we found no significant difference between all empirical relations for measuring T_{eff} as shown in Figure 4.6. The transformation equation between various H- and K-band indices in our study are given in Table 4.4.

4.4.2 Validation of the derived empirical relations

To investigate the reliability of our established correlations we applied our empirical relation to determine log g and T_{eff} by estimating CO indices using all the spectra (25) of K−M giants from TNG spectral library (Mármol-Queraltó et al., 2008) and compared the evaluated parameters with the literature values[1] as well as with those derived in Chapter

[1]https://webs.ucm.es/info/Astrof/ellipt/CO.html

Table 4.2: Comparison between goodness of fit for various correlations.

Index	T	N	R	Rsqr	SEE	a0†	a1†	a2†	Remarks*
					T_{eff}	= f(Index) :			
D_{CO-H}	107	98	0.94	0.89	161	14054 ± 375	−9103 ± 330	-	1
	70	66	0.94	0.89	141	14888 ± 477	−9838 ± 429	-	2
I_{CO-H}	107	100	0.95	0.90	159	5088 ± 49	−116 ± 4	-	1
	70	64	0.95	0.90	132	5103 ± 52	−116 ± 5	-	2
D_{CO-K}	107	96	0.96	0.92	133	14711 ± 329	−8940 ± 268	-	1
	70	67	0.96	0.93	116	14882 ± 384	−9071 ± 318	-	2
I_{CO-K}	107	99	0.97	0.95	110	5891 ± 51	−124 ± 3	-	1
	70	67	0.98	0.96	85	5774 ± 47	−119 ± 3	-	2
					log g	= f(Index) :			
D_{CO-H}	97	91	0.89	0.78	0.32	14.83 ± 0.78	−12.35 ± 0.69	-	1
I_{CO-H}	97	91	0.89	0.80	0.31	2.67 ± 0.10	−0.16 ± 0.01	-	1
D_{CO-K}	97	92	0.92	0.84	0.28	17.17 ± 0.75	−13.32 ± 0.61	-	1
I_{CO-K}	97	93	0.93	0.87	0.26	3.99 ± 0.13	−0.19 ± 0.01	-	1
					T_{eff}	= f(Index, log g) :			
D_{CO-H}	97	93	0.98	0.96	95	7660 ± 447	−3737 ± 376	386 ± 26	1
I_{CO-H}	97	91	0.98	0.97	88	4041 ± 76	−52 ± 5	358 ± 25	1
D_{CO-K}	97	92	0.97	0.95	106	7908 ± 658	−3653 ± 513	372 ± 35	1
I_{CO-K}	97	92	0.98	0.97	85	4780 ± 133	−75 ± 6	257 ± 32	1

Notes. T - total nos. of data points; N - no. of points used for fitting after eliminating 2σ outliers; R - correlation coefficient; Rsqr - coefficient of determination; SEE - standard error of estimate.
† T_{eff} = a0 + a1 × Index + a2 × log g.
*1 - Fitting with all the sample stars.
*2 - Fitting with sample stars; $T_{eff} \geq 3400$.

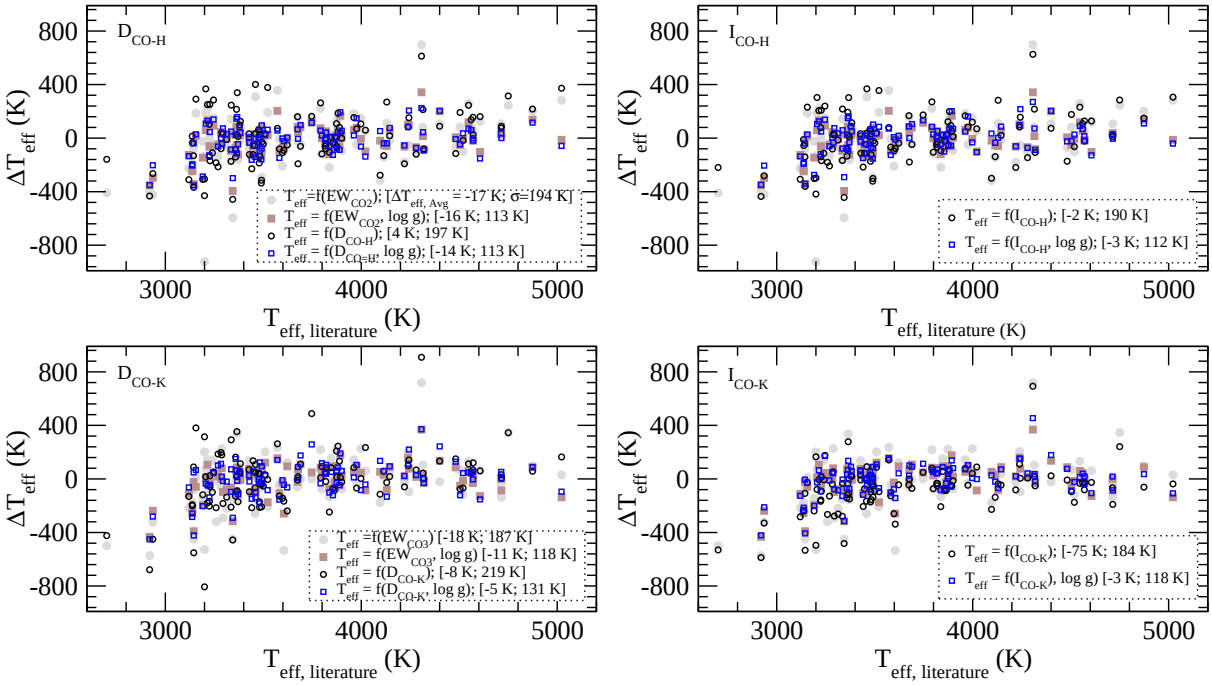

Figure 4.5: Comparison of T_{eff} given in the Table 1 of Chapter 3 and those derived from various correlations. Here, we consider only those giants (97 out of 107), which have known log g value. It is found that the SEE of the fit improved when log g is considered. Figure also shows the comparison between different indices.

Table 4.3: Comparison between different indices.

Indices	SEE				Remarks
	T_{eff} = *f*(Index)		log g = *f*(Index)	T_{eff} = *f*(Index, log g)	
	Case I	Case II			
$EW_{CO(1.62)}$	140	124	0.29	78	Chapter 3
D_{CO-H}	161	141	0.32	95	This work
I_{CO-H}	159	132	0.31	88	This work
$EW_{CO(2.29)}$	130	104	0.29	90	Chapter 3
D_{CO-K}	133	116	0.28	106	This work
I_{CO-K}	110	85	0.26	85	This work

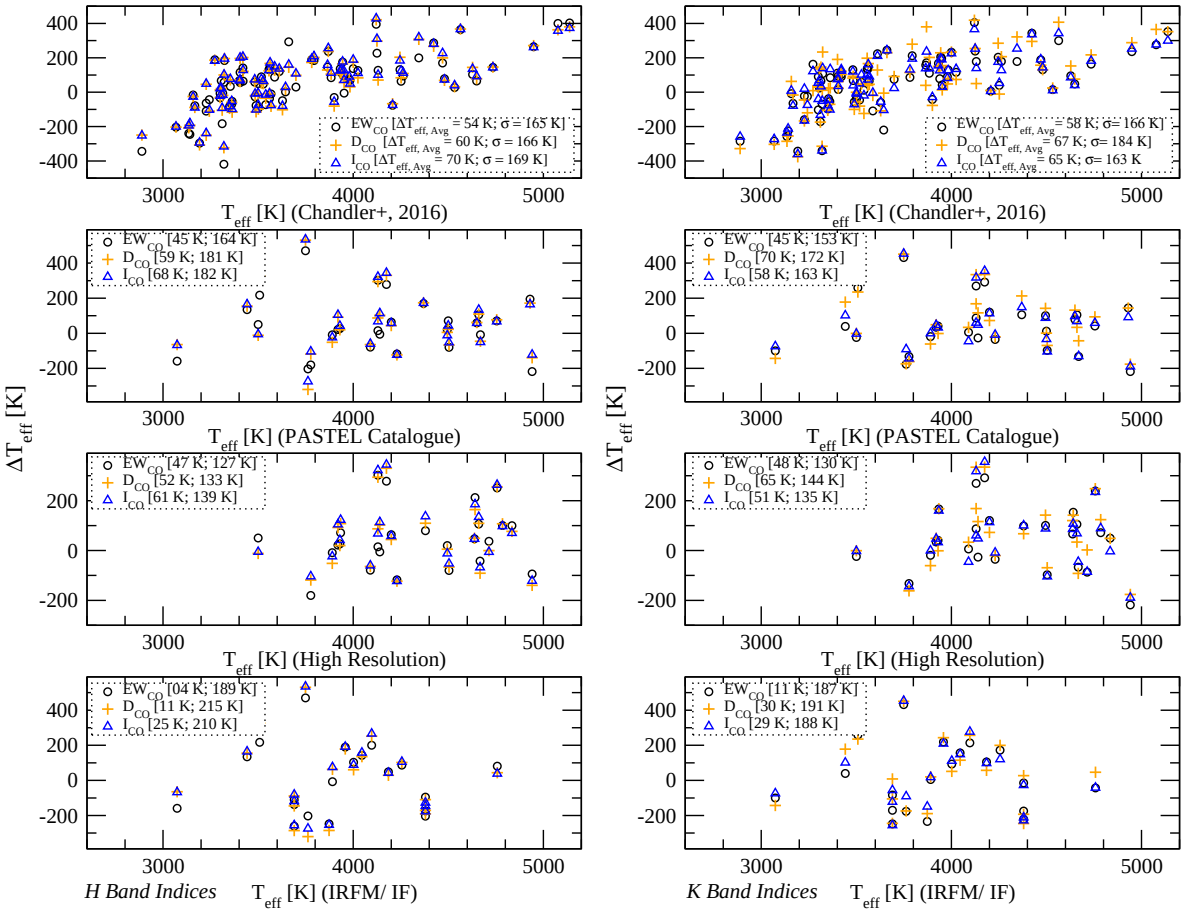

Figure 4.6: Comparison of T_{eff} estimated from previous studies and those derived from our T_{eff} – CO index – log g relation. We provide the comparison for both H-band (left panel) and K-band(right panel) indices. The residuals are plotted in the figure.

3. Additional details about TNG spectral library can be found in Chapter 2. First we measured the log g using both indices (D_{CO-K} and I_{CO-K}). The average difference and standard deviation of log g from the literature are $\Delta \log g_{Avg} = 0.12\ cm/s^2$ and $\sigma = 0.51\ cm/s^2$, $\Delta \log g_{Avg} = 0.19\ cm/s^2$ and $\sigma = 0.52\ cm/s^2$ for D_{CO-K} and I_{CO-K}, respectively. The T_{eff} are estimated using the measured log g and indices. The T_{eff} are on average

Table 4.4: Transformation equations between different CO band strength definitions

Equation	R	R_{sqr}	SEE
$D_{CO-H} = (0.999 \pm 0.005) + (0.029 \pm 0.001)\mathrm{EW}_{CO(1.62)}$	0.95	0.90	0.016
$I_{CO-H} = (0.883 \pm 0.351) + (2.317 \pm 0.070)\mathrm{EW}_{CO(1.62)}$	0.96	0.91	1.181
$D_{CO-H} = (0.987 \pm 0.001) + (0.013 \pm 0.001)I_{CO-H}$	0.99	0.99	0.003
$D_{CO-K} = (1.035 \pm 0.008) + (0.011 \pm 0.001)\mathrm{EW}_{CO(2.29)}$	0.92	0.84	0.020
$I_{CO-K} = (2.110 \pm 0.386) + (0.810 \pm 0.020)\mathrm{EW}_{CO(2.29)}$	0.97	0.94	0.933
$D_{CO-K} = (1.003 \pm 0.006) + (0.013 \pm 0.001)I_{CO-K}$	0.97	0.94	0.013

139 K and 111 K hotter than literature value with a standard deviation, $\sigma = 207$ K and 182 K for D_{CO-K} and I_{CO-K}, respectively. However, the log g derived using various correlations in this chapter as well as in Chapter 3 are provides similar deviation, whereas T_{eff} derived using I_{CO-K} based correlations provides smaller deviation. Comparison of derived parameters using different indices are shown in Figure 4.7.

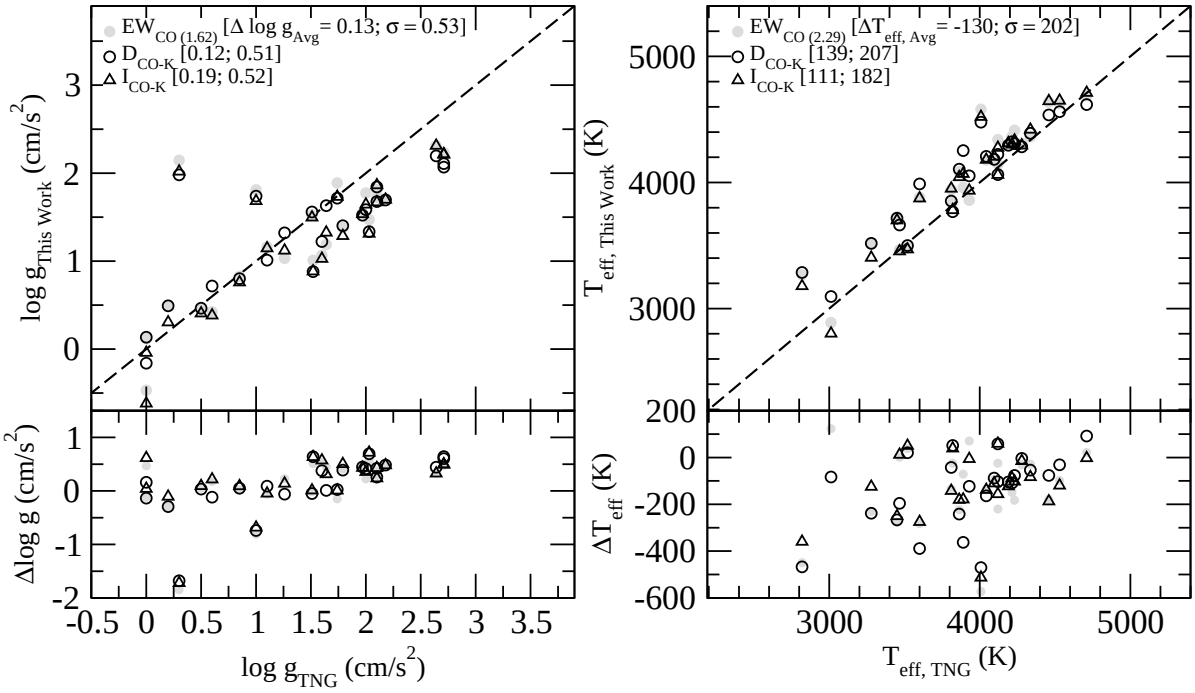

Figure 4.7: Comparison of log g and T_{eff} derived by Mármol-Queraltó et al. (2008) and those derive from our calibrations using TNG spectra. The residuals are plotted at the bottom panel.

4.4.3 H_2O-K2 index as spectral diagnostics for the effective temperature and spectral type for cool giants ($T_{eff} \leq 3600$ K)

In the previous section, we see that various CO definitions able to produce reliable correlation for precise estimation of T_{eff} either when $T_{eff} \geq 3400$ K or when the contribution of log g has been taken into account. Here we made an additional effort to inspect the possibility of finding an index that could evaluate fundamental parameters more accurately than all CO definitions at $T_{eff} < 3600$ K. To carry out this task, we study the H_2O-K2 index as an indicator of T_{eff} and ST for the giant stars following Rojas-Ayala et al. (2012). The authors used this index for characterization of dwarfs, and here we are attempting for cool giants. Figure 4.8 shows that the strength of water absorption increases (value of H_2O-K2 index decreases) with (V−K) colour index. For earlier M-giants water absorption strengths are small, whereas below $T_{eff} < 3600$ K (V−K > 4.5) strengths considerably increase and behave linearly with T_{eff}. Therefore, to establish the calibrating relation between H_2O-K2 index and T_{eff}, we consider the sample stars with $T_{eff} \leq 3600$ K.

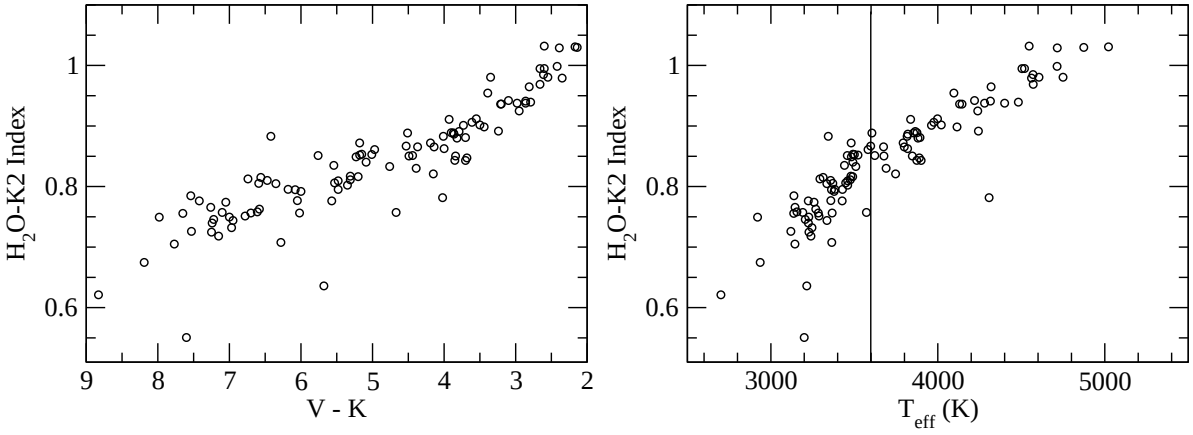

Figure 4.8: Figure represents the behaviour of H_2O-K2 index with V–K colour index (left) and T_{eff} (right) for all the 107 giants.

We have 57 giants having $T_{eff} \leq 3600$ K in our sample. 4 out of 57 stars are excluded due to limiting 2σ outliers and remaining stars are used to calibrate the H_2O-K2 index as a proxy for T_{eff}. To establish the correlation, we performed linear least square regression between H_2O-K2 indices and T_{eff} using the equation 4.4, which provides a correlation with SEE 88 K. The correlated relation of H_2O-K2 with T_{eff} and residuals of fit are shown in Figure 4.9. Therefore, from spectral calibration of H_2O-K2 index, the T_{eff} of

cool ($T_{eff} < 3600$ K) M giants could be predicted with a typical accuracy of 88 K.

$$\begin{aligned} T_{eff} &= a + b \times (H_2O - K2) \\ a &= 1731 \pm 180 \\ b &= 2047 \pm 229 \\ SEE\ (T_{eff}) &= 88K \end{aligned} \tag{4.4}$$

To investigate H_2O-K2 index behaviour with ST, the same sample for calibrating T_{eff} are considered here. To establish the correlation, we performed a linear least square regression between H_2O-K2 index and ST using the equation 4.5. We excluded here four giants due to limiting 2σ outliers and remaining 53 stars are adopted to calibrate H_2O-K2 index as a proxy for ST with SEE 1.06 as shown in Figure 4.9. Therefore, we can predict the ST from such correlation with a typical accuracy of 1 subtype for cool M giants.

$$\begin{aligned} ST &= a + b \times (H_2O - K2) \\ a &= 20.256 \pm 2.197 \\ b &= -19.905 \pm 2.799 \\ SEE\ (ST) &= 1.060K \end{aligned} \tag{4.5}$$

The H_2O-K2 index provides us with a good correlation with T_{eff} and ST in the limited range $T_{eff} \leq 3600$ K for cool giants. The metallicity dependence on H_2O-K2 index is beyond the scope of this chapter from such low-resolution spectra. Further investigation is also required to understand the behaviour of H_2O-K2 index properly for late-type giants. It is known that many M-stars are variable, and variability plays a significant role in water absorption. The measurement of fundamental parameters from the H_2O-K2 should be regarded with caution in case of long period variable like Mira, where the atmosphere changes with pulsational cycle (e.g., Ghosh et al. 2018), because pulsating stars have stronger water absorption than static giants with the same effective temperature (e.g., Bessell et al. 1989; Alvarez & Plez 1998), and Mira variable with very similar optical spectra can have very different near-infrared spectra (Lançon & Wood, 2000).

4.4.4 Theoretical models predictions of spectral indices

We explore the behaviour of atomic or molecular features of the cool giants in NIR H- and K-band with T_{eff}, log g and $[M/H]$ qualitatively using BT-NextGen synthetic model

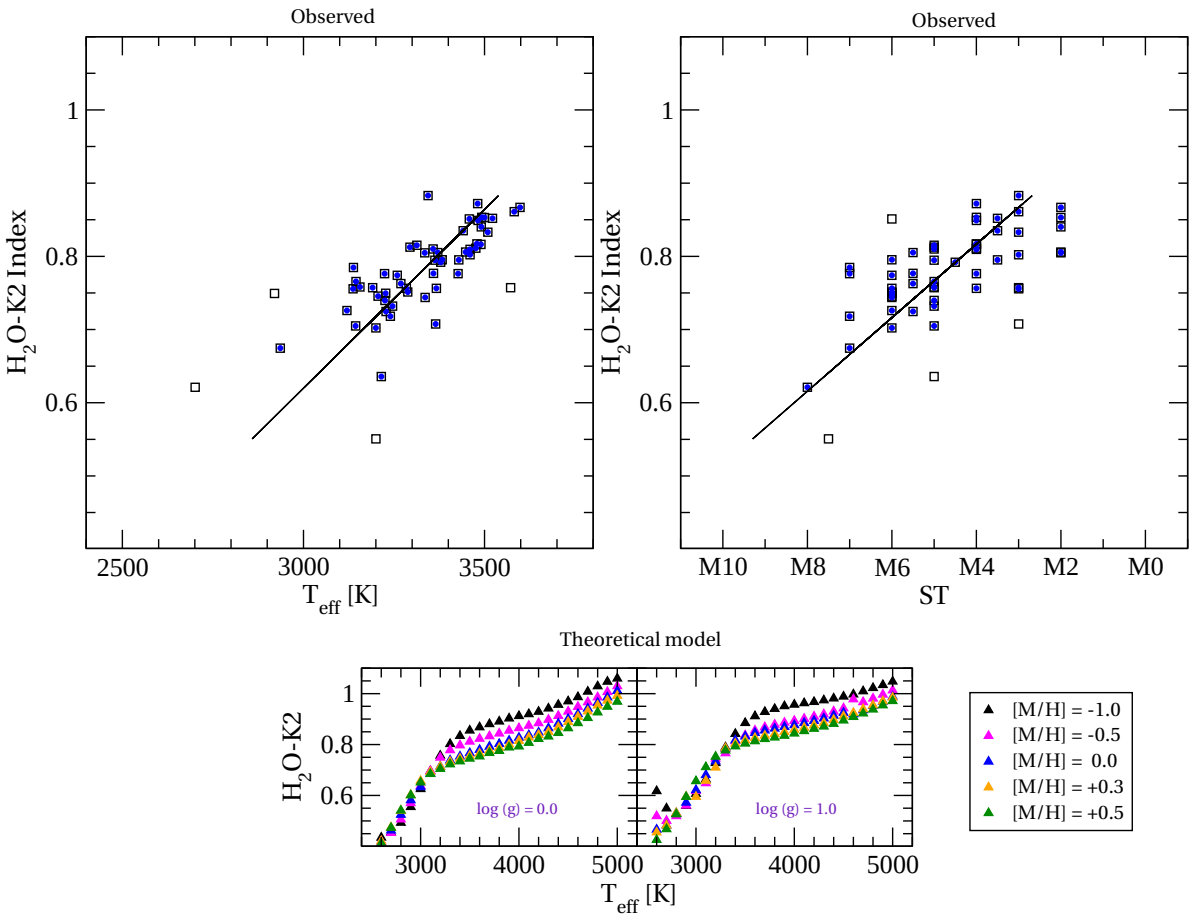

Figure 4.9: The top panels represent the correlation of the H_2O−K2 index with T_{eff} (top left) and ST (top right) for the observed sample. The square represents all the stars of our sample (107 giants). The blue dot represents the stars from our sample used for empirical relation. The solid line shows our best-fit relation. The bottom panels (from left to right) show the behaviour of D_{CO-H} with T_{eff} for different log g qualitatively for BT-NextGen Phoenix synthetic model spectra, while each bottom panel represents the behaviour of D_{CO-H} with T_{eff} for different $[M/H]$. The behaviour of the synthetic model is provides for log g = 0.0 and log g = 1.0, as the log g of our explored giants at $T_{eff} \leq 3600$ K lies in between 0.0 to 1.0.

spectra (Allard et al., 2012). Additional details about the model can be found in Chapter 2. For this study, we adopt the model grids ranging from 2600 to 5000 K, 0.0 to 3.0 and −1.0 to +0.5 in the respective parameter space. The synthetic spectrum is convolved with a Gaussian to degrade the spectral resolution as TIRSPEC spectral resolution (R ∼ 1200).

The behaviour of all the indices (representing the band strength of ^{12}CO at 1.62 and 2.29 μm) with T_{eff} are demonstrated in Figure 4.1, Figure 4.2, Figure 4.3 and Figure 4.4 for various $[M/H]$ as well as log g. For all log g and $[M/H]$ models, the indices increases as temperature decreases, peak at a certain temperature, and then begins to decrease below that temperature. The peak of the H-band indices arises at around 3200 K for all models. However, for K-band, the peak of the indices occur at a certain temperature depending

on $[M/H]$ and log g. It is noted that the peak shifts towards warm temperature with decreasing $[M/H]$ and increasing log g. Furthermore, all the indices decreases as $[M/H]$ decreases for sub-solar synthetic models. However, K-band indices appear insensitive to the $[M/H]$ for solar and super-solar models, whereas H-band indices are appreciably influenced by $[M/H]$ even in solar and super-solar models and increases with $[M/H]$. Further, all the indices increase with decreasing log g. It should be noted that the H-band indices show more pronounced variation with $[M/H]$ and log g than K-band indices, which agree with Origlia et al. (1993). However, no such conclusive evidence is found from the observational data. We only see that both H- and K-band indices provide the log g with similar dispersion. The variations of the indices (hence, ^{12}CO bands strength) and the contrasting behaviour in H- and K-band can be explained by the effect of CO column density, microturbulent velocity and pressure dependence of the H^- abundance on CO band strength (see, Origlia et al. 1993). These might be the reasons for improved correlation of all the indices from Case I to Case II of observed samples. It is also important to mention that the model overestimates the strengths of H-band indices in comparison to the observed sample.

The behaviour of H_2O-K2 index with T_{eff} for different $[M/H]$ and log g is shown in Figure 4.9. Tha behaviour of the index with T_{eff} almost imitate the observation as shown in Figure 4.8. It is worth to note that within specific temperature range H_2O-K2 index varies linearly with T_{eff}, and in this linear region, H_2O-K2 index appears insensitive to $[M/H]$. The H_2O-K2 index begins to saturate afterwards. Furthermore, H_2O-K2 index shows negligible sensitivity with gravity for log $g = 0.0$ to log $g = 1.0$. Therefore, according to the model grids, the H_2O-K2 index varies almost linearly with T_{eff} <3600 K for $0.0 \leq \log g \leq 1.0$ and also, upto this T_{eff} the index seems independent of both $[M/H]$ and log g. Here, we restrict our discussion only on models with log g equal to 0.0 and 1.0 as the log g of our explored giants that show considerable water absorption at $T_{eff} \leq 3600$ K lies in between 0.0 to 1.0.

4.5 Summary and Conclusions

We study different K-band CO indices for ^{12}CO (2−0) available in the literature to evaluate the T_{eff} and the log g. We also define *new H-band CO indices* for ^{12}CO (6−3) similar to K-band indices, and compare quantitively all the H- and K-band indices for finding the optimal index. We investigate the effectiveness of H_2O-K2 index for measuring fundamental parameters in case of cool giants. Furthermore, the behaviour of all the indices

with fundamental parameters for the observed samples is compared with the behaviour of BT-NextGen Phoenix theoretical model grids. The main results are as follows.

1. The H- and K-band ^{12}CO bandheads indices provide new reliable empirical relations with T_{eff}, and they are reasonably good temperature indicator above 3400 K. Among them the percent absorption index in K-band provides the best result.

2. We obtained new empirical calibrations between log g and CO indices. We found that all the CO indices are very good log g indicator and any of them could be used for log g estimation.

3. We studied the dependency of log g in effective temperature−index correlation and showed that empirical relations become more reliable on the inclusion of log g. We obtained the smallest dispersion in case of equivalent width versus effective temperature correlation for ^{12}CO bandheads at 1.62 μm. However, we noticed that all other CO indices are efficient to provide a reliable correlation with a typical accuracy below 100 K when we consider the log g contribution. The effect of metallicity in effective temperature−index correlation is out of the scope of this chapter. Further investigations would be highly appreciable especially for metal-poor stars.

4. We implemented a water index, which was originally applied for dwarf stars, as an effective temperature and spectral type indicator for cool giants. We showed that this index tightly correlated with the effective temperature below 3600 K ($V - K > 4.5$) and spectral type later than M4, and could be used to characterize reliably in later M spectral region. However, for large amplitude AGB variables like Mira variable, the water index may not be appropriate to evaluate fundamental parameters in the presence of cycle to cycle variable atmosphere.

5. The predicted behaviours of CO indices with effective temperature and surface gravity from the theoretical model grids are consistent with the observations. However, we are unable to study the behaviour of metallicity for our observed sample because of the small metallicity range of our solar-neighbourhood bright giants. The additional information could be noted from the theoretical models − the peak of the indices occur at a certain temperature and decreases both sides of it, the H-band CO indices show more pronounced variation with surface gravity and metallicity than the K-band indices that might be due to the effect of CO column density, microturbulent velocity and pressure dependence of the H^- abundance on CO band strength. However, established correlations between surface gravity and index did not show more dependence of surface gravity on H-band indices than K-band rather produce

almost similar dispersion. The water index behaves quite similarly with observed one and shows linear variation with the effective temperature below 3600 K and surface gravity below 1.0. Furthermore, we see that water index seems independent of both surface gravity and metallicity up to 3600 K. Therefore, we conclude that water index versus effective temperature correlation is free from the effect of the surface gravity and the metallicity.

Chapter 5

Characterisation of a new Oxygen-rich Mira variable

This chapter is based on the paper Ghosh et al. (2018).

Title: Phase-dependent Photometric and Spectroscopic Characterisation of the MASTER-Net Optical Transient J212444.87+321738.3: An Oxygen-rich Mira
Authors: **Supriyo Ghosh**, S. Mondal, R. K. Das, D. P. K. Banerjee, F. J. Hambsch and S. Dutta
Year : 2018
Journal: The Astronomical Journal, 155, 216

In this chapter, we have studied an object, which was discovered in 2013 as MASTER-net Optical Transient J212444.87+321738.3 (hereafter, J2124+32) towards the Cygnus constellation. We present the results of long-term optical/NIR photometric and spectroscopic observations to characterise the object. Our study confirmed that the object is an O-rich Mira variable. From best-fit light curve, we determine the period of the object and study the wavelength dependent variability. We construct SED from NIR to far-IR data and evaluate dust temperature, optical depth and mass-loss rate. A rare study of time-dependent variation of optical/NIR atomic and molecular features (e.g., TiO, NaI, Ca I, H_2O and CO bands), as commonly observed in Mira variables, is also presented in this chapter.

5.1 Introduction

The object J2124+32 (RA= 21h 24m 44.87s , Dec =+32d 17m 38.3s) was first detected from Mobile Astronomical System of TElescope Robots (MASTER) Optical Transient (OT) alert on 2013 March 13 with 10.7 mag at unfiltered CCD (Tiurina et al., 2013). The MASTER Global Robotic Net[1] consists of several identical observing instruments at different observatories (e.g., MASTER-Amur, MASTER-Tunka, MASTER-SAAO) that provide very fast sky-survey (128 deg^2 per hour) with limiting magnitude 19−20 (Lipunov et al., 2016, 2017). The primary goals of the MASTER-net are to observe gamma-ray bursts (GRB) in alert mode. However, it discovers many OTs in the survey mode. The other identifications of the object (J2124+32) is USNO-B1.0 1222-0647260 (B1=18.78, R1=14.96, B2=20.88, R2=16.32, I=13.14), 2MASS 21244500+3217377 (J=7.82 ± -0.03, H=5.97 ± -0.02, K=4.82 ± -0.02) and WISE J212444.98+321737.73.440 (W1=3.44 ± -0.13, W2=2.21 ± -0.10, W3=-0.43 ± -0.03, W4=-1.28 ± -0.01) (Tiurina et al., 2013). The colour-combined (BRIR) finder chart is shown in Figure 5.1.

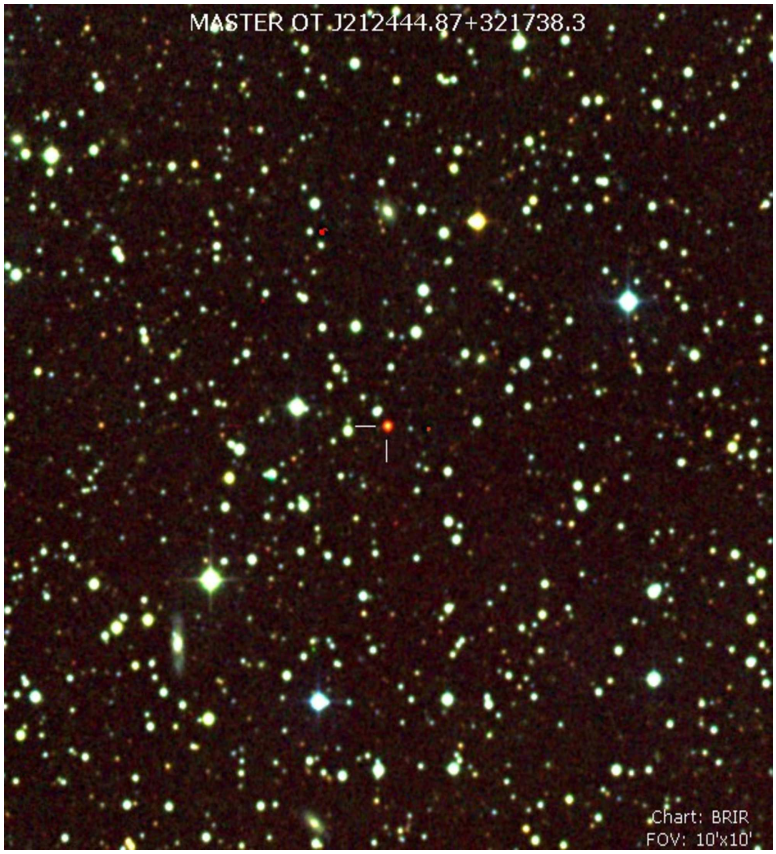

Figure 5.1: colour-combined (BRIR) finder chart of the object.
Source of Image : Tiurina et al. (2013)

[1] http://observ.pereplet.ru/

Mira variables are in the AGB phase, which is the late evolutionary stage of low-to-intermediate mass stars before becoming into planetary nebulae. They are long-period (100−1000 days) pulsating variable with a large visible amplitude of more than 2.5 mag, and generally surrounded by circumstellar matter from huge mass loss rates of $\sim 10^{-8} - 10^{-4}\ M_{\odot}\ yr^{-1}$ (Jura & Kleinmann, 1990; Habing, 1996; Mattei, 1997; Herwig, 2005). Mira variables have a low effective temperature (< 3500 K), cool extended atmospheres (radius up to few $100R_{\odot}$), and luminosity can reach up to a few $10^3 L_{\odot}$ (Mattei, 1997). The high mass loss and a relatively low surface temperature of these evolved stars provide a habitable zone for several molecules such as TiO, VO, H_2O, and CO in their extended atmospheres. These molecules play important roles in the spectral appearance of Mira variable stars at visual and NIR wavelengths (Lançon & Wood, 2000; Gautschy-Loidl et al., 2004; Aringer et al., 2009a; Nowotny et al., 2010).

Spectroscopic studies are extremely valuables to understand pulsating atmospheres and mass loss of Mira variables throughout the outer layer (Hinkle et al., 1982; Alvarez et al., 2000; Castelaz & Luttermoser, 1997; Castelaz et al., 2000; Lançon & Wood, 2000; Tej et al., 2003b). Because of the pulsation and stellar wind, the atmosphere of stars in the AGB phase deviates from hydrostatic equilibrium and show local variations. Phase-dependent spectroscopic studies are very efficient to probe the atmosphere of the stars, and such studies are limited in the literature. From phase-dependent spectroscopy of a Mira variable, o Ceti, Joy (1926) found the variation of temperature and TiO band with the magnitude and appearance of hydrogen emission line with maximum intensity at or shortly after maximum visual brightness. From radial velocity, excitation temperatures and lines broadening measurements using high-resolution spectroscopy, it is evident that two separate line forming regions of the atmosphere sometimes contribute towards the spectrum of H_2O (except maximum light), CO ($\Delta\nu = 2$), and OH (Hinkle, 1978; Hinkle & Barnes, 1979a; Nowotny et al., 2010). More complex stratification may also exist (e.g., Tej et al. 2003a; Tsuji 2009).

5.2 Observations and Data Reduction of J2124+32

Following the OT announcement, we have started spectro-photometric monitoring observations on the object in optical/NIR wavelength since 2013 March 20. Optical imaging observations were performed using a front-illuminated 4K × 4K CCD camera on the 40 cm $f/6.8$ Optimized Dall Kirkham (ODK) telescope at the private observatory ROAD (Remote Observatory Atacama Desert) in Chile (Hambsch, 2012). The source was monitored in optical I-band and unfiltered CCD (400−900 nm) filter-band (Clear, C) over

Table 5.1: Log of photometric and spectroscopic observations

Date of Observation	Observation Type	Spectral Band	Int. Time (s)	No of Frames	Telescope	Remarks
2013-Mar-20	Photometry	$J/H/K$	0.4/0.2/0.2	5* [21/21/21]	1.2m Mt. Abu	clear sky
2013-Mar-22	Photometry	$J/H/K$	0.5/0.4/0.2	5* [11/11/21]	1.2m Mt. Abu	clear sky
2013-Apr-28	Photometry	$J/H/K$	2/1/0.3	5* [15/15/25]	1.2m Mt. Abu	clear sky
2013-Apr-29	Photometry	$J/H/K$	0.5/0.5/0.2	5* [31/31/31]	1.2m Mt. Abu	clear sky
2013-May-27	Photometry	$J/H/K$	0.3/0.7/1	5* [15/15/35]	1.2m Mt. Abu	clear sky
2013-May-28	Photometry	$J/H/K$	1/1/0.3	5* [21/21/35]	1.2m Mt. Abu	clear sky
2013-May-30	Photometry	$J/H/K$	0.3/0.5/1	5* [15/15/15]	1.2m Mt. Abu	clear sky
2013-Jun-20	Photometry	$J/H/K$	0.3/0.5/1	5* [15/15/15]	1.2m Mt. Abu	clear sky
2013-Oct-30	Photometry	$J/H/K$	0.3/0.5/1	5* [15/15/15]	1.2m Mt. Abu	clear sky
2015-May-08	Photometry	$J/H/K$	0.3/0.5/1	5* [15/15/15]	1.2m Mt. Abu	clear sky
2013-Apr-02 - 2014-Aug-31	Photometry	I/CV	60/30	515/515	40cm Chile	...
2013-Mar-20	Spectroscopy	$J/H/K$/KA	120/90/60/60	2*1	1.2m Mt. Abu	clear sky
2013-Apr-28	Spectroscopy	$J/H/K$/KA	90/75/60/60	2*1	1.2m Mt. Abu	clear sky
2013-May-30	Spectroscopy	$J/H/K$/KA	90/60/60/60	2*1	1.2m Mt. Abu	clear sky
2013-Oct-15	Spectroscopy	600−920 nm	1800	1	2m HCT	clear sky
2014-May-21	Spectroscopy	600−920 nm	300	1	2m HCT	clear sky
2014-Aug-18	Spectroscopy	H/K	30/30/20/10	2*5	2m HCT	clear sky
2014-Aug-19	Spectroscopy	600−920 nm	300	1	2m HCT	clear sky
2014-Oct-06	Spectroscopy	YJ/HK	100/100	2*7	2m HCT	clear sky
		600−920 nm	600	1		
2014-Dec-12	Spectroscopy	YJ/HK	100/100	2*7	2m HCT	clear sky
		600−920 nm	600	1		
2015-Jan-13	Spectroscopy	YJ/HK	100/100	2*7	2m HCT	clear sky
2015-Jan-18	Spectroscopy	600−920 nm	900	1	2m HCT	clear sky
2015-July-05	Spectroscopy	YJ/HK	100/100	2*5	2m HCT	clear sky
		600−920 nm	1	1		
2015-Aug-11	Spectroscopy	YJ/HK	100/100	2*5	2m HCT	clear sky
2016-Dec-19	Spectroscopy	HK	100	2*5	2m HCT	clear sky

550 days during 2013 April 02 to 2014 August 31. The accuracy of these observations varies from 0.004 at I=10.40 to 0.047 at I=14.30, while from 0.007 at C= 12.35 to 0.045 at C=15.70 mag respectively.

The NIR photometric and spectroscopic observations were carried out using NICMOS-3 on 1.2 m Mt. Abu telescope, India, and TIRSPEC on 2.01 m HCT at Hanle, India. The NICMOS3 has 256 × 256 HgCdTe detector array and provides a resolution R ≈1000; while TIRSPEC has 1024 ×1024 Hawaii-1 array and provides resolution R ≈1200. The spectral coverage of NICMOS-3 were on JHK-bands. The spectrograph in the NICMOS-3 instrument does not cover the whole K-band in a single shot. We observed in two parts: the first part covers 1.9−2.3 μm (termed as K), and the second part covers 2.1−2.4 μm with some overlap (termed as KA). The TIRSPEC spectra were taken at $YJHK$ bands. Additional details of TIRSPEC can be found in (Ninan et al., 2014). Photometric observations in JHK'-bands were taken in five dithered positions, and multiple frames are taken in each dithered position to get better signal to noise ratio (SNR). In the spectroscopic observing mode, the spectra were taken simultaneously at two different

positions along the slit one after another to subtract the sky, and several frames were observed to improve SNR. We have estimated the SNR of our spectra as ∼50 (J-band), ∼80 (H-band), ∼80−100 (K-band) for TIRSPEC data, while the SNR is ∼30 (JHK) for NICMOS-3 data. A log of our observations is mentioned in Table 5.1.

The optical spectra are taken using HFOSC instrument on the 2.01 m HCT at Hanle, India. The HFOSC instrument has several grisms covering different wavelength range and resolutions, and we have used Grism No. 8 (Gr#8) for our studies, which covers the wavelength range of 580−920 nm and provides a resolution R ≈ 2200[2]. Additional details of the telescopes and instruments can be found in Chapter 2.

The details description of the optical and NIR photometric data analysis can be found in Section 2.3. The data reduction was performed with the help of standard tasks of the IRAF. The aperture photometry was carried out with these processed images using the APPHOT package of IRAF. The zero-points of photometry were determined using the standard stars.

The spectroscopic analysis was done using APALL task of IRAF. The TIRSPEC data was reduced with TIRSPEC pipe-line[3] (Ninan et al., 2014), and was cross-checked with the IRAF reduction. Both techniques agree well. Additional details on spectroscopic data analysis can be found in Chapter 2.

5.3 Result and discussion

5.3.1 Optical Light Curves and Period

Figure 5.2 shows the optical light curves in the I-band and unfiltered (400−900 nm) CCD (Clear, C). The amplitudes of optical variability are estimated to be ∼4.00 mag and ∼3.4 mag in the I band and unfiltered CCD, respectively. Such a large amplitude of variability with a long-term period is only observed in a case of Mira-like variables (Whitelock et al., 2003). The general criteria for being a Mira variable is having amplitude variability in the I-band greater than 1.0 mag (Soszyński et al., 2012).

For determination of the period of this object, we used the Lomb−Scargle (LS) periodogram (Lomb, 1976; Scargle, 1982), the algorithm publicly available at the starlink[4] software database. The LS method is used to find out significant periodicity even with

[2] https://www.iiap.res.in/iao_hfosc
[3] https://github.com/indiajoe/TIRSPEC/wiki
[4] http://starlink.eao.hawaii.edu/starlink

unevenly sampled data and verified successfully in several cases to determine periods from such sparse data sets (Mondal et al., 2010). The left bottom panel of Figure 5.2 shows the periodograms of the light curves determined from the LS method. We found the period to be 512 ± 100 days, and a significant uncertainty in period is due to the limited time coverage, which does not cover a complete periodic cycle. The period is also verified from PERIOD04[5] (Lenz & Breger, 2005), which provides the same result.

As noted in Lebzelter et al. (1999), the classical method for deriving a period using Fourier analysis-like LS method does not always provide satisfying results for light curves of AGB variables. Alternatively, we have used Fourier decomposition technique with the fitting of the following function as in Ngeow et al. (2013),

$$m\ (t) = A_0 + \sum_{\kappa=1}^{N} A_\kappa sin(\kappa\omega t + \phi_\kappa) \tag{5.1}$$

where $\omega = 2\pi/P$, P is the period in days, A_κ and ϕ_κ represent the amplitude and phase-shift for κth-order respectively, and N is the order of the fit. To fit the light curve, we use up to third-order terms. From χ^2 minimization technique, we find a best-fitted period of 465±30 days on our light curves. The solid black line is the Fourier fit, which is shown in Figure 5.2 along with observed data in the respective panels. The estimated period of this red object is consistent with those of the red Large Magellanic Cloud (LMC) Miras ($J - K \geq 2.08$) having periods of 300−500 days (Ita et al., 2004). It is also noted the greater falltime (F_t, 275 days) of the light curve than the risetime (R_t, 190 days). The phase of the light curve can be calculated following the equation as,

$$\begin{aligned} \phi(t) &= \frac{\phi}{2f} && 0 \leq \phi < f \\ &= \frac{\phi - 1}{2(1-f)} + 1 && f \leq \phi \leq 1 \end{aligned} \tag{5.2}$$

where $\phi = (t - t_0)/P$, t_0 is the phase and f is asymmetry parameter which represents the risetime over the total period. The value of f lies between 0 to 1. The light curves starts ($\phi = 0$) at t= 2456345 JD. Note that we determined all the phase from the Equation 5.2.

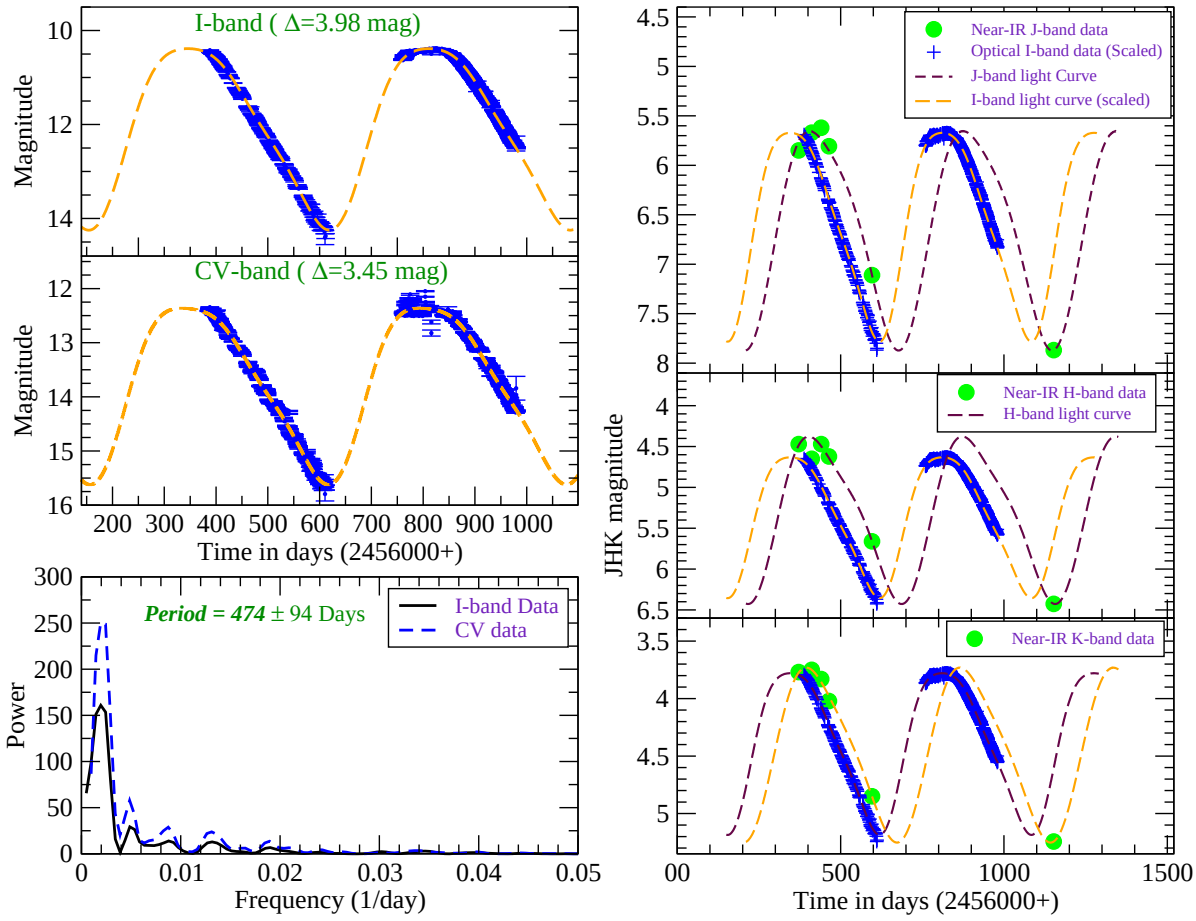

Figure 5.2: The left panels show the optical light curves of J2124+32 with fitting using Equation (1) in the I-band (left top) and unfiltered CCD in 400−900 nm (C) (left middle). The periodograms of optical light curves are shown in the left bottom panel. The NIR JHK light curves of J2124+32 are shown in the right three panels (JHK'), where the filled circles are our observed NIR data points, while the solid lines are fitted light curve with $P = 465$ days. The optical I-band light curve (scaled with NIR light curves) is over-plotted on NIR light curves for comparison.

Table 5.2: Near-IR JHK' Photometry

Date of Obs. (UT)	Optical Phase	Telescope/Instrument	J (mag)	H (mag)	K (mag)	$(J-K)$ (mag)
2013 Mar 22.02	0.049	Mt. Abu/NICMOS-3	5.852 ± 0.055	4.467 ± 0.062	3.765 ± 0.049	2.087
2013 Mar 24.01	0.051	Mt. Abu/NICMOS-3	5.642 ± 0.044	4.483 ± 0.035	3.765 ± 0.034	1.877
2013 Apr 28.93	0.118	Mt. Abu/NICMOS-3	5.668 ± 0.043	4.654 ± 0.052	3.751 ± 0.010	1.917
2013 Apr 29.98	0.119	Mt. Abu/NICMOS-3	5.557 ± 0.021	4.510 ± 0.023	3.720 ± 0.012	1.837
2013 May 27.92	0.169	Mt. Abu/NICMOS-3	5.621 ± 0.051	4.466 ± 0.063	3.827 ± 0.045	1.794
2013 May 28.95	0.170	Mt. Abu/NICMOS-3	5.718 ± 0.047	4.452 ± 0.053	3.752 ± 0.048	1.966
2013 Jun 20.83	0.213	Mt. Abu/NICMOS-3	5.807 ± 0.034	4.621 ± 0.024	4.021 ± 0.029	1.786
2013 Oct 30.50	0.450	Mt. Abu/NICMOS-3	7.110 ± 0.020	5.660 ± 0.030	4.850 ± 0.020	2.260
2015 May 08.91	1.60	Mt. Abu/NICMOS-3	7.868 ± 0.017	6.426 ± 0.06	5.243 ± 0.015	2.625
1998 Jun 18.00[6]		2MASS/NICMOS	7.825 ± 0.026	5.971 ± 0.017	4.818 ± 0.015	3.007
Average		Mt. Abu/NICMOS3	6.093±0.257	4.859±0.220	4.077±0.17	2.016
Amplitude (light curve)		Mt. Abu/NICMOS3	2.2	1.9	1.5	

5.3.2 Near-Infrared light curves

NIR JHK'-bands photometric observations were carried out during 2013 March 20 to 2015 May 09 in a sparse sampling of the Mira cycle, and JHK' magnitudes are listed in Table 5.2. Our JHK' magnitudes on the first two epoch are reported immediately at ATEL (Mondal et al., 2013). The NIR JHK' light curves are shown in the right panels of Figure 5.2. For comparison, the optical I-band light curve is also overplotted on those NIR light curves after scaling with JHK' magnitudes. The light curve is fitted to the Equation 5.1 mentioned above with the same period of the optical light curve fit. The amplitudes (peak to peak) of the variability are estimated from our light curves to be $\Delta J \sim 2.2$ mag, $\Delta H \sim 1.9$ mag and $\Delta K \sim 1.5$ mag, respectively. These optical/NIR light curves confirm typical Mira behaviour of strong wavelength dependence, i.e., the pulsation amplitude decreases with increasing wavelength (Smith et al., 2002b). Bessell et al. (1996) showed that colours such as $(V - K)$ change much more with phase than near-IR colours [e.g., $(J-H)$,$(H-K)$, $(J-K)$], which is another way of saying that visual amplitudes are larger than near-IR amplitudes. The fact that the pulsation amplitude decreases with increasing wavelength is a result of the changes in T_{eff} that accompany the changes in luminosity, which is exacerbated by the dependence of TiO opacities on temperature. Another interesting feature, a phase lag of about 60 days, corresponding to ∼0.13 of phase, between the optical and NIR maxima or minima is observed here in Figure 5.2, which is seen in Mira variables (Smith et al., 2002b). Such phase lag in oxygen-rich Miras may be due to the opacity of TiO molecules in their atmosphere (Smith et al., 2006), and even large visual amplitude might be due to the formation and destruction of TiO molecules during the passage of periodic shock waves (Reid & Goldston, 2002). The 2MASS $(J - K)$ colour is 3.0 mag (Cutri et al., 2003). We also find a large $(J - K)$ colour index, ranging from 1.78 to 3.0 mag (Table 5.2), which is, again, consistent with the source being an extreme red Mira variable (Ita et al., 2004; Whitelock et al., 2000). We rule out that the object is a semi-regular variable, as they are not this degree of red.

5.3.3 Distances and Luminosity

To estimate the distance to the source, we have used the period−luminosity (PL) relation for the Miras based on the distance modulus of the LMC to be 18.50± 0.02, the PL relation is taken from Ita & Matsunaga (2011) expressed as

$$M_K = (-3.675 \pm 0.076) \log P + (1.456 \pm 0.173) \quad (5.3)$$

[5] http://www.univie.ac.at/tops/Period04

According to the relation, the absolute K-band magnitude of the source is estimated to be $M_K = -8.34\pm 0.34$ mag. We have also examined other available PL relations in Feast et al. (1989) and Whitelock et al. (2008), and the value of M_K is within uncertainty limit. The Galactic interstellar extinction in the direction of the source is $A_V = 0.57$ ($A_K = 0.05$; Schlafly & Finkbeiner 2011) or $A_V = 0.68$ ($A_K = 0.06$; Schlegel et al. 1998). Taking $A_K = 0.05$, we have obtained the distance, d, to the object, 3.27±0.02 kpc using the relation $m_k - M_K = 5 \log d - 5 + A_K$. The uncertainties in the distance measurement come from the estimated period, PL relation, and photometric error of calculating K-band magnitude. We have also estimated bolometric magnitude M_{bol} using the following PL relation for Miras (Hughes & Wood, 1990).

$$M_{bol} = -3.22 - 7.76[\log(P/day) - 2.4] \pm 0.38 \tag{5.4}$$

We have estimated the bolometric magnitude of $M_{bol} = -5.29 \pm 0.38$ corresponding to luminosity ∼10250 $L_\odot$, which is consistent with other PL relation of Feast et al. (1989). The O-rich Miras with P $\geq$ 420 days are over luminous (Feast et al., 1989; Hughes & Wood, 1990), which is consistent with our result. Feast et al. (1989) showed that for few Miras, which have periods > 420 days, are 0.7 mag brighter than expected extrapolation of PL relation. Also, Whitelock et al. (2003) suggested that Miras with periods >400 days have higher luminosities due to hot bottom burning. Putting our object on the mass-Luminosity relation in Figure 6 of Hughes & Wood (1990), the object with $P = 465$ days and $M_{bol} = -5.29$ lies between the mass (M) range of 1.0−1.5 $M_\odot$.

To understand the galactic location of the new Mira variable, we have estimated the scale height of the object from the distance above the galactic plane (Z) following Jura & Kleinmann (1992). We find that the scale height of the object is about 270 pc which agrees with the thin disk population as given by Habing (1988); Jura & Kleinmann (1992); Eggen (1998); Jurić et al. (2008).

5.3.4 Spectral Energy Distribution

We use near to far-infrared multi-wavelength photometric data to generate the SED of the source J2124+32. The fluxes, used here for the SED fit, are taken from our JHK' measurements and archival mid- to far-infrared catalogs. The mean JHK' are estimated from the NIR light curves. The mid-IR 3.35, 11.6, and 22.1 μm data are taken from AllWISE Data Release (Cutri & et al., 2013); 8.61, 18.4 μm from $AKARI$/IRC all-sky Survey (ISAS/JAXA, 2010; Ishihara et al. 2010); 12, 25 μm from $IRAS$ Faint Source Catalog (IPAC 1992) and Far-IR 65, 90 μm data from $AKARI$/FIS; 60 μm from $IRAS$.

Table 5.3: MoD Models for J2124+32 for Three Different Cases

Star	L (L⊙)	$\tau_{0.55}$	T_c [K]	p	χ^2_{red} [8]	Remarks
	9331 ± 1545	10.064 ± 2.489	1000 fixed	2.0 fixed	819	T_c, p fixed
J2124+32	9255 ± 1659	9.913 ± 2.746	1000 fixed	1.95 ± 0.29	818	T_c fixed
	9282 ± 1590	11.178 ± 3.975	1248 ± 511	1.75 ± 0.28	806	All free

The observed JHK' magnitudes are converted to flux densities using the zero magnitudes flux from (Bessell et al., 1998).

The radiative transfer code, MoD, are used to model the dusty circumstellar shell of Mira variable. The MoD works to find best-fitted parameters, e.g., luminosity (L), dust optical depth ($\tau_{0.55}$), dust temperature at the inner radius (T_c), and slope of the density law (p), in the minimization process. The quality of the fit is obtained through a χ^2 analysis. Additional details of MoD can be found in Chapter 2.

The interstellar reddening (A_V), hydrostatic model atmosphere, the effective temperature of the model atmosphere, distance (D), outer radius in a unit of inner radius, dust properties, etc. are provided as an input in the master-input file. The adopted dust species are taken as mixture of $Mg_{0.8}Fe_{1.2}SiO_4$:AlO:Fe = 100:0:5, calculated using the distribution of hollow spheres (DHS) with a mean grain size $a = 0.15$ μm and a maximum volume fraction of a vacuum core $f_{max} = 0.7$ μm (M. A. T. Groenewegen 2018, private communication). We adopted such dust composition because our spectroscopic studies concluded that the star is O-rich, as will be discussed in subsequent sections. The MARCS[7] hydrostatic model atmospheres (Gustafsson et al., 2008b) were used for the spectra of the central stars. The outer radius is set to 1600 times the inner radius, where dust temperature becomes approximately 20 K. In the model, the distance, d, of 3.27 kpc and A_V were adopted as an input to the standard model as discussed in the previous section. The L, τ, T_c and p could be fitted or set to fixed values.

To obtain the best fit of the photometric data, we generated multiple SEDs considering MARCS model atmospheres of temperature range 2600−3600 K in step of 200 K and setting other free parameters (e.g., L, $\tau_{0.55}$, T_c, p) as either fixed or variable, as listed in Table 5.3. The model provides a minimum reduced χ^2 value at MARCS model atmospheres of temperature 2800 K, and the parameters of MoD fitting at that temperature for different cases are provided in Table 5.3. Our best-fit SEDs of all photometric measurements for various cases are shown in Figure 5.3. We got the minimum value of reduced χ^2 when all the parameters were set free. The χ^2 of the fit is typically large

[7] http://marcs.astro.uu.se/

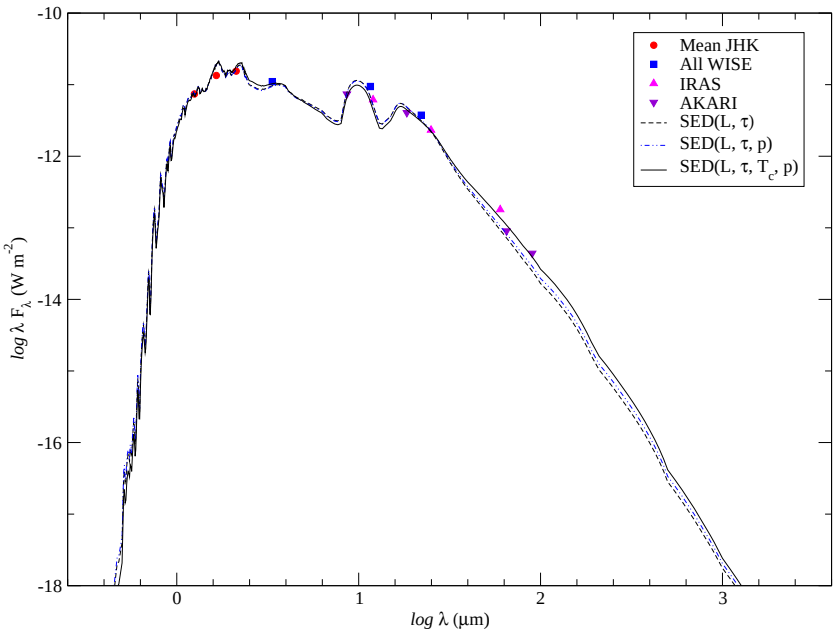

Figure 5.3: The SED of the target is shown here using multi-wavelength data from NIR to far-IR, while the insets show different data source, e.g., our mean JHK', All *WISE*, *AKARI*, *IRAS* data. The SED (L, τ) means fitted SED is shown, with L, τ as variables and T_c, p fixed. The same is true for SED (L, τ, p) and SED (L, τ, T_c, p).

as we include a significant JHK' variability in our SED fit and non-simultaneous taking of the photometric data. The provided errors are therefore internal errors scaled to a reduced χ^2 of 1 (M. A. T. Groenewegen 2018, private communication). The best-fitted SED provides $L = 9282 \pm 1590\ L_\odot$ that is comparable to our P-L based estimation in the earlier section, $\tau = 11.178 \pm 3.975$, $T_c = 1248 \pm 511$ K, and $p = 1.75 \pm 0.28$. The best-fit parameters, dust properties and actual grain size translate into a current mass-loss rate of $0.7 \times 10^{-6} M_\odot yr^{-1}$ by assuming a dust-to-gas ratio of 0.005 and an expansion velocity of 10 km/s.

5.3.5 Optical/NIR spectroscopic studies

Multi-epoch optical/NIR spectroscopic studies on Mira variables at different variability phases probe the dynamic stellar atmosphere and help us also to understand the pulsational related variations of fundamental parameters. The visual spectra of the object taken at several variability phases are shown in Figure 5.4. The optical spectra are dominated by molecular absorption bands of TiO and VO in the wavelength range of 7000−9000 Å, like red M stars (Castelaz et al., 2000; Rayner et al., 2009; Bessell et al., 1989; Fluks et al., 1994). A visual comparison shows that all the optical spectra of the MASTER OT object correspond to O-rich spectral types later than M7.

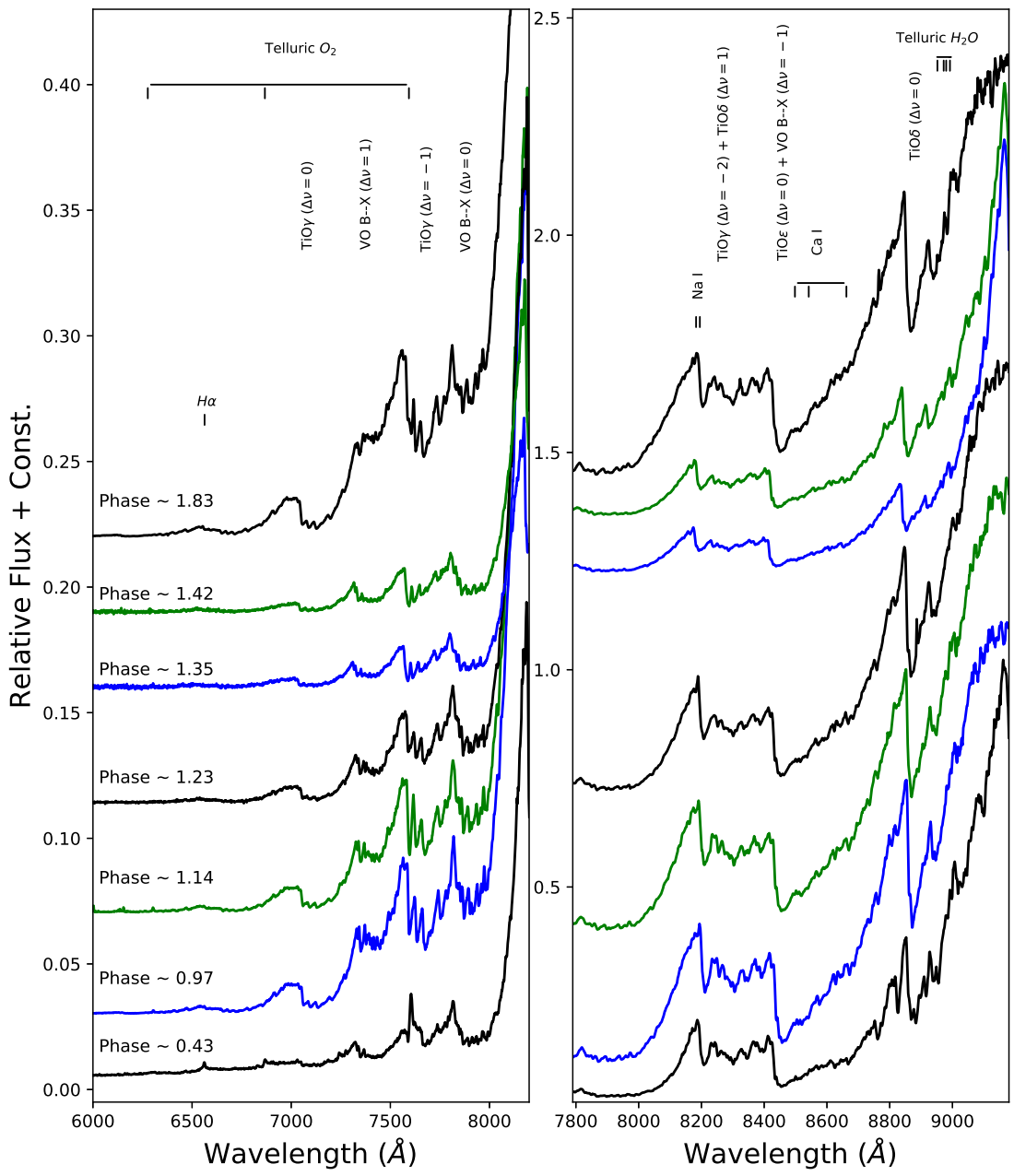

Figure 5.4: The top two panels show the optical spectra of the object in the range 6000−9200 Å, in which visible features of TiO and VO bands at different phases of the Mira can be clearly seen, including H_α emission at phase 0.43. The spectra have been normalized to unity at 9165 Å and offset by constant values 0.0, 0.03, 0.07, 0.11, 0.16, 0.19, and 0.22 (left panel) and 0.0, 0.06, 0.36, 0.70, 1.20, 1.35, and 1.40 (right panel), respectively, with respect to the bottom-most spectra.

The NIR spectra were taken immediately after transient alert of Tiurina et al. (2013) and continued over several variability phases as listed in Table 5.1. The JHK spectra are shown in Figure 5.5. Molecular features of the TiO and VO bands dominate in the J-band spectra, as shown in the first panel of Figure 5.5. But no ZrO twin features at

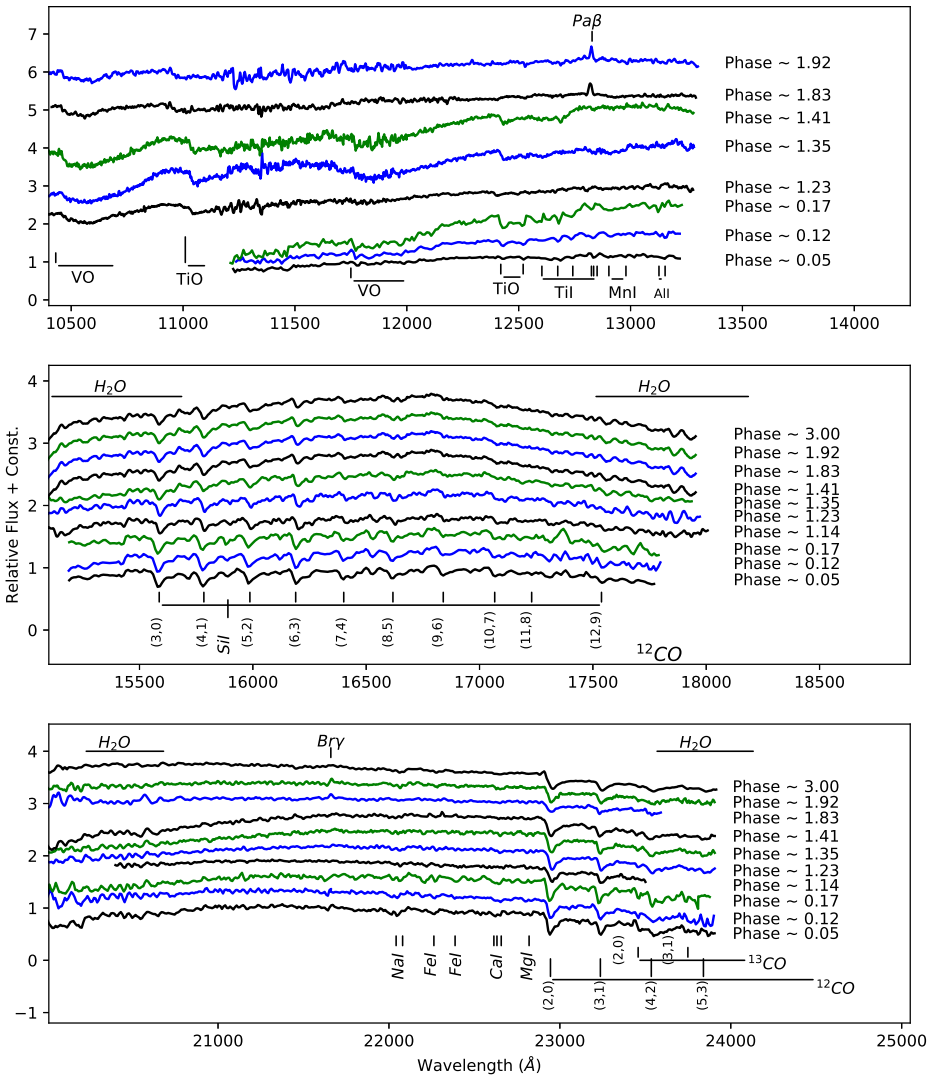

Figure 5.5: The NIR JHK-band spectra in the wavelength range 1.02−2.39 μm at eight different phases of the Mira are shown here in the first, second, and third panels, respectively. The first three NIR spectra from the bottom (phase ∼0.05, 0.12, 0.17) are taken with the NICMOS-3 instrument on 1.2 m Mt.Abu telescope, and rest are observed with TIRSPEC instrument on 2.0 m HCT. In J-band, molecular bands like TiO, VO, and few atomic lines are present in the spectra. The Paβ emission line appears at two phases (1.83 and 1.92). The H-band spectra in the wavelength range 1.52−1.80 μm show strong four ^{12}CO-second overtone bands including several OH lines. In the K-band spectra, the ^{12}CO first overtone bands are dominated features in the spectra, and Na I and Ca I are seen at 2.20 μm and 2.26 μm, respectively. The Brγ (at 2.16 μm) emission line appears at phases 1.83, 1.92, and likely at 0.05. The spectra have been normalized to unity at 12000 Å (J-band), 16500 Å (H-band), and 21700 Å (K-band), and offset by constant values 0.0, 0.30, 0.60, 0.11, 1.70, 2.40, 3.30, 4.20, and 5.10 (first panel), respectively, with respect to the bottom-most spectra of the same panel (J-band), and 0.30 to each spectrum of H- and K-band).

1.03, and 1.06 μm is seen here, which is a primary indicator for S-type Mira stars (Hinkle et al., 1989; Wright et al., 2009). The most prominent feature of the VO band is seen in

one of our spectra, which covers from 1.02 μm, which signifies it is an oxygen-rich M−type star (Wright et al., 2009).

In the second panel of Figure 5.5, the H-band spectra show the ^{12}CO second overtone series at 1.5582, 1.5780, 1.5982, 1.6189, 1.6397, 1.6610, 1.6840, and 1.7067 μm including OH molecular bands all over the band (Rayner et al., 2009). These second overtone series develop at the objects having a photospheric temperature of $\leq$ 5000 K, and their strength is dependent on the photospheric temperatures (Lançon et al., 2007). The OH molecular bands are prominent in M-type stars, very weak in S-type, and absent in carbon stars, as all oxygen is locked up in CO. No C_2 band at 1.77 μm is seen here, as observed in carbon-rich Miras.

The K-band spectra are shown in the most bottom panel of Figure 5.5. The ^{12}CO first overtone series at 2.2935, 2.3227 μm, neutral atomic lines of Na I doublet at 2.20 μm, Ca I triplet at 2.26 μm are seen in our spectra, which are original features in M-type evolved stars (Rayner et al., 2009). The ^{12}CO(2−0) first overtone band heads are the strongest absorption feature in the K-band in cool stars, and their strength depends on both luminosity and effective temperature (Ramirez et al., 1997; Cesetti et al., 2013). The first overtone of ^{13}CO is also visible in our spectra, though its strength is relatively weak compared to ^{12}CO first overtone series.

The Hα emission line is seen only at phase ∼0.43. The Paβ emission line appears in two visual phases, 1.83 and 1.92. The Brγ appears at phase 1.83 and reach maximum intensity at 1.92. These emission lines appear in the spectra due to shock wave generation in the Mira atmosphere. It should be noted that Hα is seen at phase 0.43, while Paβ and Brγ are seen near maximum phase. Other studies find Balmer lines usually around maximum phase (e.g., Fox et al. 1984b; Fox & Wood 1985).

The overall low-resolution continuum shape of J, H, and K spectra turn downwards at the end of the band, indicating absorption due to broad H_2O absorption features centered at 1.4, 1.9, and 2.7 μm in our spectral coverage (Rayner et al., 2009). It is clearly visible that the continuum shape is changing over the variability phases.

Phase dependent spectral variability

The variation in the absorption depth of TiO and VO with T_{eff} is well documented for some time (Merrill et al., 1962). Lockwood (1972) found that TiO band-strength indices decrease in stars later than M7, and they saturate in M9 Miras. We explore the phase variation of the $[TiO]_2$ index centered at 7100 Å as described in O'Connell (1973).

However, the $[TiO]_2$ index shows no significant variation over the phase. Note that we do consider the optical phase variation here.

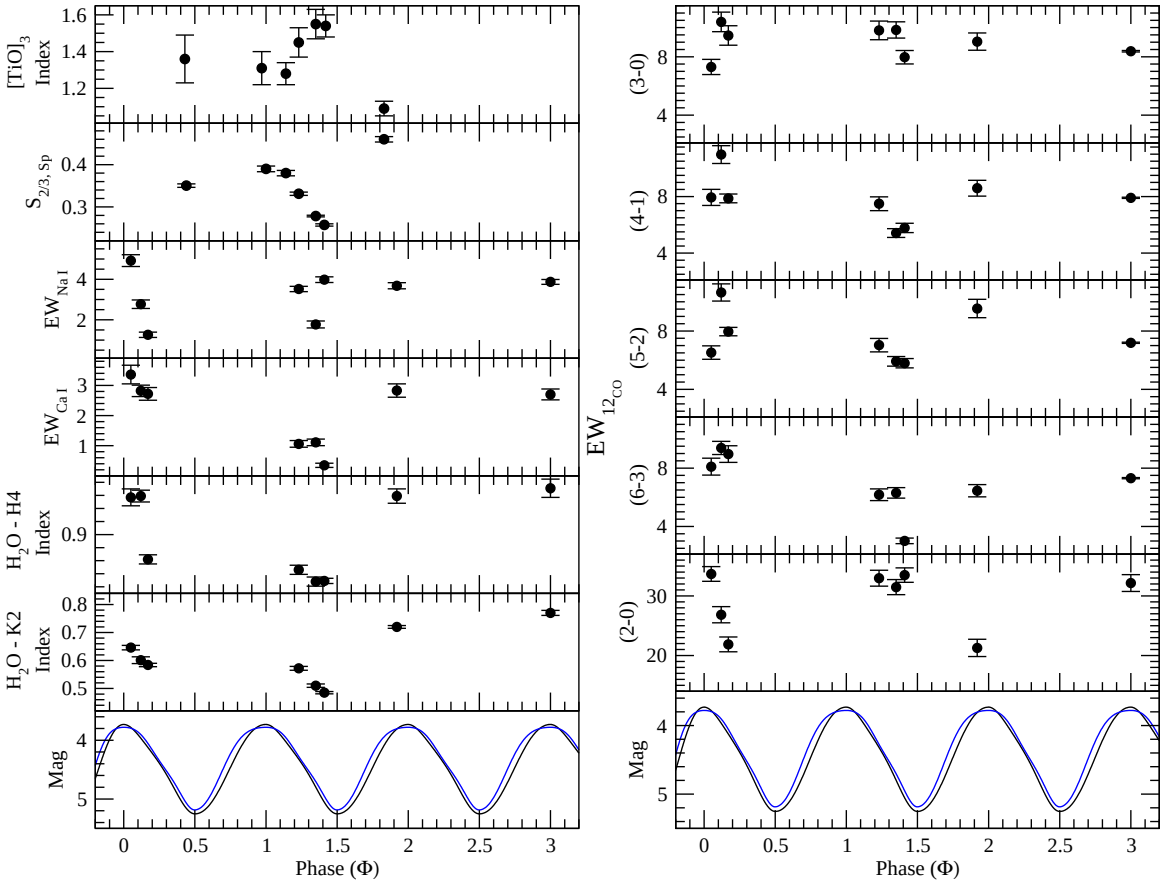

Figure 5.6: The phase variation of $[TiO]_3$, $S_{2/3,Sp}$, Na I, Ca I, H_2O-K2 equivalent width/index are shown with the visual phase. The bottom panel shows the K-light curve (black) and I-light curve (scaled with K-light curve).

Table 5.4: Definitions of Spectral Bands

Feature	Bandpass (μm)	Continuum bandpass (μm)	Ref
$[TiO]_3$	0.8455−0.8725	0.8390−0.8410, 0.8700−0.8725	1
Na I	2.204−2.211	2.191−2.197, 2.213−2.217	2
Ca I	2.258−2.269	2.245−2.256, 2.270−2.272	2
$^{12}CO(3-0)$	1.5550−1.5625	-	2
$^{12}CO(4-1)$	1.5752−1.5812	-	2
$^{12}CO(5-2)$	1.5952−1.6020	-	2
$^{12}CO(6-3)$	1.6170−1.6220	-	2
$^{12}CO(2-0)$	2.289−2.302	2.270−2.272, 2.275−2.278 2.282−2.286, 2.288−2.289	2

Note. [1]Zhu et al. (1999); [2]Ramirez et al. (1997).

Another triple-headed absorption bands of TiO at 8433, 8442, 8452 Å, $[TiO]_3$, is considered following Zhu et al. (1999) for such phase variation studies. The $[TiO]_3$ is defined as,

$$[TiO]_3 = -2.5 \log\left(\frac{F_\lambda}{F_C}\right) \tag{5.5}$$

where, F_λ is flux at λ, and F_C is the interpolated continuum at λ. The pseudo-continuum was generated in the left window of the band at 8390−8410 Å, and the right windows at 8700−8725 Å. Then, we normalized the spectrum by the continuum, and measure the $\frac{F_\lambda}{F_C}$ in the range 8455−8470 Å. As shown in Figure 5.6, the $[TiO]_3$ index shows significant variation with the pulsation phase; it increases as the visual brightness decreases, becomes constant at certain phases (saturation effect), and then further decreases with increasing visual brightness.

Figure 5.4 shows three strong absorption bands 706−724 nm (band1), 770−807 nm (band2) and 829−857 nm (band3), which are related to spectral types of static giants (Fluks et al., 1994). The flux ratio at different bands is defined by Fluks et al. (1994). We studied the flux ratio at those bands and found that the band2 to band3 ratio (as $S_{2/3,Sp}$) shows pronounced variation with phase as shown in Figure 5.6. The $S_{2/3,Sp}$ reaches maximum at the visual maximum and reaches its minimum at the visual minimum.

We have measured the equivalent widths (EWs) for the atomic spectral features Na I at 2.206 μm, Ca I at 2.263 μm. The continuum bands for Na I and Ca I are taken from Ramirez et al. (1997) and mentioned in Table 5.4. The spectra were normalized by the local pseudo-continuum, and EWs of the particular atomic features were estimated by using splot task in the IRAF by fitting a Gaussian function to each feature. The Na doublet is present in the 2.2051−2.2099 μm region but blended with metallic lines like Si I (2.2069 μm), Sc I (2.2058 and 2.2071 μm) and V I (2.2097 μm) in our low-resolution spectra. The Ca triplet appears in the 2.2609-2.2665 μm regions and is very sensitive to temperature. The third and fourth panels of Figure 5.6 show their phase variation. The atomic lines, in particular, are weak features that are very difficult to measure in low-resolution spectra, and no significant trend with phase are apparent, except possibly for Ca.

In the 1.5−2.4 μm region, the first-overtone ($\Delta\nu$=2) and the CO-second overtone ($\Delta\nu$ = 3) band heads of CO are the dominant features in the spectra as mentioned in the earlier section. We studied the phase-dependent variations of these 2−0 (first overtone) and 3−0, 4−1, 5−2, 6−3 (second overtone) ^{12}CO band heads. We estimated the EWs of CO at different phase considering the local continuum as mentioned in Table 5.4. The continuum has been fitted with a first-order spline fitting function (linear interpolation) at

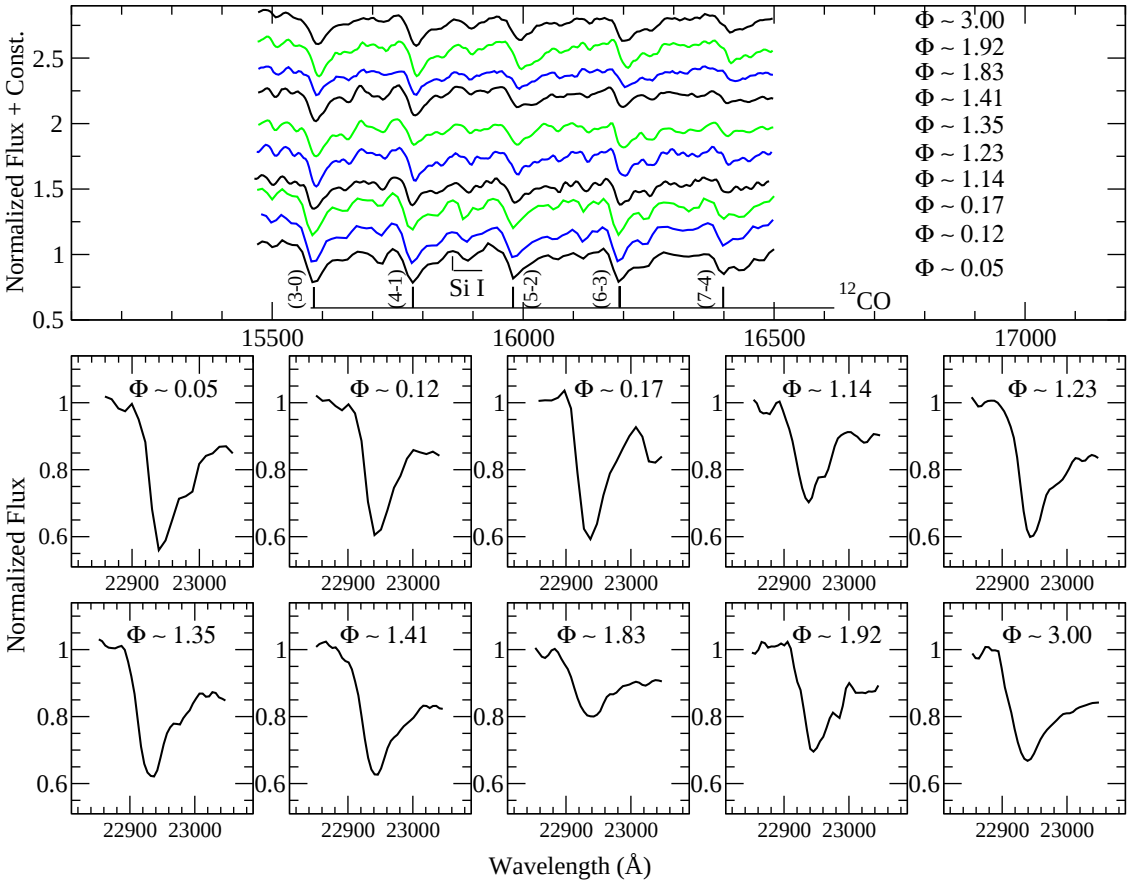

Figure 5.7: The changing shape of CO-second overtones and one CO first overtone at 2.29μm with phases are shown here

peak points. We estimated the EWs of CO at different phases, as shown in Figure 5.6. The EWs of the 3−0 and 4−1 band heads does not demonstrate any significant change during the pulsation cycle. The EWs of the 2−0 first overtone band change significantly. The EWs of the 5−2 and 6−3 band heads showed weak variation. The result should be taken with caution, as such small variations might occur due to the computational artifacts, continuum selection, and blending effect from the weak OH-lines. The shock wave, in general, propagates through the Mira atmosphere (CO first overtone forming-layer) in between optical phase $\sim 0.1-0.2$, which alters velocity profile known from high-resolution spectra (Hinkle & Barnes, 1979b; Nowotny et al., 2010). Even in our low- to intermediate-resolution spectra, the CO absorption features appear to change in Figure 5.7. It is expected that the combination of modified individual lines will also modify the shape of the band as a whole.

The shape of the NIR spectra in Miras is dominated by strong, and broad water bands centered at 1.4 μm, 1.9 μm, and 2.7 μm regions (Johnson et al., 1968). The depth of water bands vary with Mira phases and become strongest at minimum light (Strecker

et al., 1978). Due to this water absorption, the H- and K-band spectra bend downward at the end of both bands. Thus, the curvature of the spectral changes depending on the water absorption. To quantify water absorption in our data, we measured the H_2O-H4 and H_2O-K2 indices, which shows the curvature variation of the spectra. The H_2O-K2 Index is taken from Rojas-Ayala et al. (2012) and also explored for cool K–M giants in Chapter 4. Here, the same index is used for a Mira variable on the phase-dependent study.

For the H-band spectra, several authors defined spectro-photometric indices to measure water absorption (e.g., Allers et al. 2007; Wright et al. 2009; Scholz et al. 2012). Here, we define a new H_2O-H4 index as,

$$H_2O-H4 = \frac{\langle F(1.531-1.541)\rangle/\langle F(1.670-1.690)\rangle}{\langle F(1.670-1.690)\rangle/\langle F(1.742-1.752)\rangle} \tag{5.6}$$

where $\langle F(a-b)\rangle$ represents the median flux level in the wavelength range defined by a and b in μm.

In Figure 5.6, the phase variation of these two H_2O-H4 and H_2O-K2 indices is shown. The smaller value of H_2O indices in H and K corresponds to greater amounts of H_2O opacity. The signification variations of these indices are apparent in Figure 5.6. In Figure 5.6, we see that the H_2O-H4 and H_2O-K2 indices show significant variation with the pulsation cycles, and the value of indices are strongest at visual maximum while weak at a visual minimum, i.e., H_2O opacity is stronger at the visual minimum. Our result confirms the trends already seen by Strecker et al. (1978).

Spectral type

The depth of the triple-headed absorption band of TiO (8432, 8442, and 8452 Å) at the optical spectra is an excellent spectral type (ST) indicator. Following Zhu et al. (1999), we estimate the ST of the object at a different variability phase, which is defined as the $[TiO]_3$ index ([TiO] at 8450 Å).

$$ST = 2.43 + 6.65[TiO]_3 - 1.12[TiO]_3^2 \tag{5.7}$$

We have measured the $[TiO]_3$ index using the Equation 5.5 from the spectra as described in the earlier Section. The ST is estimated using the above relation in the Equation 5.7, and the STs at different phases are shown in Table 5.5. The ST of the object varies from M8.5 to M10 over the phase of the pulsation cycle in our limited phase coverage. The

Table 5.5: Phase-dependent Study

Date of Obs.	Optical Phase	$[TiO]_3$ Index	$S_{2/3,Sp}$	Na I 2.20 μm	CaI 2.26 μm	CO 3-0	CO 4-1	CO 5-2	CO 6-3	CO 2-0	H_2O-H4 Index	H_2O-K2 Index	Sp. $Type$[1]
2013 Mar 21.99	0.05	...	...	4.92±0.29	3.36±0.31	7.30±0.52	7.94±0.57	6.52±0.46	8.1±0.58	33.68±1.23	0.96±0.01	0.65±0.01	...
2013 Apr 29.99	0.12	...	...	2.77±0.21	2.82±0.19	10.39±0.67	10.97±0.63	10.64±0.59	9.38±0.45	26.84±1.36	0.96±0.01	0.60±0.01	...
2013 May 30.95	0.17	...	...	1.26±0.13	2.72±0.21	9.46±0.67	7.87±0.31	7.96±0.29	8.96±0.57	21.87±1.24	0.86±0.01	0.58±0.01	...
2013 Oct 15.57	0.44	1.36±0.13	0.350 ± 0.004	...	...	...	...	...	...	...	...	...	M9.5
2014 May 21.91	1.0	1.31±0.09	0.390 ±0.007	...	...	...	...	...	...	...	...	...	M9
2014 Aug 18.72	1.14	...	...	1.37±0.11	1.10±0.12	8.03±0.44	6.02±0.33	6.22±0.34	6.023±0.32	18.65±1.08	0.90±0.011	...	...
2014 Aug 19.83	1.14	1.28±0.06	0.380±0.006	...	...	...	...	...	...	...	...	...	M9
2014 Oct 06.73	1.23	1.45±0.08	0.331 ±0.003	3.52±0.13	1.06±0.11	9.81±0.64	7.49±0.49	7.03±0.46	6.173±0.40	32.97±1.33	0.85±0.01	0.57±0.01	M9
2014 Dec 12.55	1.35	1.55±0.08	0.278 ±0.002	1.77±0.17	1.11±0.11	9.84±0.56	5.42±0.31	5.92±0.33	6.30±0.36	31.47±1.27	0.83±0.01	0.51±0.01	M10
2015 Jan 13.58	1.41	...	...	3.98±0.14	0.35±0.07	7.97±0.46	5.78±0.33	5.788±0.32	3.01±0.19	33.49±1.21	0.83±0.01	0.48±0.01	...
2015 Jan 18.56	1.41	1.54±0.06	0.257 ±0.003	...	...	...	...	...	...	...	...	...	M10
2015 July 05.79	1.83	1.09±0.04	0.460 ±0.006	1.94±0.09	1.57±0.17	6.85±0.31	6.66±0.30	6.03±0.27	4.32±0.20	19.52±0.93	0.93±0.01	...	M8.5
2015 Aug 11.88	1.92	...	...	3.68±0.15	2.83±0.22	9.04±0.59	8.59±0.56	9.54±0.63	6.45±0.42	21.27±1.45	0.96±0.01	0.72±0.01	...
2016 Dec 19.54	3.00	...	...	3.87±0.12	2.70±0.18	8.38±0.05	7.91±0.04	7.19±0.04	7.31±0.04	32.15±1.41	0.97±0.01	0.77±0.01	...

Note. [1]The spectral type has been estimated using the correlation with $[TiO]_3$ Index.

saturation effect of $[TiO]_3$ is problematic to estimate the STs over phases, as described in the earlier Section.

5.4 Summary and conclusion

From long-term optical/NIR photometric and spectroscopic observations, we have characterized the MASTER OT J2124+32. Our main results are summarized as follows :

1. From the best-fit of optical/NIR light curves, we estimated the variability period of the object as 465 ± 30 days. The strong wavelength-dependent variability amplitudes in optical to NIR wavelengths are observed as ΔI $\sim$ 4 mag, ΔC (400–900 nm) $\sim$ 3.4 mag, $\Delta J \sim$ 2.2 mag, $\Delta H \sim$ 1.9 mag and $\Delta K \sim$ 1.5 mag. Such large periods and strong wavelength-dependent variability amplitude are seen in Miras only. Interestingly, a phase lag of ∼60 days between the optical and NIR light curves is also seen, like for Mira variables. Large (J – K) NIR colours varying 1.78–3.0 mag over phases, signifies that it is a red object, like cool Miras.

2. From the PL relation, the distance to the source is estimated to be 3.27 ± 0.02 kpc. The absolute bolometric magnitude is determined as -5.29 ± 0.38 mag, corresponding to the luminosity of ∼10,250 $L_\odot$.

3. Using DUSTY-based MoD code, we have fit the SED for NIR to far-IR data. The best-fit SED of all photometric measurements provides an effective temperature of 2800 K and dust shell temperature 1248 K. The SED provides luminosity of the object 9282 of $L_\odot$, which is comparable to the P-L based estimation, and a mass-loss rate of $0.7 \times 10^{-6} M_\odot yr^{-1}$.

4. From Optical/NIR spectra, we find that the source has many of the spectral signatures of a cool M-type star. The spectral features indicate that it is an O-rich Mira, as it shows the most prominent feature of VO band and TiO bands. We rule out S- or C-type nature as ZrO bands at 1.03 and 1.06 μm and C_2 band head at 1.77 μm are absent.

5. The phase-dependent of optical/NIR spectral features are studied. Notable variable features in all atomic and molecular lines (e.g., TiO, Ca I, H_2O and CO bands) over phases are seen here, which are like commonly observed in Miras. Our optical spectral data show an apparent variation of the spectral type of the object over the pulsation cycle.

In conclusion, all of these observational properties of the object J2124+32 confirms that it is a new O-rich Mira variable toward Cygnus.

Chapter 6

Characterisation of a poorly known high-luminous OH/IR star

This chapter is based on the following paper.

Title: Spectroscopic and photometric monitoring of a poorly known high-luminous OH/IR star
Authors: **Supriyo Ghosh**, S. Mondal, R. K. Das, and S. Dutta
Year :
Journal: Astronomy & Astrophysics (submitted)

In this chapter, we present optical/NIR photometric and spectroscopic observations of the MASTER-Net optical transient J183012.04+093342.6 (hereafter, J1830+09) towards the Ophiuchus constellation. We have performed long-term optical/near-infrared (NIR) photometric and spectroscopic observations to characterize the object. The variability period of the object are estimated from optical R- and I-band light curves. We construct the SEDs from multi-wavelength photometric and IRAS-LRS spectral data applying radiative transfer model that provides the luminosity, dust mass-loss rate, optical depth and grain density. A rare study on the time-dependent variation of optical/NIR atomic and molecular features (e.g., TiO, NaI, Ca I, H_2O and CO bands), as commonly observed in OH/IR stars, is also presented in this chapter.

6.1 Introduction

The object on J183012.04+093342.6 (hereafter, J1830+09, RA= 18h 30m 12.04s , Dec =+09d 33m 42.6s) was reported on 2013 April 22 from MASTER Optical Transient alert with 11.8 mag at unfiltered CCD (Balanutsa et al., 2013). J1830+09 is an OH/IR star detected in the 1612 MHz OH maser line with Arecibo radio telescope, which surveys the IRAS sources with flux densities $\leq$2 Jy at 25 μm, with declination $0^{\rm deg} < \delta < 37^{\rm deg}$, and appropriate colours of AGB stars (Olnon et al., 1984; Jiménez-Esteban et al., 2005b). The object is located in the Region IIIa of IRAS two-colour ([12]−[25] vs. [25]−[60]) diagram (see Chapter 1, van der Veen & Habing 1988b) that represents the population of variable stars with more evolved O-rich circumstellar shells. The IRAS LRS spectrum (Olnon et al., 1986) of the object shows strong silicate dust (O-rich dust) emission feature at 9.7 μm indicating the population of group E in the LRS spectral classification (see, Kwok et al. 1997). In addition, simultaneous observations of H_2O and SiO masers are found recently toward the object using the individual 21 m telescopes of the Korean VLBI Network (Cho et al., 2017). The radial velocity of the object is 12.6 km/s (Lewis, 1997) and outflow velocity of the shell is 10.6 km/s (Lewis, 1994). The other identifications of the object are IRAS 18278+0931, USNO-B1.0 0995-00363063 and 2MASS J18301210+0933425.

OH/IR stars are a class of long-period (several hundred days) large amplitude (1 mag bolometric) variables with huge mass-loss rates ($> 10^{-5}$ $M_\odot yr^{-1}$, Baud & Habing 1983) representing the thermally pulsing asymptotic giant branch (TP-AGB) phase, which is the last evolutionary stage of low- to intermediate-mass ($0.8 \leq M \leq 8$ $M_\odot$) stars before becoming into planetary nebulae. The detail depiction of pulsation mechanism and mass-loss process are presented in Chapter 1. Due to high mass-loss rates and dust formation circumstellar envelops (CSE) develop, which eventually become opaque to visible light (Habing, 1996) and emit at infrared (IR) wavelengths (Bedijn, 1987). The OH/IR stars are oxygen-rich (C/O<1, O-rich), and they often show OH (at 1612, 1665, and 1667 MHz), H_2O (mostly at 22 GHz), and SiO (mostly at 43 and 86 GHz) maser from the circumstellar thin shell (Elitzur, 1992; Gray, 2012). Thus, the OH counterpart of the name comes because of the OH maser emission in those stars (Blommaert et al., 2018).

Almost all known OH/IR stars are found through either 1612 MHz OH surveys especially in the Galactic plane and the Galactic center [e.g., Baud et al. 1981; Zijlstra et al. 1989; Sevenster et al. 2001) or through various systematic surveys (for example, the Arecibo surveys − Eder et al. 1988; Lewis et al. 1990b; Chengalur et al. 1993b], which have been conducted for those sources with IRAS (IRAS Point Source Catalogue (1988)) colours resembling those of OH/IR stars (see, e.g., Olnon et al. 1984) as they emit most of the

energy between 2 and 60 μm by the circumstellar dust (e.g., Kleinmann et al. 1981). The database of OH masers in circumstellar shells can be found in Engels & Bunzel (2015). Sevenster et al. (1995) found two very distinct samples regarding density distribution, kinematics and astrophysical properties of galactic OH/IR stars: one very close to the galactic centre and the other in the bulge and the disk. Studies based on galactic bulge (e.g., Blommaert et al. 2018) and galactic disk (e.g., Habing 1988) OH/IR stars showed their very similar luminosity distribution with a peak at around 5000 $L_{\odot}$ indicating low initial mass ($< 2\ M_{\odot}$) population of AGB stars. However, an appreciable number of OH/IR stars with a luminosity well-above 10 000 $L_{\odot}$ exist in both galactic disk (e.g., Habing 1988) and bulge (e.g., Ojha et al. 2007), which indicate an evolution from the massive progenitors. These high luminous stars are classified as a "high-luminosity group" by Jiménez-Esteban & Engels (2015). It is expected that low-mass AGB stars experience moderate mass-loss and form thin CSE, whereas massive AGB would reach the high mass-loss regime, form thick CSE and become optically obscured (Jiménez-Esteban & Engels, 2015; Mouhcine, 2002). Furthermore, Chen et al. (2001) and Likkel (1989) observed the reddest, hence highest mass-loss rates OH/IR stars, in the galactic disk and supported the evidence of higher progenitor masses. Moreover, the reddest OH/IR stars lie preferentially in the galactic plane, and thus the OH/IR stars at high galactic latitudes are unlikely to evolve as very red objects (e.g., Eder et al. 1988). Those massive objects are young and show larger expansion velocity than other OH/IR stars (Baud et al., 1981; Baud & Habing, 1983).

Several molecules (e.g., TiO, VO, H_2O, and CO), which are formed in the extended atmospheres of AGB stars due to high mass loss and the relatively low surface temperature, play important roles in the spectral appearance of stars at optical and NIR wavelengths (Lançon & Wood, 2000; Gautschy-Loidl et al., 2004; Aringer et al., 2009b; Nowotny et al., 2010). It has been found that the shapes of the spectral energy distributions (SEDs) and the depth of the silicate features (at 9.7 and 18 μm) show significant variation mainly due to change in the properties of the central star as well as CSE around the OH/IR stars, depending on the pulsation phase (e.g. Le Bertre 1988; Suh et al. 1990; Suh & Kim 2002).

The study based on extensive photometric and spectroscopic observations with the pulsation phase provide a wealth of information about the light curve, temporal variation on atmosphere, fundamental parameters, and mass-loss of AGB stars (Hinkle et al., 1982; Alvarez et al., 2000; Castelaz & Luttermoser, 1997; Castelaz et al., 2000; Lançon & Wood, 2000; Tej et al., 2003a). The photometric light curves provide the oscillating behaviour of brightness, surface temperature, radius, atmospheric structure and opacity (Le Bertre, 1992; Castelaz et al., 2000). The variation of spectral features with pulsation phase is

sensitive to the pulsation history as well as provides the local information (Alvarez et al., 2000; Ghosh et al., 2018). Moreover, individual spectral features vary considerably and independently (Alvarez & Plez, 1998; Ghosh et al., 2018) over the phase. However, estimation of fundamental parameters is a challenging task considering the effects, like wavelength dependent diameter variation (e.g., Thompson et al. 2002; Ireland et al. 2004; Mondal & Chandrasekhar 2005), dust and water-absorption in NIR spectra (Schultheis et al., 2003; Vanhollebeke et al., 2006). The theoretical self-excited dynamical models of O-rich stars have been developed and applied successfully to constrain the observations (Tej et al., 2003a; Ireland et al., 2004; Wittkowski et al., 2008). However, no model still can interpret the exact dynamical variation of AGB atmosphere or spectral variations at late spectral type with pulsation. Such time-dependent or phase-dependent data are sparse in the literature and much needed to set constraints to model the complex convective atmosphere of the AGB stars.

Considering the rare time-dependent study of AGB star in the literature, we have performed phase-dependent photometry and spectroscopy to characterize an object MASTER-Net Optical Transient J212444.87+321738.3, which has been presented in Chapter 5. The object was selected from the list of optical transients discovered by MASTER based on large $(J - K)$ colour index, which turns out to be a classical O-rich Mira variable. The atomic and molecular features (e.g., TiO, Na I, Ca I, H_2O, CO) in 0.6−2.5 μm range of the object display significant variation over the pulsation period of 465 days. Immediately, the question arises whether the time-dependent variations of OH/IR stars are similar to classical Mira variables?

To counter this question, we have studied a known OH/IR star, J1830+09, selecting from MASTER optical transient alert. Following the OT announcement, we have started spectro-photometric monitoring observations on the object in optical/NIR wavelength using different telescope facilities. We present here pulsation phase-dependent photometric and spectroscopic characterisation of MASTER OT J1830+09. The main motivation of this paper is to characterize an OH/IR star as well as understand the variations of spectral features with the pulsation phase.

6.2 Observations and data reduction

The optical photometric and spectroscopic observations were carried out using HFOSC on the 2.01 m HCT at Hanle. The source was monitored in the optical R- and I-band over 11 epochs during 2014 August 19 − 2018 April 17 using 2K × 2K HFOSC imaging CCD (field of view of about 10 × 10 arcmin^2 with a plate scale of 0.296 arcsec pixel^{-1}).

For spectroscopy, we have used Grism no. 8 (Gr#8, 580−900 nm) of the instrument with a resolving power of ≈ 2200[1].

Table 6.1: Log of photometric and spectroscopic observations

Date of Observation	Observation Type	Spectral Band	Int. Time (s)	No of Frames	Telescope	Remarks
2013-May-28	Photometry	$J/H/K$	1/1/0.4	5* [15/15/25]	1.2 m Mt. Abu	clear sky
2014-Aug-19	Photometry	R/I	80/4	3/3	2 m HCT	clear sky
2015-July-05	Photometry	R/I	150/20	3/3	2 m HCT	clear sky
2015-Oct-06	Photometry	R/I	150/20	2/2	2 m HCT	clear sky
2015-Nov-19	Photometry	R/I	150/20	1/2	2 m HCT	clear sky
2016-Feb-15	Photometry	R/I	100/12	3/3	2 m HCT	clear sky
2016-May-08	Photometry	R/I	100/5	3/3	2 m HCT	clear sky
2016-Jun-26	Photometry	R/I	100/5	3/3	2 m HCT	clear sky
2016-Nov-02	Photometry	R/I	120/7	3/3	2 m HCT	clear sky
2017-Apr-07	Photometry	R/I	60/600	2/2	2 m HCT	clear sky
2017-Jun-25	Photometry	R/I	20/500	2/2	2 m HCT	clear sky
2018-Apr-17	Photometry	R/I	20/400	2/2	2 m HCT	clear sky
2013-May-28	Spectroscopy	$H/K/KA$	120/120/120	2*1	1.2 m Mt. Abu	clear sky
2013-Oct-15	Spectroscopy	600−900 nm	2400	1	2 m HCT	clear sky
2013-Nov-07	Spectroscopy	600−900 nm	1800	1	2 m HCT	clear sky
2014-Aug-19	Spectroscopy	600−900 nm	300	1	2 m HCT	clear sky
2014-Oct-29	Spectroscopy	HK	100	2*5	2 m HCT	clear sky
2015-Mar-02	Spectroscopy	HK	100	2*3	2 m HCT	clear sky
		600−900 nm	1800	1		
2015-July-05	Spectroscopy	600−900 nm	1500	1	2 m HCT	clear sky
2015-Oct-07	Spectroscopy	HK	100	2*5	2 m HCT	clear sky
		600−900 nm	2000	1		
2015-Nov-20	Spectroscopy	HK	100	2*7	2 m HCT	clear sky
2016-Feb-15	Spectroscopy	600−900 nm	2000	1	2 m HCT	clear sky
2017-Apr-07	Spectroscopy	HK	100	2*11	2 m HCT	clear sky

The NIR photometric and spectroscopic observations were acquired using NICMOS-3 on 1.2 m Mt. Abu telescope, India, and TIRSPEC on 2.01 m HCT at Hanle, India. The NICMOS3 has 256 × 256 HgCdTe detector array and provides a resolution R ≈1000; while TIRSPEC has 1024 ×1024 Hawaii-1 array and provides a resolution ≈1200. The spectral coverage of NICMOS-3 were on H and K-bands. The TIRSPEC spectra were taken at HK cross-disperse mode. Photometric observations (on 2013 May 28) in JHK'-bands were taken in five dithered positions, and multiple frames are taken in each dithered position to get better SNR. In spectroscopic observing mode, the spectra were taken at two different positions along the slit one after another, immediately to subtract the sky, and several frames were observed to improve SNR. The estimated SNR is ∼50−80 (H-band) and ∼70−120 (K-band) for TIRSPEC data, while the SNR is ∼30 (HK) for NICMOS-3 data. A log of our observations is mentioned in Table 6.1.

The photometric and spectroscopic data were reduced with the help of standard tasks of IRAF. The TIRSPEC data was reduced with TIRSPEC pipe-line (Ninan et al., 2014). The additional details of the reduction can be found in Chapter 2.

[1] `https://www.iiap.res.in/iao_hfosc`

6.3 Result and discussion

6.3.1 Optical light curves and period

The optical light curves in the R- and I-band are shown in Figure 6.1 and time-series RI magnitudes are listed in Table 6.2. To estimate the period of the object, we applied Fourier decomposition technique following Ngeow et al. (2013),

$$m\ (t) = A_0 + \sum_{\kappa=1}^{N} A_\kappa sin(\kappa\omega t + \phi_\kappa) \tag{6.1}$$

where $\omega = 2\pi/P$, P is the period in days, A_κ and ϕ_κ represent the amplitude and phase−shift for κ^{th}-order, respectively, and N is the order of fit. We fit the light curves considering up to second order terms of the equation, and find the best fit from χ^2 minimization technique. The best-fit light curve provides a period of 575 ± 30 days. The amplitude of variability is ∼4.00 mag and ∼3.5 mag in the R- and I-band, respectively. We find the greater fall time (F_t, 350 days) of the light curve than the rise time (R_t, 225 days). The phase of the light curve can be calculated following the equation as,

$$\begin{aligned} \phi(t) &= \frac{\phi}{2f} && 0 \leq \phi < f \\ &= \frac{\phi - 1}{2(1-f)} + 1 && f \leq \phi \leq 1 \end{aligned} \tag{6.2}$$

where $\phi = (t - t_0)/P$, t_0 is the phase and f is asymmetry parameter which represents the risetime over the total period. The value of f lies between 0 to 1. The light curves starts ($\phi = 0$) at $t = 2456329$ JD. Note that we determined all the phase from the Equation 6.2.

The NIR photometric observations were carried out on 2013 May 28.92 UT yielding magnitudes of $J = 6.46 \pm 0.04$ mag, $H = 5.15 \pm 0.05$ mag, $K = 4.37 \pm 0.04$ mag. Comparing with 2MASS JHK measurements (made on 1999 July 23 yielding magnitudes of $J = 7.02 \pm 0.03$, $H = 5.47 \pm 0.03$ and $K = 4.52 \pm 0.02$, Cutri et al. 2003) and fitting of two available NIR data points with the same optical period indicates the NIR amplitudes in $\Delta J \approx 1.80$ mag, $\Delta H \approx 1.10$ mag, and $\Delta K \approx 0.50$ mag.

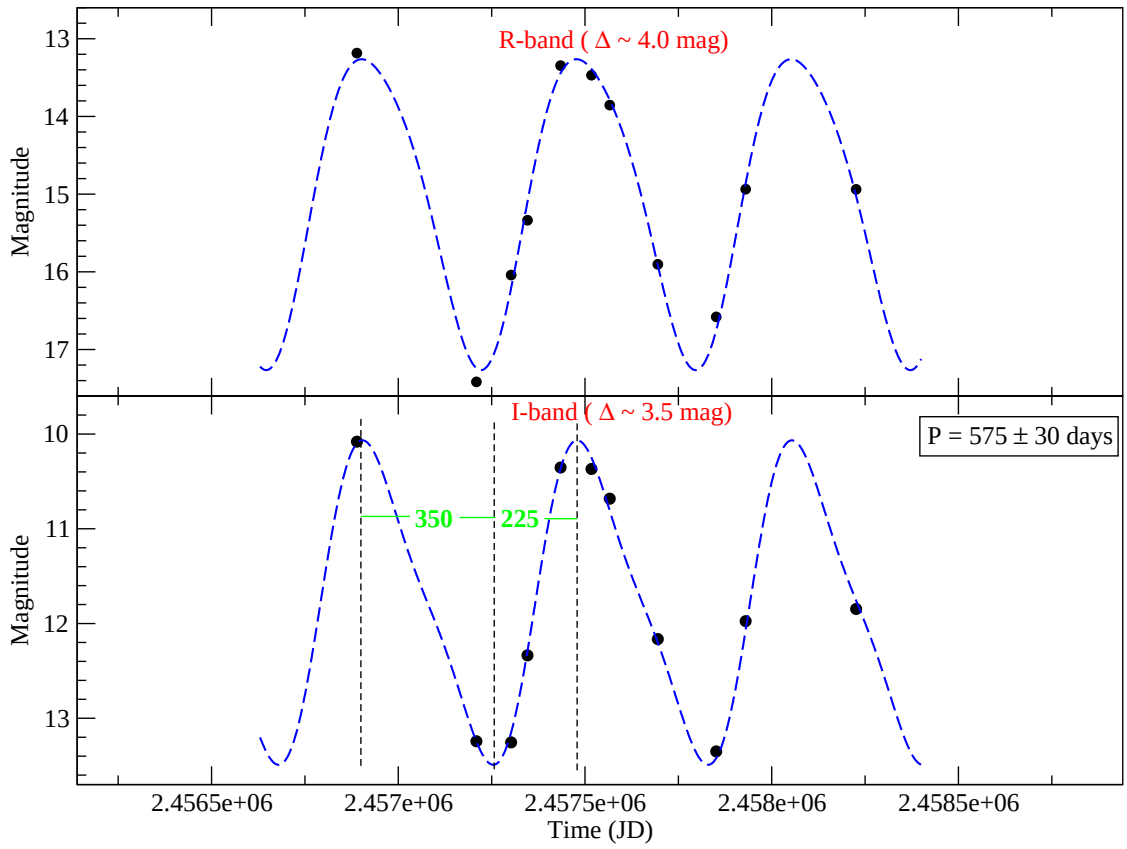

Figure 6.1: Figure shows the optical light curves of J1830+09 with fitting using Equation 6.1 in R-band (top) and I-band (bottom), where the filled circles are our observed data points, while the dashed lines are fitted light curves with P= 575 days. The vertical lines are marked on the maximum and minimum light positions to show the different rise and fall time.

Table 6.2: Optical RI photometry

Date of Obs. (UT)	Optical phase	Telescope/Instrument	R (mag)	I (mag)	$(R-I)$ (mag)
2014 Aug 19.75	0.97	HCT/HFOSC	13.185 ± 0.003	10.080 ± 0.002	3.105
2015 July 05.67	1.44	HCT/HFOSC	17.416 ± 0.018	13.243 ± 0.003	4.173
2015 Oct 06.69	1.61	HCT/HFOSC	16.041 ± 0.005	13.254 ± 0.004	2.787
2015 Nov 19.55	1.70	HCT/HFOSC	15.337 ± 0.007	12.336 ± 0.004	3.001
2016 Feb 15.98	1.90	HCT/HFOSC	13.346 ± 0.005	10.353 ± 0.003	2.993
2016 May 08.83	2.05	HCT/HFOSC	13.469 ± 0.009	10.369 ± 0.005	3.100
2016 Jun 26.83	2.12	HCT/HFOSC	13.854 ± 0.003	10.682 ± 0.003	3.172
2016 Nov 02.53	2.31	HCT/HFOSC	15.903 ± 0.011	12.164 ± 0.003	3.739
2017 Apr 07.92	2.55	HCT/HFOSC	16.580 ± 0.007	13.350 ± 0.004	3.234
2017 Jun 25.65	2.72	HCT/HFOSC	14.936 ± 0.005	11.975 ± 0.003	2.961
2018 Apr 17.60	3.25	HCT/HFOSC	14.939 ± 0.005	11.847 ± 0.004	3.092
Average	...	...	15.001	11.787	3.214

6.3.2 Distances and luminosity

The distance to the source is determined using the period−luminosity (PL) relation of Ita & Matsunaga (2011) based on O-rich Mira variables in the Large Magellanic Cloud

(LMC) with periods longer than 400 days ($\log P \sim 2.6$). Adopting the distance modulus of the Large Magellanic Cloud (LMC) to be 18.50 ± 0.02, the PL relation

$$M_K = (-6.850 \pm 0.901) \log P + (9.725 \pm 2.493) \tag{6.3}$$

provides the absolute K-band magnitude of the source to be $M_K = -9.18 \pm 0.34$ mag, which is consistent with the derived value from the quadratic PL relation for O-rich Mira variables in Yuan et al. (2017). The galactic interstellar extinction in the direction towards the source is A_V=0.56 (A_K=0.06; Schlafly & Finkbeiner 2011) or A_V=0.65 (A_K=0.08; Schlafly & Finkbeiner 2011). Applying the relation $m_k - M_K = 5 \log d - 5 + A_K$ and considering A_K=0.06, we obtain the distance, d, to the source 5.14 ± 0.4 kpc. The uncertainties in the distance measurement come from the estimated period, PL relation and photometric error of calculating K-band magnitude.

We have also estimated the bolometric magnitude M_{bol} using the PL relation of Whitelock et al. (1991) based on LMC O-rich Mira variables with $P < 420$ days (Feast et al., 1989) and galactic disk OH/IR stars with phase-lag distances (van Langevelde et al., 1990) expressed as :

$$M_{bol} = -1.85(\pm 0.24) - 2.55(\pm 0.10) \log P \tag{6.4}$$

The relation provides the bolometric magnitude of $M_{bol} = -5.19 \pm 0.13$ corresponding to the luminosity ∼9350 $L_\odot$, which is consistent with the PL relation of Feast et al. (1989). More discussion on the PL relation is described in the later section.

6.3.3 Spectral Energy Distribution

We made use of broadband optical I-band to far-IR multi-wavelength data and IRAS LRS spectra to create the SED of the source. The fluxes, used here for the SED fit, are obtained from the archival 2MASS (Cutri et al., 2003) at 1.23, 1.66 and 2.16 μm; AllWISE (Cutri & et al., 2013) at 3.35, 4.6, 11.6, and 22.1 μm; the AKARI/IRC (ISAS/JAXA, 2010; Ishihara et al. 2010; Yamamura et al. 2010) at 8.61, 18.4 and 90 μm; and IRAS (IPAC 1992) at 12, 25 and 60 μm data. We also included our three epoch (at the maximum, minimum and middle of the light curve) I-band variability data and one epoch JHK' measurements. The observed I and JHK' magnitudes are converted to flux densities

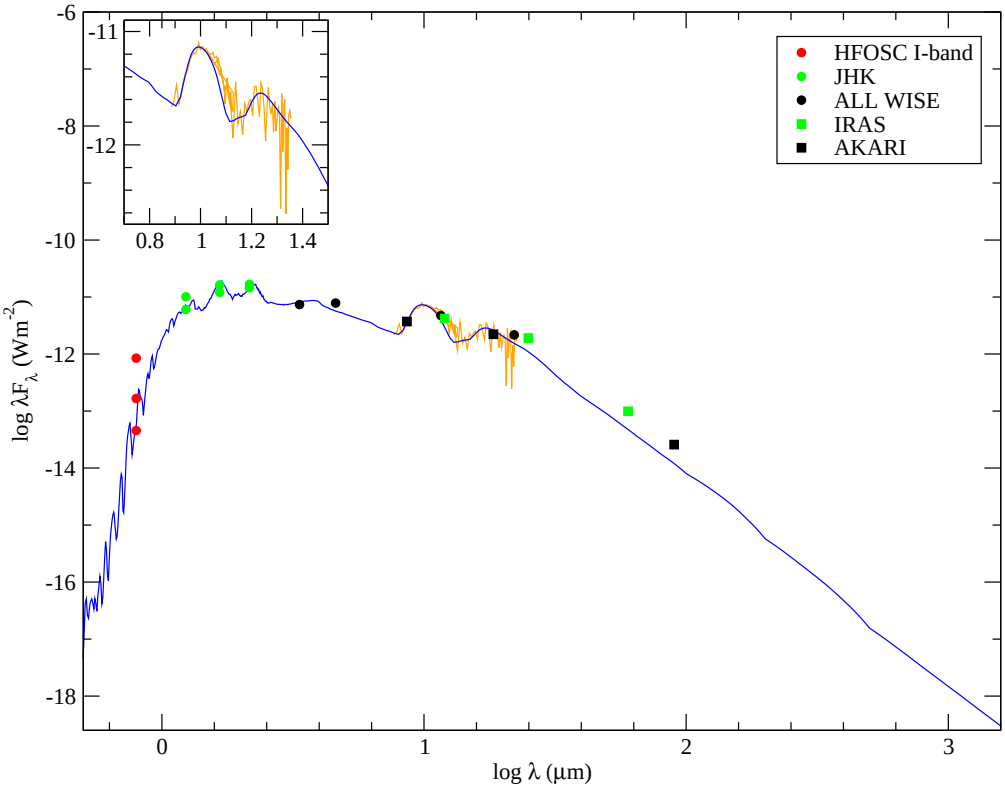

Figure 6.2: The SED of the target is shown here using multi-wavelength data from optical I-band to far-IR, while the inset (top-right) show different data source, e.g., our JHK measurements as well as 2MASS, All WISE, AKARI, IRAS data. The inset in the top-left corner shows the MoD fit of IRAS LRS spectra in zoom.

using the zero magnitudes for Vega, as described in Groenewegen (2006). The IRAS LRS spectrum was taken from the database[2] maintained by Kevin Volks.

To fit the SED, we have used the MoD, which works to find best-fit parameters, e.g., luminosity (L), dust optical depth ($\tau_{0.55}$), dust temperature at the inner radius (T_c) and slope, p, of the density distribution ($\rho \sim r^{-p}$) by using photometric-, spectroscopic- and visibility-data as well as one dimensional intensity profiles in the minimization process. Here, we consider photometric and spectroscopic data as the data of the latter two are unavailable in the literature. In general, the errors of the spectroscopic fluxes are scaled typically by a factor of 0.2 to provide roughly equal weight in the photometry and spectroscopy data to the overall data set (Blommaert et al., 2018). The quality of the fit is obtained through a χ^2 analysis. The additional details about the MoD can be found in Chapter 2.

In the present model, one shell model is considered and the outer radius is set to 2000 times the inner radius, where dust temperature becomes approximately 20 K, typical of

[2] http://isc83.astro.unc.edu/iraslrs/getlrs_test.html

Table 6.3: Parameters of MoD modelling.

Star	L ($L_\odot$)	$\tau_{0.55}$	T_c (K)	p	R_{in} (R_{star})	$\dot{M}_d$ ($10^{-7} M_\odot yr^{-1}$)	ρ (g cm^{-2})	χ^2_{red}
J1830+09	17367 ± 827	9.47 ± 0.58	1200	2	4.38	11.5	2.65	835

Note. The mass-loss rate ($\dot{M}_d$) is estimated by assuming a dust-to-gas ratio of 0.005 and an expansion velocity of 10 km/s.

the ISM. The distance (d) of 5.14 kpc and A_V are adopted as an input to the standard model as discussed in the previous section. The MARCS[3] hydrostatic model atmospheres (Gustafsson et al., 2008b) of 2600 K (and log g = 0.0, 1 M$_\odot$, and solar metallicity) are used for the spectra of the central stars. The adopted dust species are taken as mixture of $Mg_{0.8}Fe_{1.2}SiO_4$:AlO:Fe=100:0:10, calculated using the 'distribution of hollow spheres' (DHS, Min et al. 2003) with a mean grain size a= 0.2 μm and a maximum volume fraction of a vacuum core f_{max}=0.7 μm, that is appropriate for interstellar silicate dust grains (Min et al., 2007). We adopted such dust composition because the OH/IR star is an O-rich source. The L, τ, T_c and p could be fitted or set to a fixed value.

To get the best fit, we generated multiple SEDs considering the dust temperature at the inner radius fixed to 1200 K, assuming r^{-2} density law and making the L and $\tau_{0.55}$ as free parameters. The MoD fit SED is shown in Figure 6.2. The χ^2 of the fit is typically large as the object is a large amplitude variable and non-simultaneous taking of the photometric data from different catalogues. The provided errors are therefore internal errors scaled to a reduced χ^2 of 1. The resulting parameters of the best-fit SED are listed in Table 6.3.

Figure 6.3 shows the comparison between various PL relations available in the literature, where we have placed the luminosity (M_{bol} = −5.86) of the object obtained from the SED modelling, which we adopt here. The obtained luminosity falls well above that (M_{bol} = −5.2) from the PL relation of Whitelock et al. (1991) and that (M_{bol} = −5.4) from the extrapolated PL relation of Feast et al. (1989). However, our result is consistent the luminosity (M_{bol} = −6.2) from the PL relation of Hughes & Wood (1990) and that (M_{bol} = −6.0) from Ita & Matsunaga (2011) derived with O-rich LMC Mira variables of period > 420 days. Thus, our object fits very well into the PL relation found for Mira variables in the LMC indicating the evolution of OH/IR stars from Mira variables and could be considered as an extension of the optically known Mira variables toward greater masses and longer periods. Furthermore, it has to be noted that the bolometric magnitudes derived from different PL relations are about 1 mag, which could be pulsation dependent variation of variable OH/IR stars (Engels et al., 1983; Blommaert et al., 1998). It is

[3] `http://marcs.astro.uu.se/`

also unlikely to exist any unique PL relation for all AGB stars, and mass and evolution of AGB stars might play a significant role in the PL diagram (van der Veen, 1989; Whitelock, 1995; Blommaert et al., 1998).

To study the galactic location of our object, we have estimated the z-scale height of the object following Jura & Kleinmann (1992), which is estimated to be ∼300 pc. The estimated scale height suggests the thin disk population (Habing, 1988; Jura & Kleinmann, 1992; Jurić et al., 2008). It is also worth to mention here, the object does not satisfy the colour criteria of Habing et al. (1985) to be a bulge star. Furthermore, the analysis of the flux distribution of IRAS sources suggests that the objects with $F_{12\mu m} > 12$ are likely stars from the galactic disk population (Blommaert et al., 2018). Moreover, van der Veen & Habing (1990) considers the area ($15^{\rm deg} < l \leq 30^{\rm deg}$, $2^{\rm deg} < b \leq 10^{\rm deg}$), where our source belongs, contains only a contribution from the disk. We thus conclude that our object is an OH/IR star in the galactic thin disk.

In this section, we compare important parameters of our object with known OH/IR stars in the galactic disk to understand the AGB evolution. The luminosity of the object obtained from the SED modelling is 17367 ± 827 $L_{\odot}$. Thus, the object belongs to a member of high-luminosity disk OH/IR stars population. Also, the estimated period of the object, 575 ± 30, agree well as the distribution of disk OH/IR stars span a wide range of periods from 200 to 2200 days (Engels et al., 1983; Herman et al., 1984; van Langevelde et al., 1990). It is to be noted that the disk OH/IR stars extend from shorter periods nearby optical Mira variables with P < 300 days having weaker OH emission to longer period OH/IR stars having strong OH emission. Furthermore, General Catalogue of Variable Stars (Kholopov et al., 1998) listed around 50 Arecibo sources (OH-emission) having period in between 145−660 days on the basis of optical observations and found that they are mostly well known Mira variables.

A number of studies on mass-loss rate found that it strongly depends on the pulsation period of the AGB star (e.g., Vassiliadis & Wood 1993; De Beck et al. 2010). De Beck et al. (2010) showed that the mass-loss rate linearly increases with the period of AGB stars below 850 days and becomes constant from approximately 850 days onward. Following De Beck et al. (2010), we have estimated the mass-loss rate of the object, $\sim 3.95\times10^{-06}$ $M_{\odot}$/yr. The MoD fit yields the mass-loss rate, 11.5×10^{-07} $M_{\odot}$/yr, which we adopt here. Considering the scatter around the relation (up to a factor of 10) in De Beck et al. (2010), we can remark that the mass-loss rate obtained from both methods are consistent.

Following the mass-luminosity relation in Figure 6 of Hughes & Wood (1990), the object having $P = 575$ days and $M_{bol} = -5.86$ lies in the mass (M) range of 2.5−4.0 $M_{\odot}$. Moreover, it is consistent with the fact that OH/IR stars with $P < 800$ days have mass

range in between 2 to 3 $M_{\odot}$ (Blommaert et al., 1994; Wood et al., 1998). The presence of masers and a signature of silicates in the IRAS LRS spectra imply the O-rich chemistry of the object. Furthermore, our optical/NIR spectroscopic observations confirm the O-rich nature of the object, which is described in the later section. In contrast, high-luminous ($\sim$10000 $-$ 25000 $L_{\odot}$) objects with such mass-range (2$-$4 $M_{\odot}$) and solar metallicity end their life in AGB phase as C-rich stars (Marigo & Girardi, 2007; Jiménez-Esteban & Engels, 2015). Possible reasons might be that the object belongs to an earlier evolutionary phase with O-rich chemistry or the transition to C-rich chemistry might be delayed due to super-solar metallicity as predicted by the models (Weiss & Ferguson, 2009).

OH/IR stars in the galactic bulge provides the advantage of a common distance (van der Veen & Habing, 1990), whereas the uncertain distances in the galactic disk stars are the main drawback of mean luminosity determination. As discussed in the earlier section 6.3.2, the distance to the object is estimated from the distance modulus. Alternatively, we can estimate the distance from the luminosity and the bolometric flux. We have used the luminosity as provided by MoD fit, and the bolometric flux is calculated from IRAS 12 μm flux density following the relation in Nakashima et al. (2000) and the bolometric correction from van der Veen & Breukers (1989). Then, the relation, $d = \sqrt{L/(4\pi F_{bol})}$ provides the distance to the object is about 5.3 kpc, which is consistent with the previous estimation. However, the distance calculation in this method is based on two assumptions $-$ the object only emits in the mid-infrared region and interstellar extinction is negligible at these wavelengths. It has to be noted that the parallax measurement for this star is available in the Gaia database [second data release, Gaia Collaboration 2018 (Gaia Collaboration et al., 2018b)]. However, the derived distance from PL-relation ($\sim$5.14 kpc) is inconsistent with the estimated distance ($\approx$ 990 pc) from the Gaia parallax by Bailer-Jones et al. (2018). To check the reliability of the Gaia parallax estimated distances in Bailer-Jones et al. (2018) of such AGB stars, we compile 274 AGB stars from various literature and compare the estimated distances from Gaia parallax (Bailer-Jones et al., 2018) to the distances measured with other methods as shown in Figure 6.3. We find that distances from Gaia parallax are mostly inconsistent with the distance by other techniques beyond 2 kpc. Therefore, care should be taken to consider Gaia parallax of the AGB stars beyond 2 kpc. Possible reasons might be the resulting displacement of the stellar photocentre due to the convection-related variability of the complex stellar surface of AGB stars Chiavassa et al. (2018).

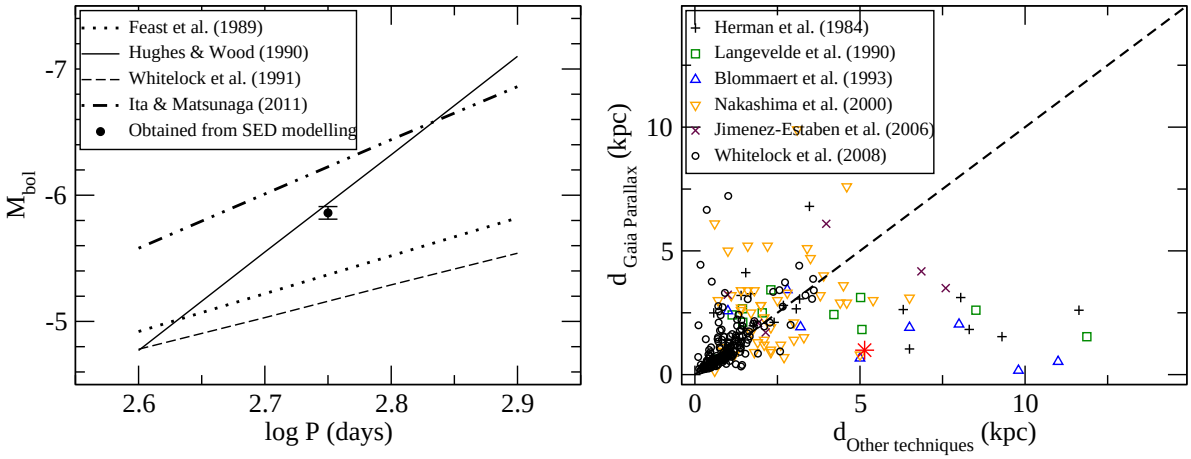

Figure 6.3: The left panel shows the comparison between various PL relations and the luminosity obtained from SED modelling, and the estimated distances of AGB stars from Gaia parallax are compared to the literature in the right panel. The black dot in the left panel and star symbol in the right panel refer to J1830+09. The estimated distances from Gaia parallax ($d_{GaiaParallax}$) are taken from Bailer-Jones et al. (2018), and $d_{Other\ techniques}$ represent the distances taken from various literature (19 OH/IR stars from Herman et al. (1984), 11 OH/IR stars from van Langevelde et al. (1990), 8 OH/IR stars from Blommaert et al. (1993), 46 AGB stars from (Nakashima et al., 2000), 6 AGB stars from Jiménez-Esteban et al. (2006a) and 184 AGB stars from (Whitelock et al., 2008)). For Jiménez-Esteban et al. (2006a) only, we estimated distances of AGB stars from provided periods in that paper using the P-L relation of Ita & Matsunaga (2011).

6.3.4 Optical/NIR spectroscopic studies

The time-dependent spectroscopic observations, however very rare, provides important information about the stellar interior and dynamical atmosphere of AGB stars. The optical and NIR spectra of the object with variability phases are shown in Figure 6.4 and Figure 6.5, respectively. The spectra show lots of atomic or/and molecular features as commonly seen in O-rich LPVs, like molecular absorption bands of TiO and VO in the wavelength range of 7000 to 9000 Å (Castelaz et al., 2000; Rayner et al., 2009; Bessell et al., 1989; Fluks et al., 1994; Ghosh et al., 2018), ^{12}CO-second overtone series at 1.5582, 1.5780, 1.5982, 1.6189, 1.6397, 1.6610, 1.6840, 1.7067 μm including OH molecular bands all over the H-band (Lançon & Wood, 2000; Rayner et al., 2009), and ^{12}CO first overtone series at 2.2935, 2.3227 μm as well as neutral atomic lines of Na I doublet at 2.20 μm, Ca I triplet at 2.26 μm and Mg I at 2.28 μm in the K-band (Rayner et al., 2009; Ghosh et al., 2018). The second overtone series develop to those objects having a photospheric temperature $\leq$ 5000 K, and their strength is dependent on the photospheric temperature (Lançon et al., 2007).

It is found that the two ends of the H- and K-band spectra bend downwards due to broad H_2O absorption features centred at 1.4 μm, 1.9 μm & 2.7 μm in our spectral coverage indicating the overall change of the low-resolution continuum shape (Rayner et al., 2009;

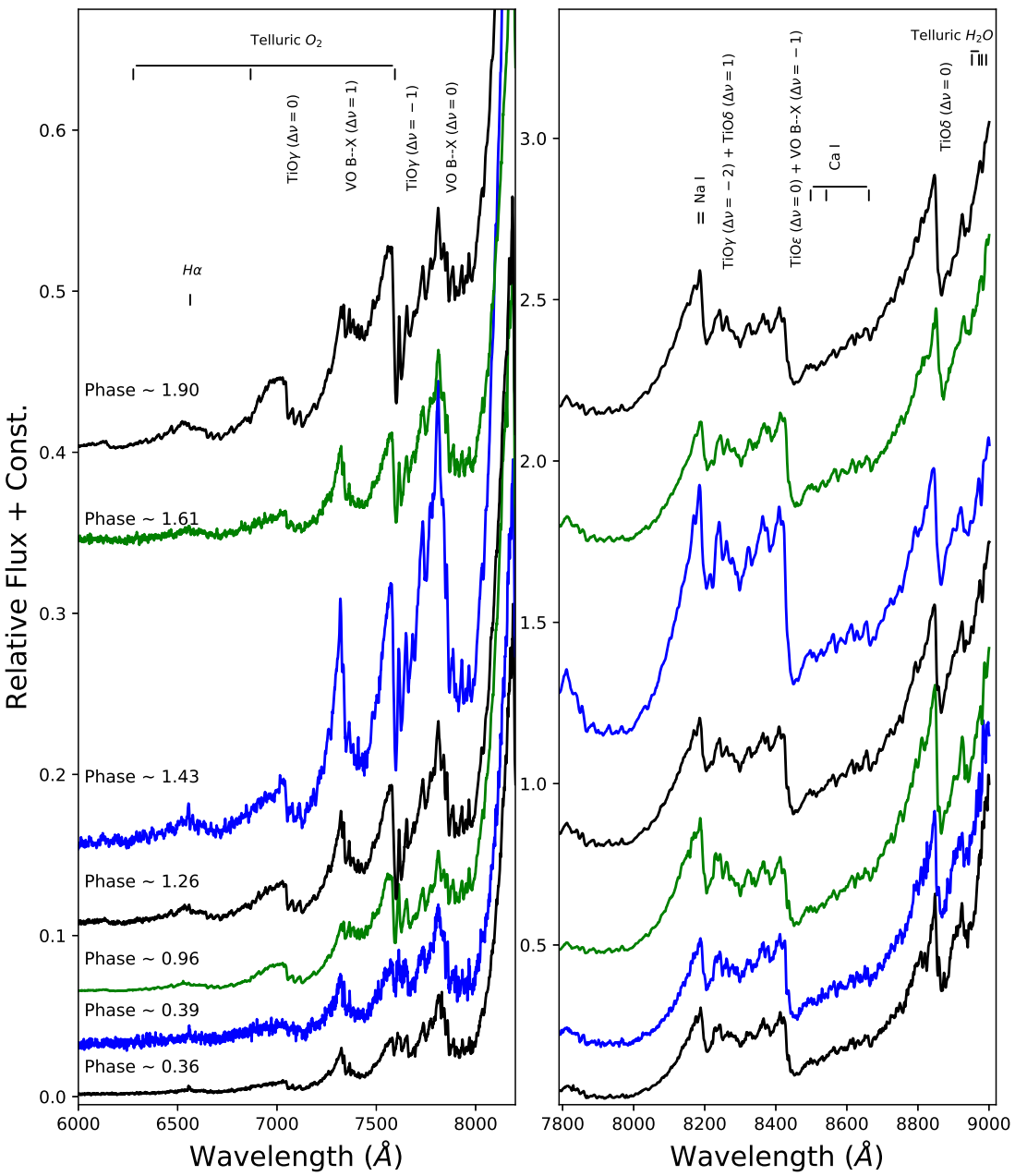

Figure 6.4: The optical spectra of the object are presented in the range 6000−9000 Å, which show visible features of TiO and VO bands at different phases. The spectra have been normalized to unity at 9165 Å, and offset by constant values 0.0, 0.025, 0.065, 0.105, 0.140, 0.335, 0.40 (left panel) and 0.0, 0.15, 0.42, 0.75, 1.05, 1.70, 2.05 (right panel) respectively with respect to the bottom-most spectra.

Ghosh et al., 2018). Moreover, the depth of water bands, hence the curvature, varies with phases and becomes strongest at the minimum light (Strecker et al., 1978).

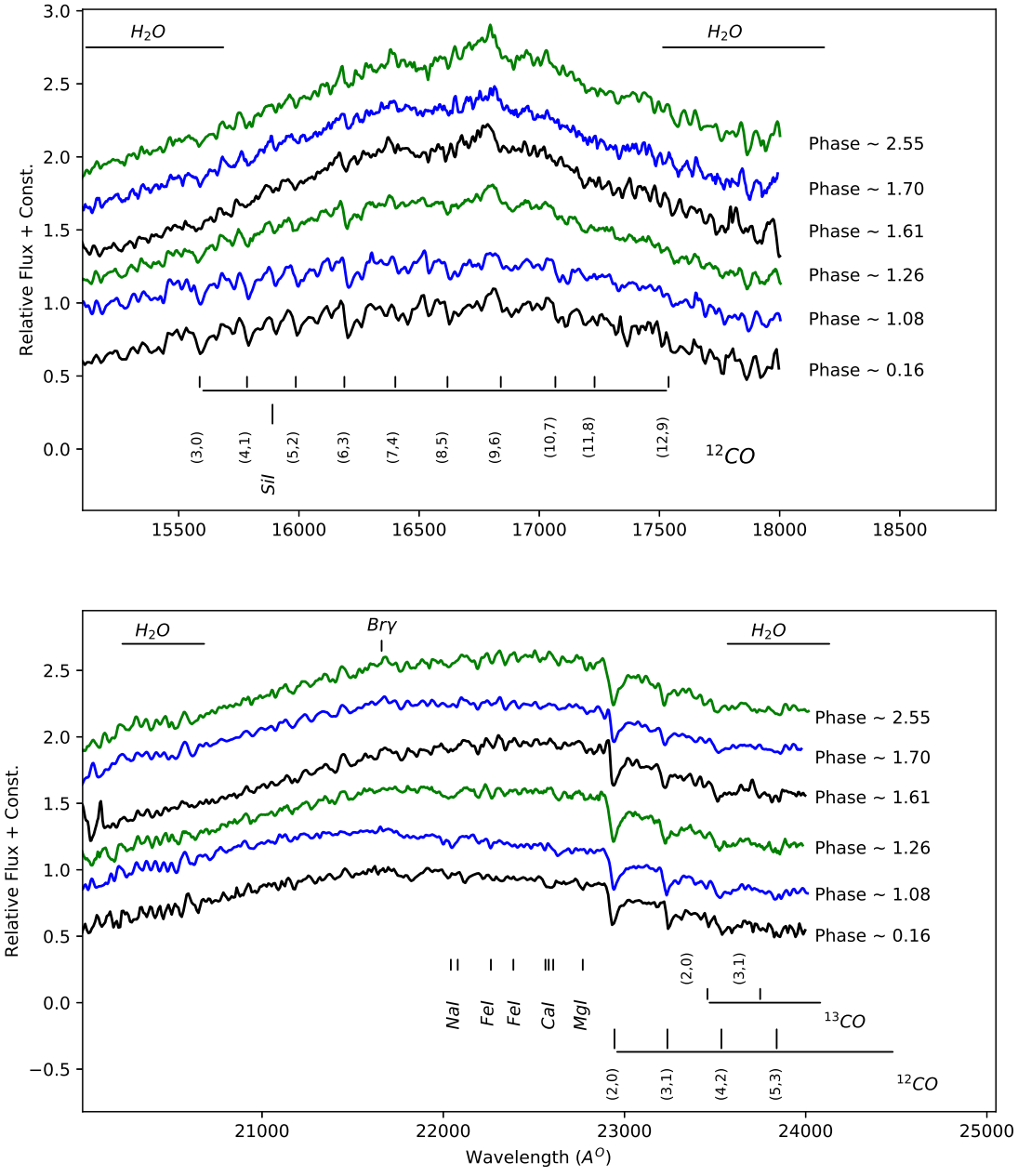

Figure 6.5: The NIR HK-band spectra in the wavelength range 1.50−2.39 μm at six different phases are shown here in the 1^{st} and 2^{nd}, respectively. The NIR spectra at the bottom (phase ∼0.16) are taken with the NICMOS-3 instrument on 1.2 m Mt.Abu telescope, and rest are observed with TIRSPEC instrument on 2.0 m HCT. The H-band spectra in the wavelength range 1.52−1.80 μm show strong four ^{12}CO second overtone bands including several OH lines. In the K-band spectra, the ^{12}CO first overtone bands are dominated features in the spectra, and Na I, Ca I and Mg I are seen at 2.20 μm, 2.26 μm and 2.28 μm, respectively. The spectra have been normalized to unity at 16500 Å (H-band), 21700 Å (K-band), and offset by constant value 0.30 with respect to the bottom-most spectra of the same panel.

Phase dependent spectral variability

Multi-epoch optical/NIR spectroscopic studies on Mira variables at different variability phases probe the dynamic stellar atmosphere and help us also to understand the pul-

sational related variations of fundamental parameters. The variation in the absorption depth of TiO and VO with T_{eff} is well documented from long before (Merrill et al., 1962). Lockwood (1972) found that TiO band-strength indices decrease in stars later than M7, and it saturates in M9 Mira variables. We explore the phase (optical) variation of $[TiO]_2$ index centred at 7100 Å (O'Connell, 1973), and $[TiO]_3$ index of triple-headed absorption bands at 8433, 8442, 8452 Å (Zhu et al., 1999). The $[TiO]_3$ index shows significant variation with the pulsation phase, it increases as the visual brightness decreases as shown in Figure 6.6. However, $[TiO]_2$ index shows no significant variation over the phase. Furthermore, we measure the flux ratio ($S_{2/3,Sp}$) of two strong absorption bands 770−807 nm and 829−857 nm (see Figure 6.4) that is actually related to the spectral type of static giants (Fluks et al., 1994). The $S_{2/3,Sp}$ shows no pronounce variation, rather becomes constant over phase as shown in the Figure 6.6. This is because of the saturation effect of TiO bands.

Table 6.4: Definitions of spectral bands

Feature	Bandpass (μm)	Continuum bandpass (μm)	Ref
$[TiO]_3$	0.8455−0.8725	0.8390−0.8410, 0.8700−0.8725	1
Na I (2.21 μm)	2.2040−2.2107	2.1910−2.1966, 2.2125−2.2170	2
Ca I (2.26 μm)	2.2577−2.2692	2.2450−2.2560, 2.2700−2.2720	2
Mg I (2.28 μm)	2.2795−2.2845	2.2700−2.2720, 2.2850−2.2874	3
^{12}CO(3−0) (1.58 μm)	1.5752−1.5812	1.5705−1.5745, 1.5830−1.5870	4
^{12}CO(6−3) (1.62 μm)	1.6175−1.6220	1.6145−1.6175, 1.6255−1.6285	5
^{12}CO(2−0) (2.29 μm)	2.2910−2.3020	2.24200−2.2580, 2.2840−2.2910	4
^{12}CO(3−1) (2.32 μm)	2.3218−2.3272	2.2325−2.2345, 2.2695−2.2715	4

Note. [1]Zhu et al. (1999); [2]Frogel et al. (2001); [3]Silva et al. (2008); [4]Ghosh et al. (2019); [5]Silva et al. (2008).

We have estimated the EWs of the metallic lines Na I at 2.206 μm, Ca I at 2.263 μm, and Mg I at 2.28 μm. The selected continuum bands and feature bands for these lines are listed in Table 6.4. To measure EWs, we follow the method as describe in Ghosh et al. (2019) using the IDL script[4] (Newton et al., 2014). The third and fourth panels of Figure 6.6 show their phase variation. Both Na I and Ca I are maximum at the visual maximum and reaches its minimum at the visual minimum. This phase variation suggests the anti-correlation between these two metallic lines and water absorption. This anti-correlated behaviour confirms the trends already found by Lançon & Wood (2000). Moreover, The Ca I and NaI features are very weak and very difficult to measure in low-resolution spectra. Also, these lines are seriously blended with other elements such as Sc, Ti, V, Si, and S at low-temperature (Ramirez et al., 1997), and thus, a significant contribution

[4]https://github.com/ernewton/nirew

of EWs comes from those species. Furthermore, it should be noted that at certain phase EWs of Na I and Ca I becomes negative. Vanhollebeke et al. (2006) also found the negative values of Na I and Ca I for a large fraction of the OH/IR stars. The authors demonstrated that strong water absorption depress the continuum, and consequently, the lines seem to appear in emission. Furthermore, the NIR spectra are strongly affected by the dust formation around the stars. Curiously, the metallic line Mg I shows different characteristic than Na I and Ca I, and shows pronounced variation with phase. This line becomes minimum at the visual maximum and reaches its maximum value after the visual minimum. We have seen the variation of this line with phase somewhat correlates with the variation of water absorption. We anticipate that Mg I can be a good temperature indicator at low temperature, and suggest follow up observation for long-period variables in high-resolution.

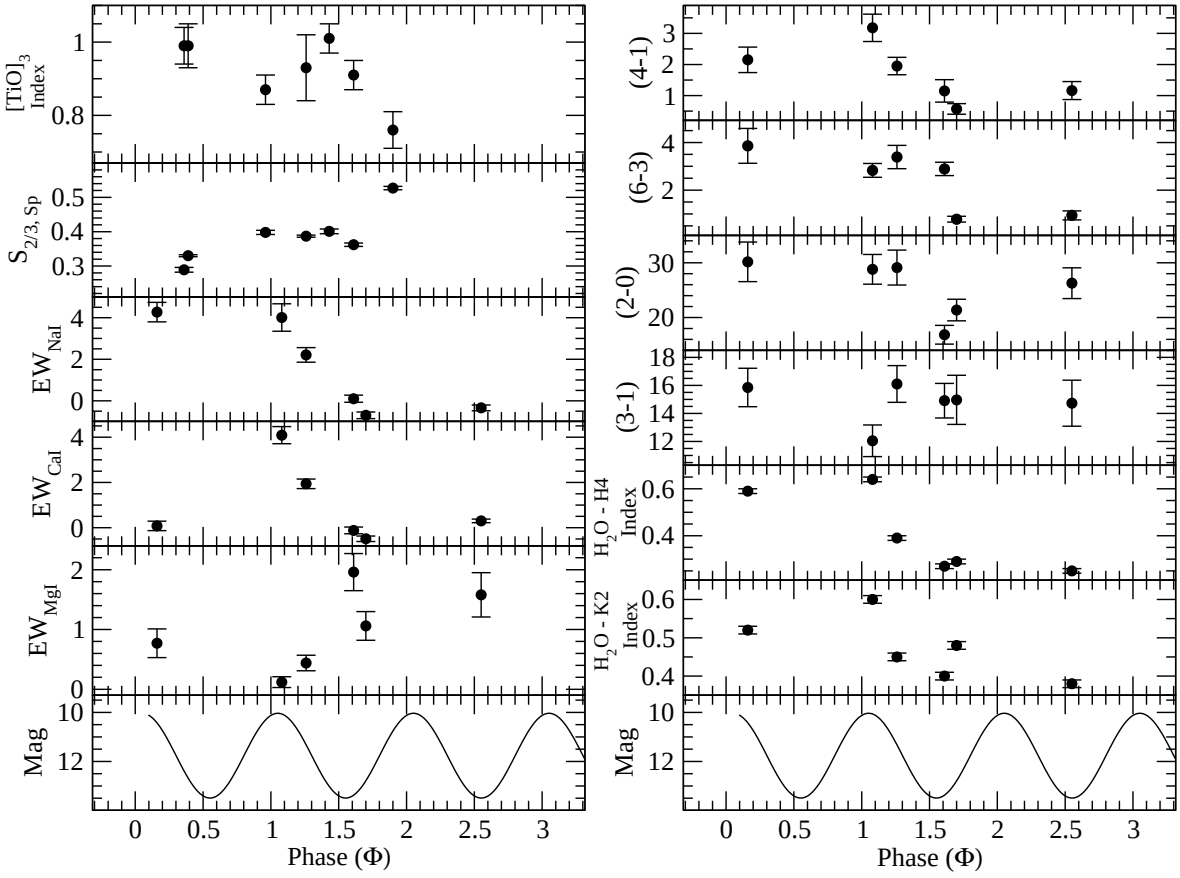

Figure 6.6: The phase variation of $[TiO]_3$, $S_{2/3,Sp}$, Na I, Ca I, Mg I, CO, and H_2O–K2 equivalent width/index are shown with the visual phase. The bottom panel shows I-band light curve.

We explored the phase-dependent variations of the 2−0, 3−1 (first overtone) and 4−1, 6−3 (second overtone) ^{12}CO bandheads. The EWs of CO at different phase are estimated considering the local continuum bands and feature bands as mentioned in Table 6.4, and estimated EWs with phase are shown in Figure 6.6. The EWs of 2−0, 3−1, and 6−3

bandheads does not demonstrate any significant change during the pulsation cycle except around phase 1.7. The EWs of 4−1 first overtone band show significant variation over the pulsation phase and becomes minimum at about phase$\sim$ 1.7. It is noted that the measurement of second overtone bands should be taken as a caution because of difficulty in continuum selection and blending effect from the OH-lines.

It is worth noting that the minimum of metal lines (except Mg I) and CO absorption strength occurs around phase 1.7 i.e., at the rising part of the light curve (see Figure 6.6). Moreover, no reduced absorption strength of these features was found at any other phases in comparison to phase around 1.7. This interesting behaviour may be attributed to the line blurring and veiling (Merrill, 1940; Lançon & Wood, 2000). Furthermore, it suggests that the metal lines and CO bands originate from the deep region of photosphere which undergoes through a certain state at around phase 1.7 due to emerging of a shock wave as predicted from pulsation models (e.g., Bessell et al. 1996). However, our low-resolution spectra limit the investigation of line doubling and the change in velocity profile as studied in the literature (Hinkle & Barnes, 1979b; Nowotny et al., 2010).

To quantify the water absorption at different phases, we determine the H_2O–H4 and H_2O–K2 indices as defined in Ghosh et al. (2018) and Rojas-Ayala et al. (2012), respectively, which represent the curvature variation of the spectra. The variation of these two H_2O–H4 and H_2O–K2 indices with phases are shown in Figure 6.6. The greater value of H_2O indices in H and K bands corresponds to smaller amounts of H_2O opacity. The H_2O–H4 and H_2O–K2 indices significantly vary with the pulsation cycles, the value of indices are strongest at visual maximum while weakest at around phase 1.7 i.e. H_2O opacity is stronger at the visual minimum, which is consistent with the trends found by Strecker et al. (1978). It is known for a long time that LPVs have so strong water bands that the static giant of similar spectral types cannot even reach (Johnson & Méndez, 1970). Moreover, the OH/IR star with pulsation period 575 days show much deeper water absorption at certain phase than the O-rich Mira variable of period 465 days studied in Chapter 5, which suggests the maximum strength of water bands somewhat related to the pulsation period. This result is consistent with the prediction of pulsation models (e.g., Bessell et al. 1996) and observations (e.g., Matsuura et al. 1999). However, the bands' strength of water increase with decreasing metallicity (Decin, 2000), and also LPVs show very different NIR spectra with similar optical spectra and global energy distributions (Lançon & Wood, 2000).

Table 6.5: Phase-dependent variation of spectral features

Date of Obs.	Optical Phase	$[TiO]_3$ Index	$S_{2/3,Sp}$	CO 4−1	CO 6−3	H_2O-H4 Index	Na I 2.20 μm	CaI 2.26 μm	Mg I 2.26 μm	CO 2−0	CO 3−1	H_2O-K2 Index	Sp. $Type^1$
2013 May 28.92	0.16	...	...	2.15 ± 0.41	3.86 ± 0.73	0.59 ± 0.01	4.27 ± 0.47	0.08 ± 0.21	0.77 ± 0.24	30.17 ± 3.61	15.85 ± 2.02	0.52 ± 0.01	...
2013 Oct 15.52	0.36	0.99 ± 0.05	0.289 ± 0.007	...	...	...	...	...	...	...	...	...	M8
2013 Nov 07.57	0.39	0.99 ± 0.06	0.330 ± 0.003	...	...	...	...	...	...	...	...	...	M8
2014 Aug 19.75	0.96	0.87 ± 0.04	0.398 ± 0.006	...	...	...	...	...	...	...	...	...	M7
2014 Oct 29.54	1.08	...	...	3.18 ± 0.44	2.83 ± 0.29	0.64 ± 0.01	4.01 ± 0.66	4.09 ± 0.38	0.12 ± 0.09	28.80 ± 2.72	12.05 ± 1.83	0.60 ± 0.01	...
2015 Mar 02.93	1.26	0.93 ± 0.09	0.387 ± 0.003	1.95 ± 0.28	3.39 ± 0.49	0.39 ± 0.01	2.21 ± 0.35	1.94 ± 0.21	0.44 ± 0.13	29.12 ± 3.19	16.10 ± 1.91	0.45 ± 0.01	M7.5
2015 July 05.67	1.43	1.01 ± 0.04	0.401 ± 0.007	...	...	...	...	...	...	...	...	...	M8
2015 Oct 07.69	1.61	0.91 ± 0.04	0.362 ±0.005	1.15 ± 0.36	2.89 ± 0.28	0.27 ± 0.01	0.10 ± 0.17	-0.12 ± 0.15	1.96 ± 0.31	16.85 ± 1.71	14.91 ± 1.23	0.40 ± 0.01	M7.5
2015 Nov 20.55	1.70	...	...	0.57 ± 0.17	0.78 ± 0.12	0.29 ± 0.01	-0.70 ± 0.16	-0.49 ± 0.12	1.06 ± 0.24	21.36 ± 1.97	14.97 ± 1.75	0.48 ± 0.01	...
2016 Feb 15.98	1.90	0.76 ± 0.05	0.527 ± 0.005	...	...	...	...	...	...	...	...	...	M7
2017 Apr 07.92	2.55	...	...	1.16 ± 0.29	0.94 ± 0.19	0.25 ± 0.01	-0.34 ± 0.14	0.30 ± 0.08	1.58 ± 0.37	26.27 ± 2.81	14.73 ± 2.14	0.38 ± 0.01	...

Note. [1]The spectral type has been estimated using the correlation with $[TiO]_3$ Index

Spectral type

The visual comparison shows that the optical spectra of the object correspond to O-rich spectral types later than M7. Moreover, we estimate the spectral type (ST) of the object quantitatively at different variability phase using the correlation between ST and $[TiO]_3$ index ([TiO] at 8450 Å) as in Zhu et al. (1999). The estimated STs at different phases are shown in Table 6.5. The ST of the object varies from M7 to M8 over the phase of the pulsation cycle in our limited phase coverage. The saturation effect of $[TiO]_3$ is problematic to estimate the STs over phases as described earlier.

6.4 Summary and conclusion

We have characterized the time-dependent properties of the MASTER OT J1830+09 from long-term optical/NIR photometric and spectroscopic observations. Our main results are summarized as follows.

1. We have estimated the variability period of 575 ± 30 days from the best-fit of optical RI-band light curves with wavelength-dependent variability amplitudes $\Delta R \sim 4.0$ mag and $\Delta I \sim 3.5$ mag.

2. From Period-Luminosity (PL) relation, the distance to the source is estimated as 5.14 ± 0.4 kpc, which is inconsistent with the distance from Gaia parallax. We found that the Gaia parallaxes of AGB stars are reliable up to 2 kpc.

3. Using DUSTY based MoD code, we have done the SED fitting the optical to far-IR data and LRS IRAS spectral data. The best fit SED provides luminosity of the object 17367 $L_\odot$ ($M_{bol} \sim 5.86$ mag), optical depth 9.47 at 0.55 μm and mass-loss rate of $11.5 \times 10^{-7} M_\odot yr^{-1}$.

4. The spectra of the object at different variable phase are presented covering the optical range from 0.6 to 0.9 μm and NIR range from 1.5 to 2.4 μm. Notable variation in spectral features in all atomic and molecular lines (e.g., TiO, Na I, Ca I, Mg I, H_2O and CO bands) over phases are seen illustrating the sensitivity of the spectral features to the dynamical atmosphere of the pulsating object. The strength of metal lines (except Mg I) and CO absorption becomes minimum at around phase 1.7 indicating the line blurring and veiling. We have seen that the variation of Mg I line show nice correlation with the phase of the pulsating object and the variation of water absorption, which could be used as a potential temperature indicator of such cool objects.

Chapter 7

Summary and Future perspectives

This thesis is devoted to the study of cool and evolved stars from an observational point of view. This thesis work is directed toward a twofold aim: to provide the improved empirical correlations between stellar parameters and dominant spectral features of K−M giants, and to characterise O-rich AGB stars from time-dependent spectroscopic and photometric data. To achieve our aim, we have carried out photometric or/and spectroscopic observations from optical to NIR bands using the HFOSC and TIRSPEC instrument on the 2.01 m HCT, and NICMOS-3 instrument on the 1.2 m Mt. Abu Telescope. Additionally, we have used archival photometric/spectroscopic data and theoretical models. The most important results obtained from our studies as well as perspectives for future work are as follows.

7.1 Summary

7.1.1 A new TIRSPEC spectral library for K−M giants:

In Chapter 3 of this thesis, we have constructed a new NIR (1.50–2.45 μm) spectral library of 72 cool giants observed at a resolving power of R $\sim$ 1200 with the medium resolution infrared spectrograph, TIRSPEC, on the 2.0 m HCT on Hanle, India. The sample giants have an effective temperature ranging from 2700 K to 5000 K, well-established MK spectral classifications spanning over K0−M8, and surface gravity less than 3.5 cms^{-2}. It is worth to mention that the sample includes about 60 per cent giants having spectral

type M3 or beyond, and none of the existing libraries contains a large sample of later M3 giants for such empirical calibration.

7.1.2 Empirical correlations for fundamental parameters:

In Chapter 3 of this thesis, assembling 107 giants (rest giants are adopted from IRTF spectral library), we studied the behaviour of spectral features with fundamental parameters. From newly established empirical relations, we found that the ^{12}CO first-overtone bandhead at 2.29 μm and ^{12}CO second-overtone bandhead at 1.62 μm are a reasonably good indicator of temperature, especially above 3400 K, and surface gravity. Furthermore, both CO bandhead are good spectral type indicator for K- and M-giants with a typical accuracy of 1 sub-type, when K- and M-giants are considered independently. We calibrated a new empirical relation to measuring metallicity from EWs of Na I, Ca I and CO, which reproduces literature value with an average dispersion of $\sim$ 0.2 dex in the range $-0.6 <$ [Fe/H] $< +0.3$. We showed that the dispersion in the empirical relations is significantly improved incorporating surface gravity in the effective temperature versus equivalent width correlations, however, the inclusion of metallicity does show no change in the previous prediction of the effective temperature.

7.1.3 Finding of the optimal CO index:

In Chapter 4, we further extended our study in search of the optimal CO index from different index definitions. We adopted two different index definitions from the literature for K-band and defined two new H-band indices similar to those K-band indices. We found that these indices also can predict the effective temperature precisely above 3400 K, and the surface gravity also. Similar to the equivalent width, those empirical relations become more precise considering the effect of surface gravity. Comparative studies of these indices showed that all are efficiently predicting the surface gravity, however, the effective temperatures are reliably estimated either when the sample giants are warmer than 3400 K or if we do incorporate the surface gravity in those relations.

7.1.4 Exploration of H_2O-K2 index for cool static M-giants:

In Chapter 4, for precise characterisation of cooler giants of effective temperature below 3600 K or spectral type beyond M4, we are the first to explore the K-band water index (H_2O–K2), which was originally defined for dwarf stars, and found that the water index

efficiently predicts the effective temperature with a typical accuracy of 90 K or better and the spectral type with an accuracy of 1 sub-type. We found that the effective temperature can precisely be estimated below 3400 K only from the water index when surface gravity is not known. However, such relation may not be appropriate for variable AGB stars, like Mira variables or OH/IR stars, as found in other studies.

7.1.5 Qualitative studies of the spectral indices from the BT-NextGen Phoenix model atmosphere:

In Chapter 3 and Chapter 4 of this thesis, we study the behaviour of spectral indices with fundamental parameters (effective temperature, surface gravity and metallicity) qualitatively from BT-NextGen Phoenix model atmospheres and compare with our observational data. We found that the strength of atomic lines (Si I at 1.59, Na I at 2.20 and Ca I at 2.26 μm) and molecular lines (^{12}CO at 1.58, 1.62, 2.29 and 2.32 μm) predicted from theoretical model spectra appears to behave similarly with the observations of K−M giants in the range 5000 to 3000 K. However, below 3000 K, the behaviour is still inconclusive from the observed data because of the dearth of the sample. The Si I strength shows an increasing trend with decreasing temperature from 5000 K, and decreases beyond 3500 K. The Si I strength also shows the dependence on the surface gravity and metallicity. The strength of Na I doublet, Ca I triplet and CO overtone bandheads increase as temperature decreases, becomes maximum at a certain temperature, and decrease below that temperature for any metallicity and surface gravity. The strength of both Na I and Ca I vary with log g and $[M/H]$, which could be accounted for the dispersion in the observed data. The strength of the CO-bands also varies with the metallicity and the surface gravity. We found that the strength of CO second overtone bandhead at 1.62 μm is more sensitive with metallicity and surface gravity than CO first overtone bandhead at 2.29 μm. The H_2O–K2 index might be potential effective temperature indicator for cool giants below 3600 K. This index appears insensitive with the surface gravity and the metallicity.

7.1.6 Characterisation and confirmation of a O-rich Mira variable:

In Chapter 5 of this thesis, from long-term optical/NIR photometric observations, we found that the MASTER OT J212444.87+321738.3 showed large (J – K) NIR colours, varying 1.78–3.0 mag over phases, which signifies a red object like cool Mira variable. We estimated the variability period 465 ± 30 days from the best-fit optical/NIR light curves.

The strong wavelength-dependent variability amplitudes of the object ranging from ΔI $\sim$ 4 mag to ΔK $\sim$ 1.5 mag are observed from the optical and NIR light curves, as commonly seen in Mira variables. The spectroscopic observations showed the occasional appearance of optical Hα and NIR Paβ, Brγ emission lines at certain phase like Mira variables. The optical/NIR spectral features showed the presence of prominent VO and TiO bands, indicating the O-rich nature of the new Mira variable, and the absence of the ZrO bands at 1.03 and 1.06 μm, as well as C2 band-head at 1.77 μm, ruled out the S- or C-type nature. All of these observational properties of the object confirmed that the object is an O-rich Mira variable.

7.1.7 Monitoring of a poorly known OH/IR star

In Chapter 5 of this thesis, we have performed long-term optical/NIR photometric and spectroscopic monitoring to characterize an Arecibo OH/IR star. The variability period 575 $\pm$ 30 days was estimated from R- and I-band light curves with variability amplitude of ΔR(I) $\sim$4.0(3.5) mag. The corresponding progenitor mass infers in the range 2.5$-$4 $M_{\odot}$ assuming solar metallicity, and the reliable distance estimation of the object is $\sim$ 5.14 kpc from the period-luminosity relation. The spectral properties are similar like O-rich AGB stars.

7.1.8 Implementation of the MoD code:

In Chapter 3 and Chapter 4 of this thesis, we implemented the radiative transfer code, More of Dusty (MoD), to construct the SED from the multi-wavelength observational data to understand the nature of the object and mass-loss for a new Mira variable and a poorly known OH/IR star.

The best fit SED of all NIR to far-IR photometric measurements of the Mira variable provided luminosity of the object 9282 L$_{\odot}$, dust shell temperature of 1248 K, the optical depth of 11.178 at 0.55 μm and mass-loss rate of 0.7 $\times$ 10^{-6} $M_{\odot}$ yr^{-1}.

For OH/IR star, the best fit SED from multi-wavelength photometric and IRAS-LRS spectral data provides luminosity of the object $\sim$ 17367 $L_{\odot}$, optical depth at 0.55 μm $\sim$ 9.47 and mass-loss rate $\sim$ 11.5 $\times$ 10^{-7} M$_{\odot}$ yr^{-1}. The estimated luminosity indicates that the object belongs to the high-luminosity group of OH/IR stars.

7.1.9 Time-dependent spectroscopy of AGB stars:

Chapter 3 and Chapter 4 of this thesis present rare time-dependent study of two O-rich AGB stars–a new O-rich Mira variable and a poorly known OH/IR star. Such a study provides a unique way to probe the atmosphere of the pulsating variables. To study the time-dependent spectral variability, we have estimated the strength of spectral features (e.g., TiO, Na I, Ca I, CO, H_2O) as commonly observed in optical/NIR spectra of O-rich AGB.

We study the time-dependent variation of TiO bandhead at 7100 Å , triple-headed TiO bands at 8433, 8442, 8452 Å, and flux ratio of two absorption bands 7700−8070Å and 8290−8570 Å. The TiO bandhead at 7100 Å showed no variation for both AGB stars. The triple-headed TiO bands and the flux ratio of two absorption bands 7700−8070 Å and 8290−8570 Å showed pronounced variation for Mira variable, while no variation is apparent for OH/IR star. This signifies the saturation effect of TiO bands.

The two NIR metallic lines, Na I at 2.20 μm and Ca I at 2.26 μm, showed significant variation over the phase for OH/IR star, however, for Mira variable, no significant trends of Na with phase is apparent, except possibly for Ca. The metallic line at 2.28 μm, Mg I, shows different behaviour than Na I and Ca I, and significantly varies with the pulsation cycle. We predict that Mg I could be a good temperature indicator at low temperature for AGB stars. However, this line is only explored for OH/IR star.

We also explored the phase variation of the CO-first overtone and CO-second overtone bandheads in the 1.5−2.4 μm region. The strength of CO-first overtone bandhead at 2.29 μm change significantly for Mira variable, while there is no conclusive evidence of CO-variation over the phase for OH/IR star.

To quantify the water absorption at different phases, we determined H_2O–K2 index, which represents the curvature variation of the K-band spectra. Similar to the H_2O–K2 index, we defined H_2O–H4 index in this work to measure the curvature variation of the H-band spectra. Both the indices show significant variation with the pulsation cycle and becomes strongest at the visual maximum.

In conclusion, we found that the study of the time-dependent spectral variability is challenging with TiO and CO features as they tend to be saturated for cool M-star and with metallic lines as significant contribution comes from the low-excitation lines in low-resolution spectra at low-temperature. We showed that the H_2O–H4 and H_2O–K2 indices are very promising to study the low-resolution continuum variation with phase for AGB stars, however, these indices may not be appropriate to evaluating fundamental parameters because of the cycle to cycle variable atmosphere of large amplitude AGB stars.

7.2 Future perspectives

In the study on the spectral calibration of K−M giant, we have shown the effect of surface gravity on the effective temperature versus CO indices correlation. We have mainly collected data of sample giants at the solar-neighbourhood, and also the metallicity of most of the giants are unavailable in the literature. Therefore, metallicity dependence on the effective temperature versus CO indices correlation could not be explored. The exploration of the empirical relationship with the sample giants covering a wide range in metallicity will be a natural continuation of this study. Obtaining the empirical relations for the galactic bulge or globular cluster stars would be an important extension, and this would allow to comparing the results of different populations with the works presented in this thesis.

The Kepler mission has demonstrated that low-mass stars host small planets at a high rate. M-dwarfs are becoming most preferential targets for potentially habitable exo-planet searches via almost all current search methods because of their small size and low mass. Therefore, the characterisation of those dwarfs is a very important problem to counter. It is interesting to perform a similar study as in this thesis, for a sample of standard dwarfs stars using atomic and/or molecular features from simultaneous H and K-band spectra, and this would help to characterize the planet-hosting stars required to exo-planet surveys.

In this work, we present phase-dependent data of two O-rich AGB stars with limited time coverage and study the time-dependent variations of atomic and molecular features to understand the dynamic atmosphere of those objects. However, it is not well understood how atomic and molecular features behave in the full pulsation cycle. Longer time series of these observations, eventually covering the whole light curve, is needed for details understanding of the variability in the continuum radius and in extended molecular layers. Our study with the low-resolution spectra present the difficulties of firm conclusion about the time-dependent behaviour of the individual lines because of the blending with low-excited lines at low-temperature. Therefore, the high-resolution spectrograph (e.g., HESP at HCT, PARAS at Mt. Abu telescope) is well suited to conducting such time series of observations. It would be very interesting to collect simultaneous spectroscopic observations as well as interferometric imaging (with VLTI, ALMA etc.) to constrain the model-predicted intra- and inter-cycle variability and to understand the interaction between pulsation, convection, and mass-loss. Time-dependent investigation not only in O-rich AGB but a sample of C-rich Mira, Semi-regular and Irregular would also help in resolving the ongoing physical processes in the AGB. Comparison between observations and model atmospheres (e.g., CODEX, DARWIN) are needed to investigate the stellar

atmospheres in detail. More time-dependent data from the large sample of stars are required to settle the discrepancies between models and observations, and to yield a clear evolutionary scenario.

Towards the end of the AGB evolution, stars lose mass at a high rate. As a result, dust and gas enshroud the central star completely, forming CSEs. However, the detail of this mass-loss process and the structure and chemistry of CSEs are still not understood very well. In this context, the Herschel, operating at far-infrared to submillimetre wavelength region, will be an excellent mission of investigating properties of AGB stars, particularly, the mass-loss process because of the prominent continuum and line radiation at this very wavelength region by the gas and dust in the extended CSE. Further, the transition from AGB to post-AGB with steadily declining pulsation amplitudes takes place during the obscured phase, at least in the more massive stars. To understand the fading out of pulsation during AGB to post-AGB transition, a monitoring program with a large sample of AGB along the evolutionary sequence needs to perform. Since most of the stars (at the end of their lives) are deeply embedded those AGB cannot be monitored in the optical or the NIR. Monitoring program based on the bright and relatively stable OH maser at radio wavelength could be interesting to study the transformation of the variability characteristics.

Bibliography

Adibekyan, V. Z., Sousa, S. G., Santos, N. C., et al. 2012, A&A, 545, A32

Alard, C., Blommaert, J. A. D. L., Cesarsky, C., et al. 2001, ApJ, 552, 289

Ali, B., Carr, J. S., Depoy, D. L., Frogel, J. A., & Sellgren, K. 1995, AJ, 110, 2415

Allard, F., Hauschildt, P. H., Alexander, D. R., & Starrfield, S. 1997, ARA&A, 35, 137

Allard, F., Homeier, D., & Freytag, B. 2012, Philosophical Transactions of the Royal Society of London Series A, 370, 2765

Allard, F., Lawlor, T., Alexander, D. R., & Hauschildt, P. H. 1995, in Bulletin of the American Astronomical Society, Vol. 27, American Astronomical Society Meeting Abstracts, 1432

Allen, D. A., Hyland, A. R., Longmore, A. J., et al. 1977, ApJ, 217, 108

Allers, K. N., Jaffe, D. T., Luhman, K. L., et al. 2007, ApJ, 657, 511

Alonso, A., Arribas, S., & Martínez-Roger, C. 1999, A&AS, 139, 335

Alvarez, R., Jorissen, A., Plez, B., Gillet, D., & Fokin, A. 2000, A&A, 362, 655

Alvarez, R., & Plez, B. 1998, A&A, 330, 1109

Aringer, B., Girardi, L., Nowotny, W., Marigo, P., & Lederer, M. T. 2009a, A&A, 503, 913

—. 2009b, A&A, 503, 913

Arlandini, C., Käppeler, F., Wisshak, K., et al. 1999, ApJ, 525, 886

Asplund, M., Grevesse, N., Sauval, A. J., & Scott, P. 2009, ARA&A, 47, 481

Bailer-Jones, C. A. L., Farnocchia, D., Meech, K. J., et al. 2018, AJ, 156, 205

Balanutsa, P., Denisenko, D., Lipunov, V., et al. 2013, The Astronomer's Telegram, 5030

Baldwin, J. R., Frogel, J. A., & Persson, S. E. 1973, ApJ, 184, 427

Barber, R. J., Tennyson, J., Harris, G. J., & Tolchenov, R. N. 2006, MNRAS, 368, 1087

Barthes, D., Chenevez, J., & Mattei, J. A. 1996, AJ, 111, 2391

Baud, B., & Habing, H. J. 1983, A&A, 127, 73

Baud, B., Habing, H. J., Matthews, H. E., & Winnberg, A. 1979a, A&AS, 35, 179

—. 1979b, A&AS, 36, 193

—. 1981, A&A, 95, 156

Bedijn, P. J. 1987, A&A, 186, 136

Beichman, C. A., Neugebauer, G., Habing, H. J., Clegg, P. E., & Chester, T. J., eds. 1988, Infrared astronomical satellite (IRAS) catalogs and atlases. Volume 1: Explanatory supplement, Vol. 1

Benson, P. J., Little-Marenin, I. R., Woods, T. C., et al. 1990, ApJS, 74, 911

Bessell, M. S., Brett, J. M., Scholz, M., & Wood, P. R. 1989, A&A, 213, 209

Bessell, M. S., Castelli, F., & Plez, B. 1998, A&A, 333, 231

Bessell, M. S., Scholz, M., & Wood, P. R. 1996, A&A, 307, 481

Bethe, H. A. 1939, Physical Review, 55, 434

Blackwell, D. E., & Lynas-Gray, A. E. 1998, A&AS, 129, 505

Blackwell, D. E., & Shallis, M. J. 1977, MNRAS, 180, 177

Blommaert, J. A. D. L., Groenewegen, M. A. T., Justtanont, K., & Decin, L. 2018, MNRAS, 479, 3545

Blommaert, J. A. D. L., van der Veen, W. E. C. J., & Habing, H. J. 1993, A&A, 267, 39

Blommaert, J. A. D. L., van der Veen, W. E. C. J., van Langevelde, H. J., Habing, H. J., & Sjouwerman, L. O. 1998, A&A, 329, 991

Blommaert, J. A. D. L., van Langevelde, H. J., & Michiels, W. F. P. 1994, A&A, 287, 479

Blum, R. D., Ramírez, S. V., Sellgren, K., & Olsen, K. 2003, ApJ, 597, 323

Blum, R. D., Sellgren, K., & Depoy, D. L. 1996, AJ, 112, 1988

Boeche, C., Smith, M. C., Grebel, E. K., et al. 2018, AJ, 155, 181

Bogdanov, M. B., Taranova, O. G., & Shenavrin, V. I. 2015, Astronomy Reports, 59, 385

Bordé, P., Coudé du Foresto, V., Chagnon, G., & Perrin, G. 2002, A&A, 393, 183

Bowen, G. H. 1988, ApJ, 329, 299

Bowers, P. F., & Sinha, R. P. 1978, AJ, 83, 955

Bruntt, H., Frandsen, S., & Thygesen, A. O. 2011, A&A, 528, A121

Busso, M., Gallino, R., & Wasserburg, G. J. 1999, ARA&A, 37, 239

Campbell, L. 1955, Studies of Long Period Variables

Casagrande, L., Ramírez, I., Meléndez, J., Bessell, M., & Asplund, M. 2010, A&A, 512, A54

Castelaz, M. W., & Luttermoser, D. G. 1997, AJ, 114, 1584

Castelaz, M. W., Luttermoser, D. G., Caton, D. B., & Piontek, R. A. 2000, AJ, 120, 2627

Caswell, J. L., & Haynes, R. F. 1975, MNRAS, 173, 649

Cenarro, A. J., Cardiel, N., Gorgas, J., et al. 2001, MNRAS, 326, 959

Cenarro, A. J., Gorgas, J., Cardiel, N., Vazdekis, A., & Peletier, R. F. 2002, MNRAS, 329, 863

Cenarro, A. J., Peletier, R. F., Sánchez-Blázquez, P., et al. 2007, MNRAS, 374, 664

Cesetti, M., Pizzella, A., Ivanov, V. D., et al. 2013, A&A, 549, A129

Chandler, C. O., McDonald, I., & Kane, S. R. 2016, AJ, 151, 59

Chen, P. S., Szczerba, R., Kwok, S., & Volk, K. 2001, A&A, 368, 1006

Chen, Y.-P., Trager, S. C., Peletier, R. F., et al. 2014, A&A, 565, A117

Chengalur, J. N., Lewis, B. M., Eder, J., & Terzian, Y. 1993a, ApJS, 89, 189

—. 1993b, ApJS, 89, 189

Chiavassa, A., Freytag, B., & Schultheis, M. 2018, A&A, 617, L1

Cho, C.-Y., Cho, S.-H., Kim, S., et al. 2017, ApJS, 232, 13

Clerke, A. M. 1902, A Popular History of Astronomy During the Nineteenth Century (4th Edition)

Cushing, M. C., Rayner, J. T., & Vacca, W. D. 2005, ApJ, 623, 1115

Cutri, R. M., & et al. 2012, VizieR Online Data Catalog, 2311

—. 2013, VizieR Online Data Catalog, 2328

Cutri, R. M., Skrutskie, M. F., van Dyk, S., et al. 2003, VizieR Online Data Catalog, 2246

da Silva, L., Girardi, L., Pasquini, L., et al. 2006, A&A, 458, 609

Dallier, R., Boisson, C., & Joly, M. 1996, A&AS, 116, 239

Das, R. K. 2009, PhD thesis, Gujarat University, Ahmedabad, India

De Beck, E., Decin, L., de Koter, A., et al. 2010, A&A, 523, A18

Decin, L. 2000, PhD thesis, Catholique University of Leuven Department of Physics and Astronomy ¡EMAIL¿Leen.Decin@ster.kuleuven.ac.be¡/EMAIL¿

Deutsch, A. J. 1956, AJ, 61, 174

Deutsch, A. J., & Merrill, P. W. 1959, ApJ, 130, 570

di Benedetto, G. P., & Rabbia, Y. 1987, A&A, 188, 114

Dyck, H. M., van Belle, G. T., & Thompson, R. R. 1998, AJ, 116, 981

Eder, J., Lewis, B. M., & Terzian, Y. 1988, ApJS, 66, 183

Eggen, O. J. 1998, AJ, 115, 2435

Eisenstein, D. J., Weinberg, D. H., Agol, E., et al. 2011, AJ, 142, 72

Elitzur, M. 1992, ARA&A, 30, 75

Engels, D. 2005, Mem. Soc. Astron. Italiana, 76, 441

Engels, D., & Bunzel, F. 2015, A&A, 582, A68

Engels, D., Habing, H. J., Olnon, F. M., Schmid-Burgk, J., & Walmsley, C. M. 1984, A&A, 140, L9

Engels, D., Kreysa, E., Schultz, G. V., & Sherwood, W. A. 1983, A&A, 124, 123

Evans, II, N. J., & Beckwith, S. 1977, ApJ, 217, 729

Fadeyev, Y. A., & Gillet, D. 2004, A&A, 420, 423

Feast, M. W., Glass, I. S., Whitelock, P. A., & Catchpole, R. M. 1989, MNRAS, 241, 375

Fedele, D., Wittkowski, M., Paresce, F., et al. 2005, A&A, 431, 1019

Feldmeier-Krause, A., Kerzendorf, W., Neumayer, N., et al. 2017, MNRAS, 464, 194

Feuillet, D. K., Bovy, J., Holtzman, J., et al. 2016, ApJ, 817, 40

Figer, D. F., McLean, I. S., & Morris, M. 1995, ApJ, 447, L29

Figer, D. F., McLean, I. S., & Najarro, F. 1997, ApJ, 486, 420

Fluks, M. A., Plez, B., The, P. S., et al. 1994, A&AS, 105, 311

Förster Schreiber, N. M. 2000, AJ, 120, 2089

Fox, M. W., & Wood, P. R. 1985, ApJ, 297, 455

Fox, M. W., Wood, P. R., & Dopita, M. A. 1984a, ApJ, 286, 337

—. 1984b, ApJ, 286, 337

Freytag, B., & Höfner, S. 2008, A&A, 483, 571

Freytag, B., Liljegren, S., & Höfner, S. 2017, A&A, 600, A137

Frogel, J. A., Persson, S. E., Aaronson, M., & Matthews, K. 1978, ApJ, 220, 75

Frogel, J. A., Stephens, A., Ramírez, S., & DePoy, D. L. 2001, AJ, 122, 1896

Fukue, K., Matsunaga, N., Yamamoto, R., et al. 2015, ApJ, 812, 64

Gaia Collaboration, Prusti, T., de Bruijne, J. H. J., et al. 2016, A&A, 595, A1

Gaia Collaboration, Babusiaux, C., van Leeuwen, F., et al. 2018a, A&A, 616, A10

Gaia Collaboration, Brown, A. G. A., Vallenari, A., et al. 2018b, A&A, 616, A1

Gallino, R., Arlandini, C., Busso, M., et al. 1998, ApJ, 497, 388

García-Hernández, D. A., Zamora, O., Yagüe, A., et al. 2013, A&A, 555, L3

Garćia-Lario, P. 1992, PhD thesis, U. La Laguna, Spain

García-Lario, P. 1992, PhD thesis, La Laguna University

Garrison, R. F. 1994, in Astronomical Society of the Pacific Conference Series, Vol. 60, The MK Process at 50 Years: A Powerful Tool for Astrophysical Insight, ed. C. J. Corbally, R. O. Gray, & R. F. Garrison, 3

Gáspár, A., Rieke, G. H., & Ballering, N. 2016, ApJ, 826, 171

Gautschy-Loidl, R., Höfner, S., Jørgensen, U. G., & Hron, J. 2004, A&A, 422, 289

Gehrz, R. D., & Woolf, N. J. 1971, ApJ, 165, 285

Ghosh, S., Mondal, S., Das, R., et al. 2018, AJ, 155, 216

Ghosh, S., Mondal, S., Das, R., & Khata, D. 2019, MNRAS, 484, 4619

Gillet, D. 1988, A&A, 192, 206

Gillet, D., Ferlet, R., Maurice, E., & Bouchet, P. 1985, A&A, 150, 89

Glass, I. S., & Evans, T. L. 1981, Nature, 291, 303

Glass, I. S., Matsumoto, S., Carter, B. S., & Sekiguchi, K. 2001, MNRAS, 321, 77

Glass, I. S., Schultheis, M., Blommaert, J. A. D. L., et al. 2009, MNRAS, 395, L11

Gobrecht, D., Cherchneff, I., Sarangi, A., Plane, J. M. C., & Bromley, S. T. 2016, A&A, 585, A6

González-Fernández, C., Cabrera-Lavers, A., Hammersley, P. L., & Garzón, F. 2008, A&A, 479, 131

Gorbatskii, V. G. 1961, Azh, 38, 256

Gray, D. F. 1992, The observation and analysis of stellar photospheres.

Gray, M. 2012, Maser Sources in Astrophysics

Gray, R. O., & Corbally, J., C. 2009, Stellar Spectral Classification

Greene, T. P., & Meyer, M. R. 1995, ApJ, 450, 233

Groenewegen, M. A. T. 2006, A&A, 448, 181

—. 2012, A&A, 543, A36

Groenewegen, M. A. T., & Whitelock, P. A. 1996, MNRAS, 281, 1347

Groenewegen, M. A. T., Wood, P. R., Sloan, G. C., et al. 2007, MNRAS, 376, 313

Guandalini, R., Busso, M., Ciprini, S., Silvestro, G., & Persi, P. 2006, A&A, 445, 1069

Guha Niyogi, S., Speck, A. K., & Onaka, T. 2011, ApJ, 733, 93

Gustafsson, B., Edvardsson, B., Eriksson, K., et al. 2008a, A&A, 486, 951

—. 2008b, A&A, 486, 951

Habing, H. J. 1988, A&A, 200, 40

—. 1996, A&ARv, 7, 97

Habing, H. J., Olnon, F. M., Chester, T., Gillett, F., & Rowan-Robinson, M. 1985, A&A, 152, L1

Habing, H. J., & Olofsson, H., eds. 2003, Asymptotic giant branch stars

Hambsch, F.-J. 2012, Journal of the American Association of Variable Star Observers (JAAVSO), 40, 1003

Haniff, C. A., Scholz, M., & Tuthill, P. G. 1995, MNRAS, 276, 640

Hanson, M. M., Conti, P. S., & Rieke, M. J. 1996, ApJS, 107, 281

Hanson, M. M., Kudritzki, R.-P., Kenworthy, M. A., Puls, J., & Tokunaga, A. T. 2005, ApJS, 161, 154

Hauschildt, P. H., Allard, F., & Baron, E. 1999a, ApJ, 512, 377

Hauschildt, P. H., Allard, F., Ferguson, J., Baron, E., & Alexander, D. R. 1999b, ApJ, 525, 871

Hayden, M. R., Bovy, J., Holtzman, J. A., et al. 2015, ApJ, 808, 132

Heiter, U., Kupka, F., van't Veer-Menneret, C., et al. 2002, A&A, 392, 619

Hekker, S., & Meléndez, J. 2007, A&A, 475, 1003

Herman, J. 1983, PhD thesis, Ph. D. thesis, University of Leiden (1983)

Herman, J., & Habing, H. J. 1985, Phys. Rep., 124, 257

Herman, J., Isaacman, R., Sargent, A., & Habing, H. 1984, A&A, 139, 171

Herwig, F. 2005, ARA&A, 43, 435

Hinkel, N. R., Timmes, F. X., Young, P. A., Pagano, M. D., & Turnbull, M. C. 2014, AJ, 148, 54

Hinkle, K. H. 1978, ApJ, 220, 210

Hinkle, K. H., & Barnes, T. G. 1979a, ApJ, 227, 923

—. 1979b, ApJ, 234, 548

Hinkle, K. H., Hall, D. N. B., & Ridgway, S. T. 1982, ApJ, 252, 697

Hinkle, K. H., Lebzelter, T., & Scharlach, W. W. G. 1997, AJ, 114, 2686

Hinkle, K. H., Wilson, T. D., Scharlach, W. W. G., & Fekel, F. C. 1989, AJ, 98, 1820

Ho, A. Y. Q., Ness, M. K., Hogg, D. W., et al. 2017, ApJ, 836, 5

Hoefner, S., Jorgensen, U. G., Loidl, R., & Aringer, B. 1998, A&A, 340, 497

Hoffleit, D. 1943, Science, 97, 536

—. 1997, Journal of the American Association of Variable Star Observers (JAAVSO), 25, 115

Höfner, S., Gautschy-Loidl, R., Aringer, B., & Jørgensen, U. G. 2003, A&A, 399, 589

Höfner, S., & Olofsson, H. 2018, A&ARv, 26, 1

Huang, Y., Liu, X.-W., Yuan, H.-B., et al. 2015, MNRAS, 454, 2863

Hughes, S. M. G., & Wood, P. R. 1990, AJ, 99, 784

Husser, T.-O., Wende-von Berg, S., Dreizler, S., et al. 2013, A&A, 553, A6

Hyland, A. R., Becklin, E. E., Frogel, J. A., & Neugebauer, G. 1972, A&A, 16, 204

Iben, Jr., I., & Renzini, A. 1983, ARA&A, 21, 271

Ireland, M. J., & Scholz, M. 2006, MNRAS, 367, 1585

Ireland, M. J., Scholz, M., & Wood, P. R. 2004, MNRAS, 352, 318

—. 2008, MNRAS, 391, 1994

Ishihara, D., Onaka, T., Kataza, H., et al. 2010, A&A, 514, A1

Ita, Y., & Matsunaga, N. 2011, MNRAS, 412, 2345

Ita, Y., Tanabé, T., Matsunaga, N., et al. 2004, MNRAS, 353, 705

Ivanov, V. D., Rieke, M. J., Engelbracht, C. W., et al. 2004, ApJS, 151, 387

Ivezic, Z., & Elitzur, M. 1997, MNRAS, 287, 799

Ivezic, Z., Nenkova, M., & Elitzur, M. 1999, ArXiv Astrophysics e-prints, astro-ph/9910475

Jiménez-Esteban, F. M. 2004, PhD thesis, Universidad Autónoma de Madrid

Jiménez-Esteban, F. M., Agudo-Mérida, L., Engels, D., & García-Lario, P. 2005a, A&A, 431, 779

—. 2005b, A&A, 431, 779

Jiménez-Esteban, F. M., & Engels, D. 2015, A&A, 579, A76

Jiménez-Esteban, F. M., García-Lario, P., Engels, D., & Manchado, A. 2006a, A&A, 458, 533

—. 2006b, A&A, 458, 533

Jiménez-Esteban, F. M., García-Lario, P., Engels, D., & Perea Calderón, J. V. 2006c, A&A, 446, 773

Jofré, E., Petrucci, R., Saffe, C., et al. 2015, A&A, 574, A50

Johansson, L. E. B., Andersson, C., Goss, W. M., & Winnberg, A. 1977a, A&AS, 28, 199

—. 1977b, A&A, 54, 323

Johnson, H. L., Coleman, I., Mitchell, R. I., & Steinmetz, D. L. 1968, Communications of the Lunar and Planetary Laboratory, 7, 83

Johnson, H. L., & Méndez, M. E. 1970, AJ, 75, 785

Jones, H. R. A., Longmore, A. J., Allard, F., & Hauschildt, P. H. 1996, MNRAS, 280, 77

Jones, T. J., Bryja, C. O., Gehrz, R. D., et al. 1990, ApJS, 74, 785

Joy, A. H. 1926, ApJ, 63, doi:10.1086/142979

—. 1947, ApJ, 106, 288

—. 1954, ApJS, 1, 39

Joyce, R. R. 1998, AJ, 115, 2059

Joyce, R. R., Hinkle, K. H., Wallace, L., Dulick, M., & Lambert, D. L. 1998, AJ, 116, 2520

Jura, M., & Kleinmann, S. G. 1990, ApJ, 364, 663

—. 1992, ApJS, 79, 105

Jurić, M., Ivezić, Ž., Brooks, A., et al. 2008, ApJ, 673, 864

Kaifu, N., Buhl, D., & Snyder, L. E. 1975, ApJ, 195, 359

Karovicova, I., Wittkowski, M., Ohnaka, K., et al. 2013, A&A, 560, A75

Karovicova, I., White, T. R., Nordlander, T., et al. 2018, MNRAS, 475, L81

Kerschbaum, F., Lebzelter, T., & Lazaro, C. 2001, A&A, 375, 527

Kholopov, P. N. 1987, General Catalogue of Variable Stars.

Kholopov, P. N., Samus, N. N., Frolov, M. S., et al. 1998, in Combined General Catalogue of Variable Stars, 4.1 Ed (II/214A). (1998)

Kleinmann, S. G., Gillett, F. C., & Joyce, R. R. 1981, ARA&A, 19, 411

Kleinmann, S. G., & Hall, D. N. B. 1986, ApJS, 62, 501

Knowles, S. H., Mayer, C. H., Cheung, A. C., Rank, D. M., & Townes, C. H. 1969, in BAAS, Vol. 1, Bulletin of the American Astronomical Society, 249

Kovtyukh, V. V. 2007, MNRAS, 378, 617

Kovtyukh, V. V., Soubiran, C., Bienaymé, O., Mishenina, T. V., & Belik, S. I. 2006, MNRAS, 371, 879

Kurtev, R., Borissova, J., Georgiev, L., Ortolani, S., & Ivanov, V. D. 2007, A&A, 475, 209

Kurtev, R., Georgiev, L., Borissova, J., et al. 2001, A&A, 378, 449

Kurucz, R. L. 1992, in IAU Symposium, Vol. 149, The Stellar Populations of Galaxies, ed. B. Barbuy & A. Renzini, 225

Kwok, S., Volk, K., & Bidelman, W. P. 1997, ApJS, 112, 557

Lambert, D. L., Gustafsson, B., Eriksson, K., & Hinkle, K. H. 1986, ApJS, 62, 373

Lançon, A., Hauschildt, P. H., Ladjal, D., & Mouhcine, M. 2007, A&A, 468, 205

Lançon, A., & Wood, P. R. 2000, A&AS, 146, 217

Lancon, A., & Rocca-Volmerange, B. 1992, A&AS, 96, 593

Lazaro, C., Hammersley, P. L., Clegg, R. E. S., et al. 1994, MNRAS, 269, 365

Le Bertre, T. 1988, A&A, 190, 79

—. 1992, A&AS, 94, 377

Le Borgne, J.-F., Bruzual, G., Pelló, R., et al. 2003, A&A, 402, 433

Le Squeren, A. M., Sivagnanam, P., Dennefeld, M., & David, P. 1992, A&A, 254, 133

Lebzelter, T., Hinkle, K. H., & Hron, J. 1999, A&A, 341, 224

Lebzelter, T., Nowotny, W., Hinkle, K. H., Höfner, S., & Aringer, B. 2014, A&A, 567, A143

Lebzelter, T., & Obbrugger, M. 2009, Astronomische Nachrichten, 330, 390

Lebzelter, T., Heiter, U., Abia, C., et al. 2012, A&A, 547, A108

Lejeune, T., Cuisinier, F., & Buser, R. 1997, A&AS, 125, 229

Lenorzer, A., Vandenbussche, B., Morris, P., et al. 2002, A&A, 384, 473

Lenz, P., & Breger, M. 2005, Communications in Asteroseismology, 146, 53

Lepine, J. R. D., Ortiz, R., & Epchtein, N. 1995, A&A, 299, 453

Lewis, B. M. 1994, ApJS, 93, 549

—. 1997, ApJS, 109, 489

Lewis, B. M., Eder, J., & Terzian, Y. 1985, Nature, 313, 200

—. 1990a, ApJ, 362, 634

—. 1990b, ApJ, 362, 634

Likkel, L. 1989, ApJ, 344, 350

Lindqvist, M., Winnberg, A., Habing, H. J., & Matthews, H. E. 1992, A&AS, 92, 43

Lipunov, V., Gorbovskoy, E., Afanasiev, V., et al. 2016, A&A, 588, A90

Lipunov, V. M., Kornilov, V., Gorbovskoy, E., et al. 2017, MNRAS, 465, 3656

Liu, X.-W., Yuan, H.-B., Huo, Z.-Y., et al. 2014, in IAU Symposium, Vol. 298, Setting the scene for Gaia and LAMOST, ed. S. Feltzing, G. Zhao, N. A. Walton, & P. Whitelock, 310–321

Lockwood, G. W. 1968, The Astronomical Journal Supplement, 73, 24

—. 1969, ApJ, 157, 275

—. 1972, ApJS, 24, 375

Lockwood, G. W., & Wing, R. F. 1971, ApJ, 169, 63

Lodieu, N., Scholz, R.-D., McCaughrean, M. J., et al. 2005, A&A, 440, 1061

Lomb, N. R. 1976, Ap&SS, 39, 447

Loup, C., Forveille, T., Omont, A., & Paul, J. F. 1993, A&AS, 99, 291

Luck, R. E., & Heiter, U. 2007, AJ, 133, 2464

Luo, A.-L., Zhao, Y.-H., Zhao, G., et al. 2016, VizieR Online Data Catalog, 5149

Luttermoser, D. G., & Bowen, G. H. 1992, in Astronomical Society of the Pacific Conference Series, Vol. 26, Cool Stars, Stellar Systems, and the Sun, ed. M. S. Giampapa & J. A. Bookbinder, 558

Maehara, H. 1968, PASJ, 20, 77

Magrini, L., Spina, L., Randich, S., et al. 2018, A&A, 617, A106

Malkan, M. A., Hicks, E. K., Teplitz, H. I., et al. 2002, ApJS, 142, 79

Maness, H., Martins, F., Trippe, S., et al. 2007, ApJ, 669, 1024

Marigo, P., & Girardi, L. 2007, A&A, 469, 239

Mármol-Queraltó, E., Cardiel, N., Cenarro, A. J., et al. 2008, A&A, 489, 885

Massarotti, A., Latham, D. W., Stefanik, R. P., & Fogel, J. 2008, AJ, 135, 209

Matsuura, M., Woods, P. M., & Owen, P. J. 2013, MNRAS, 429, 2527

Matsuura, M., Yamamura, I., Murakami, H., Freund, M. M., & Tanaka, M. 1999, A&A, 348, 579

Mattei, J. A. 1997, Journal of the American Association of Variable Star Observers (JAAVSO), 25, 57

McDonald, I., & Zijlstra, A. A. 2016, ApJ, 823, L38

McDonald, I., Zijlstra, A. A., & Boyer, M. L. 2012, MNRAS, 427, 343

McDonald, I., Zijlstra, A. A., & Watson, R. A. 2017, MNRAS, 471, 770

McGregor, P. J., Hyland, A. R., & Hillier, D. J. 1988, ApJ, 324, 1071

McKellar, A. 1954, J. R. Astron. Soc. Canada, 48, 81

—. 1956, J. R. Astron. Soc. Canada, 50, 243

McWilliam, A. 1990, ApJS, 74, 1075

Mennesson, B., Perrin, G., Chagnon, G., et al. 2002, ApJ, 579, 446

Merrill, P. W. 1921, ApJ, 53, doi:10.1086/142615

—. 1940, Spectra of long-period variable stars

—. 1952, ApJ, 116, 21

Merrill, P. W., Deutsch, A. J., & Keenan, P. C. 1962, ApJ, 136, 21

Merrill, P. W., & Greenstein, J. L. 1958, PASP, 70, 98

Meyer, M. R., Edwards, S., Hinkle, K. H., & Strom, S. E. 1998, ApJ, 508, 397

Min, M., Hovenier, J. W., & de Koter, A. 2003, A&A, 404, 35

Min, M., Waters, L. B. F. M., de Koter, A., et al. 2007, A&A, 462, 667

Mondal, S., & Chandrasekhar, T. 2005, AJ, 130, 842

Mondal, S., Das, R., Ashok, N. M., et al. 2013, The Astronomer's Telegram, 4931

Mondal, S., Lin, C. C., Chen, W. P., et al. 2010, AJ, 139, 2026

Morris, P. W., Eenens, P. R. J., Hanson, M. M., Conti, P. S., & Blum, R. D. 1996, ApJ, 470, 597

Morton, D. C. 1991, ApJS, 77, 119

Mouhcine, M. 2002, A&A, 394, 125

Mowlavi, N., Lecoeur-Taïbi, I., Lebzelter, T., et al. 2018, ArXiv e-prints, arXiv:1805.02035

Nakashima, J.-i., Jiang, B. W., Deguchi, S., Sadakane, K., & Nakada, Y. 2000, PASJ, 52, 275

Neugebauer, G., & Leighton, R. B. 1969, NASA Special Publication, 3047

Neugebauer, G., Habing, H. J., van Duinen, R., et al. 1984, ApJ, 278, L1

Newton, E. R., Charbonneau, D., Irwin, J., et al. 2014, AJ, 147, 20

Ngeow, C.-C., Lucchini, S., Kanbur, S., Barrett, B., & Lin, B. 2013, ArXiv e-prints, arXiv:1309.4297

Ninan, J. P., Ojha, D. K., Ghosh, S. K., et al. 2014, Journal of Astronomical Instrumentation, 3, 1450006

Norris, J. E., Bessell, M. S., Yong, D., et al. 2013, ApJ, 762, 25

Nowotny, W., Aringer, B., Höfner, S., Gautschy-Loidl, R., & Windsteig, W. 2005a, A&A, 437, 273

Nowotny, W., Höfner, S., & Aringer, B. 2010, A&A, 514, A35

Nowotny, W., Lebzelter, T., Hron, J., & Höfner, S. 2005b, A&A, 437, 285

O'Connell, R. W. 1973, AJ, 78, 1074

Ohnaka, K., Hofmann, K.-H., Schertl, D., et al. 2012, A&A, 537, A53

Ohnaka, K., Weigelt, G., & Hofmann, K.-H. 2016, A&A, 589, A91

—. 2017, A&A, 597, A20

Ohnaka, K., Bergeat, J., Driebe, T., et al. 2005, A&A, 429, 1057

Ojha, D. K., Tej, A., Schultheis, M., Omont, A., & Schuller, F. 2007, MNRAS, 381, 1219

Olivier, E. A., Whitelock, P., & Marang, F. 2001, MNRAS, 326, 490

Olnon, F. M., Baud, B., Habing, H. J., et al. 1984, ApJ, 278, L41

Olnon, F. M., Raimond, E., Neugebauer, G., et al. 1986, A&AS, 65, 607

Origlia, L., Moorwood, A. F. M., & Oliva, E. 1993, A&A, 280, 536

Ortiz, R., & Maciel, W. J. 1994, A&A, 287, 552

Ostlie, D. A., & Carroll, B. W. 1996, An Introduction to Modern Stellar Astrophysics

Oudmaijer, R. D., Waters, L. B. F. M., van der Veen, W. E. C. J., & Geballe, T. R. 1995, A&A, 299, 69

Perrin, G., Coudé du Foresto, V., Ridgway, S. T., et al. 1998, A&A, 331, 619

Perrin, G., Ridgway, S. T., Mennesson, B., et al. 2004, A&A, 426, 279

Perryman, M. A. C., de Boer, K. S., Gilmore, G., et al. 2001, A&A, 369, 339

Peterson, D. E., Megeath, S. T., Luhman, K. L., et al. 2008, ApJ, 685, 313

Pettit, E., & Nicholson, S. B. 1933a, ApJ, 78, 320

Pettit, E., & Nicholson, S. B. 1933b, in Publications of the American Astronomical Society, Vol. 7, Publications of the American Astronomical Society, 224

Pfuhl, O., Fritz, T. K., Zilka, M., et al. 2011, ApJ, 741, 108

Pickering, E. C. 1887, Nature, 36, 31

Pickles, A. J. 1998, PASP, 110, 863

Pignatari, M., Gallino, R., Heil, M., et al. 2010, ApJ, 710, 1557

Pilbratt, G. L., Riedinger, J. R., Passvogel, T., et al. 2010, A&A, 518, L1

Plez, B., Brett, J. M., & Nordlund, A. 1992, A&A, 256, 551

Price, S. D., & Walker, R. G. 1976, The AFGL four color infrared sky survey: Catalog of observations at 4.2, 11.0, 19.8 and 27.4 micrometers, Tech. rep.

Prugniel, P., & Soubiran, C. 2001, A&A, 369, 1048

Prugniel, P., Vauglin, I., & Koleva, M. 2011, A&A, 531, A165

Puxley, P. J., Doyon, R., & Ward, M. J. 1997, ApJ, 476, 120

Ramírez, I., & Meléndez, J. 2004, A&A, 417, 301

Ramirez, S. V., Depoy, D. L., Frogel, J. A., Sellgren, K., & Blum, R. D. 1997, AJ, 113, 1411

Ramírez, S. V., Stephens, A. W., Frogel, J. A., & DePoy, D. L. 2000, AJ, 120, 833

Ramsay, S. K., Mountain, C. M., & Geballe, T. R. 1992, MNRAS, 259, 751

Ranada, A. C., Singh, H. P., Gupta, R., & Ashok, N. M. 2007, Bulletin of the Astronomical Society of India, 35, 87

Ranade, A., Gupta, R., Ashok, N. M., & Singh, H. P. 2004, Bulletin of the Astronomical Society of India, 32, 311

Ranade, A. C., Ashok, N. M., Singh, H. P., & Gupta, R. 2007, Bulletin of the Astronomical Society of India, 35, arXiv:0709.4551

Rayner, J. T., Cushing, M. C., & Vacca, W. D. 2009, ApJS, 185, 289

Rayner, J. T., Toomey, D. W., Onaka, P. M., et al. 2003, PASP, 115, 362

Reffert, S., Bergmann, C., Quirrenbach, A., Trifonov, T., & Künstler, A. 2015, A&A, 574, A116

Reid, M. J., & Goldston, J. E. 2002, ApJ, 568, 931

Reid, M. J., Muhleman, D. O., Moran, J. M., Johnston, K. J., & Schwartz, P. R. 1977, ApJ, 214, 60

Reimers, D. 1975, Circumstellar envelopes and mass loss of red giant stars, ed. B. Baschek, W. H. Kegel, & G. Traving, 229–256

Reiter, M., Marengo, M., Hora, J. L., & Fazio, G. G. 2015, MNRAS, 447, 3909

Renzini, A. 1981, in Astrophysics and Space Science Library, Vol. 88, Physical Processes in Red Giants, ed. I. Iben, Jr. & A. Renzini, 431–446

Richichi, A., Baffa, C., Calamai, G., & Lisi, F. 1996, AJ, 112, 2786

Richichi, A., Ragland, S., Calamai, G., et al. 1999, A&A, 350, 491

Richter, H., & Wood, P. R. 2001, A&A, 369, 1027

Richter, H., Wood, P. R., Bolick, U., Woitke, P., & Sedlmayr, E. 2003, in Astronomical Society of the Pacific Conference Series, Vol. 288, Stellar Atmosphere Modeling, ed. I. Hubeny, D. Mihalas, & K. Werner, 344

Ridgway, S. E., Wynn-Williams, C. G., & Becklin, E. E. 1994, ApJ, 428, 609

Riebel, D., Meixner, M., Fraser, O., et al. 2010, ApJ, 723, 1195

Riffel, R., Pastoriza, M. G., Rodríguez-Ardila, A., & Maraston, C. 2008, MNRAS, 388, 803

Robertson, B. S. C., & Feast, M. W. 1981, MNRAS, 196, 111

Rojas-Ayala, B., Covey, K. R., Muirhead, P. S., & Lloyd, J. P. 2012, ApJ, 748, 93

Sackmann, I.-J., & Boothroyd, A. I. 1992, ApJ, 392, L71

Sacuto, S., Ramstedt, S., Höfner, S., et al. 2013, A&A, 551, A72

Sánchez-Blázquez, P., Peletier, R. F., Jiménez-Vicente, J., et al. 2006, MNRAS, 371, 703

Sanford, R. F. 1947, ApJ, 105, 222

Scalo, J. M., & Ross, J. E. 1976, A&A, 48, 219

Scargle, J. D. 1982, ApJ, 263, 835

Schlafly, E. F., & Finkbeiner, D. P. 2011, ApJ, 737, 103

Schlegel, D. J., Finkbeiner, D. P., & Davis, M. 1998, ApJ, 500, 525

Scholz, A., Muzic, K., Geers, V., et al. 2012, ApJ, 744, 6

Schultheis, M., Lançon, A., Omont, A., Schuller, F., & Ojha, D. K. 2003, A&A, 405, 531

Schultheis, M., Ryde, N., & Nandakumar, G. 2016, A&A, 590, A6

Schultz, G. V., Kreysa, E., & Sherwood, W. A. 1976, A&A, 50, 171

Schwarzschild, M., & Härm, R. 1965, ApJ, 142, 855

Sevenster, M. N., Chapman, J. M., Habing, H. J., Killeen, N. E. B., & Lindqvist, M. 1997a, A&AS, 122, 79

—. 1997b, A&AS, 124, 509

Sevenster, M. N., Dejonghe, H., & Habing, H. J. 1995, A&A, 299, 689

Sevenster, M. N., van Langevelde, H. J., Moody, R. A., et al. 2001, A&A, 366, 481

Silva, D. R., Kuntschner, H., & Lyubenova, M. 2008, ApJ, 674, 194

Skrutskie, M. F., Cutri, R. M., Stiening, R., et al. 2006, AJ, 131, 1163

Smith, B. J., Leisawitz, D., Castelaz, M. W., & Luttermoser, D. 2002a, AJ, 123, 948

—. 2002b, AJ, 123, 948

Smith, B. J., Price, S. D., & Moffett, A. J. 2006, AJ, 131, 612

Smith, V. V., & Lambert, D. L. 1986, ApJ, 311, 843

Sneden, C. 1973, ApJ, 184, 839

Sokolov, N. A. 1995, A&AS, 110, 553

Soszyński, I., Udalski, A., Szymański, M. K., et al. 2009, Acta Astron., 59, 239

Soszyński, I., Udalski, A., Poleski, R., et al. 2012, Acta Astron., 62, 219

Soubiran, C., Le Campion, J.-F., Brouillet, N., & Chemin, L. 2016, A&A, 591, A118

Spinrad, H., & Newburn, Jr., R. L. 1965, ApJ, 141, 965

Spinrad, H., Pyper, D. M., Newburn, Jr., R. L., & Younkin, R. L. 1966, ApJ, 143, 291

Stancliffe, R. J. 2005, PhD thesis, University of Cambridge

Steinmetz, M., Zwitter, T., Siebert, A., et al. 2006, AJ, 132, 1645

Stoehr, F., White, R., Smith, M., et al. 2008, in Astronomical Society of the Pacific Conference Series, Vol. 394, Astronomical Data Analysis Software and Systems XVII, ed. R. W. Argyle, P. S. Bunclark, & J. R. Lewis, 505

Strecker, D. W., Erickson, E. F., & Witteborn, F. C. 1978, AJ, 83, 26

Suh, K.-W., Jones, T. J., & Bowen, G. H. 1990, ApJ, 358, 588

Suh, K.-W., & Kim, H.-Y. 2002, A&A, 391, 665

Tanaka, W., Hashimoto, O., Nakada, Y., et al. 1990, Publications of the National Astronomical Observatory of Japan, 1, 259

Taniguchi, D., Matsunaga, N., Kobayashi, N., et al. 2018, MNRAS, 473, 4993

te Lintel Hekkert, P., Caswell, J. L., Habing, H. J., et al. 1991, A&AS, 90, 327

Tej, A., & Chandrasekhar, T. 2000, MNRAS, 317, 687

Tej, A., Chandrasekhar, T., Ashok, N. M., et al. 1999, AJ, 117, 1857

Tej, A., Lançon, A., & Scholz, M. 2003a, A&A, 401, 347

Tej, A., Lançon, A., Scholz, M., & Wood, P. R. 2003b, A&A, 412, 481

Terndrup, D. M., Frogel, J. A., & Whitford, A. E. 1991, ApJ, 378, 742

Thompson, R. R., Creech-Eakman, M. J., & van Belle, G. T. 2002, ApJ, 577, 447

Tiurina, N., Lipunov, V., Gorbovskoy, E., et al. 2013, The Astronomer's Telegram, 4888

Tsuji, T. 2009, A&A, 504, 543

Tuthill, P. G., Haniff, C. A., Baldwin, J. E., & Feast, M. W. 1994, MNRAS, 266, 745

Valdes, F., Gupta, R., Rose, J. A., Singh, H. P., & Bell, D. J. 2004, ApJS, 152, 251

Valenti, J. A., & Piskunov, N. 1996, A&AS, 118, 595

van Belle, G. T., Dyck, H. M., Benson, J. A., & Lacasse, M. G. 1996, AJ, 112, 2147

van Belle, G. T., Lane, B. F., Thompson, R. R., et al. 1999, AJ, 117, 521

van der Veen, W. E. C. J. 1988, PhD thesis, Leiden University, the Netherlands, (1988)

—. 1989, A&A, 210, 127

van der Veen, W. E. C. J., & Breukers, R. J. L. H. 1989, A&A, 213, 133

van der Veen, W. E. C. J., & Habing, H. J. 1988a, A&A, 194, 125

—. 1988b, A&A, 194, 125

—. 1990, A&A, 231, 404

van Langevelde, H. J., van der Heiden, R., & van Schooneveld, C. 1990, A&A, 239, 193

van Leeuwen, F., Evans, D. W., Grenon, M., et al. 1997, A&A, 323, L61

van Loon, J. T., Cohen, M., Oliveira, J. M., et al. 2008, A&A, 487, 1055

Vandenbussche, B., Beintema, D., de Graauw, T., et al. 2002, A&A, 390, 1033

Vanhollebeke, E., Blommaert, J. A. D. L., Schultheis, M., Aringer, B., & Lançon, A. 2006, A&A, 455, 645

Vassiliadis, E., & Wood, P. R. 1993, ApJ, 413, 641

Vazdekis, A., Cenarro, A. J., Gorgas, J., Cardiel, N., & Peletier, R. F. 2003, MNRAS, 340, 1317

Venkata Raman, V., & Anandarao, B. G. 2008, MNRAS, 385, 1076

Villaume, A., Conroy, C., Johnson, B., et al. 2017, ApJS, 230, 23

Volk, K., & Cohen, M. 1989, AJ, 98, 931

von Weizsäcker, C. F. 1938, Physikalische Zeitschrift, 39, 633

Wallace, L., & Hinkle, K. 1996, ApJS, 107, 312

—. 1997, ApJS, 111, 445

—. 2002, AJ, 124, 3393

Wallace, L., Meyer, M. R., Hinkle, K., & Edwards, S. 2000, ApJ, 535, 325

Weights, D. J., Lucas, P. W., Roche, P. F., Pinfield, D. J., & Riddick, F. 2009, MNRAS, 392, 817

Weiss, A., & Ferguson, J. W. 2009, A&A, 508, 1343

Westera, P., Lejeune, T., Buser, R., Cuisinier, F., & Bruzual, G. 2002, A&A, 381, 524

Whitelock, P. 1995, Ap&SS, 230, 177

Whitelock, P., & Feast, M. 1994, Ap&SS, 217, 153

—. 2000, MNRAS, 319, 759

Whitelock, P., Feast, M., & Catchpole, R. 1991, MNRAS, 248, 276

Whitelock, P., Marang, F., & Feast, M. 2000, MNRAS, 319, 728

Whitelock, P., Menzies, J., Feast, M., et al. 1994a, MNRAS, 267, 711

Whitelock, P. A., Feast, M. W., Koen, C., Roberts, G., & Carter, B. S. 1994b, MNRAS, 270, 364

Whitelock, P. A., Feast, M. W., Marang, F., & Groenewegen, M. A. T. 2006, MNRAS, 369, 751

Whitelock, P. A., Feast, M. W., & Van Leeuwen, F. 2008, MNRAS, 386, 313

Whitelock, P. A., Feast, M. W., van Loon, J. T., & Zijlstra, A. A. 2003, MNRAS, 342, 86

Willson, L. A. 1976, ApJ, 205, 172

Wilson, W. J., & Barrett, A. H. 1968, Science, 161, 778

—. 1972, A&A, 17, 385

Wing, R. F., & Lockwood, G. W. 1973, ApJ, 184, 873

Wing, R. F., Spinrad, H., & Kuhi, L. V. 1966, AJ, 71, 187

Winge, C., Riffel, R. A., & Storchi-Bergmann, T. 2009, ApJS, 185, 186

Wittkowski, M., Boboltz, D. A., Driebe, T., et al. 2008, A&A, 479, L21

Wittkowski, M., Boboltz, D. A., Ohnaka, K., Driebe, T., & Scholz, M. 2007, A&A, 470, 191

Wittkowski, M., Karovicova, I., Scholz, M., Ohnaka, K., & Boboltz, D. A. 2015, in Astronomical Society of the Pacific Conference Series, Vol. 497, Why Galaxies Care about AGB Stars III: A Closer Look in Space and Time, ed. F. Kerschbaum, R. F. Wing, & J. Hron, 327

Wong, T. K. 2017, PhD thesis, University of Bonn

Wood, P. R. 1979, ApJ, 227, 220

—. 1998, A&A, 338, 592

—. 2000, Publ. Astron. Soc. Australia, 17, 18

Wood, P. R., Habing, H. J., & McGregor, P. J. 1998, A&A, 336, 925

Wood, P. R., & Sebo, K. M. 1996, MNRAS, 282, 958

Wood, P. R., & Zarro, D. M. 1981, ApJ, 247, 247

Wood, P. R., Alcock, C., Allsman, R. A., et al. 1999, in IAU Symposium, Vol. 191, Asymptotic Giant Branch Stars, ed. T. Le Bertre, A. Lebre, & C. Waelkens, 151

Woodruff, H. C., Eberhardt, M., Driebe, T., et al. 2004, A&A, 421, 703

Woodruff, H. C., Ireland, M. J., Tuthill, P. G., et al. 2009, ApJ, 691, 1328

Woolf, N. J., & Ney, E. P. 1969, ApJ, 155, L181

Worthey, G. 1994, ApJS, 95, 107

Wright, C. O., Egan, M. P., Kraemer, K. E., & Price, S. D. 2003, AJ, 125, 359

Wright, E. L., Eisenhardt, P. R. M., Mainzer, A. K., et al. 2010, AJ, 140, 1868

Wright, N. J., Barlow, M. J., Greimel, R., et al. 2009, MNRAS, 400, 1413

Wu, Y., Singh, H. P., Prugniel, P., Gupta, R., & Koleva, M. 2011, A&A, 525, A71

Yamamura, I., Makiuti, S., Ikeda, N., et al. 2010, VizieR Online Data Catalog, 2298

Yanny, B., Newberg, H. J., Johnson, J. A., et al. 2009, ApJ, 700, 1282

Yee, S. W., Petigura, E. A., & von Braun, K. 2017, ApJ, 836, 77

Yuan, H.-B., Liu, X.-W., Huo, Z.-Y., et al. 2015, MNRAS, 448, 855

Yuan, W., Macri, L. M., He, S., et al. 2017, AJ, 154, 149

Zeilik, M. 2001, Active Learning Astronomy for Astronomy: The Evolving Universe

Zhu, Z. X., Friedjung, M., Zhao, G., Hang, H. R., & Huang, C. C. 1999, A&AS, 140, 69

Zijlstra, A. A., te Lintel Hekkert, P., Pottasch, S. R., et al. 1989, A&A, 217, 157